Mapping Human Brain Activity by Functional Magnetic Resonance Imaging of Blood Volume

Der Fakultät für Physik und Geowissenschaften
der Universität Leipzig
eingereichte

DISSERTATION

zur Erlangung des akademischen Grades
doctor rerum naturalium
(Dr. rer. nat.),
vorgelegt von

Master of Science in Physik Laurentius Huber
geboren am 9. November 1985 in Salzburg, Österreich

Leipzig, den 15. Dezember 2014

Universität Leipzig

Institut für Physik und Geowissenschaften

Max-Planck-Institut

für

Kognitions- und Neurowissenschaften

MAX-PLANCK-GESELLSCHAFT

Bibliographische Beschreibung:

Dissertation von Laurentius Huber, Universität Leipzig

Mapping Human Brain Activity by Functional Magnetic Resonance Imaging of Blood Volume

227 Seiten, 313 Literaturangaben, 70 Abbildungen, 12 Tabellen

Referat:
This dissertation describes the development, implementation, validation, optimization, and application, of a noninvasive and quantitative method for measuring cerebral blood volume changes with functional magnetic resonance imaging (fMRI) for mapping of neural activity changes.

Since its inception over twenty years ago, the field of fMRI has grown in usage, sophistication, range of applications, and impact. Nevertheless it has yet to exploit its full potential regarding, spatiotemporal resolution, signal specificity, and quantifiability of hemodynamic changes. By utilization of a new MR pulse sequence, new concepts of radio frequency pulses, and high magnetic fields (7 T), a novel fMRI method named SS-SI VASO is presented here that overcomes sensitivity limitations of other noninvasive quantitative imaging methods.

In order to validate that its signal represents changes in cerebral blood volume without other contaminations, SS-SI VASO is implemented in animal models for a close comparison with established, but invasive methods. A good agreement of blood volume sensitivity has been found with the new method compared to the established ones.

After its validation, the SS-SI VASO method and its unprecedented sensitivity was used to localize and quantify hemodynamic changes in applications where conventional oxygenation based fMRI methods are limited. (A) SS-SI VASO was used to investigate biophysical aspects of actively controlled arteries and passive balloon-like veins during activity induced hemodynamic changes. (B) SS-SI VASO was used to provide insights whether the interplay of neural activity and resultant vascular response are the same for tasks that increase neural activity compared to tasks that suppress neural activity. (C) SS-SI VASO was used to calibrate conventional oxygenation based fMRI to quantify local changes in oxygen metabolism. (D) The high sensitivity of SS-SI VASO was further used to obtain sub-millimeter resolutions and estimate activity changes between cortical layers. This enables to address questions not only *where* the brain is activated but also *how* and *whereby* this activity is evoked.

The implementation and application of this new SS-SI VASO fMRI method is a major step forward for the field of imaging neuroscience; it demonstrates that the current limitations of fMRI can be even overcome with respect to quantifiability, spatial specificity and distinguishing between vascular and neuronal phenomena.

Contents

List of Figures

List of Tables

Glossary

Abbreviation	Name
ASL	arterial spin labeling
ACDC	accounting for dynamic CSF
BOLD	blood oxygen level dependent
CNR	contrast-to-noise ratio
CSF	cerebrospinal fluid
EPI	echo planar imaging
FAIR	flow-sensitive alternating inversion recovery
FLAIR	fluid-attenuated inversion recovery
FWHM	full width half maximum
fMRI	functional magnetic resonance imaging
GE	gradient-echo
GLM	general linear model
GM	gray matter
M1	primary motor cortex
MION	monocristaline iron oxide nanoparticle
MR	magnetic resonance
MRI	magnetic resonance imaging
NBR	negative BOLD response
NIRS	near-infrared spectroscopy
OIS	optical imaging spectroscopy
PASL	pulsed arterial spin labeling
PBR	positive BOLD response
PET	positron emission tomography
PSF	point spread function
RF	radio frequency
ROI	region of interest
S1	primary sensory cortex
SAR	specific absorption rate
SE	spin-echo
SNR	signal-to-noise ratio
SI VASO	slab-inversion VASO
SS-SI VASO	slice-selective slab-inversion VASO
STD	standard deviation
tSNR	temporal signal-to-noise ratio
TR-FOCI	time resampled frequency offset corrected inversion
V1	primary visual cortex
VASO	vascular space occupancy
VERVE	venous refocusing for volume estimation
WM	white matter

Symbol	description
a	index for arterial blood, not to be confused with act for activity
act	index for activity
A	absorption coefficient or attenuation coefficient
α_{tot}	Grubb coefficient relating CBF with total CBV
α_v	Grubb coefficient relating CBF with venous CBV
b	index for blood
B_0	main magnetic field strength
B_1	magnetic field induced from RF coil
$BBPC$	blood-brain partition coefficient
β	measure of weighting between intra- and extravascular BOLD signal
c	index for capillary
$conc_i$	molar concentration of compartment i
CBF	cerebral blood flow
CBV	cerebral blood volume. If not stated differently, it denotes to the total blood volume containing arterial and venous contributions. It refers to the relative blood volume in units of ml per ml of tissue.
$CMRO_2$	cerebral metabolic rate of O_2
CVR	cerebral vascular resistance
d	dose of contrast agent
D	duration, e.g. pulse duration
δa	arterial transit time: time that blood needs to flow from large vessels within imaging slice to microvasculature
$\Delta BOLD$	relative BOLD signal change (normalized to the BOLD signal at rest) in dimensionless units
$\Delta\chi$	change in magnetic susceptibility
δt	arterial arrival time: time that blood needs to flow from the place below inversion slab into the imaging plane
$\Delta VASO$	VASO signal change
eff	index for effective
E	energy
ϵ	absorption coefficient of light
η	blood viscosity
FOV	field of view
G	magnetic field gradient
γ	gyromagnetic ratio
i	running index, e.g. across voxels
I, I_0	light intensity with and without sample

Symbol	description
H	Hamiltonian
HC	index for hypercapnia
$[HbO]$	concentration of oxyhemoglobin
$[Hbr]$	concentration of deoxyhemoglobin
$[Hbt]$	blood volume or concentration of total hemoglobin
$\hbar$	reduced Planck constant
K_B	Boltzmann constant
k	relaxation constant in iron oxide contrast agent experiments
κ	exchange rate, e.g. between intravascular and extravascular space
L	path lengths of photons in OIS
l	length of blood vessel
lab	index for laboratory frame of reference
λ	wavelength
M	BOLD calibration factor
$\vec{M}$	magnetization vector
$M_{x,y}$	magnetization in transverse plain in units of equilibrium magnetization. The indexes refer to the orientation of the magnetization vector components, not to be confused with the coordinates of the magnetization in space.
M_z	magnetization in z-direction in units of equilibrium magnetization
$\vec{\mu}$	magnetic moment of a spin
n	running index, e.g. for blood compartments
nc	index for nulling condition
nn	index for not nulled condition
θ	angle, e.g. in RF pulses as flip angle or phase skip
$\vec{\Omega}$	rotation axis, e.g. of a rotating frame of reference
p	p-value in statistical significance testing
$p_{up/down}$	probability a spin to be oriented parallel/anti-parallel to an external field
par	index for parenchyma
PS	permeability surface area product
r	radius, e.g. vessel radius
rot	index for rotating frame of reference
R_2^*	inverse of T_2^*
ρ	density in water volume per volume of tissue
$stim$	index for stimulation
S	signal

Symbol	description
t	time
tot	index for total blood including arterial and venous components
T	temperature
T_1	longitudinal relaxation time
T_2	transverse relaxation time in spin-echo sequences
T_2^*	transverse relaxation time in gradient-echo sequences
TE	echo time
TI	inversion time
TR	repetition time
TTH	transit time heterogeneity
τ	blood transit time through vasculature
v	index for venous blood
vis	index for visual stimulation
$V_{WM/GM/CSF}$	volume of WM/GM/CSF
ω	angular frequency
ξ	relative inversion efficiency
y	oxygenation
z	z-value in statistical significance testing
ζ	measure of inversion efficiency

1 Introduction

1.1 Background

The human brain is the physical structure most associated with mind or consciousness. It processes highly complex sensory impressions and provides coherent control over all actions of the body. A popular imaging method of brain structure is magnetic resonance imaging (MRI), which is based on the physical principle of nuclear magnetic resonance [Laurterbur, 1973]. The discovery of the blood oxygen level dependent (BOLD) effect in 1990 [Ogawa et al., 1990] introduced an imaging method to map not only brain structure, but also its function and activity. Hence, BOLD functional magnetic resonance imaging (fMRI) could be used to investigate brain activity noninvasively in the human brain [Bandettini et al., 1992][Turner et al., 1993]. Ever since, it has grown in usage, sophistication, impact, and range of applications. The functional principle of the BOLD imaging method is based on the fact that increased neural activity of a certain brain area is accompanied with increased energy metabolism and thus with a corresponding change in oxygenation of blood in local veins. Despite its popularity and robustness, BOLD fMRI is limited by two crucial physiological features. (A) The BOLD signal and the underlying blood oxygenation are not uniquely determined by changes in neural activity. It is also dependent on the physiological environment and therefore influenced by parameters such as the level of cerebral blood flow (CBF), cerebral blood volume (CBV), and many others. Consequently, the BOLD method is not quantitative and interpretations of its signal remain problematic. (B) The activity induced changes in blood oxygenation are not confined to the tissue region of increased activity. In fact, the biggest BOLD signal changes are usually located at large draining veins adjacent to the activated brain tissue. The interpretable spatial resolution is limited to approximately 3 mm [Turner, 2002]. Because of these limitations, it is desirable to directly measure additional physiological parameters such as CBF or CBV that may map neural activity more specifically and more quantitatively than the BOLD signal. However, when invasive methods should be avoided, measures of these parameters are usually dominated from high inherent noise level and thus limited by a low sensitivity compared to the BOLD signal.

1.2 Purpose of this thesis

The purpose of this thesis is to develop a new fMRI method that can overcome at least some of the above mentioned limitations of conventional BOLD fMRI and that can map correlates of neural activity more specifically and quantitatively such as CBF or CBV. In this thesis the focus lies on measuring CBV over measuring CBF for two major reasons. (A) Pilot experiments showed that with the available experimental setup, CBV-techniques have the potential to be considerably improved [Huber, 2011] compared to CBF-techniques [Ivanov, 2012]. (B) Invasive experiments in animals have shown that CBV changes are more specific to changes in neural activity compared to CBF [Kim et al., 2013].

The most-applied non-invasive fMRI method to measure changes in CBV has been developed by Lu et al. in 2003 and is referred to as Vascular Space Occupancy (VASO) [Lu et al., 2003]. The VASO contrast is based on the difference between longitudinal relaxation times (T_1) of tissue and blood. It is generated by applying an inversion pulse before signal acquisition, so as to effectively null the contribution of blood water magnetization at the time of signal excitation (so-called 'blood-nulling time'), while keeping substantial tissue signal for detection. Relative changes of this residual tissue signal are then associated with changes in CBV.

In this thesis, the VASO method is intended to be implemented for improved mapping of neural activity in human brain. In order to do so, the physical limitations are investigated and physical principles are applied to improve the sensitivity of VASO. The first approach to improve the sensitivity involves signal magnitude enhancement provided by applying high magnetic field strength such as 7 Tesla. However, the convergence of tissue and blood T_1 values at high fields results in disappointingly small VASO contrast making it difficult to take full advantage of the high signal-to-noise ratio (SNR) available at high fields. Furthermore at high fields, it is challenging to be in control of the sample magnetization arising from severe interferences of radio frequency (RF) fields. Here, a novel approach needs to be developed that can account for such challenges by means of a sophisticated order of slice-saturation and slab-inversion (SS-SI) gradient and RF pulses. The next goal of this thesis is to qualitatively investigate the new SS-SI VASO approach experimentally with respect to potential confounds. This needs to be done in order to ensure that its contrast reflects activity induced CBV changes as expected. For testing and debugging of new fMRI imaging methods, visual stimulation tasks with known activation signature have been helpful in the past [Belliveau et al., 1991] and should be thus used in this thesis as well. Additional quantitative validations by detailed comparisons with established invasive methods in animal models can further confirm its contrast origin.

After validation of its CBV sensitivity, the new SS-SI VASO method can be applied to address the final goal of this thesis; namely, to understand and overcome limitations of conventional BOLD fMRI with respect to its interpretability of vascular versus neuronal contributions and with respect to its coarse localization specificity of mapping neural activity.

1.3 Structure and overview of this thesis

This thesis deals with a novel method called SS-SI VASO designed to noninvasively measure changes in CBV in human brain at 7 T and it contains nine sub-studies applying it in different contexts. These sub-studies can be categorized into three chapters: Method: Studies that describe and investigate how SS-SI VASO works. Applications: Studies that investigate the advantageous and disadvantageous of SS-SI VASO with respect to other methods and assess whether SS-SI VASO can help to understand and overcome limitations of conventional BOLD fMRI. Limitations: Studies that investigate the range of experimental parameters for most accurate estimations of CBV changes with SS-SI VASO. These studies on limitations focus in particular on the robustness, the reproducibility, and the error estimation in the developed techniques.

2 Background[1]

In this chapter the physical concepts underlying MRI are introduced. Later sections of this chapter review the hemodynamic and metabolic changes accompanying neural activity and fMRI techniques to measure them.

2.1 Physical background

2.1.1 Magnetic resonance

Spin in magnetic field

Quantum mechanical spin is a basic property of elementary particles such as protons. Zeeman coupling describes the energy states of a spin in an external magnetic field in dependence of its orientation:

$$\hat{H} = -\vec{\mu} \cdot \vec{B}_0. \tag{2.1}$$

Here H denotes the Hamiltonian corresponding to Zeeman coupling. $\vec{\mu}$ stands for the magnetic moment of the spin and $\vec{B}_0$ denotes the external static magnetic field. By solving the Schrödinger equation, the difference of energy states of a single proton can be obtained:

$$\Delta E = \gamma \hbar B_0, \tag{2.2}$$

where γ denotes the gyromagnetic ratio. The energy states correspond to the orientation of the spin in the external magnetic field. Due to the low value of the reduced Planck constant $\hbar$, this energy difference is far below the thermal energy at room temperature. The distribution of energy states for a given temperature T is given by the Boltzmann distribution.

$$\frac{p_{up}}{p_{down}} = e^{-\frac{\Delta E}{K_B T}} \tag{2.3}$$

p_{up}, p_{down} are the probabilities of the spins to be oriented parallel or anti-parallel to the external magnetic field. With respect to energy, the spin state along the external field is preferred. This results in a macroscopic net magnetization parallel to the external magnetic field. Equation 2.3 suggests that the magnetization induced by the external magnetic field of 7 T at room temperature is only $\approx \frac{1}{20{,}000}$ of the maximum magnetization. This magnetization induced by the alignment of nuclear spins in the external magnetic field is the source of signal in magnetic resonance imaging.

---

[1] Parts of this chapter are based on more technical descriptions in [Huber, 2011].

Macroscopic magnetization in an RF field

In MRI, proton spins are not detected individually. The signal relies on the net magnetization of multiple water spins within a tissue volume in the order of μl. Hence individual spins do not experience a wave function collapse into their eigenstates [Hanson, 2008]. In fact, for the special case of a set of multiple spin-up/spin-down system, the expectation value of any measurement parameter of the resulting magnetization vector can be described by classical mechanics [Feynman et al., 1957].
According to Larmor precession, an external magnetic field $\vec{B}$ exerts a torque on any magnetic moment, such as the sample magnetization $\vec{M}$.

$$\frac{d\vec{M}}{dt} = \gamma\vec{M} \times \vec{B} \tag{2.4}$$

In MRI, the magnetic fields consist of a time-constant strong field $\vec{B}_0$ and a perpendicular oscillating field $\vec{B}_1$ that is induced by an RF coil. $\vec{B}_1$ is mostly adjusted to oscillate just with the Larmor frequency of a spin system within the main magnetic field $\vec{B}_0$. Conventionally, the main magnetic field's direction $\vec{B}_0$ is designated by the z-direction. During an magnetic resonance (MR) experiment, $\vec{B}_1$ is usually applied for very short periods only. Without loss of generality, this polarized RF field $\vec{B}_1(t)$ can be described with Eq. 2.5.

$$\vec{B}_1(t) = B_1\left[cos\left(\omega' t\right)\vec{e}_x - sin\left(\omega' t\right)\vec{e}_y\right] \tag{2.5}$$

Where ω' is the frequency of the oscillating RF field with respect to the frame of reference. Considering that the magnetic field is a superposition of $\vec{B}_0$ and $\vec{B}_1$, Eq. 2.4 can be expressed as:

$$\frac{d\vec{M}}{dt} = \gamma\vec{M} \times \vec{B}_{eff}, \tag{2.6}$$

with $\vec{B}_{eff} = \vec{B}_0 + \vec{B}_1(t)$ denoting the effective magnetic field. The magnetization precesses around this field with the effective Larmor frequency:

$$\omega_{eff} = \gamma B_{eff}. \tag{2.7}$$

The mathematical description of the behavior of the magnetization $\vec{M}$ can be simplified by transforming Eq. 2.6 into a rotating frame of reference. A useful relation for transforming a vector into a rotating frame of reference is Eq. 2.8 [Slichter, 1989].

$$\left(\frac{d\vec{p}(t)}{dt}\right)_{lab} = \left(\frac{d\vec{p}(t)}{dt}\right)_{rot} + \vec{\Omega} \times \vec{p}(t), \tag{2.8}$$

where $\vec{\Omega} = -\omega\vec{e}_z$. The equation of motion in the rotating frame is given by employing Eq. 2.8 in Eq. 2.6.

$$\left(\tfrac{d\vec{M}(t)}{dt}\right)_{\text{rot}} = \left(\tfrac{d\vec{M}(t)}{dt}\right)_{\text{lab}} - \vec{\Omega} \times \vec{M} = \gamma\vec{M} \times \vec{B}_{eff} + \gamma\vec{M} \times \tfrac{\vec{\Omega}}{\gamma} =$$

$$\underbrace{=}_{\vec{\Omega}\,=\,-\omega\vec{e}_z} \gamma\vec{M} \times \left(\vec{B}_{eff}\right)_{\text{rot}}$$

$$\text{with } B_{eff} \text{ in the rotating frame } \vec{B}_{eff} = \begin{pmatrix} B_1 cos\left((\omega_{RF} - \omega)t\right) \\ -B_1 sin\left((\omega_{RF} - \omega)t\right) \\ \underbrace{B_0 - \frac{\omega}{\gamma}}_{= 0 \text{ on resonance}} \end{pmatrix}. \tag{2.9}$$

Where $\omega' = \omega_{RF}$ - ω, with ω_{RF} being the frequency of the oscillating RF field in the rotating frame of reference, and ω being the frequency of the rotating frame of reference with respect to the laboratory frame of reference. On resonance, the magnetization in the rotating frame of reference is not affected by the magnetic field in z-direction, but only by a time constant B_1 field (see Eq. 2.9). In this picture, it is apparent that the influence of the RF field results in magnetization precession around an axis in the transverse plane. This precession can be used in MR experiments to flip the magnetization by an arbitrary angle θ, called flip angle:

$$\theta = \gamma \int_0^D B_1(t)\ dt, \tag{2.10}$$

where $B_1(t)$ is the amplitude of the RF magnetic field and D denotes the pulse duration. RF pulses that flip the magnetization into the transverse plane for subsequent data sampling are often called excitation pulses. RF pulses that invert the magnetization to evoke certain relaxation behavior are called inversion pulses.

Relaxation

A local magnetization cannot be assumed to be isolated. If the magnetization is not in thermodynamic equilibrium, interactions with its surrounding bring it back into equilibrium. The mechanism by which magnetization interacts with its surrounding can be described by two different relaxation components. (A) Longitudinal relaxation, associated with magnetization change parallel to the external magnetic field $\vec{B}_0$ and (B) transversal relaxation associated with magnetization change within the plane of precession and perpendicular to $\vec{B}_0$. Longitudinal and transversal relaxations are characterized by their corresponding time constants T_1 and T_2. These relaxation constants are highly dependent on the tissue properties and are the basis of most image contrasts used in MRI. T_1 relaxation can be described by energy transfer between single nuclei and the lattice they are embedded in. T_2 relaxation can be considered as dephasing of initially coherently precessing magnetizations. This dephasing can be caused by magnetic interaction between adjacent nuclei. Additional dephasing can be caused by inhomogeneities in the external magnetic field, e.g. caused by susceptibility variations and corresponding variations in Larmor frequency. The combined transversal relaxation of both extrinsic field variations and intrinsic dephasing caused by so called spin-spin interactions is referred to T_2^* relaxation.

The total behavior of magnetization including precession (Eq. 2.4) and relaxation is described with the Bloch equations:

$$\frac{dM_x(t)}{dt} = \gamma(\vec{M}(t) \times \vec{B}_{eff}(t))_x - \frac{M_x(t)}{T_2}$$

$$\begin{aligned} \tfrac{dM_y(t)}{dt} &= \gamma(\vec{M}(t) \times \vec{B}_{eff}(t))_y - \tfrac{M_y(t)}{T_2} \\ \tfrac{dM_z(t)}{dt} &= \gamma(\vec{M}(t) \times \vec{B}_{eff}(t))_z - \tfrac{M_z(t)-M_0}{T_1}. \end{aligned} \tag{2.11}$$

2.1.2 Magnetic resonance imaging

The precessing sample magnetization in an external static field is associated with an alternating magnetic field that can induce electrical current and voltage in an RF coil. This current can be sampled and used for reconstruction of MR images.
Magnetic field gradients cause magnetization at different locations to precess at different frequencies. By means of these locally specific precession frequencies, three perpendicular magnetic field gradients can be used for spatial encoding of the magnetization distribution in space.

Data acquisition and imaging

Transverse magnetization can be considered as:

$$M_{x,y}(t) = e^{-i\omega t} M(t=0)_{x,y} \overbrace{=}^{\omega=\gamma B} e^{-i\gamma B t} M(t=0)_{x,y}, \tag{2.12}$$

which is a solution of the transversal components of Eq. 2.11. $M(t=0)_{x,y}$ denotes here the magnetization components in the transverse plain at the time of image acquisition. The magnetic field B in Eq. 2.12 can be considered as a linear combination of a constant magnetic field B_0 and (presumably homogeneous) magnetic field gradients in all three spatial directions $B(x,y,z,t) = B_0 + xG_x(t) + yG_y(t) + zG_z(t)$. Including this in Eq. 2.12 gives:

$$M_{x,y}(t,x,y,z) = e^{-i\gamma B_0 t}\ e^{-i\gamma \int\limits_0^t (xG_x(t')+yG_y(t')+zG_z(t'))dt'} \qquad M_{x,y}(t=0,x,y,z). \tag{2.13}$$

The measured MR signal $S(t)$ is given as a spatial summation of MR signal from every point in space.

$$S(t) = \int\limits_x \int\limits_y \int\limits_z e^{-i\gamma B_0 t}\ e^{-i\gamma \int\limits_0^t (xG_x(t')+yG_y(t')+zG_z(t'))dt'} \qquad M_{x,y}(t=0,x,y,z)\ dx\ dy\ dz \tag{2.14}$$

The aim in MRI is to convert the signal $S(t)$ into the spatial distribution of transversal magnetization $M_{x,y}(t,x,y,z)$. Comparing the relationship between the signal in the time domain and the magnetization in the spatial domain in Eq. 2.14, the similarity to Fourier transformation becomes apparent. Based on this similarity, Eq. 2.14 can be written as a Fourier transformation:

$$S(t) = \int\limits_x \int\limits_y \int\limits_z M(t=0,x,y,z)\ e^{-i2\pi k_x x}\ e^{-i2\pi k_y y}\ e^{-i2\pi k_z z}\ dx\ dy\ dz$$

$$k_{x,y,z} = \tfrac{\gamma}{2\pi} \int\limits_0^t G_{x,y,z}(t')dt' \tag{2.15}$$

and

$$M(t=0,x,y,z) = \int\limits_{k_x}\int\limits_{k_y}\int\limits_{k_z} S(k_x,k_y,k_z)\; e^{-i2\pi k_x x}\; e^{-i2\pi k_y y}\; e^{-i2\pi k_z z}\; dk_x\; dk_y\; dk_z.$$

When transversal magnetization is localized in one slice only, Eq. 2.15 can be simplified to a two dimensional Fourier transformation. To get an intuitive picture of the conversion of the temporally changing signal to the spatial magnetization distribution, the concept of k-space can be helpful. In this picture, during signal acquisition, the k-vector is navigated throughout the k-space along a sampling path by altering the different gradient parameters in time. In most imaging methods, k-space is sampled line by line with constant velocity. This means that during data sampling, the gradient fields stay constant and the k-vector passes through the k-space with increasing time. Conventionally, the direction along acquired lines in k-space is referred to read direction and the direction across those lines is referred to phase direction. In practice, the k-space is sampled in discrete steps. Hence, MR signal generates a matrix of signal intensities for a discrete mesh of data points in k-space. To understand the conversion of the raw data from k-space, some features of Fourier transformation can be adopted: For example, the larger the k-space is, the higher the spatial resolution of the converted image becomes. And vice versa, the field of view (FOV) in the imaging space is defined with the sampling density in the k-space.

$$FOV_x = \frac{1}{\Delta k_x} \overset{\text{for } G_x = \text{ const}}{\widehat{=}} \frac{2\pi}{\gamma G_x \Delta t} \Longleftrightarrow \Delta x = \frac{1}{FOV_{k_x}} \tag{2.16}$$

When $M(x,y,z)$ in Eq. 2.15 is completely real (without imaginary components), symmetry properties of the Fourier transformation can be applied, e.g. in so-called Partial Fourier imaging.

Pulse sequence

A pulse sequence is a set of defined RF and gradient pulses, usually repeated many times during a scan session. A pulse sequence controls the magnetization manipulation before and during data acquisition. In a pulse sequence with periodically repeating RF pulses, the magnetization is approaching to a dynamic steady-state. This steady-state depends on the timing of RF pulses and relaxation.

Inversion recovery

In this thesis, an inversion recovery sequence will be of major importance. An inversion recovery sequence is based on an RF pulse that inverts the z-magnetization before the magnetization is excited (flipped into the transverse plain) for subsequent image acquisition. The magnetization can be sampled throughout its recovery to equilibrium. Inversion recovery sequences are suitable to obtain a T_1 based contrast. The time between inversion and data acquisition is called inversion time (TI). The time between two

subsequent inversions is called repetition time (TR).
According to the z-component of the Bloch equations (Eq. 2.11), the z-magnetization during an inversion recovery experiment can be described as:

$$M_z(TI) = M_0 - e^{-\frac{TI}{T_1}} \left(M_0 + M_z(t=0)\right), \tag{2.17}$$

where M_0 is the equilibrium z-magnetization and $M_z(t=0)$ is the initial condition of the z-magnetization. Typical T_1 values of human brain compartments at 7 T are summarized in Tab. 2.1.

reference	cortical GM	WM	CSF	blood
[Dobre et al., 2006]	-	-	-	2212 ± 53
[Rooney et al., 2007]	2132 ± 103	1220 ± 26	4425 ± 137	2587 ± 283
[Wright et al., 2008]	1940 ± 150	1130 ± 100	-	-
[Francis et al., 2008]	-	-	-	1950
[Abbas, 2009]	1900 ± 150	1075 ± 50	3700 ± 150	-
[Grgac et al., 2012]	-	-	-	2100 ± 90
[Wyss et al., 2013]	1954 ± 47	1285 ± 104	3867 ± 838	-
[Zhang et al., 2013]	-	-	-	2087 ± 131
[Rane and Gore, 2013]	-	-	-	2150 ± 200
approximate consensus	1950	1100	4000	2100

Table 2.1: Summary of literature values of T_1 at 7 T in ms: An approximate consensus often referred to as in this thesis is given in the last row.

EPI

Imaging data acquisition is always subsequent an excitation pulse and accompanied by switching gradients. The excitation is often accompanied by a gradient in z-direction. This so-called slice-selective gradient results in the fact that only a thin slice of the sample is in resonance with the RF field. Therefore, only the magnetization of that slice is getting excited. The gradients in read and phase encoding direction control dephasing and rephasing of the precessing magnetizations, dependent on their location within the excited slice. In a classical line-by-line k-space acquisition scheme, an excitation pulse is followed by gradients, in both, read and phase encoding direction, respectively. After that, a gradient in read direction rephases the magnetization associated with the sampling of a k-space line. This rephasing by means of switching gradients induces so-called gradient-echoes (GE). In echo planar imaging (EPI), k-space data are sampled throughout the k-space as long as the precessing magnetization in the transverse plane has not decayed away [Mansfield and Grannell, 1973]. In this way, the whole k-space of one slice can be acquired after a single excitation.

A so-called sequence diagram depicting the temporal interplay of RF field, gradient fields and, data sampling for the example of an EPI acquisition in shown in Fig. 2.1. The time it takes from the excitation pulse until the center of the k-space is reached is called echo time (TE).

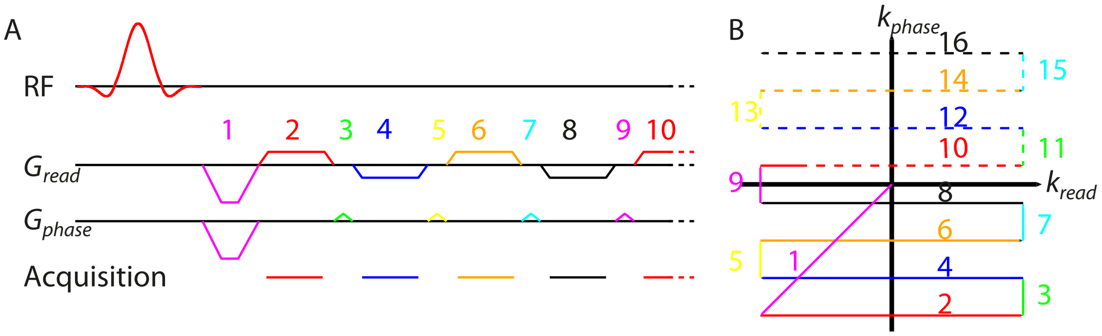

Figure 2.1: Sequence diagram and k-space data sampling in EPI: A) depicts the RF pulse and gradients during the readout in an EPI sequence. B) depicts the corresponding trajectory in k-space. It can be seen that k-space data are sampled along lines in read direction. Small blips in G_{phase} drive the trajectory in phase encoding direction.

2.1.3 High magnetic field strengths

Increased sensitivity at high field strengths

The magnetic field strength has a significant impact on the signal quality of the acquired data. According to the Boltzmann distribution (Eq. 2.3), the amount of magnetization pointing along the external field is approximately proportional to the main field strength. According to Faraday's law of induction, the voltage in the RF coil induced by the precessing magnetization is proportional to the frequency. Hence, signal increases with the square of the magnetic field. On the other hand, thermal noise generally increases linearly with frequency [Edelstein et al., 1986]. Consequently, the SNR, which is defined as the ratio of the mean signal over the standard deviation (STD) of the noise, increases proportional with increasing magnetic field strengths. Very recent experimental and numerical studies across field strength suggest that with novel coil designs, taking advantages of magnetic dipole modes, can achieve higher than linear increase of SNR with increasing field strength [Pohmann and Scheffler, 2014][Chen et al., 2014b]. Due to this SNR increase, the insatiable hunger for higher and higher sensitivities has driven the quest for higher magnetic field strengths in recent decades.

In fMRI studies, there are two primary sources of noise: thermal noise and physiological noise. Thermal noise comes about primarily from fluctuating stray currents in the sample, which can create random currents in the detector coils [Edelstein et al., 1986]. Thermal noise is completely caused by the experimental setup. The additional signal fluctuation, which can be detected in the living brain, is called physiological noise. Physiological noise is primarily caused by the movement of the body due to respiration or heartbeat. In addition, susceptibility variations resulting from neural activity in the resting brain can result in physiological noise. At high field strengths, the physiological noise is dominated by changes of the magnetic field due to respiratory motion.

In addition to SNR, temporal signal-to-noise ratio (tSNR) is a useful measure of image time course stability [Murphy et al., 2007]. It can be determined by dividing the mean signal of a time series by its standard deviation. To take full advantage of increased SNR at high field strengths, it is beneficial to adjust the acquisition parameters (e.g. resolution) such that the signal is thermal noise dominated rather than physiological noise dominated [Triantafyllou et al., 2011].

A more important quality attribute of MR images might be the contrast-to-noise ratio (CNR). In fMRI, CNR is usually defined as signal intensity differences between two activity states, scaled to image noise. This depends on SNR and on the relative functional signal changes accompanied by changes in neural activity.

Challenges of high fields

A severe limitation for in vivo imaging at high fields is the energy deposition and consequent tissue heating induced by transmission of RF pulses. The rate of energy deposition is quantifiable by the specific absorption rate (SAR). The energy of an RF pulse depends on the square of the pulse amplitude and the electrical conductivity of the imaged sample. Since the induced electric field in the tissue is proportional to ω^2 (Faraday's law of induction) [Vaughan and Griffiths, 2012], SAR increases quadratically with higher field strengths.

Another challenge of high field imaging are the increased inhomogeneities of B_1 and B_0 fields. B_1 inhomogeneities can result in inhomogeneous signal distribution in an MR image. The most critical challenge with respect to this thesis, however, is to achieve proper magnetization preparation despite these inhomogeneities. B_0 field inhomogeneities can result in image distortions and regional signal dropouts.

The reduced longitudinal relaxation rates at higher field strengths can result in less efficient temporal signal sampling.

Finally, the increased transversal relaxation rate at high field strengths can be a challenge. The correspondingly faster magnetization decay is directly associated with reduced SNR. This faster signal decay during k-space sampling can additionally result in image blurring, especially in EPI.

2.1.4 Adiabatic inversion

With the advent of ultrahigh magnetic fields, RF interactions with the human body become a critical challenge. When the RF wavelength approaches the size of the target object, diffraction and interference effects of RF far fields emerge. For example, human head images acquired at 7 T with a volume coil display a stronger signal intensity at the center compared to the periphery [Vaughan et al., 2001]. For conventional RF pulses, the flip angle is directly proportional to the B_1 magnitude ($\theta = \gamma \int_0^D B_1(t)\, dt$ (see Eq. 2.10)). Hence, the local distribution of the flip angle can result in an inhomogeneous signal intensity.

In this thesis it is essential to obtain full magnetization inversion independent of B_1 inhomogeneities. To achieve this, B_1-independent adiabatic inversion pulses can be applied[2]. Adiabatic inversion [Abraham, 1961] is a method of inverting magnetization by means of specific RF pulses. Adiabatic pulses are fundamentally different from conventional RF pulses used in MRI. Once the RF amplitude exceeds a certain threshold, the flip angle of an adiabatic pulse is independent of B_1. In contrast to conventional RF pulses, adiabatic pulses do not obey the relationship between the flip angle and the B_1 field amplitude, described in Eq. 2.10. Instead, the flip angle of an adiabatic pulse depends on how the B_1 field varies its amplitude and frequency (the phase respectively) during the pulse. One disadvantage of adiabatic inversion compared to conventional inversion is that it is usually accompanied with higher SAR values, partly due to usually longer pulse durations of adiabatic pulses compared to conventional pulses.

Adiabatic inversion is achieved by simultaneously modulating the amplitude and frequency of an RF pulse so that the orientation of the effective magnetic field B_{eff} changes its direction from the orientation along the z-axis to the orientation opposite to the z-axis, or vice versa. In an effective external magnetic field B_{eff}, the magnetization precesses along the surface of a cone around the field direction (see Eq. 2.6). Due to an additional RF field, the direction of B_{eff} and hence the axis of the 'cone of precession' can be altered. The 'cone of precession' orients rather parallel to B_0, if the irradiated RF field is below resonance, and rather anti-parallel, if RF field is above resonance. Hence, in the rotating frame of reference, the frequency of an adiabatic inversion RF pulse starts with a large negative value (below resonance), gradually increases to 0 (on-resonance) and ends at a large positive value (above resonance), or vice versa.

One of the most important quality attributes of adiabatic inversion pulses is the inversion efficiency ξ. It is defined as the ratio of the accomplished change of the z-magnetization to the largest possible change of the z-magnetization.

$$\xi = \frac{M_{z,\text{ before inversion}} - M_{z,\text{ after inversion}}}{2\ M_{z,\text{ before inversion}}} = \frac{1+\zeta}{2} \tag{2.18}$$

In this thesis, ζ is another additionally used definition of inversion efficiency. Defined as the part of z-magnetization that is perfectly inverted.

$$\zeta = -\frac{M_{z,\text{ after inversion}}}{M_{z,\text{ before inversion}}} \tag{2.19}$$

---

[2] A detailed description of the general physical principles of adiabatic inversion pulses and optimization of amplitude, phase and gradient shapes for use at high field strengths can be found in [Huber, 2011].

2.2 Biophysical background

2.2.1 fMRI relevant subdivisions of the brain

The brain can be subdivided into three main tissue types; GM, WM, and CSF (see Fig. 2.2A). In the context of fMRI, GM is of particular interest, as it contains the neuronal cell bodies and synapses participating in brain function. GM can be subdivided into cortical GM and noncortical GM (e.g. sub cortical GM, cerebellar GM, etc.). The cortical GM can be further subdivided into the Brodmann areas [Brodmann, 1909]. They are historically defined on their neuroanatomical cytoarchitectonic structure and have been correlated closely to diverse cortical functions ever since. For example, Brodmann areas 1, 2 and 3 are the primary somatosensory cortex (S1); area 4 is the primary motor cortex (M1); area 17 is the primary visual cortex (V1) (for approximate placement see Fig. 2.2A). GM is perfused from O_2- and glucose-enriched blood via large arteries at the cortical surface branching via diving arterioles into GM tissue, further branching into capillaries (Fig. 2.2B), where exchange of nutrients, byproducts, and water occurs. GM is drained in the opposite direction; blood leaves cortical tissue via diving venules into larger pial veins at the cortical surface. Microvascular vessels are fairly homogeneously distributed within GM [Weber et al., 2008], while macrovascular CBV is highest at the cortical surface, and decreasing with cortical depth [Duvernoy et al., 1981][Zhao et al., 2006]. The depicted schematic vessel geometry in Fig. 2.2B is drawn based on optical studies about brain vascularization [Duvernoy et al., 1981][Weber et al., 2008].
The next units of subdivision within cortical areas are cortical layers and cortical columns. There are up to 6 different cortical layers each containing a characteristic distribution of neuronal cell types and connections with other cortical and subcortical regions. The size and cytoarchitectonic structure of these layers is substantially different between cortical areas. Figs. 2.2C and 2.2D depict examples of primary motor cortex M1 and primary sensory cortices such as S1 or V1. In M1, layer V plays an important role. It contains the relatively large Betz cells (neurons) building the origin of the corticospinal tract. Inputs from other cortical regions terminate mainly in layer V and II/III. There is also a thalamocortical input mostly into layer V, but also into layer III and VI [Porter and Lemon, 2012]. Note that in adult humans, M1 is lacking layer IV. In S1 and V1, the most fMRI-relevant thalamocortical input terminates in layer IV [Logothetis, 2008]. Feed-back projections from other cortical areas have their synapses in upper and lower layers [Preuss et al., 1999] (Fig. 2.2D).

2.2.2 Neurophysiological correlates relevant for hemodynamic based fMRI

Neurons are active permanently. At any given time in the human brain, neurons are actively discharging by opening and closing multiple ion channels in their membranes. The corresponding fluctuations on electric field can be measured invasively with microelectrodes on and inside the brain [Logothetis et al., 2001]. This neuroelectrical activity can be broadly classified by local field potentials and spiking activity. Local field potential is generally believed to represent synaptic activity corresponding to neural input, while spiking activity represents neural output. The relationship of changes in local field

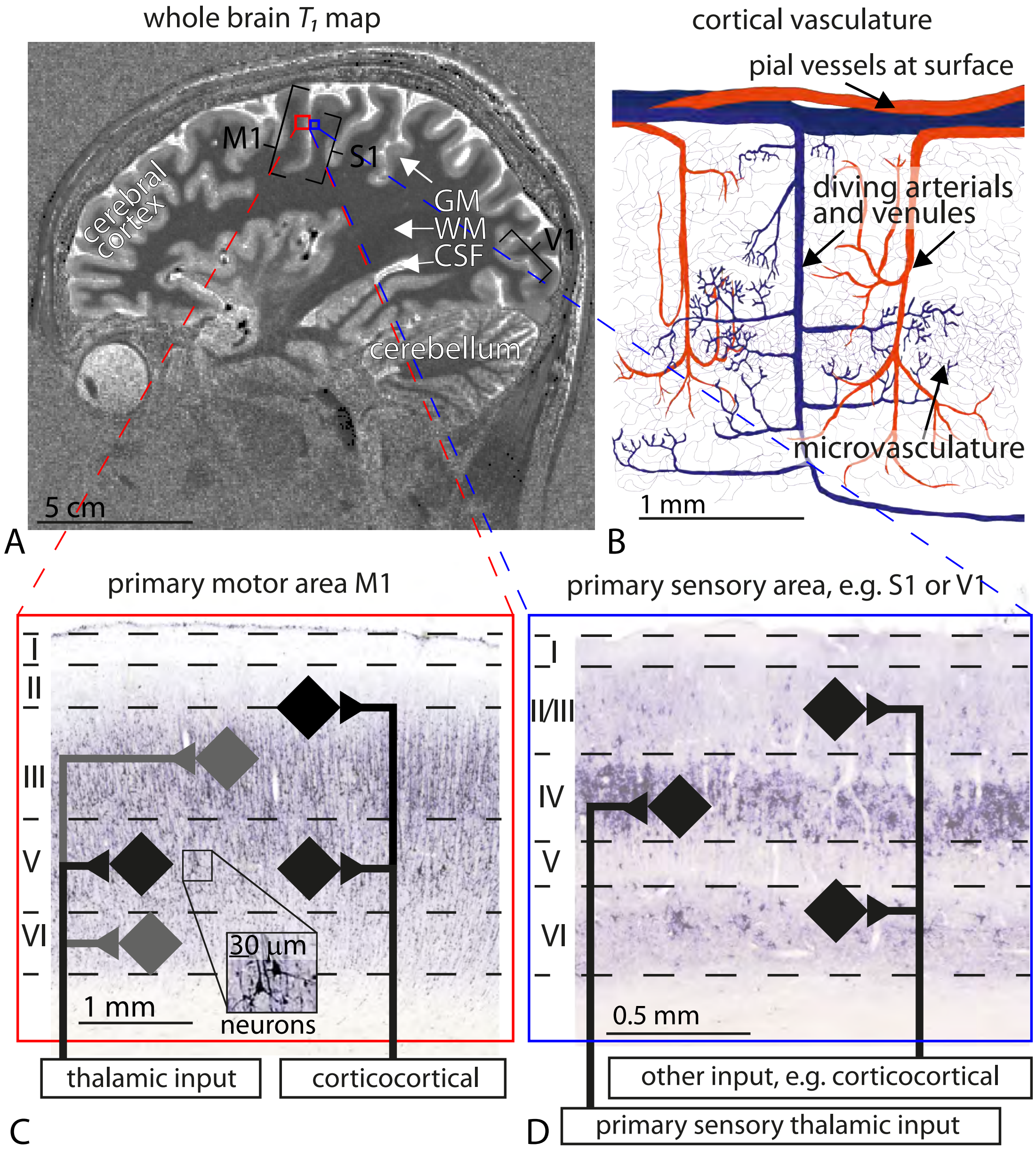

Figure 2.2: Schematic illustration of brain compartments on different spatial scales: A) depicts a T_1 map showing CSF in white, WM in dark gray, and GM surface bands in bright gray. Cortical areas M1, S1, and V1 are labeled. B) depicts the vasculature within GM. Large arteries (red) and veins (blue) are above the cortical surface. C) and D) depict the cytoarchitectonic anatomy across cortical layers. The main input pathways are schematically indicated by many of solid lines (axons) and diamonds (neurons). The background images refer to historical SMI and CTRL-1 staining, respectively.

potential and spiking activity to hemodynamic based fMRI has been examined directly and concurrently in animal studies, concluding that fMRI responses reflect neural input rather than neural output activity [Goense and Logothetis, 2008].
The human brain contributes only approximately 2% of the body mass, but it consumes approximately 20% of the bodies energy [Shulman and Rothman, 2005]. During an awake resting condition 80% of the brains energy is used for synaptic activity in contrast to spiking activity [Shulman and Rothman, 2005]. This energy demand comes mostly from restoring ion potentials and neurotransmitter cycling by converting ATP to ADP [Buxton, 2009]. It is consistent that the hemodynamics providing important nutrients such as O_2 and glucose meets the demand of activity induced increase of energy consumption [Roy and Sherrington, 1890], mostly dominated from synaptic activity.

2.2.3 Neurovascular coupling

Neural activity changes induce astrocyte and neuronal cells to send vasoactive signals into nearby arterioles and capillaries, consequently dilating. The exact neurovascular signal mechanisms remain an intense area of highly debated research, surveyed in current review articles [Howarth, 2014][Hall et al., 2014][Devor and Boas, 2012][Petzold and Murthy, 2011][Hamilton et al., 2010]. There are several partly independent signaling pathways and vascular control mechanisms.
Arteries and arterioles are surrounded with a coat of smooth muscle cells that can cause the vasculature to constrict and dilate, altering the flow resistance of blood accordingly. Astrocytes are involved in neurotransmitter recycling. They are in physical contact with both, synapses and blood vessels and have also been claimed to play a central role in cerebral vascular control. According to the immediate metabolic demand indicated, for example, by synaptic neurotransmitter releases or oxygen partial pressure changes, astrocytes control arteriole smooth muscles and thereby blood flow [Gordon et al., 2011][Iadecola and Nedergaard, 2007]. However, they are only involved in the late hemodynamic response [Nizar et al., 2013].
Capillaries are also believed to play an important role in active blood flow control mechanisms. Pericytes, which are apposed to capillaries and contain contractile proteins, dilate and contract the capillary vessel in response to different stimuli in the brain [Peppiatt and Attwell, 2004][Harrison et al., 2002][Hall et al., 2014]. Additionally, endothelial cells constituting the capillary walls plays an important role in blood volume increase [Krieger et al., 2012] and dilation propagation [Chen et al., 2014a][Anderson et al., 2006].
Independently, direct signaling pathways between neurons and blood vessels have been discussed as well [Peppiatt and Attwell, 2004].

Manipulating the vasculature with hypercapnia

Carbon dioxide (CO_2) is one of the first chemical agents found to have a strong vasodilatory effect that can nearly double the global CBF [Grubb et al., 1974]. The vasodilating effect is caused by the pH change at the arteriolar smooth muscles [Kuschinsky and Wahl, 1979] and is usually believed to have minimal effect on brain metabolism. Hypercapnia induced by breathing gas mixtures containing high fractions of CO_2 has been used in calibration of fMRI for estimation of neural activation-induced changes in oxygen metabolism [Davis et al., 1998].

2.3 Imaging physiological variables

Neural activity cannot only be located with placing electrodes directly in the brain. Hemodynamic correlates of neural activity can be visualized with functional magnetic resonance imaging. Under the assumption that local metabolic activity and the local vasculature are tightly coupled with brain function, these variables are widely used to map neural activity. There are several of these hemodynamic variables accessible with fMRI techniques used for indirect measured of neural activity. Most widely used are BOLD signal, CBF, CBV, and cerebral metabolic rate of oxygen ($CMRO_2$).

2.3.1 Imaging cerebral blood flow

In the adult resting brain, approximately 60 - 90 ml blood flows through 100 ml of GM tissue per min [Calamante et al., 1999]. CBF can be understood as a result of the interplay between pressure difference (ΔP) between the arterial and the venous blood compartments and the cerebral vascular resistance (CVR) of the vessels. Changes in CBF are modulated by diameter increase of arterioles and capillaries and corresponding reduction of CVR. CBF can be considered as:

$$CBF = \frac{\Delta P}{CVR}. \tag{2.20}$$

Autoregulation of CVR leads to a remarkably constant level of CBF, even if the pressure ΔP varies between 75 - 175 mmHg [Buxton, 2009].
According to Hagen-Poiseuille's Law, CBF can be written as:

$$\overbrace{\dot{V}}^{\text{Volume per second}} = CBF = \frac{\pi r^4 \Delta P}{8 \eta l} \propto r^4. \tag{2.21}$$

Where η is the dynamic blood viscosity, r is the vessel radius, and l denotes the length of the blood vessel.

Arterial spin labeling based CBF imaging

In the clinical context, CBF is routinely imaged, e.g. with radioactive labeled water in positron emission tomography (PET) or T_1 shortening contrast agent bolus tracking with MRI [Ewing et al., 2013]. For noninvasive functional CBF imaging at high field strengths ($\geq 7\,T$), flow-sensitive alternating inversion recovery (FAIR) [Kim, 1995] pulsed arterial spin labeling (PASL) has been the most popular method of choice [Pfeuffer et al., 2002][Bause et al., 2014][Gardener et al., 2009].
In PASL, arterial water is noninvasively tagged with magnetization inversion before it arrives at the tissue of the imaging slice. The labeling blood bolus is tagged outside the imaging slice with a short RF pulse 1 - 2 s before the image is acquired. Control images are acquired interleaved without such tagging. The signal difference between the two images is used to quantify the tagged blood that has flown into the imaging slice during that 1 - 2 s perfusion period. In order to account for functional changes

in the arterial arrival time, so called ‘quantitative imaging of perfusion using a single subtraction’ (QUIPSS II) pulses [Wong et al., 1998] can be used to obtain a properly defined bolus end, even in fMRI. In FAIR, the label is applied using a nonselective inversion pulse, while the control employs a concomitant slice-selective gradient, such that blood outside the imaging region is not inverted. Figure 2.3 depicts an example for perfusion mapping in the visual cortex with FAIR. Because of inhomogeneities in the B_1 field at 7 T [Van de Moortele et al., 2005], the blood magnetization tagging is insufficient in the lower parts of the head, visible also in the lack of contrast in the background T_1 map in Fig. 2.3. The difference of signal intensities between label and control condition arises from all the blood in the blue region outside the red region. High tilting of the imaging slices and the labeling slab can increase the bolus and thereby CNR.

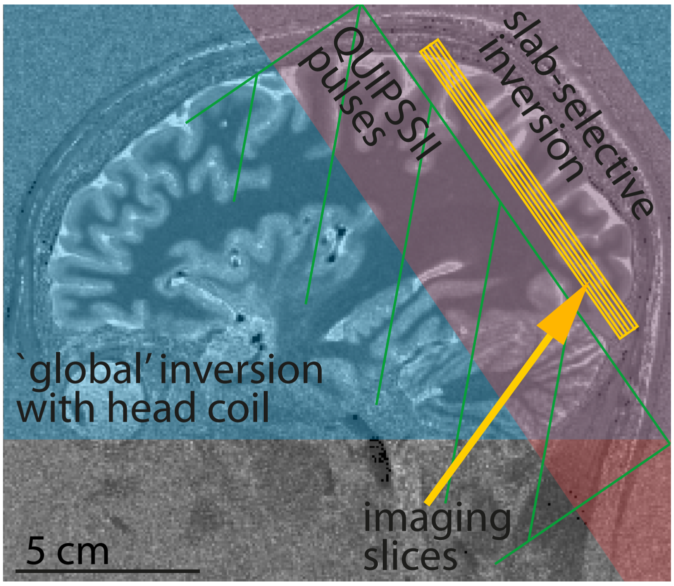

Figure 2.3: Schematic illustration of the geometrical aspects of obtaining perfusion maps with FAIR PASL: The slice and slab orientation is optimized for applications in visual cortex at high fields. The blue region outlines appropriate blood tagging for the control condition. The red region outlines the blood tagging for the label condition. In order to obtain maximum blood bolus (blood in blue region without red region), the labeling slab is highly tilted.

2.3.2 Imaging cerebral blood volume

CBV of the healthy adult brain is about 4% - 6% of the whole volume inside the skull [Grubb et al., 1974]. Considering blood vessels as cylindrical pipes, CBV of one vessel can be estimated as:

$$CBV \propto r^2. \tag{2.22}$$

Increase of neural activity correlates to a moderate increase in CBV [Buxton, 2010]. Since activity induced CBV increase is dominated from the capillaries close to the site of neural activation, CBV imaging is believed to map cerebral activity with high localized specificity [Kim and Ogawa, 2012]. In the healthy brain CBV and CBF are believed to be well correlated [Grubb et al., 1974]. In principle, however, CBF can be enhanced by increasing the velocity or the number of capillaries perfused, without an increase in CBV. To deduce an analytical connection between CBF and CBV, Eqs. 2.21 and 2.22 can be combined:

$$\overbrace{CBF \propto r^4}^{\text{Eq. 2.21}}, \overbrace{CBV \propto r^2}^{\text{Eq. 2.22}}$$

$$\Rightarrow \tfrac{CBF_{act}}{CBF_{rest}} = \left(\tfrac{r_{act}}{r_{rest}}\right)^4 = \left(\left(\tfrac{r_{act}}{r_{rest}}\right)^2\right)^2 = \left(\tfrac{CBV_{act}}{CBV_{rest}}\right)^2$$

$$\Rightarrow \tfrac{CBV_{act}}{CBV_{rest}} = \left(\tfrac{CBF_{act}}{CBF_{rest}}\right)^{\frac{1}{2}}. \qquad (2.23)$$

Grubb et al. found an empirical correlation for the quantitative relationship of CBF and CBV changes in rhesus monkeys to be:

$$\frac{CBV_{act}}{CBV_{rest}} = 0.8 \cdot \left(\frac{CBF_{act}}{CBF_{rest}}\right)^{0.38}. \qquad (2.24)$$

This correlation is likely different in arteries, capillaries and venules [Lee et al., 2001][Chen and Pike, 2010b]. The blood flow regulation mechanism of capillaries via pericytes controls CBF by increasing vascular resistance at few sites along the capillaries by throttling [Peppiatt and Attwell, 2004][Harrison et al., 2002]. This regulation of CBF is consistent with the observation that CBF increases substantially, while CBV increases moderately. A number of transient features in measurements on oxygenation response, e.g. a post-stimulus undershot has been suggested to result from differences in the temporal dynamics of CBV and CBF [Mandeville et al., 1999][Buxton et al., 1998] (see also section 2.3.3).

Iron-oxide contrast agent based CBV imaging

Exogenous contrast agents have long been used to enhance MRI and fMRI signals. The first fMRI study of human task-induced cerebral activity utilized a injection of a gadolinium chelate inducing susceptibility changes proportional to CBV [Belliveau et al., 1991]. Since gadolinium based methods have limited temporal resolution, iron oxide nanoparticles contrast agents, also traceable by their susceptibility properties have become the contrast agent of choice for high sensitivity fMRI in animals [Kim et al., 2013][Mandeville, 2012], and recently in the clinical context also in humans [Qiu et al., 2012]. Signal changes due to susceptibility arising from intravascular contrast agents can be described with the formalism given in [Tropres et al., 2001][Kim et al., 2013]:

$$\frac{S(d')}{S(d=0)} = \frac{S_{rest} e^{-\frac{4}{3}\pi\gamma B_0 \Delta\chi(d') CBV\ TE}}{S_{rest} e^{-\frac{4}{3}\pi\gamma B_0 \Delta\chi(d=0) CBV\ TE}}. \qquad (2.25)$$

Here, $S_{rest}(\rho, T_2^*$, etc.) contains signal parameters that are independent of iron oxide contrast agent injected, d is the relative dose of contrast agent in randomly oriented cylindrical vessels [Yablonskiy and Haacke, 1994], and assuming that $CBV \ll 1$, and $TE \gg \frac{1}{\delta\omega}$ [Tropres et al., 2001]. Note that CBV refers to the relative blood volume in units of ml per ml of tissue. Contrast agent induced susceptibility change $\Delta\chi(d') \approx 0.571\text{ppm} \times d'$ can be taken from the literature [Tropres et al., 2001][Kennerley et al., 2005]. Equation 2.25 can be rewritten as:

$$\frac{S(d')}{S(d=0)} \approx e^{-\Delta R_2^*(d')TE} \text{ where } \Delta R_2^*(d') \approx \frac{4}{3}\pi\gamma B_0 \Delta\chi(d') CBV. \tag{2.26}$$

And Eq. 2.26 can be simplified to:

$$\frac{S(d')}{S(d=0)} \approx e^{-\Delta R_2^*(d')TE} \underbrace{\approx}_{\Delta R_2^* \ll TE} 1 - \Delta R_2^*(d')TE, \tag{2.27}$$

where the slope of the contrast agent induced signal decay is directly proportional to CBV. In most applications $\Delta R_2^* \ll TE$ and the relative signal change is linear dependent on the susceptibility. At high magnetic fields or in voxels with very short T_2^*, this is not completely valid anymore and the decay must be considered to be exponential. Based on the measured change in R_2^*, Eqs. 2.26 and 2.27 can be used to estimate CBV:

$$CBV = \frac{\Delta R_2^*(d)}{\frac{4}{3}\pi\gamma B_0 \Delta\chi(d)}. \tag{2.28}$$

Contrast doses are usually in the range of 7 - 9 mg/kg to have a maximum contrast with minimum intravascular signal, but to still have enough extravascular signal left for acquisition. In order to minimize contaminations of susceptibility changes arising from the blood oxygenation level, measured signal intensities $S(d')$ and $S(d = 0)$ should refer to the same activation state. This means that for one measurement of activity induced CBV, two experiments must be conducted, one before contrast agent injection and one after contrast agent injection.

The most important limitation factor of iron oxide contrast agent based fMRI applications in humans is the invasiveness of the contrast agent injection.

Vascular space occupancy based CBV imaging

VASO is an fMRI method that measures CBV changes noninvasively through selective detection of signal changes in the extravascular compartment associated with changes in the nulled blood compartment [Lu et al., 2003]. The VASO contrast is based on difference between longitudinal relaxation times (T_1) of tissue and blood apparent in an inversion recovery sequence. The corresponding stead-state z-magnetization can be derived from Eqs. 2.17 and 2.19:

$$M_z(TI) = M_0 \left(1 - (1+\zeta)\, e^{-\frac{TI}{T_1}} + \zeta e^{-\frac{TR}{T_1}}\right). \tag{2.29}$$

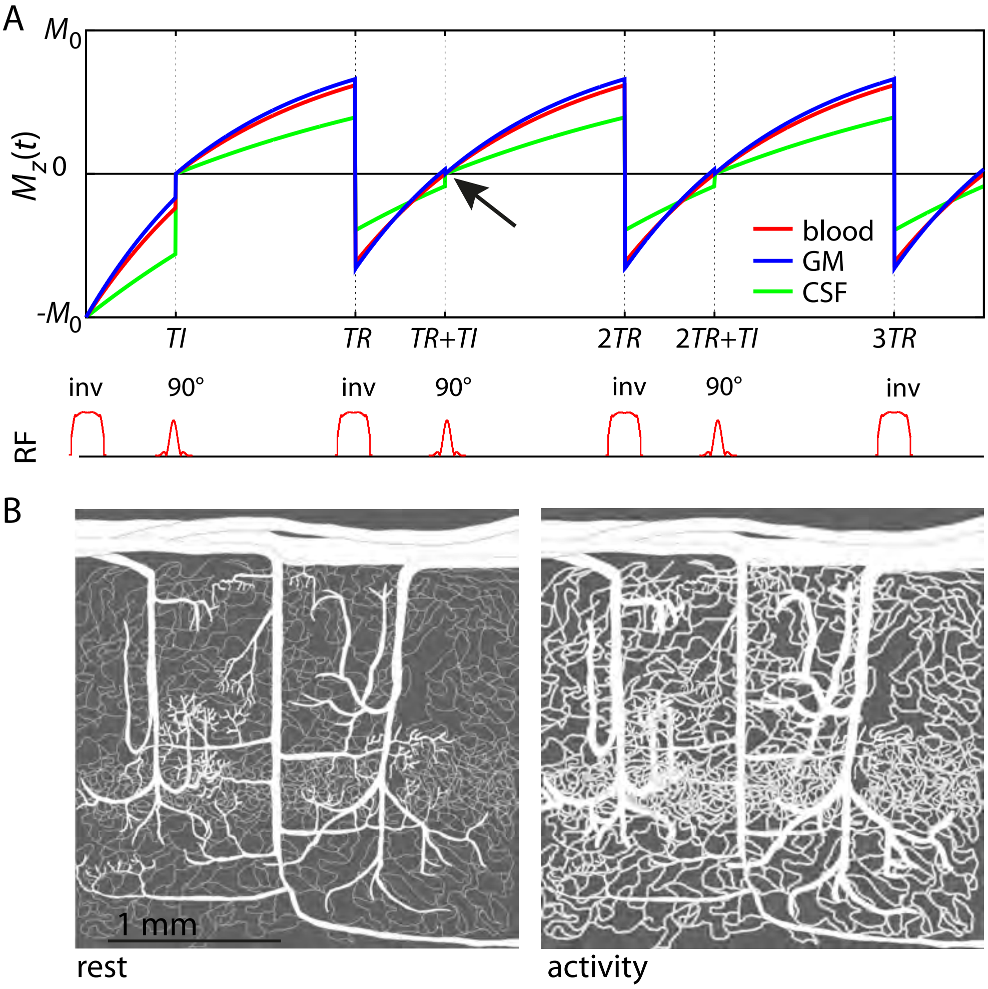

Figure 2.4: General functioning principle of VASO: (A) VASO is based on an inversion recovery sequence with TI chosen such that blood z-magnetization is nulled (black arrow). At this inversion time, GM z-magnetization is not nulled and contributing to MR signal. (B) For activity induced vasodilation, GM z-magnetization is displaced, resulting in MR signal decrease proportional to CBV increase.

The tissue-blood contrast is generated by applying an inversion pulse prior to signal acquisition, so as to effectively null the contribution of blood water magnetization at the time of signal excitation (so-called 'blood-nulling time'), while keeping substantial tissue signal for detection. This blood-nulling time can be derived by setting Eq. 2.29 to zero and solving the equation for TI:

$$TI = T_{1,b}\left(ln\left(1+\zeta\right) - ln\left(1+\zeta e^{-\frac{TR}{T_{1,b}}}\right)\right), \tag{2.30}$$

where $T_{1,b}$ it the blood longitudinal relaxation time. The expected z-magnetization of blood, GM and CSF is depicted in Fig. 2.4A. Relative changes of residual tissue signal are then associated with changes in CBV (Fig. 2.4B). VASO fMRI is the most widely used method for noninvasive mapping of CBV changes, particularly in humans and 3 T [Lu et al., 2013]. In dissociation of a large number of further developed VASO variants, the firstly proposed VASO approach is referred in this theses as 'original' VASO, following the terminology in [Lu et al., 2013].

Optical imaging spectroscopy based CBV measuring

Optical imaging spectroscopy (OIS), also known as optical intrinsic signal imaging is well established modality to measure changes in the concentration of total, deoxy-, and oxyhemoglobin, particularly in animal models and has been described in detail [Devor et al., 2012]. In short, it relies on the fact that oxy- and deoxyhemoglobin have different specific absorption coefficients as a function of wavelength. Due to light scattering and absorption, OIS is limited to the upper 1 - 1.5 mm of the cortex, generally requiring a cranial window or thinned skull to illuminate the cortex and image the reflected light with a camera. The amount of light reflected from the cortical surface is modulated by changes in the absorption coefficient of the tissue. These changes can then be related to changes in the concentrations of oxyhemoglobin (HbO), deoxyhemoglobin (Hbr) and the total hemoglobin (Hbt).

Classically with scattering, the attenuation and absorbance A of light intensity from I_0 to I can be described with the Beer-Lambert law as:

$$A = ln\left(\frac{I_0}{I}\right) = \left(\sum_{i\in\{HbO,Hbr\}} conc_i\ \epsilon_i\left(\lambda\right)\right) L(\lambda), \tag{2.31}$$

where A is the absorption or attenuation coefficient, I and I_0 are the light intensities with and without sample measured with a camera. $conc_i$ is the concentration of the compartment $i \in \{HbO, Hbr\}$ in the sample, and $\epsilon_i(\lambda)$ its absorption coefficient as a function of wavelength λ. L stands for the path length of photons through tissue. Measuring absorption A, taking the absorption coefficients ϵ_i from the literature and knowing L from Monte-Carlo-simulations of scattering photons, the concentrations c_i can be estimated. The change in attenuation of a specific wavelength of light is then given by:

$$\Delta A = L(\lambda)\left(\epsilon_{HbO}(\lambda)\Delta[HbO] + \epsilon_{Hbr}(\lambda)\Delta[Hbr]\right). \tag{2.32}$$

The blood volume changes or $\Delta[Hbt]$ is simply the summation of the changes in oxy- and deoxyhemoglobin:

$$\Delta[Hbt] = \Delta[HbO] + \Delta[Hbr]. \tag{2.33}$$

Even though, two wavelengths would be enough to determine the two concentrations $\Delta[HbO]$ and $\Delta[Hbr]$, usually three or four different wavelengths are used. The basic measuring principle of OIS is very similar to the working principle of near-infrared spectroscopy (NIRS) [Boas et al., 2014]. In contrast to OIS, NIRS is a non-invasive method and it has a much more limited spatial resolution.

2.3.3 Blood oxygen level dependent (BOLD) signal

The BOLD contrast is the MRI contrast caused by changes in blood deoxyhemoglobin. The functional effect of oxygenation of blood on the MR signal was first discovered in 1990 by Ogawa and colleagues [Ogawa et al., 1990]. Due to its noninvasiveness and its applicability for investigating working brains of human volunteers, BOLD fMRI has become the favored method in imaging neuroscience. The BOLD effect arises from two mechanisms, one biophysical and one physiological. (A) The paramagnetic deoxyhemoglobin produces magnetic field gradients around and through the blood vessels that decrease the MR signal due to induced magnetic field inhomogeneities and a corresponding dephasing of precessing magnetizations. (B) Although the increase of local $CMRO_2$ is accompanied by an increase of deoxyhemoglobin, the local CBF increase is by far the dominant contribution. This leads to an enhanced deoxyhemoglobin washout compared to resting state. Thus, brain activation is characterized by a drop in the local concentration of deoxyhemoglobin associated with an MR signal increase. The BOLD effect is not a direct measure of neural activity but rather depends on the blood flow and energy metabolism changes that arise from neural activity changes. Quantitative models, which describe the relative BOLD signal change $\Delta BOLD$ as a result of the interplay between CBF, venous CBV and $CMRO_2$, have been developed in the so-called deoxyhemoglobin dilution model [Davis et al., 1998][Hoge et al., 1999]. This model can be summarized as follows:

$$\begin{aligned} \Delta BOLD = M\left[1-\left(\frac{CMRO_2}{CMRO_{2,rest}}\right)^{\beta}\left(\frac{CBV_v}{CBV_{v,rest}}\right)\left(\frac{CBF_{rest}}{CBF}\right)^{\beta}\right] = \\ = M\left[1-\left(\frac{CMRO_2}{CMRO_{2,rest}}\right)^{\beta}\left(\frac{CBF}{CBF_{rest}}\right)^{\alpha_v-\beta}\right] = \\ = M\left[1-\left(\frac{CMRO_2}{CMRO_{2,rest}}\right)^{\beta}\left(\frac{CBV}{CBV_{rest}}\right)^{\frac{\alpha_v-\beta}{\alpha_{tot}}}\right]. \end{aligned} \tag{2.34}$$

Here, M is a calibration factor that is different between individuals and brain areas. It represents the maximum BOLD signal change that can be attained by achieving a theoretical 100% oxygen saturation in the venous vessels. It summarizes multiple physical and physiological parameters including TE, B_0, vessel geometry, susceptibility difference between blood and tissue, CBV_v, and venous baseline oxygenation. Note that the term $\Delta BOLD$ is a dimensionless quantity and refers to the relative MR signal change normalized to the baseline signal, e.g. in percent, while the terms 'BOLD contrast' or 'BOLD signal' are usually considered with respect to the qualitative contrast generation mechanism and do not denote physical variables. The β exponent in Eq. 2.34 describes the oxygenation and field strength dependence of the BOLD effect. At high field strengths, when intravascular signal is very small, it can be assumed to be $\beta = 1$ [Kida et al., 2000][Martindale et al., 2008]. The CBV or CBF terms in Eq. 2.34 can be substituted by each other by means of the Grubb relation [Grubb et al., 1974]. $\alpha_{tot} = 0.38$ is the Grubb value that describes the relationship between total CBF and total CBV. $\alpha_v = 0.18 \pm 0.02$ [Chen and Pike, 2010b] ($\alpha_v = 0.23 \pm 0.05$ [Chen and Pike, 2009]) is the Grubb value that describes the relationship between total CBF and venous CBV. The deoxyhemoglobin dilution model as given in Eq. 2.34 is based on few physical approximations and assumptions like $TE \ll \frac{1}{T^*_{2,act}} - \frac{1}{T^*_{2,rest}}$, the Fick principle[3], $CBV_{rest} \ll 1$, the Grubb relation, equal vessel sizes, and the homogeneous distribution of arteries, capillaries, and veins. Since these simplifications might not be valid across a wide range of voxel sizes, tissue types and vascular compartments, they could limit the applicability of the model in some cases. The deoxyhemoglobin dilution model is in the focus of current research, it has been widely applied [Hoge, 2012][Blockley et al., 2013][Buxton et al., 2014][Pike, 2012] and is continuously extended [Chiarelli et al., 2007][Gauthier and Hoge, 2012][Germuska and Bulte, 2014].

Since the BOLD contrast arises from a susceptibility effect, it depends on the field strengths and thus, it can fully benefit from the use of high fields, such as 7 T.
One of the most severe constraints on the spatial resolution of BOLD contrast fMRI is that blood oxygenation changes are not locally confined to the site of oxygen consumption, but also propagate downstream the vasculature tree. Hence, locally confined changes in oxygen consumption can give rise to spurious activation in veins at sites remote to the neuronal activity [Turner, 2002]. The BOLD effect is most pronounced on GE-images, indicating that the effect is primarily an increase of the local value of T_2^*. Aside of the GE-BOLD images, there is also another mechanism to measure the BOLD contrast. With the application of a 180° RF pulse right between the time of the excitation pulse and the time of signal acquisition, susceptibility induced dephasing around larger vessels can be refocused, resulting in a purely T_2 weighted so-called spin-echo (SE) contrast. The BOLD effect in SE images is theoretically less susceptible to large draining veins [Uludağ et al., 2009] but suffers from much smaller sensitivity [Norris, 2012]. If not stated differently, the term 'BOLD' in this thesis is regarded with respect to GE images and not SE images.

Time course of the BOLD response

During neural activation, the BOLD signal follows a unique evolution with an approximate shape as shown in Fig. 2.5. The precise shape of this hemodynamic response function is dependent on the activated brain area, the stimulation paradigm [Chen and

---

[3] The Fick principle is based on the continuity equation and states that all oxygen supplied by the arteries but not drained by veins must have been consumed in the tissue.

Pike, 2009][van Zijl et al., 2012], cortical depth [Yacoub et al., 2006], and the vascular compartment (arteries, capillaries or veins) [Kim and Kim, 2011]. During the first few seconds of the stimulus, the BOLD signal does not increase substantially. Some studies even report a small initial dip [Buxton, 2010][Uludağ, 2010]. The maximum is typically reached after about 5 - 8 seconds [Chen and Pike, 2009]. After stimulus cessation, the main response is followed by a pronounced post-stimulus undershoot. The post-stimulus undershot (and tentatively the initial dip as well) have been suggested to result from different evolutions of CBF, CBV and $CMRO_2$ changes [Chen and Pike, 2010b][van Zijl et al., 2012]. According to Eq. 2.34, negative BOLD signal change could be a results from increases in CBV or $CMRO_2$ without increases in CBF, or it could be a results of reduced CBF without reductions in CBV or $CMRO_2$.

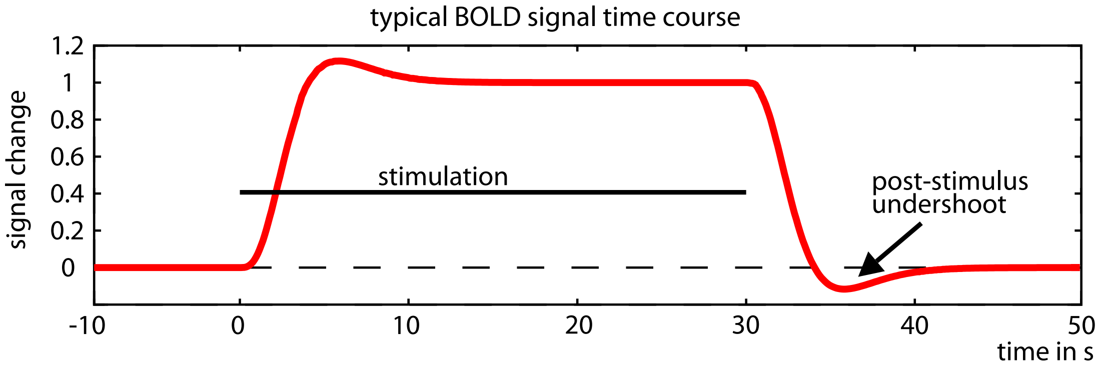

Figure 2.5: Schematic evolution of BOLD signal during neural activity: The response function is modeled for a stimulus of 30 s. Note the relatively late peak ≈ 6 s after the stimulus inception and the post-stimulus undershoot after the cessation of the stimulus.

Some studies suggest that the post-stimulus BOLD signal undershoot results from the fast recurrence to baseline in CBF, while venous CBV remains elevated after cessation of the stimulus [Mandeville et al., 1999][Buxton et al., 1998]. Other studies suggest that the undershoot is due to sustained elevation in oxygen consumption [Poser et al., 2011][Schroeter et al., 2006][Dechent et al., 2011]. There is currently no consensus on whether the post-stimulus BOLD signal undershoot is a neural, vascular or metabolic effect. More recent review articles conclude that all of the mentioned effects are partly responsible for the post-stimulus undershoot and shift the discussion on the weighting factors between those effects [Hua et al., 2011b][van Zijl et al., 2012].

2.3.4 Imaging oxygen metabolism with BOLD calibration

The most widely applied method of measuring changes of $CMRO_2$ with MRI is based on the deoxyhemoglobin dilution model (Eq. 2.34). Combining a BOLD signal measurement with an additional measurement of CBF (e.g. with ASL) or CBV (e.g. with VASO) provides a more quantitative insight into the underlying physiological changes.

However, this still does not provide sufficient information to estimate $CMRO_2$ because of unknown baseline state variables. The BOLD calibration approach seeks to measure this baseline condition summarized in M through a calibration experiment involving a hypercapnia of hyperoxia gas breathing manipulation. By means of the measured M-value, the change in $CMRO_2$ during a stimulation task can then be estimated. The functioning and application of BOLD calibration experiments is summarized in a number of recent review articles [Blockley et al., 2013][Pike, 2012][Hoge, 2012]: During the calibration experiment with hypercapnia but without a stimulation task, $CMRO_2$ can be assumed to be approximately conserved [Chen and Pike, 2010a] and Eq. 2.34 simplifies to:

$$\Delta BOLD = M \left[1 - \left(\frac{CBF}{CBF_{rest}}\right)^{\alpha_v - \beta}\right] = M \left[1 - \left(\frac{CBV}{CBV_{rest}}\right)^{\frac{\alpha_v - \beta}{\alpha_{tot}}}\right], \tag{2.35}$$

such that M can be calculated:

$$M = \frac{\Delta BOLD}{\left[1 - \left(\frac{CBF}{CBF_{rest}}\right)^{\alpha_v - \beta}\right]} = \frac{\Delta BOLD}{\left[1 - \left(\frac{CBV}{CBV_{rest}}\right)^{\frac{\alpha_v - \beta}{\alpha_{tot}}}\right]}. \tag{2.36}$$

Rearranging Eq. 2.34 and knowing M from the calibration experiment, $CMRO_2$ during a stimulation experiment can be estimated.

$$\begin{gathered} \frac{CMRO_2}{CMRO_{2,rest}} = \left(1 - \frac{\Delta BOLD}{M}\right)^{\frac{1}{\beta}} \left(\frac{CBV}{CBV_{rest}}\right)^{\frac{\beta - \alpha_v}{\beta \alpha_{tot}}} \\ \Updownarrow \\ \frac{CMRO_2}{CMRO_{2,rest}} = \left(1 - \frac{\Delta BOLD}{M}\right)^{\frac{1}{\beta}} \left(\frac{CBF}{CBF_{rest}}\right)^{1 - \frac{\alpha_v}{\beta}} \end{gathered} \tag{2.37}$$

Values of $\Delta CMRO_2$ for a visual stimulation task are reviewed to be in the range of 15% - 32% [Ivanov, 2012].

3 Method

3.1 SS-SI VASO: A method for measuring changes in cerebral blood volume with high contrast-to-noise ratio in human brain at 7 T[1]

This section describes a study to develop and examine a new method for measuring changes in blood volume. First, the necessity and challenges of such a new method at high field strengths is elucidated. After that, it is explained how the new method works. The applicability of this method is examined in vivo for a standard visual task and its results are discussed with respect to potential contaminations.

3.1.1 Motivation and challenges of developing SS-SI VASO

As noted in earlier sections, local change in CBV provides a quantitative physiological variable to detect neuronal activation and may localize changes of neural activity better than other variables accessible by fMRI, such as CBF and blood oxygenation level. In particular, CBV weighted fMRI has shown higher local specificity for the distribution of neural activity across cortical layers [Kim and Kim, 2010][Lu et al., 2004b] and location on the cortical surface [Kennerley et al., 2010] than the commonly used BOLD fMRI. However, the widespread use of CBV weighted fMRI in humans is hampered due to the invasiveness of exogenous contrast-based CBV measurements and the low SNR of noninvasive CBV weighted methods, such as VASO.

The implementation of VASO at high magnetic field strengths and the corresponding signal increase can potentially account for such CNR limitations. However, four confounding effects have hampered the implementation of VASO at high magnetic field strengths so far [Hua et al., 2012][Jin and Kim, 2008b]. First, the tissue signal at the blood-nulling time is significantly reduced due to convergence of tissue and blood T_1 values at high fields [Rooney et al., 2007]. This results in a CNR for VASO that is disappointingly small. Second, the positive BOLD signal change during neural activation increasingly counteracts the negative VASO signal change [Lu and van Zijl, 2005] with increasing magnetic field strength. Third, inhomogeneities in the RF fields and safety limits concerning SAR of emitted energy hamper efficient magnetization inversion, which is vital for blood-nulling in VASO. The fourth issue of using VASO at high fields is the higher susceptibility to blood inflow effects, resulting from the conjunction of two characteristics of high field MRI. On one hand, the inversion volume is reduced when a head coil is

---

[1] This section is summarized in the paper [Huber et al., 2014b] and it is further extended in the paper [Krieger et al., 2014b].

used for RF transmission (which is common at 7 T). The correspondingly smaller local extent of the inversion region increases the likelihood of inflow of fresh blood during the blood-nulling time. On the other hand, blood-nulling time is increased at high-fields due to longer blood T_1, which further increases the possibility of inflow effects.

Confounding BOLD signal contributions can be avoided by using a very short TE [Hetzer et al., 2011][Lu et al., 2003] or estimating the signal at $TE = 0$, while acquiring images at multiple echo times [Lu and van Zijl, 2005]. Here, a new BOLD correction mechanism is presented. To assess and eliminate BOLD contributions, data without blood-nulling (i.e. with signal changes entirely based on the BOLD effect) are acquired, interleaved with BOLD contaminated VASO data. The almost simultaneously detected BOLD signal thus permits straightforward correction of the VASO signal.

Potential methods to increase tissue z-magnetization at the time when blood water magnetization is nulled have been proposed in several studies. Tissue signal can be increased by up to a factor of 1.5 using an off-resonant magnetization transfer pulse [Hua et al., 2009][Hua et al., 2012]. The signal can also be increased by manipulating the steady-state z-magnetization with adaptations in the repetition time and inversion time of the inversion recovery sequence [Jin and Kim, 2008b][Shen et al., 2009][Wu et al., 2008][Wu et al., 2007].

Jin and Kim showed that blood z-magnetization cannot approach steady-state during TR at high fields, where the blood-nulling time is long and no body-coil is typically available [Jin and Kim, 2008b]. They suggested that the blood magnetization should be considered not to be in steady-state, and to adjust the blood-nulling time accordingly. The blood z-magnetization can be maintained in this non-steady-state by inverting the blood only in a slab within the volume included by the coil coverage. Simulations of this slab inversion VASO (SI VASO) showed that the resulting tissue signal can be significantly increased [Jin and Kim, 2008b]. Corresponding measurements in anesthetized cats at 9.4 T showed improved cortical-layer specificity compared to spin-echo BOLD signal [Jin and Kim, 2008b]. To avoid inflow of fresh blood in cat SI VASO, however, blood signal is not nulled, so that the SI VASO sequence becomes like a FAIR sequence [Kim, 1995] without a control condition and with a TI few hundred ms before blood nulling. Thus, quantitative estimation of CBV changes and distinguishing between blood flow and volume changes become difficult.

Following the method by Jin and Kim [Jin and Kim, 2008b], a slab-selective inversion pulse was implemented with potentially higher SNR compared to original VASO. In human brain at 7 T, the time for blood to flow from the lower bound of the inversion slab into the microvessels of the imaging slice (‘arterial arrival time’) is similar to the blood-nulling time. This enables TI, the inversion efficiency, and the inversion slab thickness to be mutually adjusted, so that all blood in the microvasculature is nulled, thus reducing potential inflow contamination of the VASO contrast. In order to further increase GM magnetization at the blood-nulling time, the steady-state of stationary tissue magnetization was arranged to be maximal at the nulling time of non-steady-state flowing blood. This could be achieved by applying additional 90° RF pulses in the imaging slice shortly before slab-selective inversion. The low tissue z-magnetization at the time of inversion results in a large z-magnetization at the subsequent blood-nulling time TI. These 90°

RF saturation pulses are also used to flip the tissue magnetization into the transverse plane within the BOLD signal acquisition module. This technique is described as slice-saturation slab-inversion VASO or SS-SI VASO.
The anticipated increase in functional CNR SS-SI VASO, despite the aforementioned obstacles of high-field VASO, may be used to improve the spatial resolution of CBV change measurements in healthy human brains.

3.1.2 Theory of SS-SI VASO

The pulse sequence diagram and the associated relative z-magnetization of once inverted blood, GM, and CSF are depicted in Fig. 3.1. Tissue signal increase in SS-SI VASO is achieved by manipulating the z-magnetization of flowing blood differently from that of stationary GM. As detailed below, inversion slab thickness, inversion efficiency, inversion times $TI1$ and $TI2$, and TR are adjusted such that two conditions are fulfilled. These are (A) no uninverted blood should enter the microvasculature of the imaging region during $TI1$, and (B) microvasculature of the imaging slice should be completely refreshed by magnetization outside the violet slice of Fig. 3.1B between $TI2$ of the previous TR and $TI1$ of the present TR.

Difference to other VASO methods

Even though the sequence diagrams of original VASO, SI VASO and the new SS-SI VASO seem to be very similar, the underlying signal generation is fundamentally different. For best comparison of the three methods, the expected z-magnetizations are shown in Fig. 3.2. There are three distinct aspects in which SS-SI VASO is fundamentally different from previous VASO approaches:

- In the SS-SI VASO method, the signal increase comes from the fact that stationary tissue in the imaging slice has very small z-magnetization just before the inversion pulse is played out. This is different in the original VASO or in the SI VASO method. This is the major reason for the signal increase in SS-SI VASO approach.
- The different mechanism of tissue magnetization saturation before inversion results in SI VASO and SS-SI VASO result in different inflow-outflow constraints. For example, the slice dependent refilling condition of the vasculature is a unique feature of the SS-SI VASO method compared to the original VASO or the SI VASO.
- The blood flow component of the signal change is substantially different for SI VASO and SS-SI VASO. In order to avoid inflow effects in SI VASO [Jin and Kim, 2008a], the TI has to be kept to a value shorter than the blood-nulling time. In the new SS-SI method on the other hand, these inflow effects can be avoided by applying other methods, e.g. partial inversion (see section 4.3.1). The incomplete blood nulling in SI VASO [Jin and Kim, 2008b] introduces flow weighting on top of the pure VASO contrast.

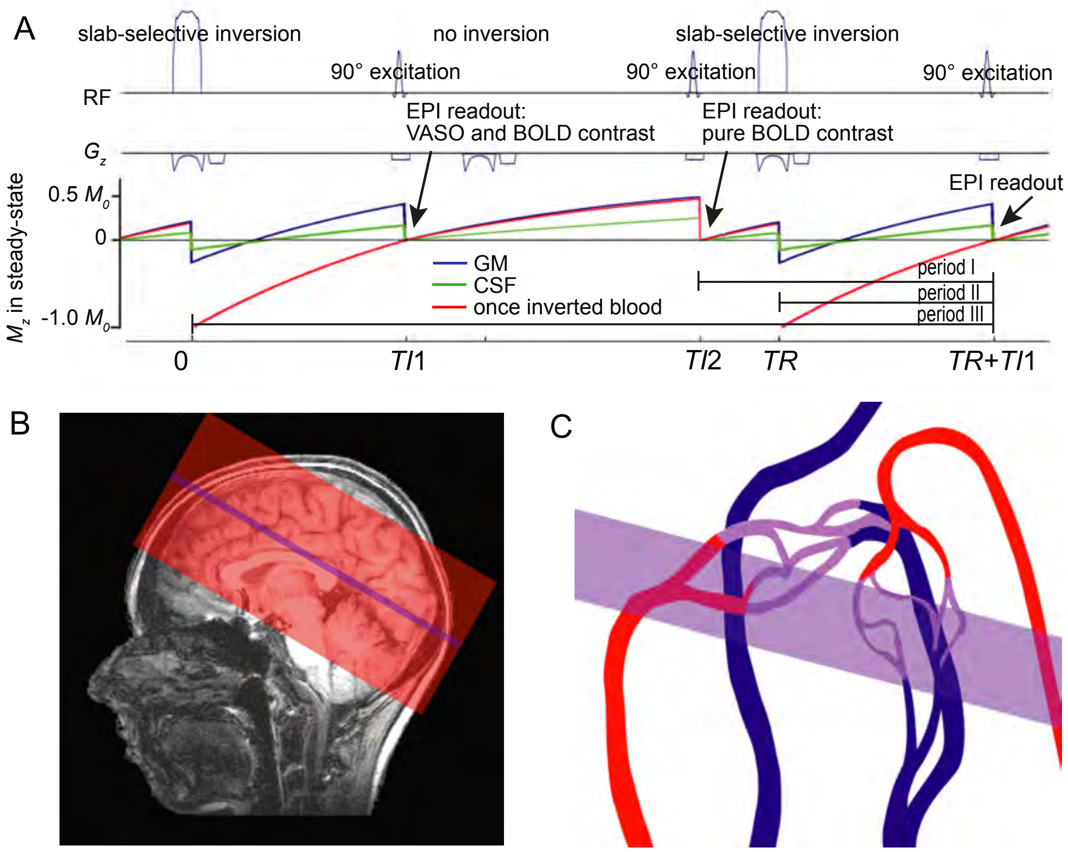

Figure 3.1: A) depicts the sequence diagram and the corresponding steady-state z-magnetization of GM, CSF and blood in SS-SI VASO. The depicted blood component refers to once inverted blood z-magnetization. Therefore, blood z-magnetization is -M_0 after inversion, independent of the magnetization before inversion. B) depicts schematically the geometry of inversion slab and imaging slice. The nulling condition requires that the (violet) imaging slice is refilled with unsaturated blood during period I. Furthermore, it is required that no blood outside of the (red) inversion slab flows into the microvasculature of the (violet) imaging slice during period II. Additionally to the refilling condition of the imaging slice during period I, the inversion slab (red) should be refilled with fresh blood during period III. C) illustrates how the vasculature of the imaging slice is refilled during consecutive 90° pulses. Even though, it contains arterial, capillary and venous compartments, the refilling time can be much shorter that the refilling time of the total vascular tree.

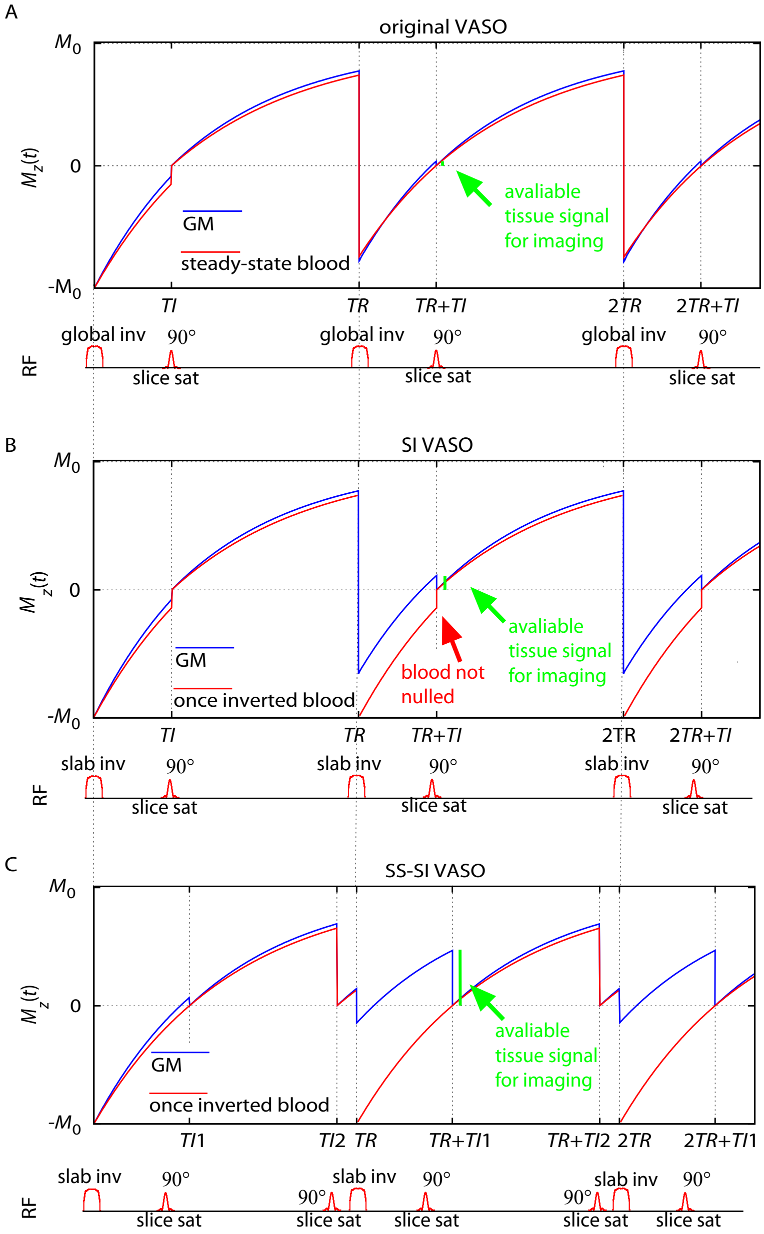

Figure 3.2: Comparison of z-magnetization evolution in original VASO, SI VASO and SS-SI VASO: (A) In the original VASO approach, available GM z-magnetization at the blood-nulling time is orders of magnitudes smaller than the equilibrium magnetization. (B) In SI VASO, GM z-magnetization at the blood-nulling time is significantly increased. (C) In SS-SI VASO, the GM z-magnetization at the blood-nulling time is further increased. Depicted z-magnetizations are based on assumed relaxation times of blood and GM: $T_{1,b}/T_{1,GM} = 2.1/1.9$ s (Tab. 2.1).

Inflow of uninverted blood magnetization:

The nulling time of once inverted blood magnetization is given by

$$TI1 = ln(2)\ T_{1,b} \tag{3.1}$$

(according to Eq. 2.17), which yields approximately 1450 ms at 7 T ($T_{1,b}$ is the T_1 of blood water), assuming $T_{1,b}$ = 2100 ms (according to review of literature values in Tab. 2.1). The inversion slab must be thick enough that no uninverted ('fresh') blood magnetization reaches the imaging slice during that time. In humans, it takes approximately 1000 - 1400 ms until blood from the upper neck region reaches the larger vessels of the occipital lobe [Chen et al., 2012][Mildner et al., 2014]. Furthermore, it takes another 400 - 500 ms until fresh blood reaches the small arterioles that dynamically change their diameter during activation [Chen et al., 2012]. These numbers suggest that the blood-nulling time is shorter than the arterial arrival time of fresh blood, and it takes longer than $TI1$ for uninverted blood magnetization to arrive in the microvasculature of the imaging slice. A more detailed and quantitative description of such inflow effects is given in section 5.1.
SS-SI VASO can also be applied in brain regions or in physiological conditions such as hypercapnia with significantly shorter arterial arrival times. A method to address and avoid corresponding inflow effects of fresh, not inverted blood is described in section 4.3.1.

Outflow of blood that has not been inverted once:

SS-SI VASO captures blood that has been inverted only once, and that has not experienced the previous excitation pulse. Therefore, two refilling conditions must be fulfilled. First, the period between blood-not-nulled and blood-nulled image acquisitions must be longer than the refilling time of the vasculature of the imaging slice (period I in Fig. 3.1). Otherwise, blood magnetization, which had experienced the previous excitation pulse, would not be completely nulled. The macro-vessels with high blood flow velocities penetrating the imaging slice are believed to be more quickly refilled than the microvasculature. Therefore, the refilling time of the microvasculature is considered in more detail. Blood velocity measurements suggest that the microvasculature is refilled in 1 - 1.5 s [Hillman et al., 2007][Kleinfeld et al., 1998][Pawlik et al., 1981]. Results of Nakagawa et al. suggest that both plasma and red cell transit times through the microvasculature are shorter than 0.5 s [Nakagawa et al., 1995]. Reviewing seven studies, the microvascular transit time was estimated to be 1.16 s [Jespersen and Østergaard, 2012]. In the review article [Kim and Bandettini, 2010], it is concluded that the typical lifetime of water in capillaries is 0.5 ms. Considering these numbers, it can be assumes that it takes less than 1 - 1.5 s until the microvasculature is refilled with fresh blood, which has not experienced the previous excitation pulse.
The second refilling condition refers to the inversion slab (red area in Fig. 3.1B) during period III. It states that there should be no twice-inverted blood magnetization in the imaging slice during VASO image acquisition. Note that period III is longer than TR. This fact can be explained with the different timing between generation of the VASO

contrast by means of inversion and VASO image acquisition. Even if not all inverted blood magnetization has left the imaging slice during the next inversion pulse, it will not contribute to the MR signal as long as no image is acquired. Only if the blood magnetization still has not left the imaging slice when the following image is acquired (after period III), it is captured and contaminates the contrast.

BOLD correction

Additional to the acquisition of BOLD contaminated VASO signal change, BOLD signal change without VASO contamination is acquired by implementing the inversion pulse only prior every second EPI readout (see Fig. 3.1A). When the BOLD contrast contribution is known, the BOLD contamination in the VASO image can be factored out.
Here a simple model is considered to explain the effect of the proposed BOLD correction. The gradient-echo signal of a voxel can be considered as the z-magnetization in the voxel at the time of excitation multiplied with an exponential dephasing term: $S \propto M_z e^{-TE/T_2^*}$, where M_z depends on the proton density, the inversion time $TI1$, and the relative volume distribution of the compartments in the voxel. T_2^* denotes the transverse relaxation time in gradient-echo acquisitions. If a voxel contains only blood and GM (no WM or CSF), the signal arising only from GM during the nulling condition (nc) can be expressed as:

$$S_{GM,nc} \propto M_{z,GM,nc} \; e^{-\frac{TE}{T^*_{2,GM}}}. \tag{3.2}$$

VASO is based on the idea that $M_{z,GM,nc}$ changes during activity and that this change is proportional to 1 - CBV. For more details about this proportionality see [Lu et al., 2003] Eq. 4. Note that CBV refers to the relative blood volume in units of ml per ml of tissue. In order to obtain $M_{z,GM,nc}$ without BOLD contamination of the T_2^*-term, this dephasing term must be factored out. In order to do so, the signal at the nulling condition is normalized to the signal that is acquired while blood is not nulled (nn). This signal can be expressed analogously as:

$$S_{par,nn} \propto M_{z,par,nn} \; e^{-\frac{TE}{T^*_{2,par}}}, \tag{3.3}$$

where the z-magnetization of the parenchyma $\mathrm{M}_{z,par,nn}$ contains both water z-magnetization within GM and water z-magnetization in blood. At the time the blood-not-nulled image is acquired, the relative z-magnetizations of blood and GM, and the proton densities of blood and tissue are very similar (proton densities are 0.87 ml/ml and 0.89 ml/ml for blood and tissue, respectively [Donahue et al., 2006]). Hence, the $\mathrm{M}_{z,par,nn}$-term can be considered to be independent of brain activation. In other words, blood volume sensitivity is obtained only when a VASO inversion preparation is applied, and signal change in the BOLD image comes only from changes in T_2^* and not from redistribution of water magnetization between intravascular and extravascular space. Thus it can be assumed that $M_{z,par,nn} \approx$ const. Hence, after normalizing S_{nc} with S_{nn}, it can be written as:

$$\frac{S_{bn}}{S_{bnn}} = \frac{M_{z,GM,nc}\ e^{-\frac{TE}{T^*_{2,GM}}}}{\underbrace{M_{z,par,nn}}_{\text{constant}}\ e^{-\frac{TE}{T^*_{2,par}}}} = \frac{M_{z,GM,nc}}{const} \approx 1 - CBV. \tag{3.4}$$

Here, it is assumed that at high field strengths the T_2^* of the parenchyma, which includes blood and tissue, is equal to the T_2^* of extravascular tissue. With this assumption, the T_2^* weighting cancels out upon division of the signals from both acquisitions, and the resulting signal is independent of BOLD changes. Hence, it is assumed that the transverse relaxation is independent of the inversion time. It must also be stressed that the BOLD correction scheme can only correct for extravascular BOLD signal change, which at 7 T accounts for approximately 90% of the total BOLD signal change at TE used in this study [Martindale et al., 2008][Donahue et al., 2010]. A complete model containing intravascular and extravascular BOLD effect is used in section 5.3 to validate that the simplifications in Eq. 3.4 are valid and to quantify that the corresponding error in VASO signal estimation is smaller than 7%.

Equation 3.4 claims only proportionality between the BOLD corrected VASO signal and CBV. According to discussions in [Lu et al., 2013], this proportionality factor depends strongly on partial voluming of CSF or WM and their T_1 contrast. Since this proportionality factor is not measured, the proposed method can be used only to estimate CBV changes, not to estimate absolute CBV. Quantitative estimations of effects of partial voluming in SS-SI VASO are carried out in section 5.4.

3.1.3 Methods

Image acquisition

The SS-SI pulse sequence was implemented in the IDEA programming environment on a Siemens MAGNETOM 7T scanner (Siemens Medical Solutions, Erlangen, Germany). For RF transmission and reception, a 24-channel receive and circularly polarized single-channel transmit head coil (Nova Medical, Wilmington MA, USA) was used. Data were acquired in five slighly tilted (Fig. 3.1) axial slices (thickness 1.5 mm, no slice gaps) with a two-dimensional single-shot GE EPI readout. The imaging parameters were: TE/TR = 19/3000 ms, nominal voxel size of 1.5 x 1.5 x 1.5 mm^3, partial Fourier factor 5/8. A time resampled frequency offset corrected inversion (TR-FOCI) pulse [Hurley et al., 2010] was implemented to achieve efficient slab-selective inversion despite B_1-inhomogeneities and SAR constraints at high field. The inversion pulse duration was relatively short (5 ms), which minimized the BOLD $T_{1\rho}$ relaxation of venous blood, which might reduce inversion efficiency. The slab-selective gradient strength was adjusted to achieve an inversion slab thickness of 14.3 cm. Since the inversion pulse is only applied prior to every second image, the inversion-pulse repetition time was 3 s.

Considering an inversion efficiency of 95%, as measured in pilot scans, leads to $TI1$ = 1330 ms for the blood-nulling time (Eq. 2.17). The timing of the sequence was adjusted such that the BOLD image acquisition was always right between two consecutive VASO images. Therefore $TI2 = TI1 + TR/2$ (see Fig. 3.1A).

Further inversion recovery measurements with multiple $TI1$s of 36/200/300/900/1100 ms were performed with acquisition parameters otherwise identical to the functional scans. Following the methods of Shin et al. [Shin et al., 2010], these data were used to generate T_1 estimates and GM maps with distortions identical to the functional data.

Ten healthy human volunteers (5 female, 23 to 33 years old) were scanned with the scan parameters described. A 6-minute duration high-contrast moving star-field paradigm (block design: 30 s rest followed by 30 s stimulation) [Huk et al., 2002] was used to induce neural activation throughout the visual cortex. This kind of basic visual stimulation paradigm was chosen as a toy example here. Because of the strong activity increase in visual cortex for this task, it is a good candidate for debugging and examining of the proposed imaging method.

To validate the BOLD correction method, seven additional volunteers (4 female, 22 to 30 years old) were scanned with a multi-echo EPI readout. Acquisition parameters were TE = 12/32/52 ms, partial Fourier factor = 5/8 and a nominal voxel size of 1.5 x 1.5 x 1.5 mm^3. All other sequence parameters remained unchanged.

To investigate the potential advantage of SS-SI VASO at 3 T, the sequence was also implemented on a MedSpec 30/100 whole-body scanner (Bruker Biospin, Ettlingen, Germany). A commercial birdcage head coil (Bruker Biospin) was used for RF transmission and reception. Two participants were scanned with SS-SI VASO parameters of $TR/TI1$ = 4000/1015 ms, TE = 14/30 ms, nominal voxel size = 3 x 3 x 4 mm^3. The TR-FOCI inversion pulse duration was increased to 10 ms.

All procedures of this study had been approved by the ethics committee of the University of Leipzig. Informed written consent was given by all participants.

Data analysis

The image-evaluation procedure is illustrated in Fig. 3.3. MR images were corrected for motion with SPM8 (Welcome Department, University College London, UK). Statistical analysis was done using FSL Feat (Version 5.98)[Worsley, 2001]. Activation areas were defined with the VASO data as a cluster of voxels having z-values above 2.3 and a significance level of $p < 0.05$ (corrected for multiple comparisons). BOLD correction, T_1-fits and the extrapolation of signal change were processed with in-house algorithms written in C++ using ODIN-libraries [Jochimsen and von Mengershausen, 2004]. In order to scale the relative VASO signal change to relative change in CBV, blood volume at rest was estimated. Therefore, the individual GM volume of every voxel was estimated based on the T_1-fit. As in previous VASO studies, blood volume at rest (CBV_{rest}) within this GM fraction was assumed to be 5.5% [Giovacchini et al., 2002][Lu and van Zijl, 2005]. CBV_{rest} was assumed to be evenly distributed within GM. The T_1-maps were also used to generate maps of CSF. Since the nominal resolution of 1.5 mm is on the order of the cortical thickness, voxels that contain the surface layers of the cortex could be identified by the partial volume fraction of CSF.

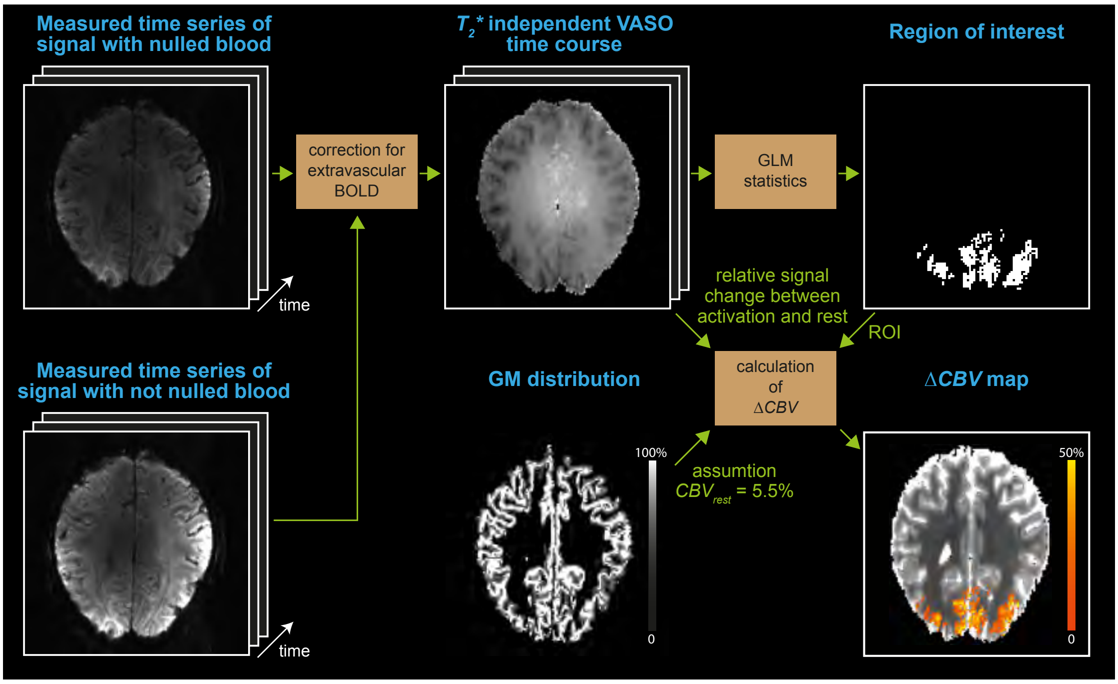

Figure 3.3: Evaluation procedure for calculating ΔCBV from the measured MR time series: In order to factor out the T_2^* dependence of activation, motion-corrected time series of blood-nulled images are normalized to motion corrected time series of images with not nulled blood. General linear model (GLM) statistics is applied to these T_2^* corrected time series to define regions of interest (ROIs). Signal changes within these ROIs are normalized with blood volume fraction at rest to relative CBV change, which is estimated from relative GM volume within each voxel.

3.1.4 Results

SS-SI VASO provides a larger GM signal than original VASO at 7 T (Fig. 3.4) and at 3 T (Fig. 3.5A). This increase results from the longer blood-nulling time ($TI1$) for once inverted blood water z-magnetization, compared to steady-state blood water z-magnetization. From calculations based on the Bloch equations (Eq. 2.11), the z-magnetization is expected to increase in GM by a factor of 8.7 at 7 T (assuming $TR/T_{1,b}/T_{1,GM}$ = 3/2.1/1.9 s of Tab. 2.1) and 3.6 for 3 T (assuming $TR/T_{1,b}/T_{1,GM}$ = 4/1.6/1.2 s [Donahue et al., 2006]). This agrees well with signal increases by factors of approximately 4 and 8 observed experimentally within GM-regions at 3 T and 7 T, respectively.

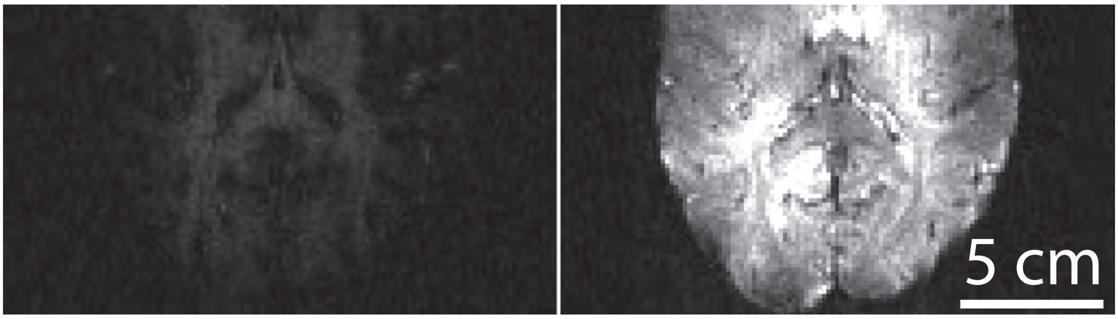

Figure 3.4: Single-shot EPI images obtained at 7 T with nominal voxel size of 1.5 x 1.5 x 1.5 mm^3, $TR = 3$ s, $TI1$ is 560 ms and 1330 ms for original and slab-selective VASO, respectively. Images are scaled identically. Gray values represent signal intensities in arbitrary units.

Three slices of ΔCBV maps obtained during visual stimulation of all 10 participants are shown in Fig. 3.6. Widespread ΔCBV increases can be seen in gray matter in the visual cortex corresponding to the central visual field. The measured relative CBV changes upon visual stimulation of the depicted regions are summarized in Tab. 1. Fig. 3.5B depicts results from two participants at 3 T. Similar to the 7 T results, CBV increases confined to gray matter in the visual cortex can be seen.

Signal time courses of BOLD and VASO signal of the ROIs depicted in Fig. 3.6 are shown in Fig. 3.7. Both time courses are very similar in their dynamics. The return to baseline after stimulus cessation is on a similar timescale in BOLD and in VASO data. The inter-subject stability is slightly greater in VASO compared with BOLD signal, as indicated by the smaller error bars. This finding holds true independent of whether the ROIs were defined from the BOLD or VASO time courses.

The echo time dependence of BOLD and VASO signal from the multi-echo experiments is depicted in Fig. 3.8. VASO signal time courses are shown for the two different BOLD correction methods: BOLD correction with dynamic division for two echo times and the BOLD correction from exponential extrapolation to $TE = 0$ ms. The latter correction method results in a larger inter-trial variation associated with larger error bars, presumably due to the low SNR of the images during the later echoes. There is no significant

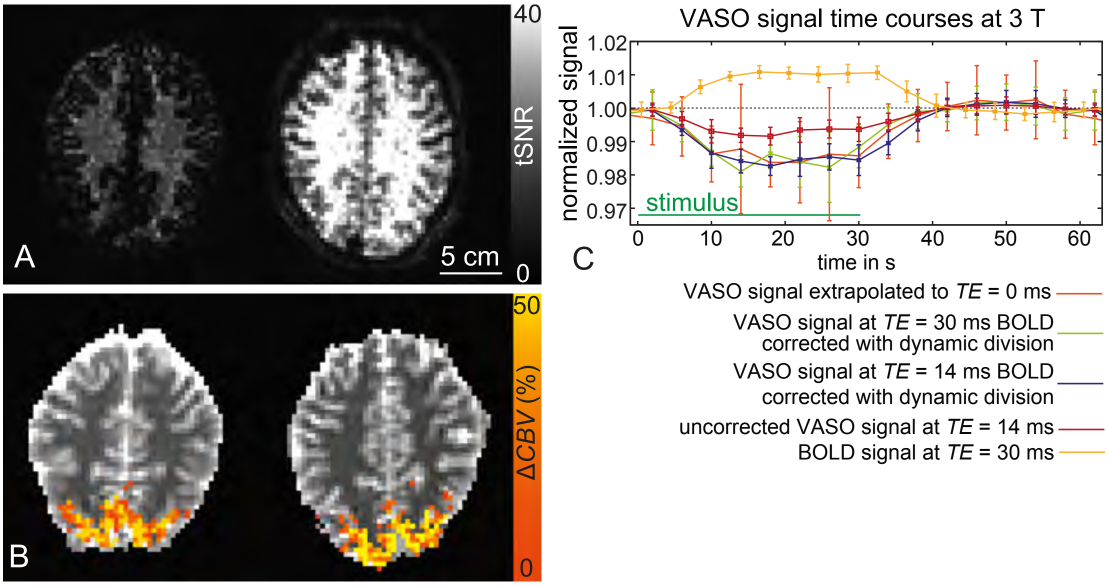

Figure 3.5: Results from two participants at 3 T: A) depicts tSNR maps of original VASO with TR/$TI1$ = 4000/625 ms and SS-SI VASO with $TR/TI1$ = 4000/1015 ms of one participant. tSNR in GM regions is 9 and 32 for original VASO and SS-SI VASO, respectively. B) depicts maps of relative CBV change in both participants within ROIs of significant signal change. C) depicts VASO signal time courses of the two participants for different BOLD correction schemes. Error bars refer to the standard deviation between consecutive activation-rest periods.

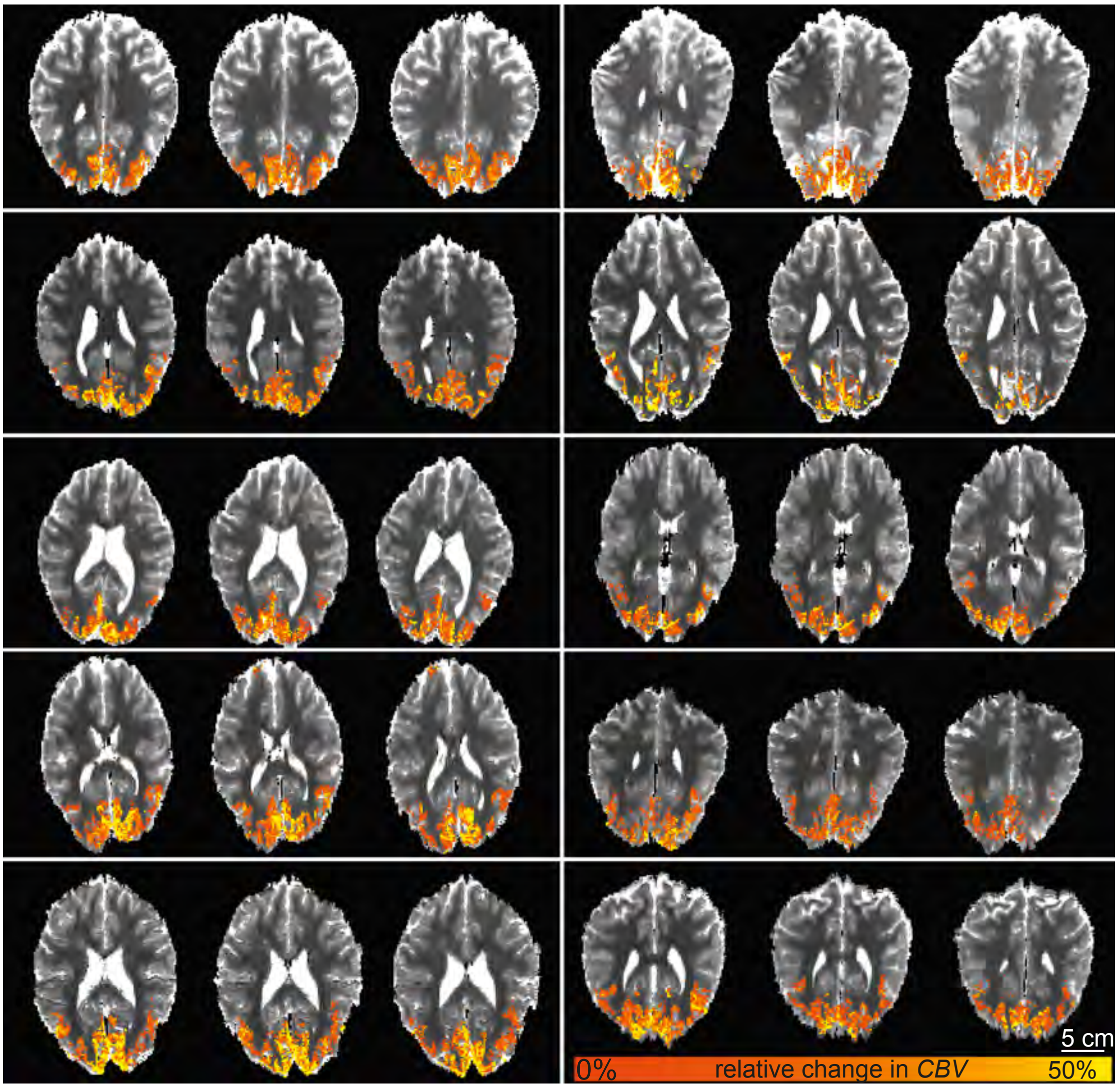

Figure 3.6: Three slices of every participant scanned at 7 T: The change in CBV is located in the visual cortex as expected. The mean change in CBV is $(28 \pm 5)\%$.

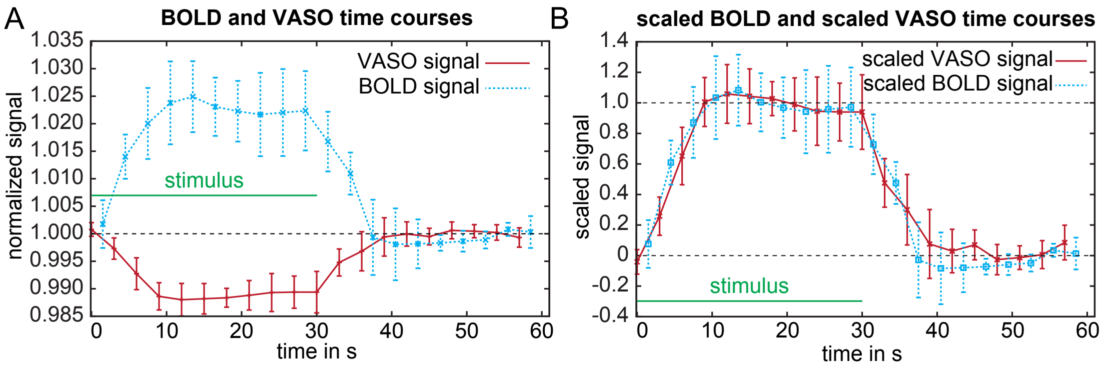

Figure 3.7: BOLD and VASO signal time courses: A) depicts normalized signal changes. B) depicts scaled BOLD and VASO signal time courses. In this and all following graphs of this thesis, error bars refer to the standard deviation across subjects, if not stated differently. Note also the smaller inter-subject variability in VASO compared to BOLD.

difference in amplitude and temporal dynamics between the two BOLD correction methods. The amplitude of the BOLD signal change on the other hand is highly dependent on TE, as expected.

BOLD corrected VASO signal time courses acquired at 3 T (Fig. 3.5C) are indistinguishable from 7 T results regarding both, the amplitude and temporal characteristics. VASO time courses without BOLD correction significantly underestimate CBV changes, even at 3 T. For $TE = 30$ ms, the VASO signal decrease is completely canceled out by the BOLD signal increase. VASO signal time courses are independent of whether the BOLD correction was performed with dynamic division (for $TE = 14$ and 30 ms) or whether BOLD correction was based on exponential T_2^* extrapolation. Inter-trial variability (error bars in Fig. 3.5C) are highest for a BOLD correction assuming a mono-exponential T_2^*-decay. VASO signal time course with $TE = 14$ ms and corrected for BOLD contaminations with dynamic division shows smallest inter-trial variability.

In GM voxels containing more than 10% partial volume of CSF, the BOLD signal change is larger compared to GM voxels that do not have partial volume of CSF ($p < 0.001$) (Fig. 3.9). On the other hand, VASO signal change is significantly ($p < 0.05$) smaller in such voxels.

3.1.5 Discussion

CBV changes: The measured average change in CBV of $(28 \pm 5)\%$ for visual stimulation is in good agreement with values reported in the literature of human studies using different CBV-sensitive modalities, such as paramagnetic contrast agents, a multi-exponential T_2 model, or positron-emission tomography summarized in Tab. 3.1.

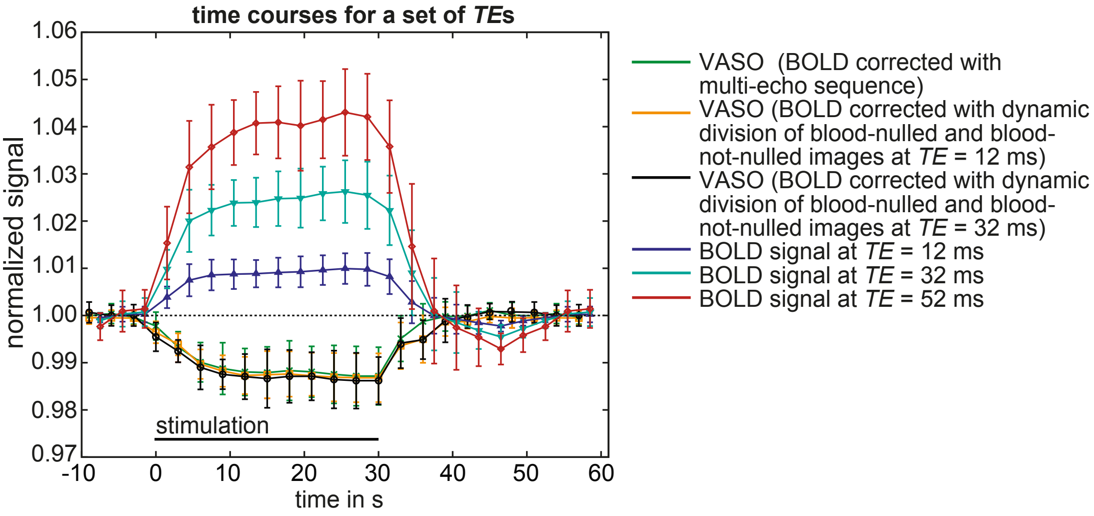

Figure 3.8: VASO and BOLD signal responses for different TEs: VASO signal time courses are depicted for different BOLD correction methods. The green line corresponds to BOLD correction with a multi-echo readout. The black/yellow lines correspond to the BOLD correction mechanism that is based on dynamic division of blood-nulled and blood-not-nulled images at $TE = 12/32$ ms. Error bars refer to standard deviation across participants. Signal time courses refer to the same stimulation paradigms, but different TEs.

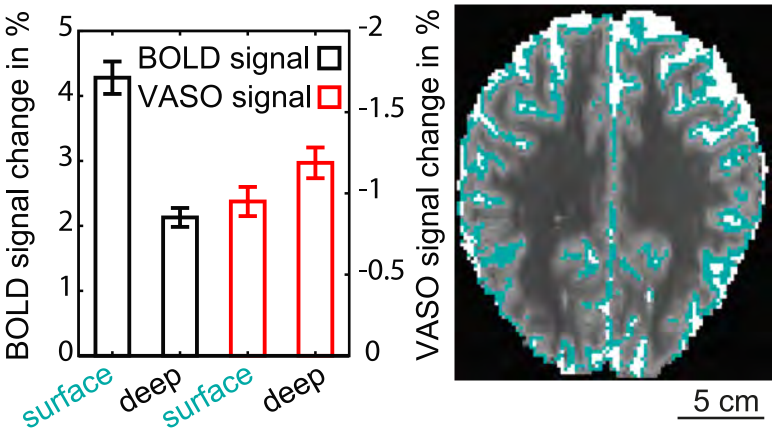

Figure 3.9: VASO and BOLD signal changes in gray matter surface voxels compared to signal change in voxels representing deeper cortical layers of the visual cortex: The BOLD signal change is dominated from surface voxels and VASO signal change is smaller in surface voxels compared to the rest of the voxels. Error bars refer to the standard error of mean across 10 participants. This discrepancy might reflect the different vascular origin of BOLD and VASO contrast. A representative map of such surface voxels across a slice through the brain is depicted on the right. The surface voxels are defined based on their partial volume signature with CSF, as described earlier (page 51).

Inter-subject stability

Despite the fact that VASO CNR is approximately only 60% of BOLD CNR, inter-subject variability appears to be smaller in VASO time courses as compared to BOLD time courses, which results in smaller inter-subject variability in average VASO signal as shown in Fig. 3.7. The measured coefficients of variation (mean standard deviation of signal at one time point during activity divided by the signal change) are 26.9% and 33.3% for VASO and BOLD signal, respectively. The greater inter-subject stability might be explained by considering that BOLD contrast depends on multiple physiological variables, while VASO depends on CBV change alone. For example, variations in venous baseline oxygenation level affect BOLD signal stability, but do not affect CBV changes [Leontiev and Buxton, 2007][Lu et al., 2008][Tjandra et al., 2005]. It must be pointed out that the echo time of 19 ms used here is close to the tissue T_2^*, which provides optimal sensitivity to BOLD signal change at 7 T. The mean T_2^* from the gray matter in the occipital lobe measured in the multi-echo data is 22 ms ± 5 ms. Therefore, it seems unlikely that inferior inter-subject stability in the BOLD results is due to sub-optimal choice of the acquisition parameters.

reference	ΔCBV	reference CBV_{rest}	comment
[Piechnik et al., 2009]	$(30 \pm 7)\%$	4%	multi-exponential T_2 fit with checkerboard
[Cohalan et al., 2009]	$(24 \pm 12)\%$	5.5%	VASO with checkerboard
[Lu et al., 2003]	46%	4.6%	VASO with checkerboard
[Wu et al., 2007]	$(40 \pm 5)\%$	6%	variant of VASO with checkerboard
[Hua et al., 2011a]	$(58 \pm 7)\%$	1.1%	change in CBV that enters the imaging slice during 2 s with checkerboard
[Lin et al., 2008]	$(37.7 \pm 2.9)\%$	5.5%	VASO with checkerboard
[Donahue et al., 2009a]	$(17 \pm 7)\%$	5.5%	VASO with checkerboard
[Tian et al., 2010]	23%	-	two photon microscopy in rats with electrical stimulation
[Hillman et al., 2007]	37%	-	estimated from diameter change of 17% (microscopy in rats with electrical stimulation)
[Gu et al., 2006]	$(33 \pm 12)\%$	4.5%	TI-fit with checkerboard
[Ito et al., 2001]	$(21 \pm 5)\%$	3%	PET study with checkerboard
[Belliveau et al., 1991]	$(32 \pm 10)\%$	-	contrast agent with checkerboard
[Frank et al., 1994]	$(23 \pm 14)\%$	-	contrast agent with checkerboard
[Pears et al., 2003]	$(28 \pm 7)\%$	4%	contrast agent with checkerboard
[Ciris et al., 2013]	44%	7.4%	multi-TI VASO
[Lu and van Zijl, 2005]	$(56 \pm 1)\%$	4.7%	VASO at 3 T with checkerboard
[Lu and van Zijl, 2005]	$(43 \pm 3)\%$	4.7%	VASO at 1.5 T with checkerboard
[Glielmi et al., 2009]	$(31 \pm 3)\%$	5.6%	biophysical model with checkerboard

Table 3.1: Literature values of the relative change in cerebral blood volume.

Activation time courses

Both VASO and BOLD signals return to baseline after a similar time (Fig. 3.7), contrasting with [Mandeville et al., 1999], but in agreement with [Dechent et al., 2011], [Poser and Norris, 2007], and the results reviewed in [van Zijl et al., 2012]. VASO signal change reflects ΔCBV mostly of arteriolar, capillary blood compartments as long as they are nulled, independent of their oxygenation level. The BOLD effect, on the other hand, is dominated by the most deoxygenated part of the vasculature. Therefore, the fast return to baseline of VASO data does not necessarily contradict predictions made by the balloon or windkessel model [Buxton et al., 1998][Mandeville et al., 1999], with the corresponding explanation of BOLD signal post-stimulus undershoot. The fast timescale of CBV change might result from the smallness or indeed absence of changes in venous CBV with short stimulus durations [Hillman et al., 2007].

Dynamic changes of CSF volume

Assuming the skull as a container of a fixed volume, increase of one compartment, e.g. CBV, must be compensated by volume decrease in another compartment, e.g. GM or CSF [Mokri, 2001]. VASO signal change is based on the idea that CBV increase is compensated by GM volume decrease only. However, dependent on the brain region stimulated, a small dynamic change in CSF volume in the range of 0.5% to 10% has been experimentally observed [Jin and Kim, 2010][Piechnik et al., 2001][Scouten and Constable, 2008]. Such stimulus dependent variations in CSF volume could cause an incorrect calculation of ΔCBV from the VASO signal change [Donahue et al., 2006][Piechnik et al., 2001][Scouten and Constable, 2008][Scouten and Constable, 2007].

In SS-SI VASO, manipulations of the stationary CSF z-magnetization can be used to minimize sensitivity to such dynamic changes in CSF volume. In SS-SI VASO, blood z-magnetization is not considered to be in steady-state, and hence the blood-nulling time is independent of TR. Therefore, TR can be adjusted as a free parameter to manipulate the relative signal weighting of GM and CSF. For TR in the order of 3 s, the MRI signal intensities of GM and CSF are similar, and the VASO signal change corresponds to changes in both of these compartments that is, a CBV increase compensated by a GM volume decrease as well as a CBV increase that is compensated with a decrease in CSF volume. If TR is approximately 5 s, both compartments - once inverted blood and steady-state CSF magnetization - are nulled simultaneously. In this case, VASO signal change reflects only CBV increase that is compensated by GM decrease, and it is insensitive to CBV increase that is compensated by CSF decrease. Thus, the sensitivity of VASO to dynamic changes in CSF can be modulated in SS-SI VASO simply by adapting TR, whereas in the original VASO [Lu et al., 2003], implementations based on more time-inefficient methods like VASO FLAIR (fluid-attenuated inversion recovery) [Donahue et al., 2006] or ACDC (accounting for dynamic CSF) VASO [Scouten and Constable, 2008] need to be applied. Such effects are discussed and quantitatively estimated in section 5.4 of this thesis.

Signal change at the cortical surface

The observation that VASO is smaller in GM voxels with significant partial-volume contributions from CSF (see Fig. 3.9) is consistent with results showing that ΔCBV is smaller in voxels closer to the pial surface, in contrast to BOLD signal [Jin and Kim, 2008b][Jin and Kim, 2008a][Kim and Kim, 2010]. It suggests that changes in CBV are independent of pial veins, which are known often to dominate the GE BOLD effect. Note that surface voxels can have different partial-volume characteristics from more typical voxels. This means, independent of the underlying layer-dependency of VASO and BOLD contrast, surface voxels are expected to show smaller signal changes corresponding to the smaller GM volume they contain. However, since BOLD signal changes are investigated in the same subset of voxels, partial-volume biases are identical in BOLD and VASO signal change. Therefore, differences between BOLD and VASO responses can be considered independent of such biases. The BOLD and VASO specificity across cortical depth is discussed in more detail in section 4.2 of this thesis.

Magnetization exchange between intra- and extravascular spaces

Similar to the original VASO, SS-SI VASO is based on a model of two separate compartments without magnetization exchange. However, magnetization exchange between intra- and extravascular spaces due to finite permeability of the capillary wall can result in CBF-dependent reduction of the GM signal [Lu et al., 2003][Wu et al., 2010]. In SS-SI VASO, the magnetization within the slice is kept at a low value during inversion. Hence, during the entire period III (Fig. 3.1) inverted blood magnetization will enter the slice and exchange with tissue magnetization that is close to zero. And vice versa, not nulled tissue magnetization permeates from intravascular into extravascular space, which can result in incomplete blood nulling in post arterial blood compartments. These effects can introduce permeability induced flow contamination in VASO. Quantitative estimations of such effects can be obtained from simulations with a multi compartment perfusion model [Wu et al., 2010] and are carried out in more detail in section 5.1.

3.1.6 Conclusions

In this study, it has been shown that the proposed SS-SI VASO yields reliable and consistent detection of CBV changes in humans at 7 T. Here, blood arrival and transit times of healthy participants are comparable to the blood-nulling time after inversion, which is used in a slab-selective approach to increase the functional CNR. With these improvements, SS-SI VASO may be a useful tool for high-resolution functional brain mapping in humans at high fields. Furthermore, the high sensitivity of the proposed method can play an important role in neuro-scientific research, where experiments are limited by low SNR, e.g. investigating neurovascular coupling in negative BOLD regions (section 4.1), in layer-dependent fMRI (section 4.2), or in calibrated BOLD fMRI (section 4.3).

3.2 Validation of SS-SI VASO with OIS [2]

In the previous section, the applicability of the new SS-SI VASO method has been shown and the results are in a physiological reasonable range. In order to ensure its sensitivity to CBV changes, it should be qualitatively compared and validated with established methods. Because the only methods with comparable resolutions that can be used for such validations rely on invasive procedures, SS-SI VASO must be implemented in an animal model. This section describes the study of implementing SS-SI VASO in rats for its validation with optical imaging spectroscopy. First, the background and challenges of such a study are described. And then, experimental results of concomitant VASO and optical measurements are shown for thorough spatiotemporal validation of blood volume weighting in VASO.

3.2.1 Introduction to the comparison between SS-SI VASO and OIS

Local changes of CBV has been suggested to provide a qualitative physiological variable that localizes neural activity better than other variables accessible by fMRI, e.g. BOLD fMRI. The most frequently applied contrast to measure dynamics of CBV in applications of human neuroscience is VASO. However, there are two major unresolved issues regarding its quantitative credibility. Firstly, VASO fMRI has not been validated with a gold standard method at high resolutions to investigate its tissue and macrovascular CBV components. Secondly, quantitative values of CBV changes of VASO in humans are usually one order of magnitude larger than values suggested from invasive modalities applied in animals.

Validation of VASO contrast

Despite the proven sensitivity of VASO fMRI for CBV changes, the signal mechanism is not completely understood and is in focus of research since ten years to date. Most critical to validate the CBV weighting in VASO is to investigate it with respect to features that are uniquely visible in CBV imaging. Otherwise it could not be disproven that the underlying contras mechanisms might actually contain CBF or BOLD weighting. For example, both, CBV and BOLD signal changes are expected to are amplified for stronger stimuli used and they are expected to stem from GM and not WM. When low resolutions (e.g. 3 x 3 x 3 mm^3) are used, the two contrasts are expected to have very similar qualitative activation patterns despite the fact that they map different physiological parameters. Hence, for thorough validation, CBV weighting of VASO must be considered on a level, where CBV can be distinguished from other physiological parameters. The literature suggests three possible approaches for validation of CBV sensitivity. A) In order to address contaminations of CBF that can mimic VASO signal change but have similar features as CBV, validation must be quantitative in physical units. B) Draining veins have been reported to show considerable flow increase and BOLD signal increase,

---

[2] The study described in this section has been summarized in the conference talks [Kennerley et al., 2013] and [Huber et al., 2014c].

but not CBV changes. Hence, high resolution validations enabling spatial distinction of draining veins should help in validation of CBV sensitivity. C) CBV time courses with slow return to baseline have been reported to be uniquely different from CBF and BOLD signal. Therefore, post-stimulus signal change can be taken as a CBV sensitive feature for validation of CBV sensitivity. Such validations could help evaluating CBV sensitivity of VASO, but have not been reported so far.

Differences between human CBVchanges in VASO and CBVchanges in invasive methodologies in animals

Features of CBV dynamics in animals have not been confirmed in human so far. The two major discrepancies concern the temporal dynamics and the magnitude of CBV changes. Human CBV sensitive fMRI studies found blood volume changes in the order of 30% - 60% [Lu et al., 2003][Belliveau et al., 1991][Lin et al., 2011][Hua et al., 2011a][Ito et al., 2001][Piechnik et al., 2009][Tuunanen et al., 2006], while animal studies with invasive methodologies report much smaller values of 10% - 20% [Mandeville et al., 1998], $\approx$ 15% [Kennerley et al., 2010], 5% [Kennerley et al., 2012a], and 4% - 7% [Lu et al., 2004b]. Independent of the absolute CBV change, the time courses CBV change seem to be qualitatively different in human VASO studies compared to animal literature. Human VASO studies suggest a fast recurrence to baseline of CBV after stimulus cessation in the range of 10 - 15 s [Lu et al., 2004a][Poser and Norris, 2007][Hua et al., 2011b][Tuunanen et al., 2006], while rat literature suggests a delayed compliance with a post-stimulus signal return to baseline in the order of 30 - 60 s [Mandeville et al., 1999][Kida et al., 2007][Kennerley et al., 2005].

Since different modalities are used to investigate functional change in CBV in rats and in humans, it is not clear whether these discrepancies of different amplitude and temporal features arise from inter-species differences, methodical differences, or anesthesia-dependent influences. Studies investigating the influence of anesthesia have suggested that anesthesia can slightly reduce the overall response amplitude, but it cannot explain the temporal CBV dynamic differences between animals and humans [Zong et al., 2012][Sicard et al., 2003][Berwick et al., 2002][Martin et al., 2006].

In order to resolve whether these differences result from the different contrast mechanisms of the invasive and non-invasive modalities used, a direct inter-species comparison between humans and animals is needed. This comparison should involve the same imaging modality and the same cortical area or stimulation task. Since VASO is a non-invasive contrast, it can be applied both in rats and in humans and is the method of choice for such comparisons. Primary somatosensory cortex is routinely stimulated in rats and humans and can provide a model to investigate brain activity across species. Similarly, hypercapnia challenge is expected to reflect similar hemodynamic control pathways in humans and rats and can be used for quantitative comparisons.

Purpose of this study

In this study, it is tried to address both of the above mentioned VASO related issues, the high resolution validation of the underlying CBV sensitivity, and the differences of quantitative CBV changes in humans and animals.
The first purpose of the present study was to adapt the VASO pulse sequence such that it can be applied in a rodent model at high fields ($\geq$ 7 T) with advanced CNR and without contaminations of flow and blood oxygenation changes. With that method, it is sought to compare the VASO contrast with concurrent 2D OIS to evaluate the underlying CBV weighting. The high spatial and temporal resolution of OIS allows using it as a gold standard technique to validate the VASO signal mechanism and sensitivity to CBF artifacts. The final goal of this study is to obtain results of CBV changes in rodents and humans that are acquired with the same non-invasive modality and therefore can be directly compared.

3.2.2 Methods

VASO was originally designed for use in human brain at low magnetic fields (1.5 T) [Lu and van Zijl, 2012]. For an application in an animal model at high fields, distinct features in physiology and magnetization dynamics must be considered. First, due to the convergence of tissue and blood longitudinal relaxation times at high magnetic field strengths and the inflow of non-inverted blood magnetization during the blood nulling time, the VASO signal can become unreliable [Hua et al., 2012] (see also section 3.1). Second, another issue of using VASO in animals at high fields is to avoid inflow effects of blood into the imaging slice that does not have the magnetization state as assumed [Jin and Kim, 2008b]. This is particularly challenging in rats, because there, the arterial arrival time is significantly shorter compared to humans [Calamante et al., 1999].
To make the VASO viable at higher field strengths ($7 =$ T) the SS-SI VASO pulse sequence was used in the current study. In order to account for the different physiology in rats compared to humans, the SS-SI VASO sequence was further advanced. Additional slice-selective and global saturation pulses were implemented to account for the different z-magnetization relaxation histories (steady-state) of stationary tissue and blood flowing into the imaging slice. This is used to increase functional contrast and avoid contamination of changes in CBF. One TR of the adapted SS-SI VASO sequence is depicted in Fig. 3.10A. Before every TR, a global adiabatic 90° spin-reset pulse is played out to be in control of the steady-state of entire magnetization within the transmit coil, independent of blood flow inside the coil from the animal hindquarter (Fig. 3.10B), in analogy to [Lu, 2008]. The amplitude and phase shape functions of that radio-frequency pulse were adapted from TR-FOCI pulse class, designed for use at 7 T [Hurley et al., 2010]. In order to convert it from an inversion pulse to a 90° saturation pulse, a 90° phase skip of the pulse amplitude was introduced half way through out the pulse, resulting in an inversion efficiency of 50%, despite B_1 inhomogeneities of the transmit coil [Mispelter et al., 2006]. A more detailed description on the operation principle of this RF pulse can be found in section 4.3. The slice-selective 90° excitation pulse prior BOLD image

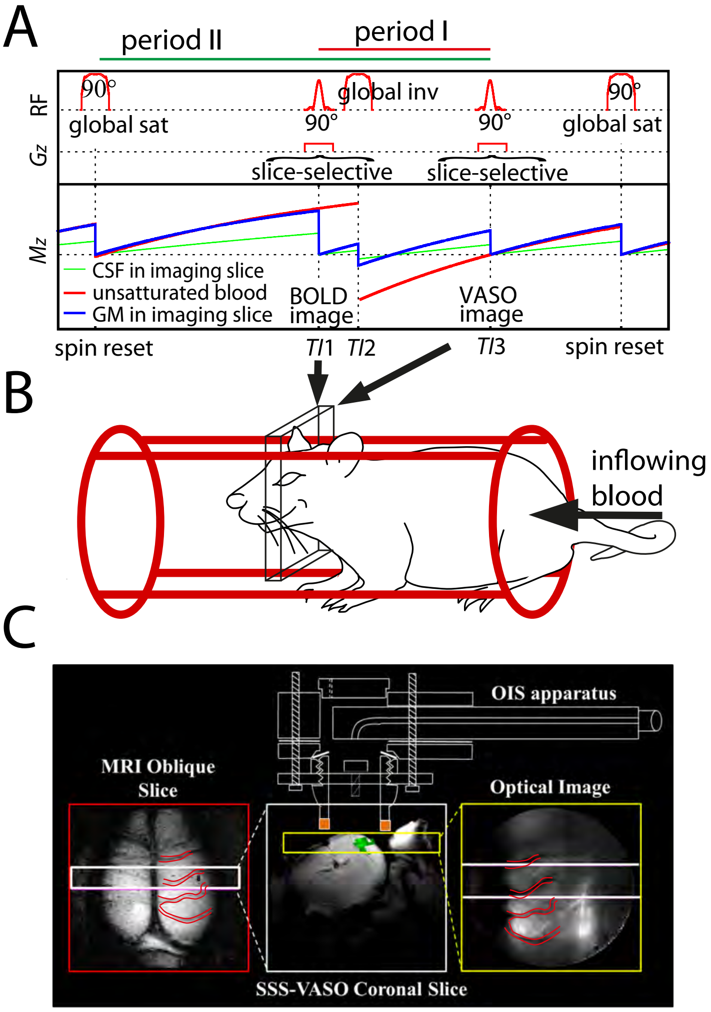

Figure 3.10: Acquisition procedure of SS-SI VASO in rats: A) depicts a sequence diagram of an adapted version of SS-SI VASO for application in rodent brain at high fields. In order to be in control of the magnetization steady-state, before every TR, a global adiabatic saturation pulse is applied. In-plane magnetization is saturated by a slice-selective 90° excitation pulse prior the acquiring of a BOLD signal image without blood nulling. After that, the global inversion is applied to introduce the VASO weighting with subsequent VASO signal acquisition at the blood-nulling time $TI3$. B) depicts the approximate position of slice-selective saturation and 'global' inversion pulses. C) depicts a schematic illustration of MR signal and optical signal acquisition. For concurrent imaging of VASO fMRI and OIS, the OIS apparatus in positioned inside the bore. Large venous vessels are visible in T_2^* weighted MR images as well as in optical images, which helps in spatial orientation for comparisons of the two contrasts.

acquisition saturates tissue magnetization in the imaging slice, but does not affect blood magnetization refilling the vasculature until the next VASO image is acquired.
All blood in the imaging slice is expected to be nulled to provide a pure VASO contrast, when two assumptions are fulfilled: First, the microvasculature of the imaging slice is refilled during the period I (Fig. 3.10A). Blood velocity and transit time measurements suggest that the microvasculature of a 2 mm imaging slice is refilled faster than 1.5 s [Ivanov et al., 1981][Kim and Bandettini, 2010][Pawlik et al., 1981][Kleinfeld et al., 1998][Kennerley et al., 2010][Hutchinson et al., 2006]. Second, no fresh (uninverted) blood from the hindquarter of the animal flows into the imaging slice during period II (Fig. 3.10A).

MR imaging parameters

All aspects of these methods and their development were performed with UK Home Office approval under the Animals (Scientific Procedures) Act of 1986. SS-SI VASO as described above was implemented in Paravision V on a 7 T rodent scanner (Bruker BioSpecAvance, 70/30, Bruker Biospin GmbH, Ettlingen, Germany). Sequence parameters were: $TR/TI1/TI2/TI3/TE$ = 3200/1100/1500/2530/10 ms. Field of view was 30 x 30 mm^2 and matrix size was 64 x 64. Since the above discussed refill condition is only fulfilled using coronal slices with the sequence parameters used, all functional experiments were performed with coronal imaging slices.

OIS

2D-OIS experiments were conducted concurrently to fMRI inside the bore as described in [Kennerley et al., 2005]. In short, a nonmagnetic endoscope was placed over a window of previously thinned skull to acquire images of the right barrel cortex with four wave lengths (575/559/495/587 nm) at an overall rate of 8Hz and special resolution of 0.2 x 0.2 mm^2. Based on the known absorption coefficients of deoxy- and oxyhemoglobin and using a heterogeneous tissue model accounting for the penetration depth of the respective wavelengths, changes in total hemoglobin concentration and its saturation could be calculated [Kennerley et al., 2012a]. Positioning and cross-validation of geometry in OIS and MRI was based on large veins, clearly visible both modalities (Fig. 3.10C).

Physiological conditions

The animal surgery and the monitoring of physiological conditions during the experiments was done as in previous studies [Kennerley et al., 2005]. In short, the right sides of the skull of four urethane-anesthetized female Hooded-Lister rats were thinned with a dental drill. Femoral veins and arteries were cannulated for drug infusion, and continuous measurements of blood pressure and blood gases. Phenylephrine (0.13 - 0.26 mg/hr) was infused to maintain blood pressure within physiological range (MABP, 100 - 110 mmHg). Animals where artificially ventilated with room air or customized gas compositions.

Stimulation design

Experiments using electrical stimulation of the whisker pad (5 Hz) consisted of 15 trials of 16 s electrical stimulation alternating with 86 s inter stimulus interval. Additional hypercapnia experiments consisted of 2 min breathing air, 5 min breathing 5% CO_2, 20% O_2, 75% N_2 and 2 min breathing air again (12 trials per animal).

Data evaluation

All images acquired in rats were motion corrected (spatial drift corrected) using SPM8 (Wellcome Department, University College London, UK). Statistical analysis was done using FSL FEAT (Version 5.98)(z-score > 1.0 and p < 0.9) without spatial smoothing. Evaluation was restricted to clusters of significant voxels in the brain region S1. BOLD correction of VASO images was done with a dynamic division of interleaved acquired BOLD weighted images as described in section 3.1. Since VASO signal change corresponds to changes in extravascular space, it is a direct measure of absolute CBV change. However, assuming a baseline blood volume fraction, relative CBV can be calculated as $\frac{\Delta CBV}{CBV_{rest}} \approx \frac{\Delta S}{S_{rest} CBV_{rest}}$ [Lu et al., 2003]. In previous studies CBV_{rest} was usually assumed to be 5.5% [Lu et al., 2013].

Human experiments

For the sake of inter-species comparisons between rodents and humans, VASO was applied in human volunteers at 7 T (MAGNETOM, Siemens Healthcare, Erlangen, Germany) during the same 5% hypercapnia condition as done in rats and during a finger touching task to evoke hemodynamic changes in somatosensory cortex. Hypercapnia experiments were conducted with the experimental parameters described in section 3.1. In short, to account for short arterial arrival time during hypercapnia, the inversion efficiency was reduced to be 75%. Further sequence parameters were $TR/TI1/TI2/TE$ $=$ 3000/765/2265/19 ms, nominal resolution 1.5 x 1.5 x 1.5 mm^3. For laminar comparisons of CBV change in S1, high-resolution VASO experiments were performed in five additional participants during a finger touching task, as described in section 4.2 of this thesis. Nominal in plane resolution of those experiments was 0.8 x 0.8 mm^2 and slice thickness of 1.5 - 2 mm. All procedures in this study applied in humans were approved by the ethics committee of the University of Leipzig. Informed written consent was given by all participants.

3.2.3 Results

Maps

Fig. 3.11 depicts activation maps acquired with OIS and SS-SI VASO. OIS maps of changes in blood oxygenation level (second column in Fig. 3.11) clearly depict large draining veins (black arrows). Corresponding maps of CBV change do not show macrovascular contributions distant from the main activation region. Vascular patterns on top of the

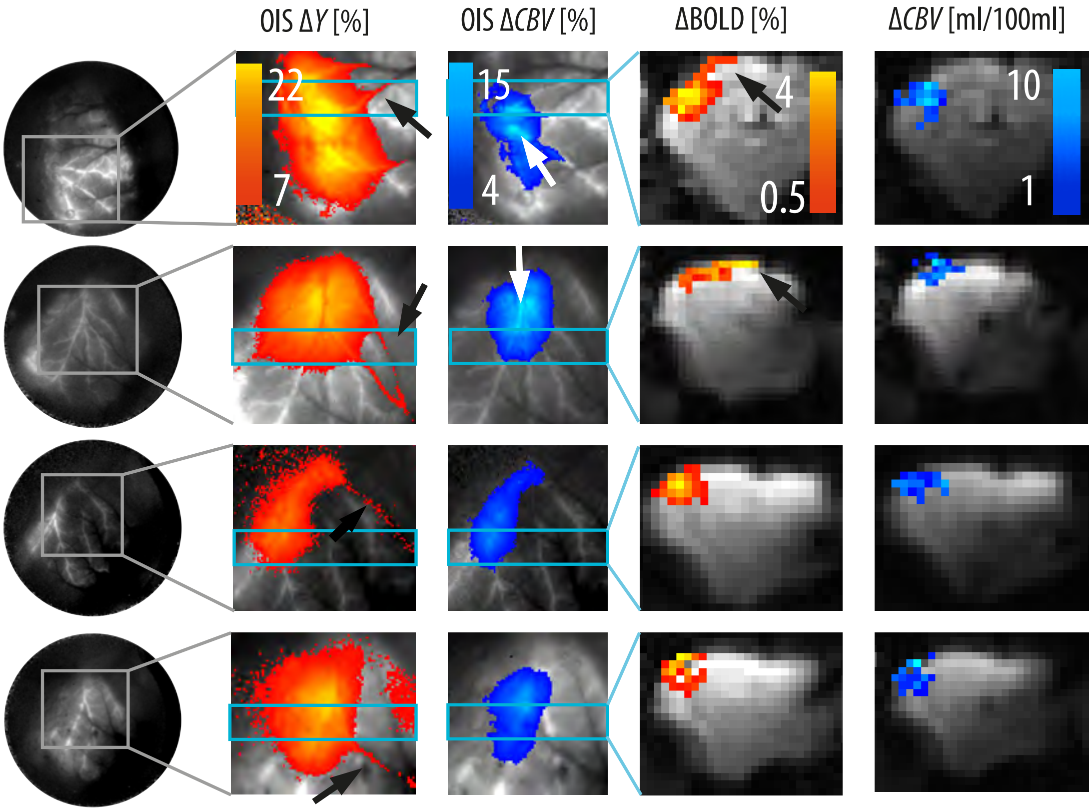

Figure 3.11: OIS and VASO activation maps of four animals: The first column depicts the total field of view of the endoscope. Changes of relative oxygenation and CBV taken from OIS measurements are depicted in the second and third columns. They are overplayed on CBV-based vascular reactivity maps with bright arteries and dark veins. It can be seen that draining veins show significant changes in oxygenation distant from activated tissue (black arrows). Maps of CBV changes seem to be more confined to activated tissue, while pial arteries contributing to CBV change can be distinguished on top of CBV change in tissue (white arrows). The third and fourth columns refer to BOLD and VASO signal change in coronal slices. The position of the coronal slice with respect to the OIS data is indicated with blue boxes. In subjects, when large pial veins are within the acquired slice, significant BOLD signal change distant of the site of highest CBV change can be seen (black arrows). Highest BOLD signal change is close to the cortical surface. Due to the lower CNR in VASO, laminar signatures of CBV change cannot be seen with the naked eye.

activated regions (white arrows) suggest that pial arteries also contribute to CBV increase. Coronal slices of BOLD signal change, show significant activation in the region of rat barrel cortex. When the imaging slice contains large draining veins (two upper rows), they can be seen in BOLD signal maps (black arrows). The BOLD signal change in those voxels might reflect intravascular BOLD effects, visible at the short TE (10 ms) used here. It can be seen that relative BOLD signal change is higher in upper cortical laminae compared to deeper cortical laminae. Maps of VASO-CBV change are depicted in the right column of Fig. 3.11. It can be seen that SS-SI VASO has enough sensitivity to map CBV changes in rats at 7 T. Even though the signal is noise dominated, voxels of significant VASO signal change can be found. Due to the high noise level, intracortical signal distribution revealing layer-dependent activation profiles cannot be seen with the naked eye on a single-subject basis. Mean CBV change in VASO data is 0.48 ± 0.18 ml/100ml. Mean tSNR in the corresponding ROIs is 5.8 ± 1.6 for VASO and 19.7 ± 6.3 for BOLD signal.

Time courses

Comparison of temporal signal evaluation of VASO-CBV and OIS-CBV is depicted in Fig. 3.12. The upper row corresponds to stimulation induced CBV increase in ROIs shown in Fig. 3.11. OIS-CBV of 7.1 ± 2.8 % is in good agreement with VASO-CBV 8.7 ± 3.3 % ($\Delta CBV = 0.48 \pm 0.18$ ml/100ml and assuming $CBV_{rest} = 5.5\%$). Time courses are very similar for VASO-CBV and OIS-CBV. Both modalities show a slow return to baseline after stimulus cessation. The high noise level in VASO makes further comparisons difficult. The bottom row in Fig. 3.12 depicts CBV time courses during hypercapnia. Again, VASO-CBV and OIS-CBV are very similar in amplitude and temporal response. OIS-CBV is 6.9 ± 4.8 % and VASO-CBV is 9.4 ± 6.2 % ($\Delta CBV = 0.52 \pm 0.34$ ml/100ml and assuming $CBV_{rest} = 5.5\%$). The depicted data refer to right hemisphere GM in the 2 mm imaging slice. Scatter plots of VASO-CBV versus OIS-CBV (Figs. 3.12B and 3.12D) suggest that the scale parameter of $CBV_{rest} = 5.5\%$ might underestimate the baseline blood volume by 10%-20%. Having data of both, BOLD response and CBV or CBF response during hypercapnia, the calibration factor M can be calculated (see section 2.3.4). Assuming $\beta = 1$ and $\alpha = 0.38$, M values are 9.1 ± 0.8 % ($TE = 19$ ms) in humans and 12.9 ± 6.0 % in rats (scaled to $TE = 19$ ms). A detailed description of the corresponding calculation is given in section 4.3.

Comparison with humans

Since VASO is a non-invasive imaging method, it can be compared between humans and rats. Fig. 3.12C depicts VASO response time courses in human GM and rat GM for 5 minutes CO_2 breathing challenges. VASO signal change in humans shows a CBV increase of 1.6 ± 0.4 ml/100ml. This suggests that the vascular reactivity of CBV is 3.1 ± 1.2 times higher in humans compared to rats. Corresponding BOLD signal changes are 1.2 ± 0.1 % ($TE = 10$ ms) in rats and 3.4 ± 0.7 % ($TE = 19$ ms) in humans, respectively. In order to compare spatial features of VASO signal change across species,

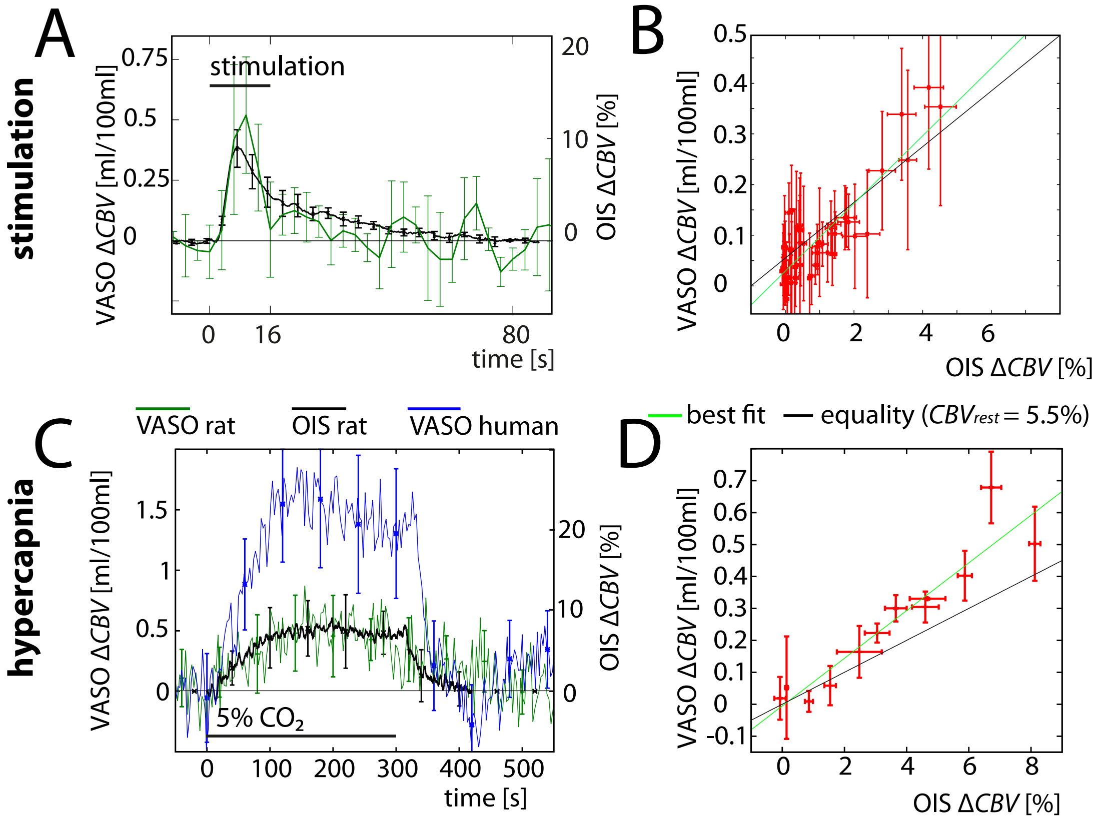

Figure 3.12: Comparison of OIS and VASO-CBV measurements in time: A) and C) depict CBV time courses during stimulation and hypercapnia, respectively. It can be seen that VASO time courses in rats are noise dominated. Point-to-point scattering is in the same range as the inter-subject standard deviation (error bars). Shapes of time courses are very similar for both modalities VASO and OIS, and all differences are within error. B) and D) show the same data in a scatter plot. For the sake of clarity, individual points refer to the averaged signal of multiple adjacent time points. Data in A) and B) refer to ROIs in S1 only, while data in C) and D) refer to the total GM of the right hemisphere within one acquired slice.

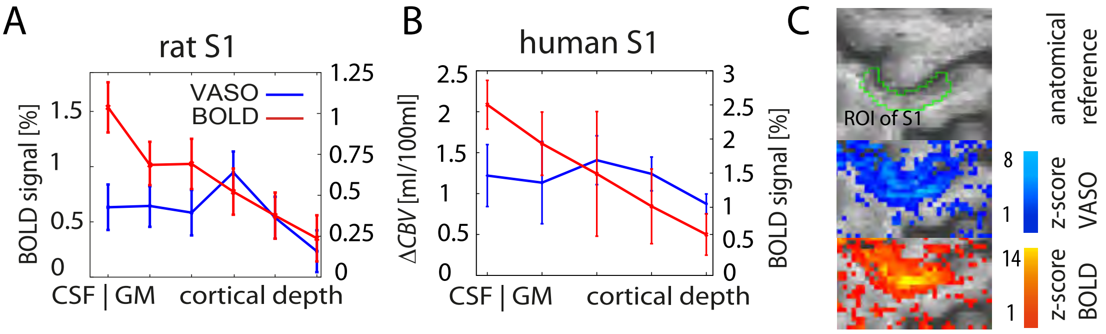

Figure 3.13: Cortical profiles of BOLD and VASO signal change in rat S1 (A) and human S1 (B): Data shown refer to averages across four rats and five human participants, respectively. Even though, voxel-wise signal changes are too noisy to show laminar-dependent signatures in signal maps of Fig. 3.11, averaging across laminae reveals different cortical profiles for VASO and BOLD fMRI. BOLD signal change is highly dominated from surface laminae, while VASO peaks in middle cortical laminae, presumably reflecting thalamocortical input. Signal changes depicted in A) refer to the ROIs given in Fig. 3.11. Signal changes depicted in B) refer to ROIs manually drawn on the posterior side of the central sulcus. An ROI of a representative subject is shown in C).

cortical profiles of stimulation induced activity in S1 is depicted in Fig. 3.13 both humans and rats, respectively. Cortical profiles of CBV change in rats and humans are very similar across species. Note, however that the absolute CBV change is approximately double in humans compared rats (different y-axis in Fig. 3.13). Depicted data refer to averages across species in S1. Corresponding S1 ROIs in rats are shown in Fig. 3.11. An S1 ROI from the human experiments of one representative subject is shown in Fig. 3.13C.

3.2.4 Discussion

When physiological characteristics of rats are accounted for in sequence design used, VASO can provide measures of CBV change in rats. Even though, VASO results are limited by high noise contributions, the CNR is sufficient to reveal activation maps of significant CBV change and corresponding time courses.

Validation of CBV weighting in VASO

Baseline CBV sensitivity at rest of non-functional VASO contrast has been validated with Gd DTPA [Uh et al., 2009] and PET [Uh et al., 2011] in large regions of interest (ROIs). Lin et al. compared the functional CBV weighting of VASO with CBV sensitive Gd DTPA method [Lin et al., 2011]. After averaging across total visual cortex, VASO signal was found to be comparable to CBV change measured with Gd DTPA across different stimulation frequencies. Jin and Kim firstly implemented a VASO version in non-human environment with ultrahigh resolution [Jin and Kim, 2008b]. This method could provide CBV weighting in deep cortical layers, where CBF effects of macrovasculature and BOLD contaminations were minimized. When excluding upper cortical layers, VASO activation patters were found to be similar compared to results from iron oxide contrast agent based fMRI acquired in previous studies.

Results presented in this section of the thesis are acquired with a method accounting for flow effects in upper cortical layers and BOLD contaminations. Hence, the presented results in this study enable first quantitative spatio-temporal validation of VASO. Data shown in Figs. 3.11 and 3.12 validate the CBV weighting of VASO in reference to the spatial sensitivity of large draining veins and with respect to temporal features such as a slow post-stimulus recurrence to baseline. VASO-CBV and OIS-CBV are the same within error with their respective quantitative CBV changes.

Differences between rats and humans

Since VASO is a non-invasive method for CBV mapping, it can provide for the first time direct high-resolution comparisons of human and animal CBV responses in GM without considerable partial volume effects. Data presented in this study suggest qualitative and quantitative differences between humans and anesthetized animals. For example, data suggest significantly stronger CBV changes in humans compared to rats and slow post-stimulus return to baseline in contrast to any earlier VASO results reported in humans. Such differences are known in the literature [Kim and Ogawa, 2012]. Due to lack of further data, it was suggested that such discrepancies are a result of different imaging modalities, rather than inter-species differences or anesthesia effects [van Zijl et al., 2012]. Since both, rat CBV and human CBV are captured with the same imaging modality here, it can be ruled out that these differences result from different imaging modalities. CBV reactivity was found to be three times larger in humans compared to rats, which might come from pre-dilated arterioles and arteries in the anesthesia protocol (including phenylephrine injection). The fact that the M-values are very similar and within error for humans and rats might reflect the lower venous baseline oxygen saturation in rats compared to humans.

Hematocrit

VASO signal changes refer to changes in total blood volume containing blood plasma volume and volume of hemoglobin. OIS on the other hand refers to changes in hemoglobin concentration. This means that the two modalities might capture different components of blood volume, when the ratio of hemoglobin volume to plasma volume (hematocrit) is not constant. For example, this is the case, when thin capillaries with small diameters were too narrow during rest for red blood cells to flow through. Since a vast body of studies report negligible hematocrit changes ($< 10\%$) during activity and hypercapnia [Kuschinsky, 1996][Pawlik et al., 1981][Keyeux et al., 1995][Villringer et al., 1994][Kleinfeld et al., 1998][Herman et al., 2009][Bereczki et al., 1993], hemoglobin volume changes and total blood volume changes are believed to be identical here.

Normalization in VASO and OIS

It must be noted that CBV weighting in VASO and OIS are normalized differently. VASO signal change refers to the total signal change, while OIS is directly proportional to relative CBV change, in units of CBV_{rest}. For direct quantitative comparisons between the two contrasts, a calibration factor CBV_{rest} must be assumed. In analogy to earlier VASO studies, a value of $CBV_{rest} = 5.5\%$ is assumed here [Lu et al., 2013]. Even though, the corresponding VASO-ΔCBV results are within error to OIS-ΔCBV results, when a value of $CBV_{rest} = 6.5\%$ would be assumed, quantitative estimates of VASO-ΔCBV and OIS-ΔCBV results would be identical.

3.2.5 Conclusions

This study used concurrent 2D-OIS and high field fMRI to quantify the signal source of a VASO pulse sequence for non-invasive assessment of CBV signal changes. Here, direct evidence is shown that the CBV derived from VASO is equivalent to CBV changes measured concurrently with 2D-OIS in rat somatosensory cortex. This is true for both, electrical stimulation and hypercapnia, respectively. The preclinical in vivo multimodal imaging data presented here can greatly increase the understanding of signal source of the VASO contrast. Comparisons between VASO results in humans and VASO results in rats confirm reported inter-species differences of CBV results. These comparisons suggest that features like smaller ΔCBV amplitude and slower return to baseline in rats compared to humans are not arising from different imaging modalities used, but must come from differences in physiology.

4 Applications of functional CBV measurements

4.1 Investigation of the neurovascular coupling in positive and negative BOLD responses[1]

Results in previous sections showed that SS-SI VASO has high sensitivity and can indeed quantitatively measure changes in blood volume. Hence, it can then be applied in neuroscientific studies, where conventional oxygenation based fMRI reaches its limits. Two examples are the detection of negative BOLD response in regions close to positive BOLD response or transitory negative BOLD response in the period after stimulus cessation. Regarding these phenomena, there is no consensus whether they directly reflect features of neural activity, or whether they are results from hydrodynamic effects of the vasculature. This section describes a study investigating the hemodynamic response in cases of negative BOLD signal. First, the corresponding literature is reviewed. A new multi compartment signal model is introduced to extend the SS-SI VASO method for measuring arterial and venous volume changes. Experimental results from humans and monkeys are shown and discussed with respect to the underlying neurovascular coupling.

4.1.1 Introduction to hemodynamics of negative BOLD responses

Negative BOLD responses (NBR) have been observed both in animals and humans. NBR can be caused by several independent mechanisms [Kim and Ogawa, 2012] including inhibitory neurogenically driven decreases in CBF [Shmuel et al., 2002], vasoconstriction in the absence of decreases in neural activity [Shih et al., 2009], or increases in $CMRO_2$ with no or insufficient CBF increases [Schridde et al., 2008][Zappe et al., 2008]. Under which circumstances the NBR has a vascular or metabolic origin has remained controversial. For this reason, and due to the potential of the negative signal to shed further light on neurovascular coupling, NBR is in the focus of current research [Hutchison et al., 2013][Mullinger et al., 2014][Schäfer et al., 2012][Smith et al., 2004][Tajima et al., 2010][Vafaee and Gjedde, 2004]. Early work suggested that the NBR was a result of non-neurally driven hemodynamic mechanisms, such as vascular steal [Harel et al., 2002][Woolsey et al., 1996]. However, recent work obtaining electrophysiological recordings simultaneously with BOLD-based fMRI, in anesthetized macaque monkeys, suggests that decreases in the $CMRO_2$ and neural activity are the major contributors (>60%) to NBR [Shmuel et al., 2006]. Further studies [Kennerley et al., 2012b][Pasley et al., 2007]

---

[1] This section is summarized in the paper [Huber et al., 2014a].

leave no room for non-neurally driven CBF contributions to NBR, and suggest that neurovascular coupling is conserved for both the positive and negative BOLD responses. There is now a general consensus that the NBR is accompanied by decreases in CBF and $CMRO_2$, as shown with fMRI in human visual and motor cortex [Pasley et al., 2007][Shmuel et al., 2002][Stefanovic et al., 2004], with fMRI in monkey visual cortex [Shmuel et al., 2006], and with fMRI and OIS in rat somatosensory cortex [Boorman et al., 2010][Kennerley et al., 2012b]. However, regardless of whether NBR is caused by neurogenic or vascular mechanisms, interpretation of energy consumption can be ambiguous. For example, it has been observed that decreases in neural activation due to increased inhibition can also be accompanied with metabolic increases [Devor et al., 2008][Logothetis, 2008] - in lay terms to turn something off requires work to be done and thus energy.

More refined layer-dependent studies of NBR in sensory motor cortex of rats and visual cortex of monkeys suggest that the NBR peaks in deeper cortical layers, while the positive GE BOLD response (PBR) peaks at the cortical surface [Boorman et al., 2010][Goense et al., 2012]. The role of CBV in NBR has remained elusive. Measurements with OIS and monocrystalline iron oxide nanoparticles (MION) reveal vasoconstriction in regions of NBR in rat somatosensory cortex [Boorman et al., 2010][Kennerley et al., 2012b] and cat extrastriate cortex [Harel et al., 2002]. In monkey striate cortex [Goense et al., 2012], CBV changes are investigated in regions of NBR with VASO [Lu et al., 2003][Yang et al., 2004] and MION. They reported a significant and surprising increase of CBV in deeper layers of the cortex during inhibitory tasks [Smirnakis et al., 2007]. Follow-up studies suggest that this increase of CBV in ROIs showing NBR is specific to stimulus and brain area [Bohraus et al., 2013]. These and earlier studies [Smirnakis et al., 2007] suggest that BOLD signal and CBV do not necessarily represent equivalent fMRI processes and mechanisms. In contrast to animal research, the role of CBV with regard to PBR and NBR has not yet been investigated in the human brain.

In this study, the earlier described multi-echo CBV-sensitive SS-SI VASO variant with BOLD correction (see section 3.1) was used to investigate the spatiotemporal characteristics of the hemodynamic response during stimuli that elicit positive and negative BOLD signal changes in human brain at 7 T. The goal of this study is to understand the underlying hemodynamic mechanisms of both PBR and NBR. This is achieved by breaking down the vascular response from BOLD signal changes, distinguishing larger pial (macro) vessels from microvasculature, and by separately investigating CBV components with arterial and venous-like oxygenation levels.

4.1.2 Theory of arterial and venous blood volume contributions in SS-SI VASO

Theory of BOLD-dependent T_2^* in SS-SI VASO

The signal intensity, S, of a parenchyma voxel acquired with blood nulling (bn) and in a control condition, where blood is not nulled (nn) can be considered as a sum of magnetizations from GM tissue and arterially oxygenated (a) and venously oxygenated

(v) blood:

$$S_{bn/nn} \propto \sum_{i \in \{GM,a,v\}} V_i \rho_i M_i \left(TI_{bn/nn}\right) e^{-\frac{TE}{T^*_{2,i}}}, \tag{4.1}$$

where V_i, ρ_i, and M_i denote the volume, proton density, and the z-magnetization of GM and blood within a voxel, respectively. TI is the inversion time and TE is the echo time. As introduced in section 3.1.2, in SS-SI VASO, the BOLD contaminated VASO images with blood nulling are acquired interleaved with purely BOLD weighted control images (without blood nulling).

Extravascular BOLD contaminations are assessed and eliminated by dynamic division of images obtained with and without blood nulling. By means of the division, the transverse relaxation term cancels out, and the resulting signal is dependent on M_z only (see section 3.1).

$$S' \approx \frac{M_{GM} e^{-\frac{TE}{T^*_{2,GM}}}}{M_{GM} e^{-\frac{TE}{T^*_{2,GM}}} + M_a e^{-\frac{TE}{T^*_{2,a}}} + M_v e^{-\frac{TE}{T^*_{2,v}}}} \approx \frac{M_{GM} e^{-\frac{TE}{T^*_{2,GM}}}}{\underbrace{M_{par}}_{const.} e^{-\frac{TE}{T^*_{2,par}}}} \tag{4.2}$$

However, this formulation does not consider the fact that there are different blood compartments with different baseline T_2^* values. Thus, it is extended here to a model that can distinguish blood components with long and short T_2^* values corresponding to arterial and venous vascular compartments.

T_2^* model to estimate 'arterial' and 'venous' CBV

In the present study, a model is developed to estimate whether blood volume changes occur in the portion of blood volume with longer baseline T_2^*, which is denoted here by 'arterial' oxygenation values, or in the portion blood volume with shorter T_2^*, which is denoted here as 'venous' oxygenation. Since 'arterial' and 'venous' blood portions are here considered based on their oxygenation level and not on anatomical structure, the terms 'arterial' and 'venous' are denoted in quotes. The separate consideration of 'arterial' and 'venous' CBV change based on their T_2^* can be regarded as distinguishing between BOLD-specific and BOLD-nonspecific CBV changes [Chen and Pike, 2010b].

A comprehensive quantitative model of the algorithm to separate the 'arterial' and 'venous' compartment of blood volume change is provided in the next section. Estimation of venously oxygenated CBV change can be intuitively understood as follows; with the procedure of dynamic division, SS-SI VASO is sensitive to volume changes of the blood component that is nulled in one condition (bn) and not nulled in the other condition (nn). Hence, for very short TE, both 'arterial' and 'venous' blood compartments are nulled for the bn condition, but in the control condition, they both contribute to the signal. Using a longer TE (e.g. $TE > 30$ ms), there is a difference in signal arising from 'arterial' and 'venous' blood. For long TEs, 'arterial' blood will be nulled for the bn condition, but not for the control condition - while 'venous' blood will be nulled in both conditions. In the blood nulled condition, 'venous' CBV is nulled due to T_1 selective nulling of the VASO contrast. In the control condition 'venous' blood contributions will be highly suppressed due to fast T_2^* relaxation and dephasing of signal from deoxygenated blood ('venous' $T_2^* \approx 12$ ms [Ivanov et al., 2013]). When the signal intensities of these two images are divided, 'venous' CBV change does not result in functional VASO signal change. 'Arterial' blood volume change, on the other hand, which is suppressed in the bn condition only, can contribute to the functional contrast. Hence, SS-SI VASO reflects the total CBV change at short TE and arterial weighted CBV changes at longer TE. A comparison of these, almost simultaneously acquired contrasts can be used to estimate 'venous' CBV change.

Mathematical description of estimation of ΔCBV_v in SS-SI VASO

As given above in Eq. 4.2, the SS-SI VASO signal incorporating 'arterial' and 'venous' CBV can be expressed as:

$$
\begin{aligned}
S \approx \frac{M_{GM} e^{-\frac{TE}{T^*_{2,GM}}}}{M_{GM} e^{-\frac{TE}{T^*_{2,GM}}} + M_a e^{-\frac{TE}{T^*_{2,a}}} + M_v e^{-\frac{TE}{T^*_{2,v}}}} = \\
= \frac{1}{1 + \frac{M_a}{M_{GM}} e^{-TE\left(R^*_{2,a} - R^*_{2,GM}\right)} + \frac{M_v}{M_{GM}} e^{-TE\left(R^*_{2,v} - R^*_{2,GM}\right)}}.
\end{aligned}
\tag{4.3}
$$

For simplicity, all magnetizations refer to z-magnetizations and are written in units of M_{tissue}; therefore $M_{GM} = 1 - CBV$. It can be assumed that the proton densities of tissue and blood are very similar (0.89 vs. 0.87 ml water/ml tissue [Donahue et al., 2010]). Only zeroth and first order terms are considered on all Taylor expansions. Equation 4.1 can be simplified to:

$$
S = \frac{M_a}{M_{GM}} e^{-TE\ \Delta R^*_a} + \frac{M_v}{M_{GM}} e^{-TE\ \Delta R^*_v}. \tag{4.4}
$$

Hence,

$$
\begin{aligned}
\Delta S = S_{act} - S_{rest} = \\
= \frac{M_{a,act}}{M_{GM,act}} e^{-TE\ \Delta R^*_{a,act}} + \frac{M_{v,act}}{M_{GM,act}} e^{-TE\ \Delta R^*_{v,act}} \\
- \frac{M_{a,rest}}{M_{GM,rest}} e^{-TE\ \Delta R^*_{a,rest}} - \frac{M_{v,rest}}{M_{GM,rest}} e^{-TE\ \Delta R^*_{v,rest}}
\end{aligned}
\tag{4.5}
$$

with $\Delta R^*_{a/v} = \frac{1}{T^*_{2,a/v}}$ and $\Delta R^*_{a/v,act/rest} = \frac{1}{T^*_{2,a/v,act/rest}} - \frac{1}{T^*_{2,GM,act/rest}}$.
Even in veins during hypercapnia, the change in T_2^* between activation and rest (12 - 16 ms) is much smaller compared to T_2^* differences between 'arterial' and 'venous' blood T_2^* of 12 - 37 ms [Ivanov et al., 2013]. Therefore:

$$
e^{-TE\left(\Delta R^*_{v,act} - \Delta R^*_{v,rest}\right)} \approx 1 - TE\left(\Delta R^*_{v,act} - \Delta R^*_{v,rest}\right). \tag{4.6}
$$

Since 'arterial' CBV is defined here by its T_2^* value to be fully oxygenated, there is no BOLD effect in arteries ($\Delta R^*_{a,act} - \Delta R^*_{a,rest} = 0$) and Eq. 4.5 can be simplified to:

$$\begin{aligned}\Delta S = \left[\frac{M_{a,act}}{M_{GM,act}} - \frac{M_{a,rest}}{M_{GM,rest}}\right] e^{-TE\ \Delta R^*_{a,rest}} + \left[\frac{M_{v,act}}{M_{GM,act}} - \frac{M_{v,rest}}{M_{GM,rest}}\right] e^{-TE\ \Delta R^*_{v,rest}} \\ + \underbrace{\frac{M_{v,rest}}{M_{GM,rest}} TE\left(\Delta R^*_{v,act} - \Delta R^*_{v,rest}\right)}_{C_1}.\end{aligned} \tag{4.7}$$

$C1$ can be considered as a higher order term that comprises the intravascular BOLD effect. According to the definition of $\Delta R^*_{a/v,act/rest}$ above, it can be rewritten as:

$$C_1 = \frac{M_{v,rest}}{M_{GM,rest}} TE \left[R^*_{v,act} - R^*_{v,rest} - \left(R^*_{GM,act} - R^*_{GM,rest}\right)\right]. \tag{4.8}$$

Since 'arterial' blood has a longer T_2^* than GM, the first term of Eq. 4.7 is amplified for longer TEs and the 'arterial' CBV change is overestimated. Since 'venous' blood has a significantly shorter T_2^* than GM, the second term of Eq. 4.7 is suppressed at longer TEs and the 'venous' CBV change is underestimated. Using literature values for 'arterial', 'venous' and GM T_2^*, the TE-dependence can be used to estimate the 'arterial' and 'venous' contributions to blood volume change according to:

$$\begin{aligned} \Delta S(TE = 0) - \Delta S(TE') = \\ \left[\frac{M_{a,act}}{M_{GM,act}} - \frac{M_{a,rest}}{M_{GM,rest}}\right] + \left[\frac{M_{v,act}}{M_{GM,act}} - \frac{M_{v,rest}}{M_{GM,rest}}\right] \\ -\left\{\left[\frac{M_{a,act}}{M_{GM,act}} - \frac{M_{a,rest}}{M_{GM,rest}}\right] e^{-TE\ \Delta R^*_{a,rest}} + \left[\frac{M_{v,act}}{M_{GM,act}} - \frac{M_{v,rest}}{M_{GM,rest}}\right] e^{-TE\ \Delta R^*_{v,rest}}\right\} = \\ \frac{CBV_{a,act} + CBV_{v,act}}{1 - CBV_{act}} - \frac{CBV_{a,rest} + CBV_{v,rest}}{1 - CBV_{rest}} \\ -\left\{\frac{CBV_{a,act}}{1 - CBV_{act}} e^{-TE'\Delta R^*_{a,rest}} - \frac{CBV_{a,rest}}{1 - CBV_{rest}} e^{-TE'\Delta R^*_{a,rest}}\right. \\ \left. + \frac{CBV_{v,act}}{1 - CBV_{act}} e^{-TE'\Delta R^*_{v,rest}} - \frac{CBV_{v,rest}}{1 - CBV_{rest}} e^{-TE'\Delta R^*_{v,rest}}\right\} - C_1. \end{aligned} \tag{4.9}$$

Assuming that the relative CBV is small compared to the relative GM volume ($1 - CBV \approx 1$) and considering that any CBV change is either 'arterial' or 'venous' ($\Delta CBV_a + \Delta CBV_v = \Delta CBV$), Eq. 4.9 can be further simplified to:

$$\begin{aligned} \Delta S(TE = 0) - \Delta S(TE') = \\ \Delta CBV - \left\{\Delta CBV e^{-TE'\Delta R^*_{a,rest}} + \Delta CBV_v \left[e^{-TE'\Delta R^*_{v,rest}} - e^{-TE'\Delta R^*_{a,rest}}\right]\right\} - C_1 = \\ \Delta CBV \left[1 - e^{-TE'\Delta R^*_{a,rest}}\right] + \Delta CBV_v \left[e^{-TE'\Delta R^*_{v,rest}} - e^{-TE'\Delta R^*_{a,rest}}\right] - C_1. \end{aligned} \tag{4.10}$$

Solved for ΔCBV_v, Eq. 4.10 becomes:

$$\Delta CBV_v = \frac{\Delta S(TE=0) - \Delta S(TE') - \Delta CBV \overbrace{\left[1 - e^{-TE'\Delta R^*_{a,rest}}\right]}^{C_2} + C_1}{\underbrace{e^{-TE'\Delta R^*_{v,rest}} - e^{-TE'\Delta R^*_{a,rest}}}_{C_3}}. \tag{4.11}$$

By means of Eq. 4.11 and the literature values given in Tab. 4.1, the multi-exponential VASO data can be used to separate 'venous' and 'arterial' CBV changes. According to Eq. 4.11, signal changes at two different TEs are needed to calculate the 'venous' CBV change. C_1 is one order of magnitude smaller than C_2 and C_3, which is consistent with the fact that at 7 T the intravascular BOLD effect is negligibly small (10% of the total BOLD signal [Donahue et al., 2010][Martindale et al., 2008]). Here, C_1 is used as a linear parameter. Neglecting it can lead to an underestimation of the 'venous' CBV change by approximately 16% (e.g. resulting in $\Delta CBV_v = 6.1\%$ instead of the true value of $\Delta CBV_v = 7.08\%$).

$T^*_{2,a}$	$T^*_{2,v}$	$T^*_{2,GM}$	ΔR^*_a	ΔR^*_v	C_2	C_3
[Ivanov et al., 2013]	[Ivanov et al., 2013]	[Donahue et al., 2010]	Eq. 4.5	Eq. 4.5	Eq. 4.11	Eq. 4.11
37.5 ms	12.2 ms	25.1 ms	-13.1 s^{-1}	42.1 s^{-1}	-0.17	-0.57

Table 4.1: Literature relaxation values of single components for separation of 'arterial' and 'venous' CBV change.

CBV_v	$R^*_{2,v,act} - R^*_{2,v,rest}$	$R^*_{2,GM,act} - R^*_{2,GM,rest}$	C_1
[Kim and Ogawa, 2012]	[Ivanov et al., 2013]	[Donahue et al., 2010]	Eq. 4.7
70% of 5.5% (CBV_{tot}) = 3.85%	$-22.4 s^{-1}$	$-0.77 s^{-1}$	-0.0098

Table 4.2: Literature values for estimation of the intra-vascular BOLD C_1 term.

4.1.3 Methods

Image acquisition

SS-SI VASO was implemented on a Siemens MAGNETOM 7T scanner (Siemens Healthcare, Erlangen, Germany). For RF transmission and reception, a 24-channel receive and circularly polarized single-channel transmit head coil (Nova Medical, Wilmington MA, USA) was used. To circumvent the effects of inflow of fresh (uninverted) blood magnetization into the microvasculature of the imaging slice, the inversion efficiency of the VASO preparation pulse was reduced, so that the blood-nulling time of the VASO sequence was shorter than the arterial arrival time. More technical details and the performance of this partial inversion pulse are discussed in section 4.3. Data were acquired in five axial slices aligned along the calcarine sulcus with a two-dimensional single-shot multi-GE EPI readout. Sequence parameters were: adjusted inversion efficiency $\xi =$ 85%, partial Fourier factor = 5/8, Grappa factor 3, $TE1/TE2/TE3/TI1/TI2/TR =$ 12/32/52/1000/2500/3000 ms. Depending on the participants' brain size, the nominal resolution was between 1.3 x 1.3 x 1.5 mm^3 and 1.5 x 1.5 x 1.5 mm^3. Maps of B_1 and the static field amplitude B_0 were acquired with a modified actual flip angle imaging (MAFI) [Boulant et al., 2009] method for each participant to ensure proper performance of the inversion pulse used (data not shown).

For the purpose of estimating voxel-wise tissue composition independent of distortions, further inversion recovery measurements with multiple TIs of 36/200/300/1200/1500 ms were performed with acquisition parameters otherwise identical to the functional scans. Four additional experiments were conducted to measure CBF changes in ROIs of PBR and NBR. To account for SAR- and B_1-constraints of PASL using a head coil at 7 T, a TR-FOCI [Hurley et al., 2010] pulse was implemented in a FAIR-QUIPSSII [Kim, 1995][Wong et al., 1998] sequence. Single-shot double-echo EPI readout was used for image acquisition. Further sequence parameters were: nominal resolution = 3 x 3 x 3 mm^3, $TE1/TE2/TI1/TI2/TR =$ 8.2/19.4/700/1700/3000 ms. All procedures of this study were approved by the ethics committee of the University of Leipzig. Informed written consent was given by all volunteers.

In order to compare VASO results acquired in humans with results from monkeys at higher resolutions, the same SS-SI VASO sequence used in the human experiments was implemented on a monkey model. These comparisons help in distinguishing between influences of methodology or experimental setup, and can provide additional insights in the interpretation of the human results in the light of previous studies. Hence, SS-SI VASO, as described above, was implemented on a 7 T vertical primate scanner (Bruker Biospec 70/60v, Bruker Biospin GmbH, Ettlingen, Germany) and used in four experiments (imaging the same monkey) employing the experimental setup described in [Goense et al., 2010]. For further details of experimental hardware (e.g. magnet and RF coils) and animal preparation (e.g. anesthesia and rotating ring stimulus presentation) please refer to [Goense et al., 2012][Logothetis et al., 1999][Pfeuffer et al., 2004]. The adapted SS-SI VASO parameters were 0.63 x 0.75 x 3 mm^3 nominal voxel size and $TE/TI1/TI2/TR =$ 7.8/785/2285/3000 ms. Experiments were approved by the local authorities (Regierungspräsidium Baden-Württemberg, Germany) and were in full compliance with the guidelines of the European Community (EUVD 86/609/EEC) for the care and use of laboratory animals.

Experimental setup

Three different 12 min visual stimulation paradigms (alternating 30 s rest vs. 30 s stimulation) were used to investigate BOLD signal and CBV changes in regions of PBR and NBR in 17 healthy human volunteers (8 female, 21 to 32 years old). Two of the paradigms consisted of a full-field flickering checkerboard (8 Hz) and a small circle flickering checkerboard (8 Hz). The small flickering checkerboard paradigm [Wade and Rowland, 2010] was chosen in this study because it induced stronger NBR in pilot experiments compared to small ring stimulation paradigms [Pasley et al., 2007][Shmuel et al., 2002][Shmuel et al., 2006]. The full field stimulation paradigm was used for comparison of the same cortical regions during different stimulations. For the sake of comparison with recently published results in monkeys, a rotating ring checkerboard (rotation $2\pi/3$ rad/s, switching rotation direction every 1.5 - 6 s) was also presented [Goense et al., 2012][Shmuel et al., 2006] (Fig. 4.1). Based on electrophysiology experiments in monkeys with similar stimuli [Shmuel et al., 2006], it can be assumed that the stimuli used here induce a neural response that is either predominantly excitatory or inhibitory, in regions of PBR and NBR, respectively. However, at the level of individual neurons, both excitation and inhibition are taking place in both NBR and PBR. The terms 'excitatory' and 'inhibitory' are thus used here to describe the stimulation paradigms and their response with regard to their net response within the considered brain regions analogous to earlier studies [Stefanovic et al., 2004]. To control attention and visual fixation, participants performed a concurrent task in which they responded to subtle color changes of a barely visible fixation point for the duration of the experiments.

Data analysis

The data analysis procedure is graphically summarized in Fig. 4.1. Magnetic resonance images were motion corrected using SPM8 (Welcome Department, University College London, UK). Statistical analysis was done using FSL Feat (Version 5.98) [Worsley, 2001]. In order to estimate voxel-wise tissue composition independent of slice orientation and image distortions, data from multiple TI experiments were used to generate fractional volume maps of GM, WM and CSF [Shin et al., 2010]. Assumed T_1 values were $T_{1,WM}/T_{1,GM}/T_{1,CSF} = 1.1/1.9/4.0$ s (Tab. 2.1). Functional ROIs were defined based on the BOLD data as a cluster of voxels having z-values above 2.0 and a significance level of $p < 0.05$ (automatically corrected for multiple comparisons in FSL based upon GRF theory), after smoothing with a kernel size of 1 mm. All further analysis was done in these ROIs defined from BOLD data meaning that the same ROIs were used for analyzing BOLD and VASO data. Analysis was done on unsmoothed data with C++ algorithms using libraries of GSL [Galassi et al., 2009] and ODIN [Jochimsen and von Mengershausen, 2004].

Surface detection

Variations of GM voxels T_1 resulting from partial voluming of CSF and WM was used to distinguish voxels containing GM and CSF ($T_1 > T_{1,GM}$) from voxels containing GM and WM ($T_1 < T_{1,GM}$) according to descriptions in section 3.1. This separation algorithm is based on the assumption that at the resolution used, simultaneous partial voluming of any voxel with both WM and CSF does not occur.

Because voxels with more CSF partial voluming also have a higher probability of containing superficial cortical layers and pial vessels, these voxels are hereafter referred to

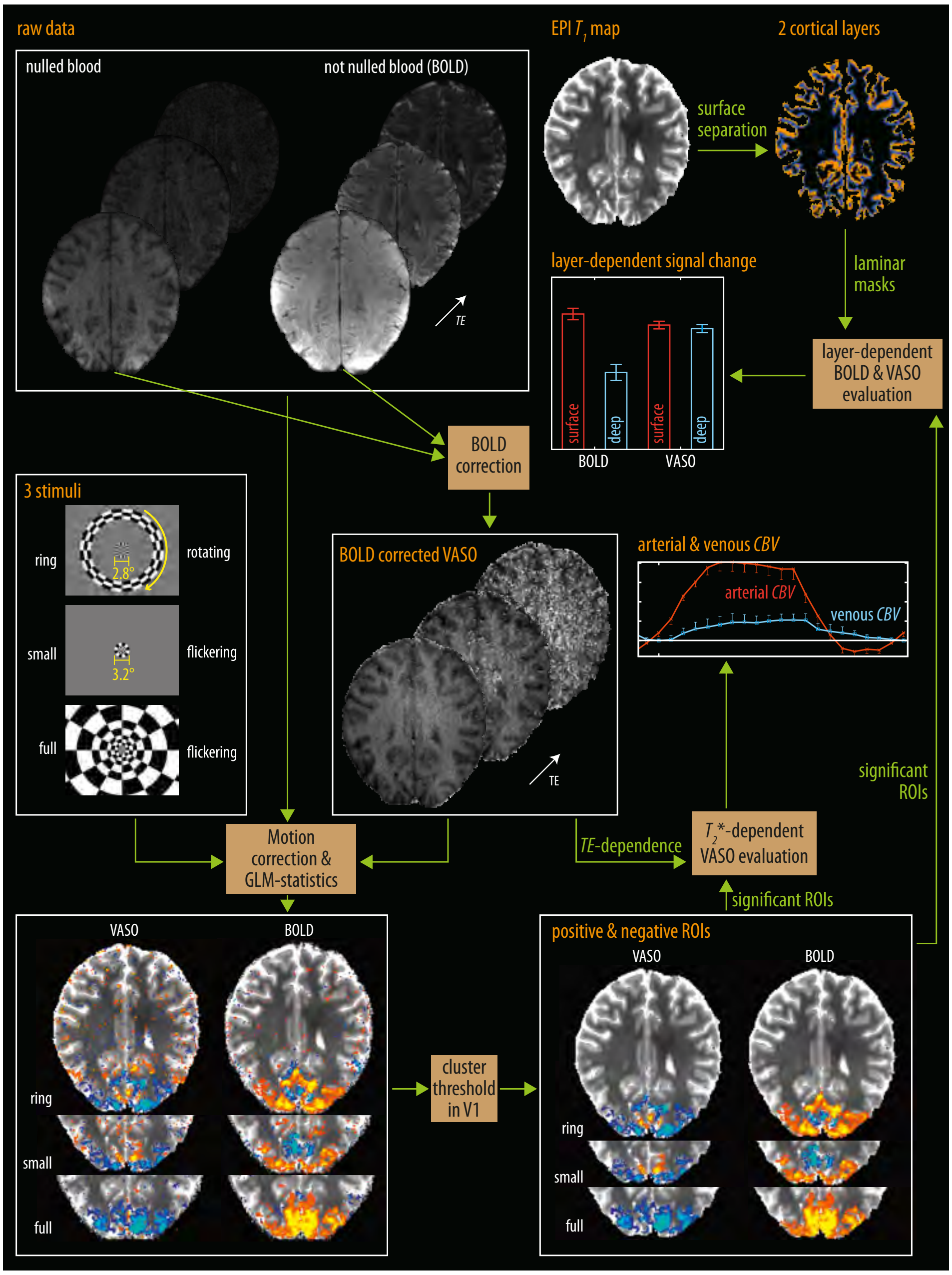

Figure 4.1: Evaluation procedure for estimating BOLD and CBV-related signal changes: Multi-echo images with and without blood nulling are acquired during three different stimulation paradigms. Time series of BOLD and BOLD corrected VASO were used to define ROIs of PBR and NBR (using FSL). Signal changes within these ROIs are considered with respect to PBR and NBR, with respect to 'arterial' and 'venous' CBV, and with respect to surface and deeper cortical laminae.

as surface GM voxels, in contrast to deeper GM voxels. The threshold of CSF partial voluming to separate the two subsets within the functional ROIs is adjusted such that the numbers of surface and deeper GM voxels are equal. This is done to avoid biases across participants with different curvature. Considering a nominal voxel size of 1.3 - 1.5 mm, the voxel size is 70% - 80% of the cortical thickness of V1 of 1.8 ± 0.2 mm [Jiang et al., 2009]. This resolution is thus insufficient to resolve laminar features, but adequate to estimate the influence of surface vasculature. Considering the laminar dependence of total CBV at rest, surface voxels are assumed to have 12% higher baseline CBV than deeper layers [Kennerley et al., 2005][Zhao et al., 2006] (see also discussion and Fig. 4.3D). Average baseline CBV within GM was assumed to be 5.5% [Lu et al., 2013].

4.1.4 Results of SS-SI VASO in negative BOLD regions

Stimulus setup

Using an eye tracker inside the MRI bore, small ($1^\circ - 1.5^\circ$ of visual field) saccadic eye movements were observed during each 12 min experiment. These saccadic movements were slightly smaller than the central circles of the stimulation paradigms. When asked, participants reported an after-image detectible for 2 - 10 s with the small flickering stimulation paradigm and 20 - 30 s with the rotation ring stimulation paradigm.

Spatial activity maps

Significant positive BOLD and corresponding negative VASO signal changes were detected for the rotating ring and small flickering stimulation paradigms in all participants. For the rotating ring stimulation paradigm, in three of the 17 participants, significant negative BOLD signal and positive VASO signal changes were detected in one hemisphere only, most probably due to suboptimal positioning of the imaging slices. The ROIs of activation and deactivation are remarkably similar in maps of BOLD and VASO signal change; the retinotopic organization of visual cortex can clearly be identified in the statistical activation maps (Fig. 4.2). The GM voxels identified as significantly modulated by the three tasks contained average volume distributions of 19% WM, 68% GM and 12% CSF.

The number of voxels in ROIs of NBR was significantly ($p < 0.0001$) smaller for the rotating rings stimulation paradigm (average number of voxels 81) compared to the small flickering checkerboard paradigm (average number of voxels 960) with resultantly decreased SNR.

Surface and deeper laminae

Differences in cortical curvature within ROIs of PBR and NBR and differences in hemodynamic response in different cortical areas can result in systematic errors when comparing signal changes across activated and deactivated regions. To avoid such bias, positive and negative responses were considered in the same ROIs, but for different stimulation paradigms. Positive (excitatory) and negative (inhibitory) responses refer to full-field

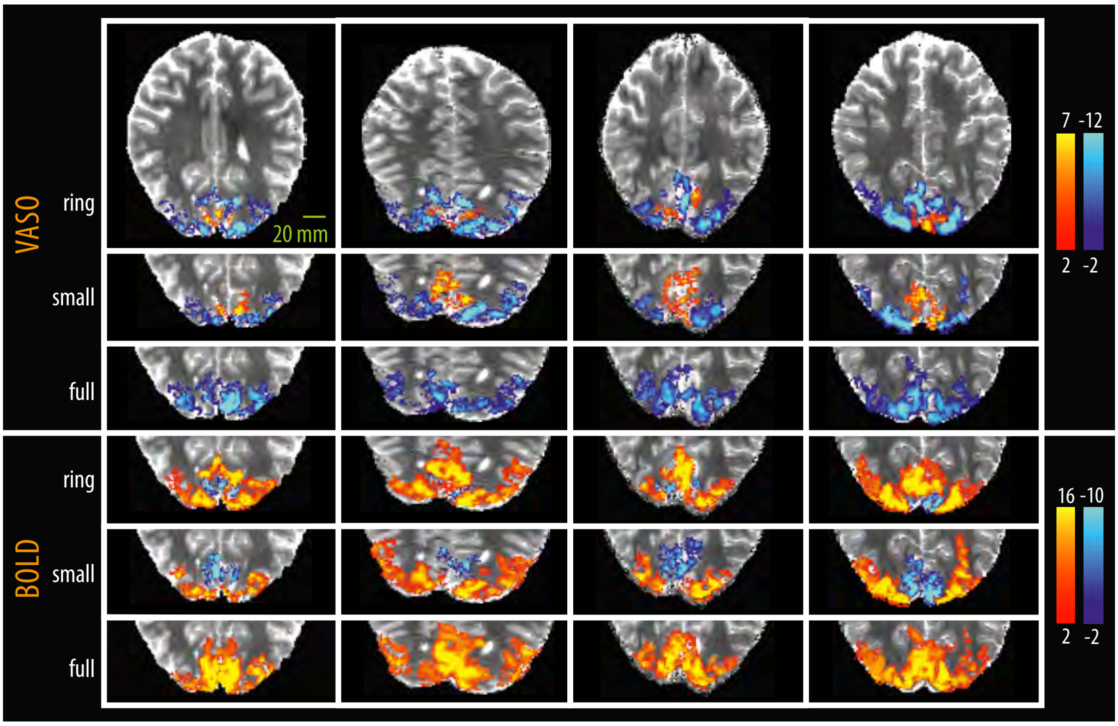

Figure 4.2: Statistical z-score activation maps of the VASO and BOLD responses to three different stimulation paradigms in four participants: ROIs of positive and negative signal changes were consistent across participants. ROIs suggesting activation and deactivation were almost identical in VASO and BOLD signal, across participants.

and small flickering checkerboard stimulation, respectively. Positive GE BOLD signal change was largely dominated by surface GM voxels. CBV on the other hand did not show this pattern and was not significantly different between surface and deeper GM voxels (Fig. 4.3A). During inhibitory tasks, NBR amplitude was larger ($p < 0.05$) in deeper laminae (Fig. 4.3B), as observed previously [Boorman et al., 2010][Goense et al., 2012]. Vasoconstriction during inhibitory tasks is highly dominated by surface GM voxels ($p < 0.001$) (CBV change in Fig. 4.3B). Regarding the sensitivity to surface vessels and deeper laminae, the change of CBV_v has a clear signature. The relative 'venous' contribution is significantly ($p < 0.001$) higher in deeper GM voxels without larger vessels (40%) compared to the surface GM voxels containing such vessels (19%) (Fig. 4.3C).

Time course analysis

VASO-CBV and BOLD signal time courses during the small flickering checkerboard stimulation paradigm are shown for ROIs with PBR and NBR in Figs. 4.4A and 4.4B, respectively. The time at which the BOLD signal crosses the baseline after stimulus cessation in ROIs of NBR (2.9 s ± 1.7 s) is significantly ($p < 0.001$) earlier compared to that of PBR ROIs (7.6 s ± 2.8 s) - consistent with previous observations [Goense et al., 2012][Kennerley et al., 2012b][Shmuel et al., 2006]. When the mean signal is averaged across each respective ROI, both BOLD signal and CBV changes have the same sign in ROIs with NBR as compared to ROIs with PBR. The mean amplitude of both CBV change and BOLD response in ROIs of NBR is (35 ± 5)% of the amplitude of the ROIs of PBR, suggesting a conserved neurovascular coupling for both cases.

'Arterial' and 'venous' CBV

To avoid any bias of unexpected and potentially different vascularization in different parts of the visual cortex [Weber et al., 2008], 'arterial' and 'venous' blood volume changes ($\Delta CBV_{a/v}$) are considered in one part of the cortex only, namely in ROIs that show NBR in response to the small circle flickering checkerboard visual stimulation. These GM voxels are considered during excitatory tasks (full-field stimulation) and inhibitory tasks (small circle stimulation). During the excitatory task, the total CBV change, ΔCBV_{tot}, of (23.7 ± 2.2)% is composed of (16.6 ± 1.6)% 'arterial' ΔCBV_a and (7.1 ± 2.4)% 'venous' ΔCBV_v. Therefore, the relative composition of ΔCBV_{tot} is 71% 'arterial' ΔCBV_a and 29% 'venous' ΔCBV_v. 'Arterial' CBV_a has a faster response and a faster post-stimulus baseline crossing, compared to the 'venous' CBV_v response (Fig. 4.5B), as observed previously in animals [Kennerley et al., 2012b][Kim and Kim, 2011][Zong et al., 2012]. 'Venous' ΔCBV_v contribution appears negligibly small compared to ΔCBV_{tot} (Fig. 4.5C) during the inhibitory task, as ΔCBV_v is not significantly different from zero.

CBF

ASL-FAIR experiments provide a sufficiently high SNR to estimate CBF changes in ROIs of PBR and NBR at 7 T (Fig. 4.6B). CBF time courses show similar dynamics compared to BOLD signal or 'arterial' CBV_a. There is a significant CBF increase in

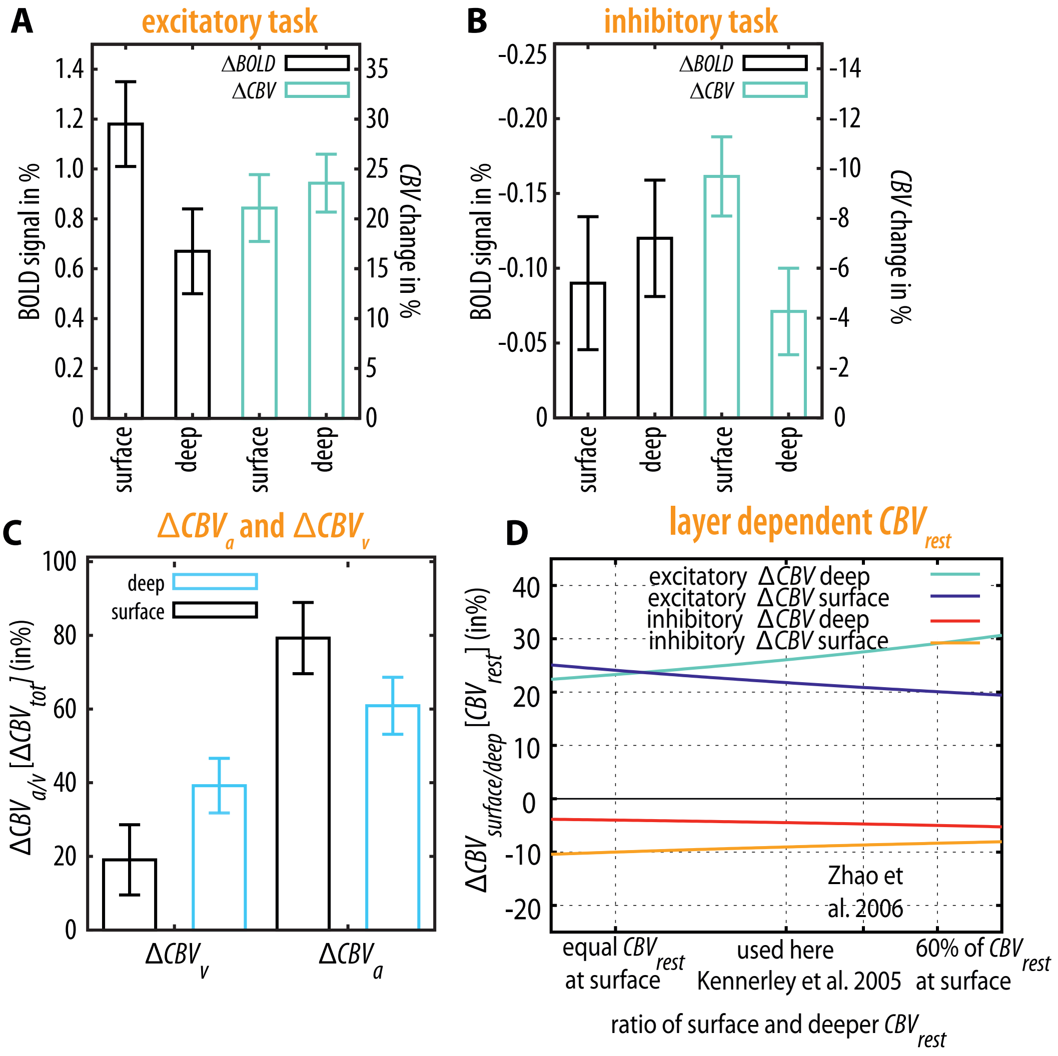

Figure 4.3: Laminar-dependence of BOLD and VASO signals: Negative responses refer to ROIs with NBR during the small flickering checkerboard stimulation paradigm. (A) For the excitatory task, GE BOLD signal was significantly dominated by signal from the cortical surface, compared to deeper gray matter. The VASO signal, on the other hand, did not exhibit this surface dominance. (B) The BOLD signal lost its surface dominance for the inhibitory task and its signal change was significantly smaller at the surface compared to deeper layers. The VASO signal change was significantly dominated by signal from the surface vessels. (C) In voxels without surface vessels, the amount of 'arterial' ΔCBV is only 63%. (D) Discussion of the effect, when CBV_{rest} distribution is assumed to be different in surface and deeper voxels.

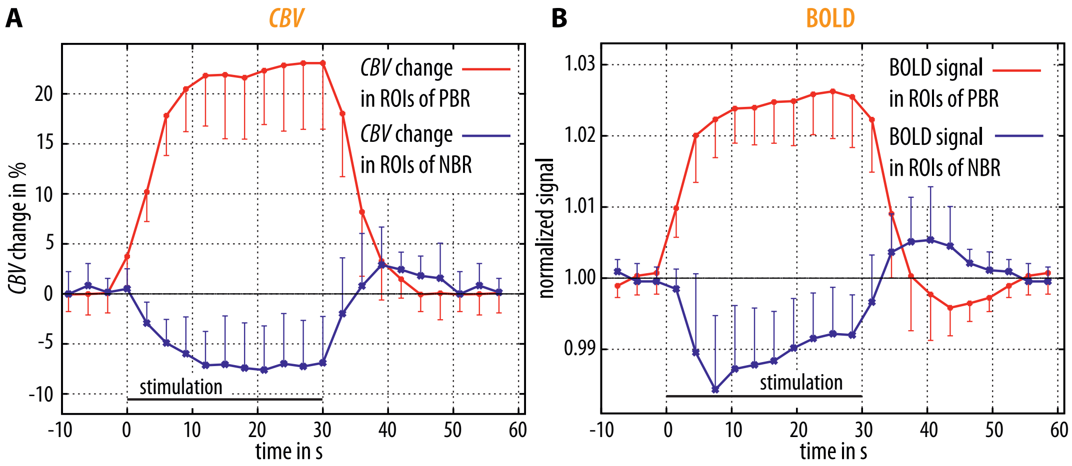

Figure 4.4: CBV and BOLD time courses in ROIs of PBR and NBR for the stimulation paradigm using the small flickering checkerboard: Post-stimulus baseline crossing was significantly faster in ROIs of NBR compared to ROIs of PBR for both CBV and BOLD signal changes.

ROIs with PBR and a significant CBF decrease in ROIs with NBR, as observed earlier in humans [Pasley et al., 2007][Shmuel et al., 2002][Stefanovic et al., 2004].

Rotating ring stimulation

The time courses in Fig. 4.7 refer to the ROIs with NBR during the rotating ring stimulation paradigm. Activation and deactivation refer to full-field flickering checkerboard and ring stimulation within these ROIs. Despite the smaller functional CNR in the ring paradigm, the same temporal features of positive and negative responses can be seen, i.e. faster post-stimulus baseline crossing as well as the laminar-dependent characteristics in CBV and BOLD signal changes. Aside from the different amplitudes of the time courses, there is no significant difference between surface and deeper GM voxels.

Monkey experiments

Positive and negative BOLD responses during a rotating ring stimulation paradigm could be detected with SS-SI VASO in monkey brain (Fig. 4.8). In the depicted sagittal slice, regions of NBR correspond to the ring of gray background, and regions of PBR correspond to the outer checkerboard ring. Maps of BOLD corrected VASO signal change indicate increase in CBV in regions of NBR, consistent with earlier experiments in monkeys [Goense et al., 2012] but in contrast to the human results in this study (Fig. 4.2).

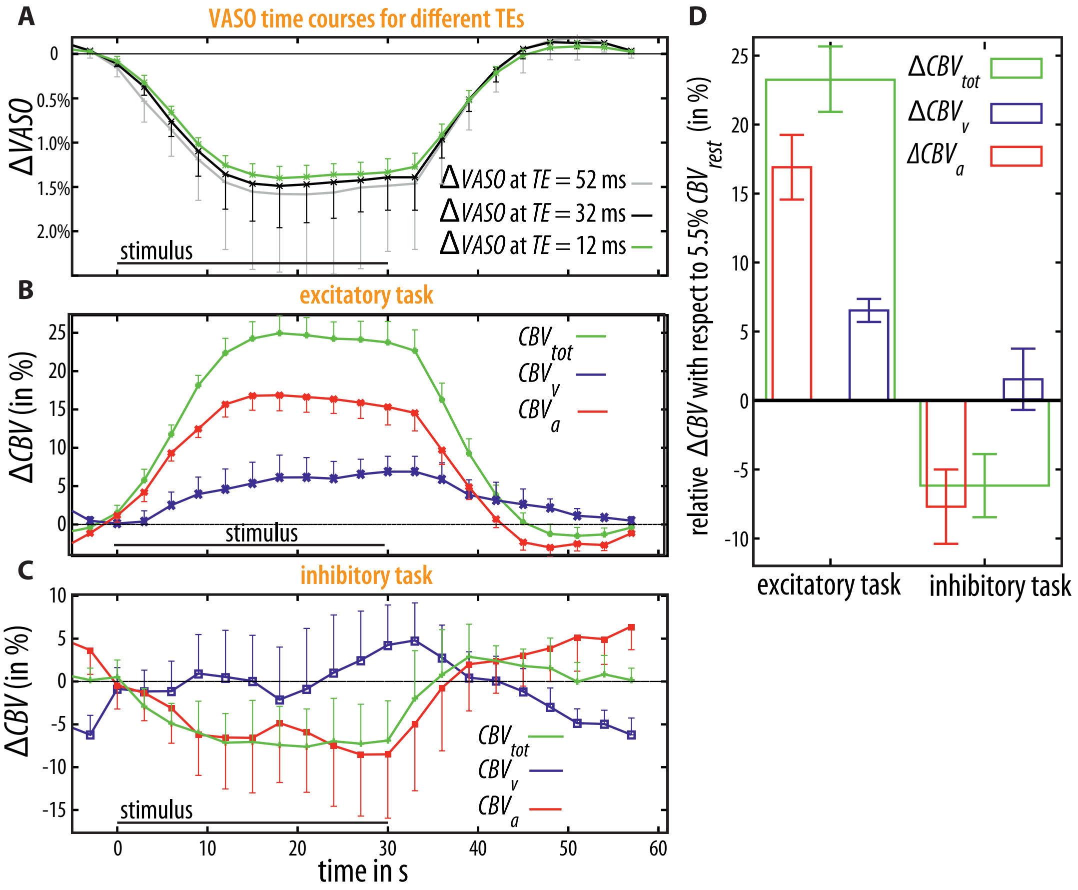

Figure 4.5: The ‘arterial’ and ‘venous’ composition of CBV changes: (A) VASO time courses for different TEs during full field flickering checkerboard stimulation. With longer TEs ($TE > 12$ ms, black and gray), the BOLD corrected VASO signal change increases. Signal changes with shorter TE reflect both, ‘venous’ and ‘arterial’ CBV change. Signal changes with longer TE captures ‘arterial’ CBV change only. It can be seen that the signal change with shorter TE has a significantly faster response compared to longer TE time courses, indicating a faster ‘arterial’ response compared to the ‘venous’ one. Time courses of total, ‘arterial’ and ‘venous’ CBV during an excitatory task are depicted in (B). ‘Venous’ CBV_v is significantly smaller than ‘arterial’ CBV_a and shows a delayed response. ‘Arterial’ CBV_a shows a distinct post-stimulus undershoot. Time courses of total, ‘arterial’ and ‘venous’ CBV during an inhibitory task (small flickering checkerboard) are depicted in (C). Again, change in total CBV_{tot} are dominated by the ‘arterial’ component. D) depicts a summary of blood volume changes during excitatory and inhibitory tasks.

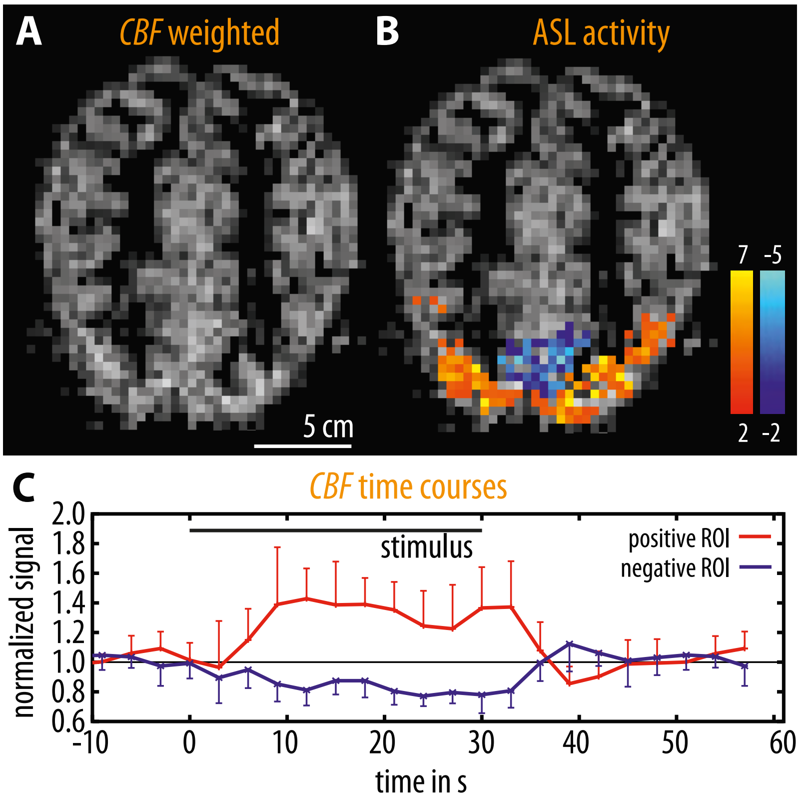

Figure 4.6: CBF in response to the small flickering checkerboard stimulation paradigm: (A) depicts the baseline perfusion weighted image of one of the participants. (B) depicts the statistical CBF activation map indicating a CBF increase and CBF decrease in regions of PBR and NBR in the same participant. (C) depicts the CBF time courses in ROIs of PBR and NBR averaged over four participants.

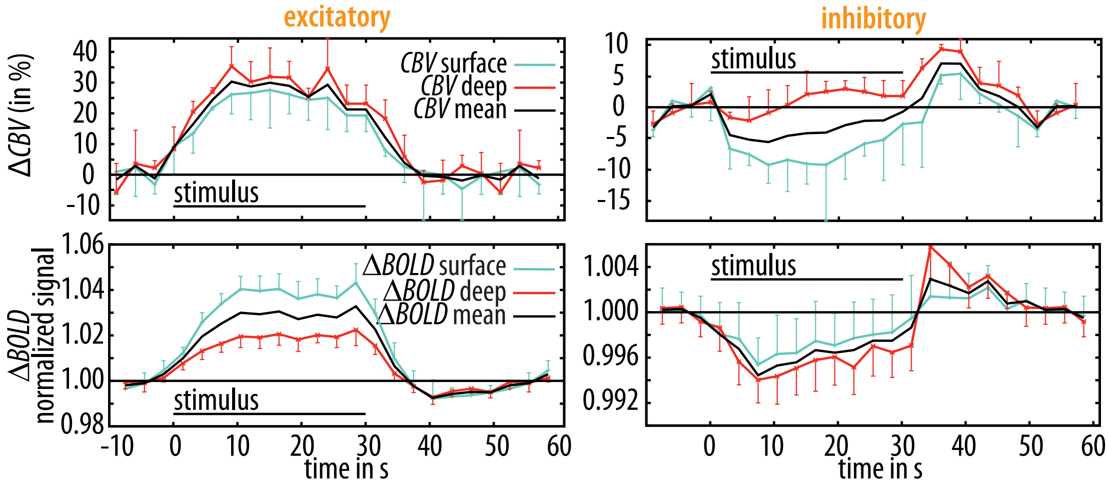

Figure 4.7: Time courses of VASO-CBV and BOLD signal during the rotating ring stimulation task: Time courses are shown for surface and deeper GM voxels within these ROIs. During the excitatory task, the BOLD signal change is dominated by surface voxels, while ΔCBV shows comparable time courses in surface and deeper laminae. During the inhibitory rotating ring stimulation paradigm, ΔCBV and BOLD signal time courses have a faster post-stimulus baseline crossing. For this task, BOLD signal loses its surface dominance and the ΔCBV seems to predominantly occur in the surface voxels.

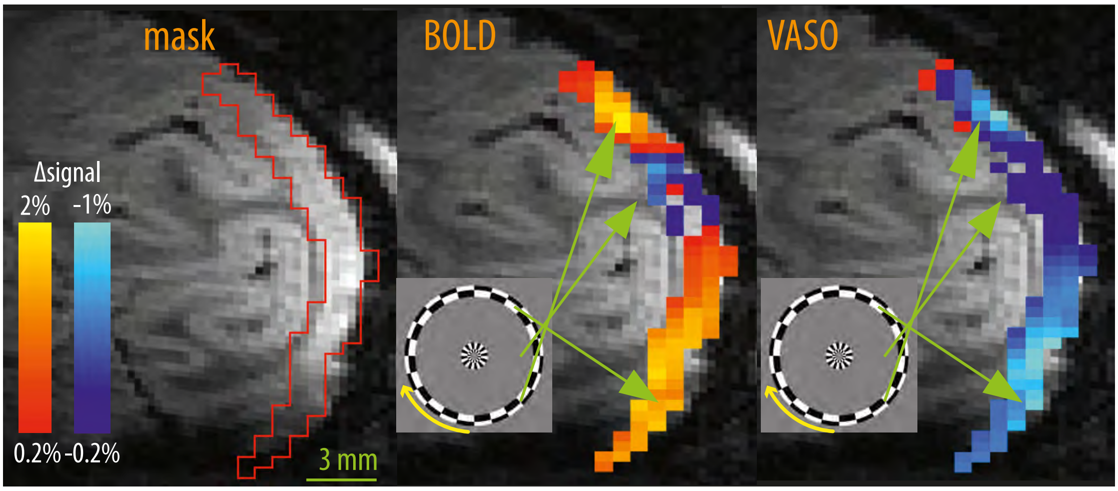

Figure 4.8: SS-SI VASO functional activation in an anesthetized monkey acquired for comparison between the results obtained in humans and monkeys: The panels show the BOLD and VASO signal change in a sagittal slice through macaque striate cortex. The ROIs of PBR showed a VASO signal decrease. Green arrows point to the regions processing the rotating checkerboard pattern. NBR in areas processing the ring of gray background, (3° – 9°, middle part of ROI) and PBR regions correspond to the checkerboard ring (9° – 11°). ROIs of NBR show a small VASO signal decrease, indicating vasodilation consistent with previous studies.

4.1.5 Discussion

The data presented in this study suggest that the effects of specific vasculature compartments on the BOLD signal changes can be investigated during excitatory and inhibitory tasks noninvasively in humans at 7 T. With the relatively high SNR of the SS-SI VASO method used here, the spatiotemporal characteristics of the interplay between BOLD responses and vasculature could be identified, such as differences in time courses and signal origin from different vascular compartments. Even though the voxel volume in FAIR experiments (3 x 3 x 3 mm^3) was eight times larger than that used with SS-SI VASO ($\leq$ 1.5 x 1.5 x 1.5 mm^3), the CNR of the functional CBV was still larger than the CNR of the functional CBF. This suggests that SS-SI VASO can be a useful tool in obtaining high SNR non-BOLD hemodynamic responses at high fields, especially with limited RF coil infrastructure available at 7 T. Given that the voxel size in this study was comparable to the cortical thickness (approx. 72%), surface GM voxels are likely to contain larger superficial arteries and veins as well as microvasculature of the middle and upper layers. Deeper GM voxels will contain microvasculature of the cortical tissue without influence from larger superficial vessels as schematically depicted in Fig. 4.9 [Duvernoy et al., 1981][Weber et al., 2008]. The additional separation into ‘arterial’ and ‘venous’ CBV provides indications which type of vessels are responsible for the detected signal changes, arteries or veins.

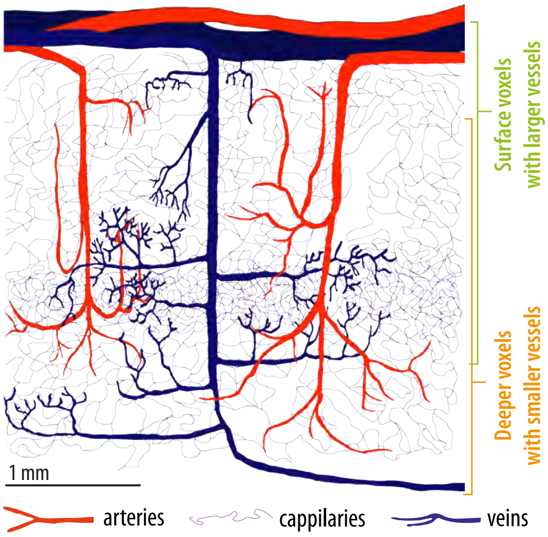

Figure 4.9: Assumed cortical vasculature distribution for the surface voxels and deeper voxels for the interpretation of the presented results. The depicted schematic vessel geometry is drawn based on optical studies a brain vascularization [Duvernoy et al., 1981][Weber et al., 2008].

The larger positive BOLD response at the surface (Fig. 4.3A) results most probably from the typical accumulation of blood oxygenation changes at the cortical surface, where the ‘venous’ blood leaves the cortex, and from the well-established GE BOLD sensitivity to larger veins [Kim and Ogawa, 2012]. The fact that VASO contrast is independent of whether the GM voxels contain larger surface vessels (Fig. 4.3A) suggests that its contrast has higher specificity to the microvasculature, similar to other CBV-sensitive modalities [Jin and Kim, 2008a][Jin and Kim, 2008b]. The same was also seen in high-resolution (500 x 500 mm^2) data obtained in macaques in the current study (data not shown). Figure 4.3C shows a relatively larger proportion of 'arterial' CBV change in surface GM voxels compared to deeper GM voxels, while the 'venous' contribution to the total CBV change occurs predominantly in deeper tissue voxels. This is consistent with the fact that the contribution of larger veins at the surface is small compared to the overall CBV change, dominated by arterioles and capillaries [Hillman et al., 2007][Lee et al., 2001]. The larger arterioles close to the cortical surface, on the other hand, can contribute to the CBV change, in addition to the smaller arterioles and capillaries.

The interpretation of the results for inhibitory tasks (Fig. 4.3B and 4.5D) is less obvious. Negative BOLD contrast shows smaller signal changes in surface voxels containing large superficial veins, and vasoconstriction is greatest in larger superficial arteries. The loss of surface dominance in the negative BOLD response can partly arise from contamination of pial vessels draining adjacent excited regions and passing though surface voxels of deactivated regions. This effect can explain artifactual BOLD signal changes up to about 3 mm away from the activated region [Turner, 2002]. Independently, it might also result from different underlying layer-dependent inhibition compared to excitation. The different laminar dependence might be also associated with an altered interplay of responses in different compartments of the vascular tree.

There are several indications in the CBV data that suggest altered dynamics within the different vascular compartments during inhibitory tasks as compared to excitatory tasks. Firstly, during inhibitory tasks the CBV change is dominant in surface GM voxels (Figs. 4.3B and 4.7). This is in contrast to the excitatory case, where the CBV change is similar within surface and deeper GM voxels. Secondly, data shown in Figs. 4.5C and 4.5D suggest that the corresponding CBV decrease comes only from fully oxygenated arterial vessels, and not from the less oxygenated microvasculature and venules. Lastly, the faster CBV return to baseline after inhibitory stimulation is a further indication that the CBV decrease for the inhibitory task has an arterial origin.

If the neurovascular coupling were the same during excitatory and inhibitory tasks, it leads one to expect the same hemodynamic control mechanisms and the same interplay between the different vascular compartments. However, the different spatiotemporal hemodynamic response and different interaction of vascular compartments suggest differing neurovascular coupling during excitatory and inhibitory tasks. This might be associated with hemodynamic control mechanisms discussed in the literature [Bandettini, 2012][Goense et al., 2012][Shmuel et al., 2006].

It must be noted that VASO is a methodology only proportional to CBV change. In order to estimate the relative CBV change from the VASO signal change, a value of CBV_{rest} needs to be assumed (usually 5.5%) [Lu et al., 2013]. Although microvascular CBV_{rest} is relatively homogeneously distributed across layers [Kim et al., 2013][Weber et al., 2008], when macro-vasculature is also included, the total CBV_{rest} was found to be largest at the cortical surface, decreasing with cortical depth [Kennerley et al., 2005][Zhao et al., 2006]. Higher CBV_{rest} at the cortical surface is associated with a smaller relative ΔCBV for the same VASO signal change. Figure 4.3D depicts the reduction in the calculated ΔCBV in the surface voxels when the high macro-vasculature CBV_{rest} in surface layers taken into account.

Limitations in separation of 'arterial' and 'venous' CBV change

Given the complexity of the vascular architecture, it is necessary to discuss the implications of the nonlinear arterio-venous separation model. Aside from the assumed T_2^* values, the model does not rely on assumptions regarding the vascular dynamics, interaction of vascular compartments, or spatial distribution of the vasculature within the MR images. Hence, it is expected to work across voxels with various vascular architectures and contributions of vascular compartments.

For every activation state (time point) four images are required (double-echo images without blood nulling and double-echo images with selective blood nulling) to calculate the 'arterial' and 'venous' CBV change. Hence, the method requires a relatively high temporal resolution of the BOLD and VASO signals. Linear interpolation between the consecutive image acquisitions and the short interval of 1.5 s ($TI2$ - $TI1$) used in this study enables the estimation of 'arterial' and 'venous' CBV time courses even during the transition periods between rest and activation.

'Arterial' and 'venous' blood are defined here based on their relaxation times and thus on their oxygenation level, and not by their anatomical architecture. Therefore, oxygenation-level defined compartments do not necessarily coincide with anatomically defined compartments. Oxygen saturation is highest in large arteries, decreasing downstream to arterioles and capillaries [Yaseen et al., 2011]. Within the venules and veins, the oxygen saturation is nearly constant, independent of vessel size [Yaseen et al., 2011]. In fact, the largest drop in oxygen saturation appears to occur within the arterioles. Therefore, changes in 'venous' (65%-oxygenated) CBV, estimated in the proposed model, might arise to a small part from these arterioles as well as from capillaries, venules and veins. In arteries and arterioles during stimulation, the majority of the total CBV change occurs almost entirely due to an increase in the amount of fully oxygenated blood [Kennerley et al., 2012a]. The CBV changes in post-arterial compartments, however, are likely to mostly contain 'venous' CBV. Since the model is based on T_2^* of two predefined oxygenation levels of arteries (Y = (98.4 ± 0.7)%) and veins (Y = (64 ± 6)%) [Lu et al., 2008][Wehrli et al., 2014], any oxygenation level in between these values is treated from the model as a superposition of a fraction of fully oxygenated arterial blood and a fraction of 64% oxygenated 'venous' blood. Intravascular changes of T_2^* can alter the sensitivity of the separation method of 'arterial' and 'venous' CBV. During a hypercapnia challenge, the 'venous' oxygenation changes from (64 ± 6)% to (72 ± 6)% with a corresponding T_2^* change of 4 ms (intravascular BOLD effect) [Ivanov et al., 2013]. The variations in T_2^* during stimulation are expected to be of the same order of magnitude (section 3.1). This intravascular BOLD contamination suggests that between activation and rest, the method of separation of 'arterial' and 'venous' changes its sensitivity in each compartment. Since the stimulus-induced T_2^* change of 4 ms is much smaller than the T_2^* difference between 'arterial' and 'venous' CBV (37 ms and 12 ms [Ivanov et al., 2013]), this contamination is believed to be negligible. This contamination is estimated and corrected for, using the variable C_1 (see theory paragraph of this section).

Uncertainties in the literature values of arterial and venous oxygen saturation can affect the arterio-venous separation model. Arterial and venous oxygen saturation variations are (98.4 ± 0.7)% and (64 ± 6)% (mean ± standard deviation across participants) [Lu et al., 2008][Wehrli et al., 2014] with corresponding uncertainties in T_2^* of ± 2 ms [Ivanov et al., 2013]. These variations come from participants dependent oxygen partial pressures [Gray and Steadman, 1964]. The corresponding uncertainty of 'arterial' and 'venous' CBV in individual participants, estimated at about 15%, is smaller than the inherent noise level of the estimation of arterial and venous CBV changes of 34% (see uncertainty of ΔCBV_v of (7.1 ± 2.4)% in the result section of this study). The inter-subject variation of venous baseline oxygen saturation values would thus result in an additional uncertainty of ΔCBV_v estimations of 1.0% that is, $\Delta CBV_v = 7.1 \pm 2.4$ (data noise) ± 1.0 (biological oxygenation variations)%. In this study the analysis was performed by averaging across participants, thus neglecting individual variations in venous oxygenation level.

The sensitivity of the separation method is significantly smaller than the sensitivity of VASO. The estimation of 'arterial' and 'venous' CBV is based on the VASO signal changes as a function of TE (Fig. 4.5A). Considering the small size of it and comparing it to the size of absolute VASO signal change, it suggests that the sensitivity of the separation method is about one twelfth of the sensitivity of VASO contrast and one twentieth of the sensitivity of BOLD contrast. Estimation of 'arterial' and 'venous' CBV changes has not been done on a basis of individual participants but across all participants, which has several implications regarding its limitations. (A) Inter-subject variation is not considered. (B) The interplay between 'arterial' and 'venous' oxygenation and blood volume can only be investigated in predefined ROIs in addition to other imaging contrasts, and not as an independent method. (C) Due to the nonlinearity of the model, it has no distributive property (average(model(x_i)) $\neq$ model(average(x_i))), therefore the result is dependent on the point of averaging in the evaluation chain. Due to the nonlinear signal transformation of the model, the nonlinear transformation of the substantial noise level and the corresponding noise amplification in data of individual participants could render the respective analysis impossible. However, since the changes in T_2^* are small compared to their absolute values (see also method section of this study), the results of this study can be considered to be in the linear regime of the nonlinear model. Hence, prior averaging with subsequent application of the model is appropriate.

Comparison with earlier studies

Arterial and venous blood volume dynamics There are a number of studies investigating the relationship between arterial and venous vasculature measured with various MR and non-MR modalities. In most of these studies, as listed below, there is consensus that the arterial contribution to the CBV change is much larger than the venous CBV contribution. For example, relative venous contributions of 34% were measured with 2D OIS in rat somatosensory cortex [Berwick et al., 2005], 30% with perfluorocarbon

MRS during hypercapnic perturbation [Lee et al., 2001], and 0 - 12% with two-photon microscopy in mouse somatosensory cortex [Hillman et al., 2007][Takano et al., 2006]. Comparing iron-oxide-based MR contrast agent and CBV_a-sensitive MRI methods [Kim and Kim, 2005], the arterial CBV change was shown to account almost alone for the total CBV change [Kim et al., 2007] with increasing venous contribution only for long stimulus durations [Kim and Kim, 2011]. Noninvasive human studies, using oxygen as an MR contrast agent, have shown that venous CBV can apparently even decrease in activated brain regions [Blockley et al., 2011]. This contradicts comparisons of CBV measured with VASO and CBV_v measured with venous refocusing for volume estimation (VERVE) [Stefanovic and Pike, 2005] showing a CBV_v contribution of 25% [Cohalan et al., 2009]. In summary, the relative 'venous' contribution of 29% measured in this study lies within the previously reported range of values given in the literature.

With respect to the temporal dynamics of the CBV response, delayed recovery of 'venous' CBV_v is often proposed to explain the delayed return to baseline after stimulus cessation [Buxton, 2010][Kim and Kim, 2011], in agreement with the Balloon or Windkessel model [Buxton et al., 1998][Mandeville et al., 1999]. The slow return to baseline of 'venous' CBV (Fig. 4.5B) in the present study, while 'arterial' CBV and CBF time courses show faster returns to baseline (Figs. 4.5B and 4.6C) is consistent with venous balloon effects. However, the two human studies investigating CBV_v dynamics failed to report a delayed venous return to baseline [Blockley et al., 2011][Stefanovic and Pike, 2005]. The significantly slower post-stimulus return to baseline of 'venous' CBV shown in this study has been seen only in animal studies so far [Kim and Kim, 2011][Mandeville et al., 1999].

CBV change in ROIs of NBR The occurrence of vascular constriction with negative BOLD response is consistent with the majority of animal studies [Boorman et al., 2010][Harel et al., 2002][Kennerley et al., 2012b]. The fast temporal CBV response shown in Figs. 4.4A and 4.7 in ROIs with NBR is consistent with findings in rats [Boorman et al., 2010][Kennerley et al., 2012b]. By contrast, [Harel et al., 2002] report a significantly slower CBV response in ROIs of NBR than in ROIs of PBR.

Since the vascular response underlying NBR can vary across various brain regions [Bohraus et al., 2013] and stimulation paradigms, it could be misleading to directly compare the neurovascular results of this study with studies investigating other cortical regions, for example, extrastriate [Harel et al., 2002], or somatosensory cortex [Boorman et al., 2010][Liu et al., 2011][Pasley et al., 2007][Stefanovic et al., 2004]. The most comparable stimulation paradigm was used in visual experiments in monkeys [Goense et al., 2012]. Their results suggest a CBV increase in ROIs of NBR. The results of the present study on humans, on the other hand, suggest a CBV decrease in these regions. The differences could be due to: (A) Differences in imaging modalities such as BOLD contamination or inflow effects in VASO could explain the conflicting results; (B) The discrepancy could be a result of differences in the experimental setup.

Comparison of the SS-SI VASO in humans and monkeys allows distinction between these possibilities. A representative map of BOLD- and VASO signal changes in a monkey scan is shown in Fig. 4.8. Throughout all four SS-SI VASO scans in the monkey, negative VASO signal changes were seen in ROIs of NBR, indicating a CBV increase in these regions. This is consistent with results presented in [Goense et al., 2012], but it contradicts the results in humans presented here. Since the same MR sequence is used in both experiments, it is hypothesized that the observed differences result from differences in the experimental setup, such as poorer visual fixation in humans, differences due to the additional task-related feedback in humans (since they are awake), or a smaller extent of negative ROIs (species differences), differences in arterial blood pressure due to anesthesia or due to differences in posture [Payne, 2006][Raz et al., 2005], differences of attention [Moradi et al., 2012], or differences in interstitial space and CSF dynamics during anesthesia [Xie et al., 2013] etc. Since the architecture of the cortical (micro) vasculature of striate cortex is very similar in monkeys and humans [Keller et al., 2011][Weber et al., 2008], different vascularization is not expected to be responsible for the afore-mentioned differences observed in humans and monkeys.

Hypothetical mechanism underlying negative BOLD contrast The spatially extended CBV increase in regions of monkey V1 that show negative BOLD responses [Goense et al., 2012] has been discussed in the context of increased venous afterload and increased venous back pressure [Bandettini, 2012][Goense et al., 2012][Smirnakis et al., 2007]. When the drainage of blood from ROIs of NBR is hampered due to increased venous back pressure arising from surrounding excited regions, the passively controlled vascular compartments can dilate for hydrodynamic reasons, independently of CBF decrease and vasoconstriction in the arterial compartments. This hypothetical mechanism provides explanations for several features of the results presented. (A) Venous back pressure can be understood as a local phenomenon. Since in monkeys the negative BOLD ROIs have the same spatial scale as the cortical thickness (3 - 6 mm, see Fig. 4.8) the venous back pressure could have a stronger effect as compared with humans, where the negative BOLD ROIs are much larger in extent (10 - 30 mm, see Fig. 4.2) and neighboring excited regions are much further away. (B) The venous back pressure can only influence the passive downstream vascular compartments and not the actively controlled arterioles close to the cortical surface. This is consistent with the observation that in ROIs of NBR vasoconstriction is confined to fully oxygenated arteries (Figs. 4.5C and 4.5D) close to cortical surface (Figs. 4.3B and 4.7) and not in the more passively controlled microvasculature in the tissue. Comparative fMRI studies between humans and monkeys, for example, using hemi field visual stimulation or varying the size of the negative ROI, could help to investigate the validity and extent of the above hypothesis. An additional hypothetical mechanism can be associated with the different amplitude of fMRI response in human and monkey experiments. BOLD fMRI responses and neural activity is smaller during anesthesia than in the alert condition [Goense and Logothetis, 2008][Martin et al., 2006]. Dependent on the extent of the stimulus (e.g. stimulation frequency), the interplay of inhibitory and excitatory circuits could vary, resulting in positive and negative fMRI response respectively [Logothetis et al., 2010]. Hence, the different amounts of cortical input in the different conditions considered here may also cause very different hemodynamic responses.

Independently of the mismatching responses in different vasculature compartments, BOLD signal can have an additional weighting mechanism between microvasculature and larger surface vessels during excitation and inhibition. The relationship between TE and $T^*_{2,b}$ has a great influence on layer dependent BOLD signal [Koopmans et al., 2011]. Similarly, the opposite signs of $T^*_{2,b}$ change in excitatory and inhibitory tasks influence the TE - $T^*_{2,b}$ relationship and, therefore, can influence the sensitivity in surface and deeper layers.

4.1.6 Summary and conclusions

Here methods and models are developed to investigate simultaneously the spatiotemporal characteristics of BOLD contrast and vascular responses during excitatory and inhibitory stimulation in humans. The observed responses were considered with regard to their sources in surface vessels versus microvasculature, and vascular compartments of arterially and venously oxygenated blood. By these means, features of the neurovascular coupling accessible so far only in animal models could be investigated in humans. The observed excitatory and inhibitory characteristics of CBV and BOLD contrast, together with their dependence on cortical depth and 'arterial' vs. 'venous' compartments, are in good agreement with the animal literature. Even though the interplay of mean CBV, CBF and BOLD signal changes is similar for neural excitatory and inhibitory stimulation, some aspects of the neurovascular coupling are significantly different for the two cases, such as the temporal response, cortical depth dependence, and the weighting between 'arterial' and 'venous' contributions. Excitatory stimulation is associated with increased CBV responses in all vascular compartments, while inhibitory stimulation evokes decreases in the hemodynamic response predominantly in the larger superficial arterial vessels. These variations in the relationship between 'arterial' and 'venous' CBV and BOLD changes suggest different underlying hemodynamic control mechanisms for positive and negative BOLD responses.

4.2 High resolution VASO[2]

Results in the previous section showed that SS-SI VASO can help in understanding limitations of conventional BOLD fMRI, e.g. during the BOLD post-stimulus undershoot and in the case of inhibitory stimuli - cases where the interpretation of BOLD signal to have its origin in neuronal-driven metabolism changes or vascular plumbing artifacts are problematic. Another severe limitation of BOLD fMRI aside of its interpretability is its local specificity at high resolutions. This section describes a study with the aim to investigate these specificity limitations with the goal to assess whether they can be overcome by the application of SS-SI VASO.

In this section of the thesis, the challenges of high resolution fMRI are reviewed and discussed with respect to technical innovations for improving the sensitivity of SS-SI VASO to enable such high resolutions in the first place. Experimental results from humans, rats, and monkeys are shown and discussed with respect to the local specificity to laminar dependent neural activity.

4.2.1 Introduction into layer-dependent blood volume fMRI

In sub-millimeter spatial resolution, fMRI enables measurement of BOLD responses as a function of cortical depth in human and animal brains. If layer-dependent differences in neural metabolism could be inferred from high resolution fMRI responses, insight might be provided for instance, on the question, how differences in afferent and efferent connectivity affect processing in a given brain region. At these higher spatial resolutions, the fMRI contrast is dominated by thermal noise [Triantafyllou et al., 2005] rather than physiological noise, and therefore, it can fully benefit from the use of the very high available field strengths, such as 7 Tesla. Layer-dependent fMRI at high fields might therefore enable a new level of brain research, with the potential not only to detect which brain area is activated, but also how it is activated. For example, Trampel et al. investigated the increased activity in primary motor cortex (M1) associated with motor imagery as compared with an actual motion task, demonstrating that the layer dependence of the ensuing activation differs strikingly for the two conditions [Trampel et al., 2012]. In another example, layer-dependent fMRI was used to study the input characteristics of sensory cortex, and thus to investigate the restructuring of brain connectivity consequent upon denervation-induced plasticity [Yu et al., 2014]. In the visual system, layer-dependent fMRI can help to address questions regarding the feedforward-feedback pathways during excitatory and inhibitory stimuli [Goense et al., 2012]. The limiting factor of such investigations in the human brain is that the noninvasive high-sensitivity fMRI modalities recording the effects of vascular changes are not only specific to the neural activity within individual cortical layers but also sensitive to changes in blood parameters, such as oxygenation that propagate across the cortex. In particular, because GE BOLD signal also arises from draining veins [Turner, 2002], it may be difficult to interpret the signal unambiguously in terms of spatially specific underlying neural activity. GE BOLD responses are weighted towards the site of relatively large pial veins, which are draining the area of

---

[2] This section is summarized in the paper [Huber et al., 2015a].

activated cortex [Polimeni et al., 2010][De Martino et al., 2013]. There is evidence from animal studies, however, that relative CBV changes peak in deeper cortical layers, closer to the site of metabolic activity changes [Goense et al., 2012][Kennerley et al., 2005][Kim et al., 2013]. While invasive contrast-agent-based CBV weighted fMRI methods have yielded promising results in animal studies, a layer-dependent analysis of CBV change in humans has been precluded so far by the inherently low CNR of VASO and other noninvasive CBV-based fMRI methods.

Purpose of this study

In this study, a VASO-based fMRI approach is proposed that enables simultaneous noninvasive acquisition of CBV and BOLD signal changes at high field (7 T) in human motor cortex with sub-millimeter resolution. The cortical-depth dependence of CBV-based VASO fMRI is compared in detail with BOLD fMRI. The VASO-CBV results are validated in animal models using fMRI measures of CBV changes with established iron-oxide-based contrast agents. To elucidate the local specificity of the different modalities, VASO and iron-oxide-based fMRI data are compared with GE BOLD data, which is affected by unwanted sensitivity to large translaminar blood vessels. The final goals of this study are A) to assess whether CBV-based fMRI in humans is sensitive enough to distinguish small hemodynamic responses in tasks designed for investigation of input and output cortical layers, and B) to investigate whether the proposed high-CNR CBV-based fMRI method can overcome specificity limitations of GE BOLD and thus allow quantitative noninvasive measurements of layer-dependent activity profiles to be used in human fMRI.

4.2.2 Methods of layer-dependent VASO

Challenges for high-resolution fMRI

fMRI in human brain at conventional field strengths at submillimeter spatial resolution suffers from inadequate CNR for the study of cortical layer dependence of brain activity. Advanced imaging technologies are thus required. Early human laminar fMRI results were typically acquired with higher in-plane resolution compared to the slice thickness [Yacoub et al., 2008] and laminar profile analysis has relied on scanning flat, relatively unsulcated GM regions with image slices orthogonal to the cortex [Ress et al., 2007][Koopmans et al., 2010]. The use of cortical surface analysis of fMRI data acquired with isotropic resolution has helped to expand the application of layer-dependent fMRI over larger areas of folded cortex [De Martino et al., 2013][Koopmans et al., 2011][Polimeni et al., 2010][Siero et al., 2011][Siero et al., 2013][Trampel et al., 2012]. The present study considers the ‘hand-knob’ region of human primary motor cortex, which has a relatively simple and predictable folding pattern. For such a structure, it is feasible to adopt the earlier strategy of using a slice thickness greater than the in-plane resolution, with its consequent gain in CNR. This is appropriate for the use of VASO, which is a technique for scanning a limited number of slices and has somewhat lower CNR compared with BOLD. Another critical issue in high-resolution fMRI in humans is the broadening of the point spread function in the phase-encoding direction due to the often-required longer duration of the acquisition window with respect to T_2^* decay, also referred to as T_2^* blurring [Hetzer et al., 2011][Kemper et al., 2014]. This problem can be circumvented by the use of a small imaging matrix, which is made feasible by reducing the size of the field of view or using a high parallel imaging acceleration factor. Since the spatial extent of the ROIs of this study is on the same scale as the extent of the receive fields of individual coil elements, high acceleration tends to result in a relatively high g-factor penalty. Furthermore, because this study deals with relatively small predefined ROIs in M1, large areal coverage is not required. Pilot experiments showed that the highest tSNR was achieved using a selection of individual receiver coil elements in a surface-coil like fashion, without additional acceleration. Therefore, in this study small field of views are captured without parallel imaging acceleration.

Blood volume sensitivity in VASO and iron-oxide-based fMRI

Intravenous injection of paramagnetic intravascular contrast agents, such as iron oxide nanoparticles, affects the extravascular water signal in proportion to the CBV [Mandeville, 2012]. The normalized iron-oxide-based signal can be written along Eq. 2.25 as:

$$\frac{S(d)}{S(d=0)} = e^{-k(d)CBV}, \tag{4.12}$$

where CBV is the relative blood volume per volume of tissue in units of ml/100ml, $k(d)$ is a function of contrast agent dose d, its susceptibility difference from the surroundings, the echo time TE, and field strength [Kim et al., 2013][Tropres et al., 2001]. In order to avoid potential contamination by BOLD changes to the tissue susceptibility, $S(d)$, and $S(d = 0)$ should refer to the same activation state (rest or activity). Functional iron-oxide-based signal change can be written as:

$$\frac{\Delta S}{S_{rest}} \approx \frac{e^{-k(d)CBV_{act}} - e^{-k(d)CBV_{rest}}}{e^{-k(d)CBV_{rest}}} \approx -\frac{\Delta CBV}{CBV_{rest}}, \tag{4.13}$$

with $\Delta CBV = CBV_{act} - CBV_{rest}$ and assuming that $k(d) \ll CBV_{rest}$. In contrast, VASO signal change can be described as [Lu et al., 2013]:

$$\frac{\Delta S}{S_{rest}} \approx -\frac{-\Delta CBV}{1 - CBV_{rest}} \approx -\Delta CBV. \tag{4.14}$$

Comparing Eqs. 4.13 and 4.14 makes it clear that both iron-oxide-based and VASO signal changes are linearly proportional to changes in CBV, with different normalization factors. The normalization must be kept in mind, when considering brain areas with inhomogeneous CBV_{rest} distributions, such as the different cortical layers in layer-dependent fMRI analysis [Goense et al., 2007][Weber et al., 2008]. When the baseline CBV distribution across cortical laminae is known, iron oxide signal changes can be used to estimate absolute CBV changes in units of ml per tissue in addition to the relative CBV change in units of percent [Kim and Kim, 2011].

Measurement parameters

MRI data acquisitions were conducted in six healthy participants (3 females, age = 24-32 years). All procedures were approved by the ethics eommittee of the University of Leipzig. Informed written consent was given by all volunteers. SS-SI-VASO was implemented on a MAGNETOM 7 T scanner (Siemens Healthcare, Erlangen, Germany) equipped with an SC72 gradient coil (Siemens Healthcare). For RF transmission and reception, a single-channel-transmit/24-channel-receive head coil (Nova Medical, Wilmington, MA, USA) was used. The positioning of the functional slices and flip-angle adjustment were based on previously acquired whole-brain MP2RAGE T_1 maps [Marques et al., 2010] and MAFI B1 maps [Boulant et al., 2009]. The image acquisition and evaluation pipeline is summarized in Fig. 4.10. Functional BOLD and VASO data were acquired in five axial slices aligned perpendicular to the participants' M1 area, using a two-dimensional single-shot EPI readout. Sequence parameters were as follows: $TE/TI1/TI2/TR =$ 18/1000/2500/3000 ms, excitation flip angle $\theta = 130°$ (see discussion of this section), partial Fourier factor = 5/8, and a corresponding vendor-provided homodyne online image reconstruction algorithm was used. In order to obtain a blood nulling time at $TI1$ = 1000 ms, which is approximately 200 ms lower than the estimated arterial arrival time in the sensorimotor cortex [Mildner et al., 2014], the inversion efficiency was adjusted to be equal to 85%. This corresponds to a sensitivity decrease of approximately 31%. The blood nulling time is calculated based on the assumed value of blood T_1 = 2100 ms [Zhang et al., 2013], following earlier VASO studies at 7 T (sections 3.1 and 4.1). Nominal in-plane resolution was 0.78 x 0.78 mm^2. Since human M1 cortex has a thickness of approximately 4 mm [Fischl and Dale, 2000], up to 5 voxels are evaluated for the layer-dependency. The imaging matrix was 64 x 64 and the field of view was 50 mm. Effective gradient parameters used during EPI were as follows: strength = 40 mT/m; slew rate = 198 T/m/s. In all participants, k-space acquisition took less than 40 ms with a bandwidth of 1132 Hz/pixel in read direction. Based on simulations assuming a tissue T_2^* of 28 ms [Koopmans et al., 2008][Pfeuffer et al., 2004], the corresponding T_2^*-blurring and PSF broadening results in a signal leakage of 14% from one voxel into the neighboring voxels along the phase-encoding direction. This blurring is not corrected for and results in slightly coarser resolution than the nominal voxel size. Depending on the participants' M1 curvature, the nominal slice thickness was 1.2 - 2 mm. In order to minimize aliasing artifacts, phase oversampling between 0 and 15% was used depending on the individual anatomy. In order to determine the border between GM and CSF independently of distortions, T_1 maps were calculated from additional inversion-recovery EPI acquisitions with multiple inversion times (TIs) of 36/200/300/1200/1500 ms, and with acquisition parameters otherwise identical to the functional scans.

A 12-min unilateral finger-tapping stimulation paradigm (alternating 30-s rest vs. 30-s tapping) was used to induce BOLD and VASO signal changes in the central sulcus. The tapping consisted of pinch-like motion and touch with a self-paced frequency of approximately 0.25 - 0.75 Hz. Two 12-min stimulation experiments were done in each participant, one with tapping of right-hand fingers and one with tapping of left-hand fingers.

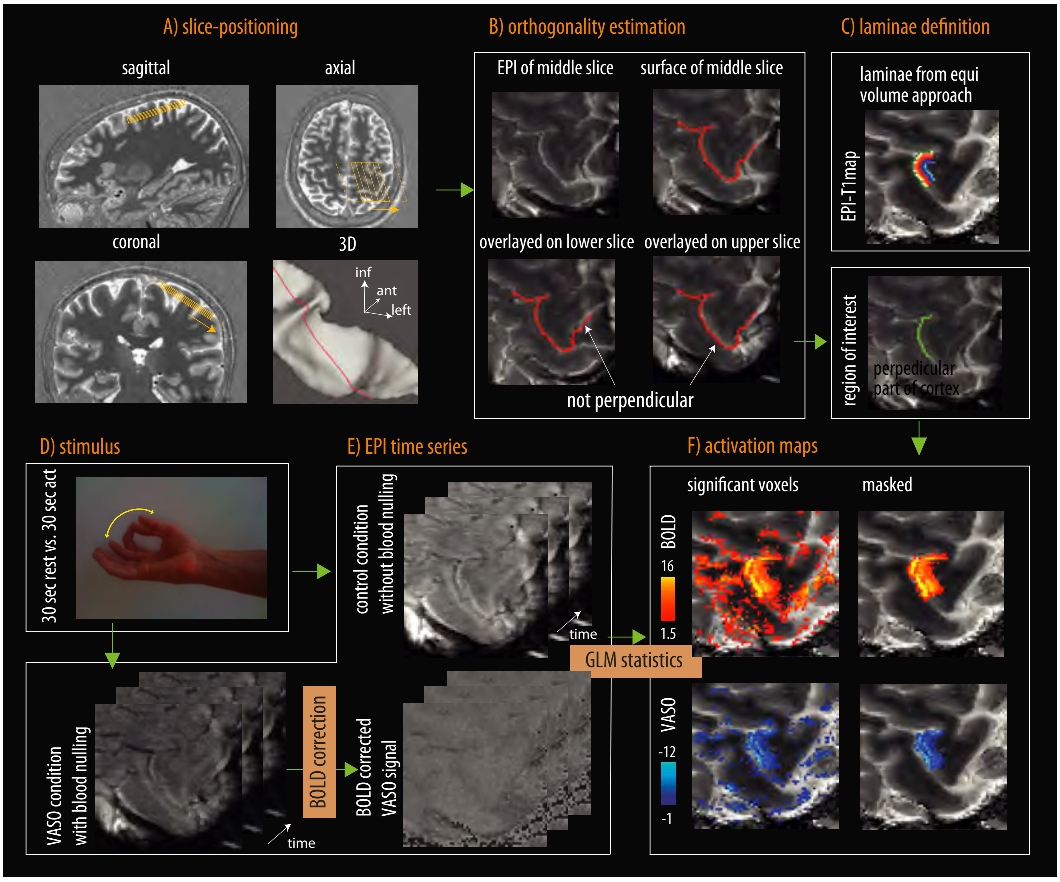

Figure 4.10: Acquisition and evaluation procedure to obtain layer-dependent VASO and BOLD signal changes: EPI slice orientation is planned on previously acquired anatomical T_1-maps to position the imaging slices perpendicular to the cortical surface of the motor cortex (A). Orthogonality is verified by projecting the cortical surfaces onto adjacent slices (B). Cortical laminae are calculated from IR-EPI T_1-maps in the regions where the slices are perpendicular to the cortex (C). Interleaved acquisition of VASO and BOLD time series during a finger-tapping task (D,E) are motion corrected and evaluated to obtain statistical activation maps of BOLD signal change and BOLD-corrected VASO signal change (F).

Data analysis

Signals from all receive channels were reconstructed separately, and the resulting tSNR characteristics were evaluated. Channels with unstable signal or severe aliasing artifacts (between 0 and 8) were excluded from the subsequent sum-of-squares combination (see Fig. 4.11). The perpendicularity of the acquired slices with respect to the cortical surface was quantified by comparing the CSF position in the central sulcus across adjacent slices. The GM and CSF border of the middle slice was projected onto the adjacent slices. All regions, where the displacement of the surfaces defined by the projected border between adjacent slices was more than half of the voxel size were excluded from further analysis. This orthogonality threshold corresponds to a slice tilting of approximately 15° from its optimal perpendicular orientation. Due to incomplete blood nulling in outer slices, all signal-change analyses were done on the middle slice only.

Because M1 has more than double the thickness of the primary somatosensory cortex (S1), the slice orientation was optimized with respect to M1, and all data analyses were focused on the anterior GM bank of the central sulcus. Signal changes in S1 and the posterior side of the central sulcus were not included in the ROIs for quantitative analysis, if not stated differently. Cortical laminae were calculated based on the equi-volume approach [Waehnert et al., 2014], applied directly on EPI images, without the need for distortion correction or registration to a high-resolution anatomical data set. Here, the terms ‘cortical laminae’ and ‘layer-dependent’ refer to sets of voxels defined by the equi-volume contouring method, and therefore do not directly refer to the cytoarchitectonically defined cortical layers. However, it should be mentioned that the method used provides highly realistic cortical contours (see [Waehnert et al., 2014]). In order to obtain robust signal changes within these cortical laminae, signals were averaged over the last 15 s of the tapping period, disregarding the transition period of the first 15 s. All MR images were motion corrected using SPM8 (Wellcome Department, University College London, UK). Statistical analysis was done using FSL FEAT (Version 5.98) [Worsley, 2001] without spatial smoothing. In order to minimize bias from the layer-dependent noise distribution, the z-score threshold in all depicted activation maps was kept well below the mean detection threshold for activity in M1. Doing so, relatively noisy voxels in upper cortical layers are not excluded from the analysis. Cortical profiles were calculated from the raw (unthresholded) data.

Parameters of the animal experiments

The VASO-CBV results acquired in humans were validated by comparing them with well-established iron-oxide-based fMRI methods in animals at even higher spatial resolutions. Thus, the same SS-SI-VASO sequence as used in the human experiments was implemented in laboratories using iron-oxide-based fMRI in monkey or rat models. In order to obtain results that are comparable and in compliance with earlier studies in these laboratories, SS-SI-VASO experiments were conducted with the best-established stimulus protocols on each site, that is, whisker stimulation in rats [Kennerley et al., 2005] and visual stimulation in monkeys [Goense et al., 2010].

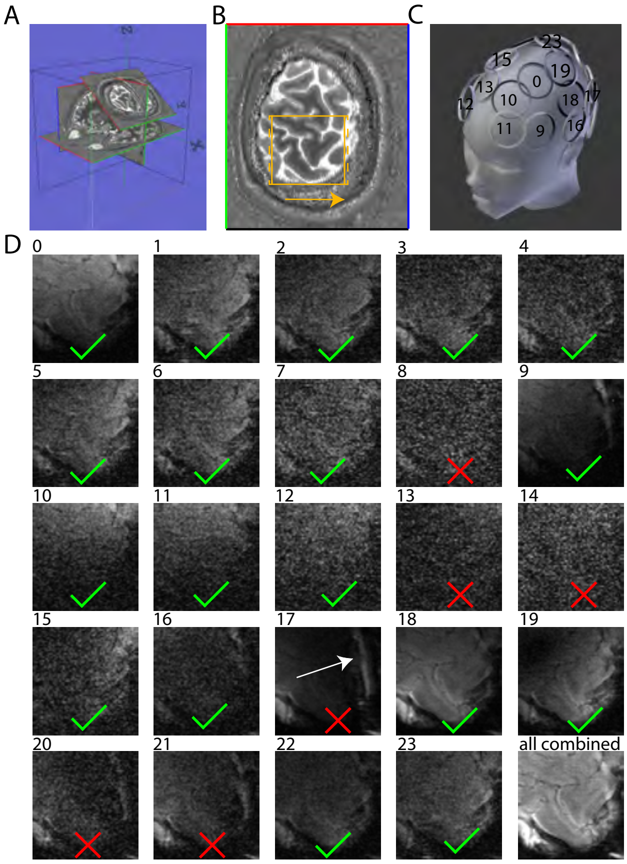

Figure 4.11: In A), the slice of functional EPI acquisition is represented as the tilted slice: In B) the anatomical scan of this slice is depicted. The field of view of the EPI acquisition is outlined with the yellow square. The yellow arrow denotes the phase encoding direction. The dashed region refers to 10% phase oversampling. C) depicts the approximate placement of the 24 coil elements. D) depicts the signal arising from each of the coil elements. The coil elements with index numbers 0, 18, and 19 are placed very close to the left sensory motor cortex. Coil elements with the index number of 4, 8, 13, and 14 are placed over the right occipital and temporal lobe and do not contribute much to the SNR. The aliasing artifacts can become stronger than the signal in the ROI of the hand nob (e.g. white arrow). Dependent on the position of the aliasing artifacts, they can become intolerable and the signal from the corresponding coils should be excluded from further analysis. Green check marks and red crosses refer to coil elements that were included and excluded from the analysis in this representative subject.

Experiments in monkeys

SS-SI-VASO, as described above, was implemented on a 7 T vertical primate scanner (Bruker Biospec 70/60v, Bruker Biospin, Ettlingen, Germany) employing the stimulation setup described in earlier papers [Goense et al., 2012]. For further details of experimental hardware (e.g. magnet and RF coils) and animal preparation (e.g. anesthesia) the reader is referred to previously publishes studies [Goense et al., 2010][Logothetis et al., 2001][Pfeuffer et al., 2004]. Functional experiments with BOLD signal and iron oxide contrast agent were acquired with a nominal resolution of 0.375 x 0.5 x 2 mm^3, 8 GE EPI acquisition segments, 15 slices, volume $TR = 6$ s, $TE = 20/9.6$ ms. Ferumoxytol (Feraheme, AMAG Pharmaceuticals, Waltham, MA, USA) was injected at a dose of 8 mg/kg. The SS-SI-VASO parameters were $TE/TI1/TI2/TR = 7.8/785/2285/3000$ ms and 0.633 x 0.75 x 3 mm^3 nominal voxel size. VASO images were non-linearly registered to the iron oxide and BOLD data using the software package MIPAV [Bazin et al., 2013]. fMRI response in V1 was evoked by means of a rotating ring checkerboard presentation (alternating 30-s rest vs. 30-s stimulation) [Goense et al., 2012]. Experiments were approved by the local authorities (Regierungspräsidium Baden-Württemberg, Germany) and were in full compliance with the guidelines of the European Community (EUVD 86/609/EEC) for the care and use of laboratory animals.

Experiments in rats

SS-SI-VASO, as described above, was also implemented on a 7 T rodent scanner (Bruker BioSpec, 70/30, Bruker Biospin) as reported in [Kennerley et al., 2013] employing the experimental setup described in [Kennerley et al., 2012b]. In order to account for the faster blood flow in rats as compared with primates [Calamante et al., 1999], a global adiabatic 90° spin-reset pulse was played out before every TR, to control the steady-state of the entire magnetization within the transmit coil [Lu, 2008]. The amplitude and phase shape functions of this pulse were adapted from the TR-FOCI pulse class, designed for use at 7 T [Hurley et al., 2010]. In order to convert this pulse from an inversion pulse to a 90° saturation pulse, a 90° phase skip of the pulse amplitude was introduced halfway through the pulse duration, resulting in an inversion efficiency of 50%. The TR time was set at 3200 ms, and a BOLD image was acquired 1100 ms after global saturation. The inversion pulse was applied 400 ms thereafter, and the VASO image was acquired at the blood nulling time 1030 ms after the inversion. TE was equal to 13.1 ms, while the nominal voxel size was 0.46 x 0.46 x 3 mm^3, similarly to the experimental methods described in section 3.2. The functional response in S1 was induced by electrically stimulating the left whisker pad (alternating 86-s rest vs. 16-s stimulation) [Kennerley et al., 2005]. Experiments with iron oxide contrast agent (MION with dose of 9 mg/kg) were conducted with the same EPI acquisition parameters. All aspects of these methods and their development were performed with UK Home Office approval under the Animals (Scientific Procedures) Act 1986.

4.2.3 Results of the layer-dependent VASO study

Statistical maps of the BOLD and VASO signal changes for all human subjects are shown in Fig. 4.12. The corresponding cortical profiles are shown in Fig. 4.13. A robust negative VASO signal change (indicating CBV increase) was detected across participants and across the ROIs. VASO z-scores are approximately 70% of those of the BOLD signal. This shows that a physiologically meaningful quantity, such as ΔCBV, can be measured noninvasively with VASO in humans at a laminar level with sensitivity comparable to that of GE BOLD. Average relative signal changes across all cortical laminae and participants in M1 are (4.3 ± 0.7)% for BOLD contrast and (2.3 ± 0.5) ml/100ml for VASO, respectively.

Intracortical signal distribution

Figures 4.12 and 4.13 show highest BOLD activity at or outside the cortical surface, decreasing with cortical depth as expected [De Martino et al., 2013][Goense et al., 2012][Kim et al., 2013][Polimeni et al., 2010]. VASO signal change, on the other hand, has its peak 1 - 2 voxels (0.8 - 1.6 mm) deeper within GM. This position corresponds to the upper or middle cortical lamina. This difference between VASO and BOLD signal was obtained robustly across all participants (Fig. 4.12). Within GM, VASO signal change tends to decrease in deeper layers similar to BOLD.

Time courses

The normalized time courses shown in Fig. 4.14 suggest relatively small lamina-dependent differences in response dynamics compared to the absolute signal-change magnitude. In the BOLD signal time courses at the cortical surface, a trend towards a stronger overshoot after task onset is seen, and a stronger undershoot after task offset. The time course during the post-stimulus undershoot is significantly different for surface laminae compared to deeper cortical laminae ($p < 0.05$ after multiple-comparison correction across time steps), but the time course differences do not reach statistical significance during the overshoot period. The feature of stronger overshoot in superficial compared to deeper laminae is more pronounced, however, in VASO time courses. In the period 12 - 21 s after task onset, upper cortical laminae show significantly greater relative signal change compared to the deeper cortical laminae ($p < 0.05$ after multiple-comparison correction across time steps).

Functional response in the ipsilateral hemisphere

Imaging the left central sulcus during a left-hand finger-tapping task yielded statistically significant signal changes. M1 shows a positive BOLD signal change and CBV increase, while ipsilateral S1 shows a negative BOLD and CBV decrease in all participants (Fig. 4.15). Average signal changes of ipsilateral BOLD and VASO responses were (1.4 ± 0.5)% and (0.75 ± 0.2) ml/100ml respectively in M1 and (-0.7 ± 0.3)% and (-0.3 ± 0.1) ml/100ml in S1, respectively. The mean negative responses in S1 are smaller not only

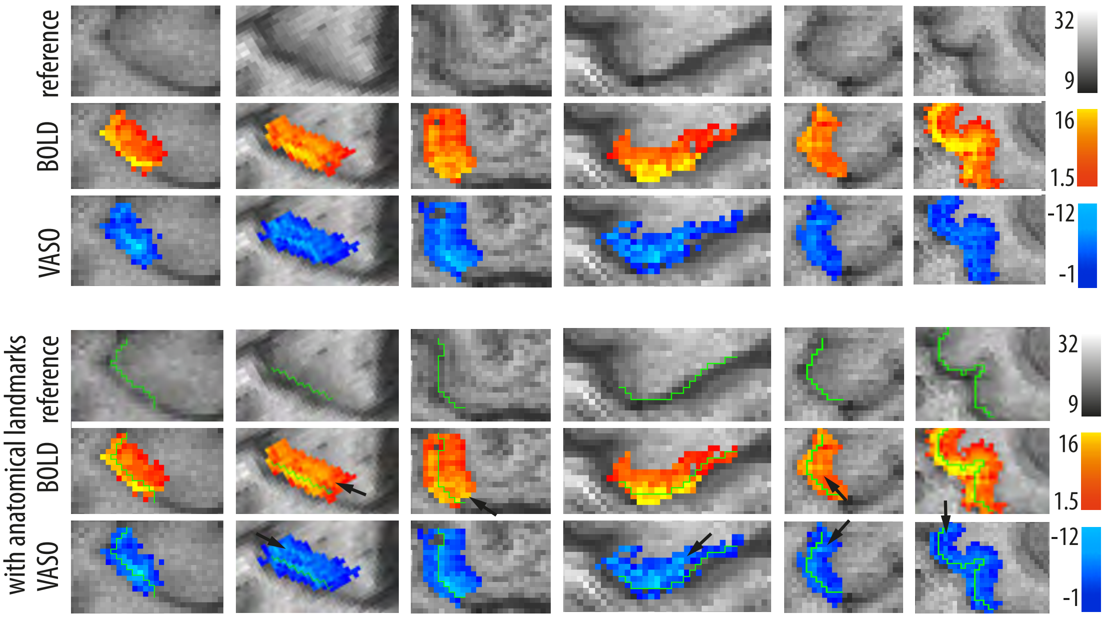

Figure 4.12: z-scores of BOLD and VASO activations on the contralateral side in the GM ROIs of M1: For easy visualization of the cortical surfaces, manually drawn green lines are overlaid onto the maps. These green lines are drawn to stress the different signal origin of VASO and BOLD signal and do not necessarily indicate to the GM-CSF border. Across all participants, highest BOLD signal is seen above the cortical surface (above the green reference line). Inside GM, the BOLD signal decreases with cortical depth. VASO signal activity, on the other hand, peaks inside GM and below the green reference line. Inside GM, VASO signal decreases with cortical depth similar to BOLD. Indications of increased functional activity in deeper cortical laminae are visible in some cases (black arrows). The reference image used as a background corresponds to the tSNR map of the EPI fMRI time series. Nominal in-plane resolution is 0.78 x 0.78 mm^2 and slice thickness is 1.2 - 2 mm.

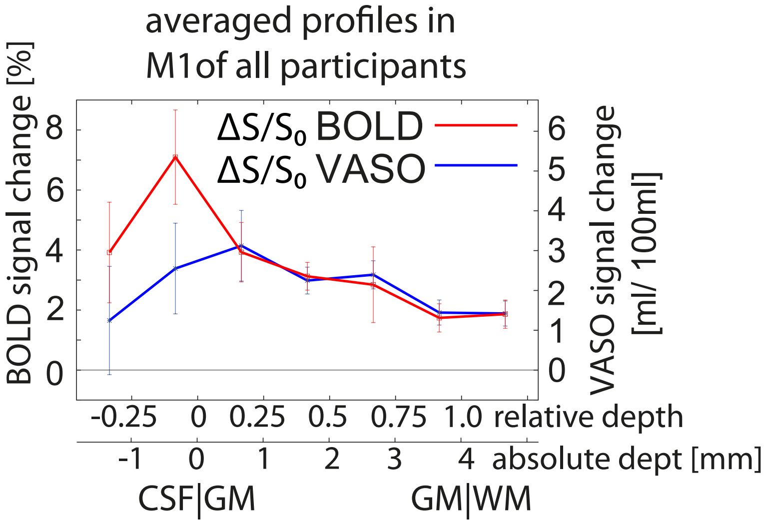

Figure 4.13: Averaged cortical profiles of BOLD and VASO in human M1: BOLD signal change peaks at or above the cortical surface, while VASO peaks slightly deeper and inside GM. The point of zero cortical depth is defined as the border between GM and CSF. With the resolutions used in this study, this borderline is usually not distinguishable from the voxels with maximal CSF partial voluming. The x-axis refers to cortical depth in volume units normalized to cortical thickness and in units of mm, respectively. Since the GM-WM border is not very pronounced in M1, cortical thickness is taken from the literature assumed to be 4 mm [Fischl and Dale, 2000] in all participants.

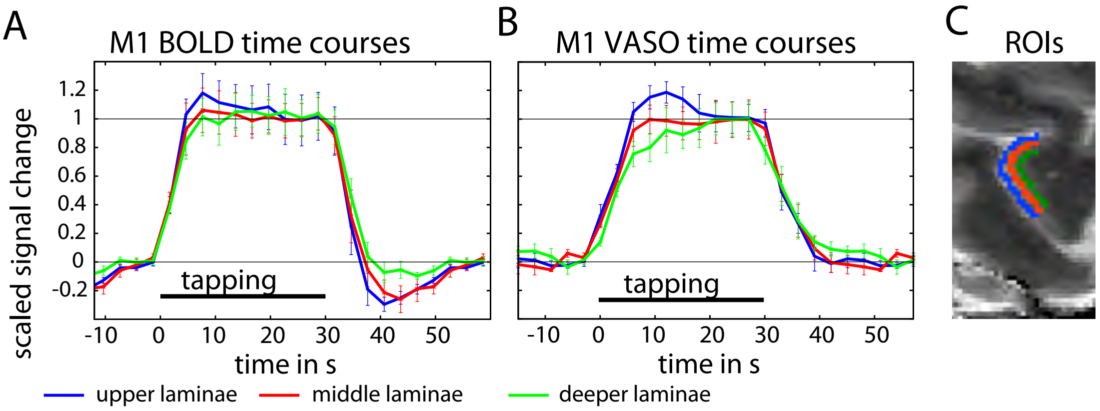

Figure 4.14: Time courses for BOLD and VASO signal at different cortical depths are depicted in panels A) and B). Compared to the amplitude of the total signal change, the differences in time courses for different cortical depths are relatively small. There is a tendency of stronger BOLD signal overshoot and undershoot at the cortical surface. An overshoot approximately 10 s after stimulus onset is also clearly visible in VASO, while the post-stimulus signal does not show a clear laminar signature. Cortical-depth-dependent differences in signal time courses could potentially reflect: local differences in neural activity, different neuro-vascular coupling, or different macrovascular contributions for different cortical laminae. For the sake of clarity, only three time courses are depicted corresponding to: cortical surface, middle cortical laminae, and deep cortical laminae. The respective ROIs are depicted in panel C) for a representative subject

in amplitude compared with M1, but also in spatial extent. This means that the signal response averaged over a combined ROI across S1 would show a positive overall response ((0.19 ± 0.11) ml/100 ml for VASO and (0.15 ± 0.16)% for BOLD), as seen in earlier studies using coarser resolution or after spatial smoothing, where activated voxels contain signal from both sides of the sulcus [Dettmers et al., 1995][Shibuya et al., 2014]. Low noise in the profiles and time courses and minimal point-to-point scatter is shown in Fig. 4.15B (cortical profiles) and Fig. 4.15C (time courses). This indicates that the relatively small ipsilateral responses are highly robust, and implies that the averaged data are not noise-dominated.

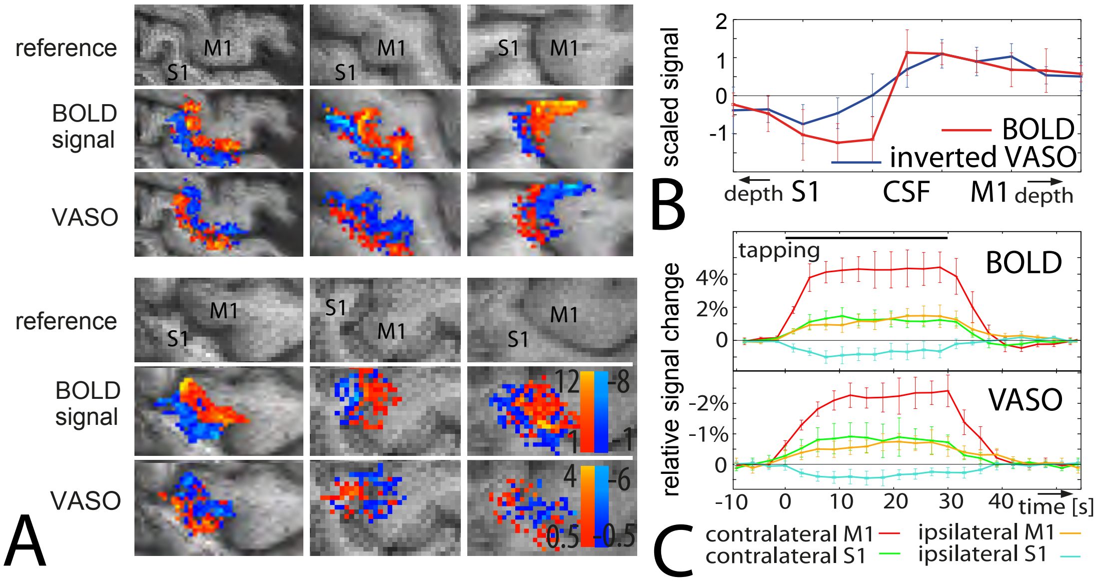

Figure 4.15: Statistical activation maps of BOLD and VASO are showing the ipsilateral responses, i.e., left M1 and S1 for tapping with the left hand are depicted in A). M1 showed positive BOLD signal and CBV increase, while S1 showed negative BOLD and CBV decrease in all participants. Z-scores are overlaid on tSNR maps of the fMRI EPI-time series. B) depicts cortical profiles of BOLD and VASO signal change in S1. On both sides of the central sulcus, VASO signal change peaks in deeper cortical laminae compared to BOLD. Despite presumable partial voluming of positive and negative responses in the CSF region of the central sulcus, BOLD signal change shows a sharp signal jump. C) depicts mean time courses of BOLD and VASO signal in ROIs of M1 and S1 during right hand finger tapping and left hand finger tapping. In order to avoid partial voluming between M1 and S1, the signal from the upper laminae is excluded.

Validation with animal results

The cortical profiles of BOLD and VASO signal change in rat S1 and monkey M1 are highly consistent across the species (Fig. 4.16) and are also very similar to humans (Fig. 4.13). In all species, BOLD signal is highest at the cortical surface and has a variably pronounced 'shoulder' in the middle cortical laminae (Fig. 4.13 and Fig. 4.16). The VASO signal change peaks below the cortical surface across species and brain regions with comparable signal changes in the upper and middle laminae. The corresponding values of ΔCBV [ml/100ml] recorded with VASO in upper / middle laminae are 2.6 ± 0.4 / 2.2 ± 0.4 in human M1; 2.3 ± 0.3 / 2.0 ± 0.2 in monkey V1; and 1.2 ± 0.2 / 1.1 ± 0.2 in rat S1. Cortical profiles of iron-oxide-based fMRI are comparable with VASO signal profiles, but with small differences at the cortical surface, where VASO shows a trend towards higher relative signal changes compared to those obtained with iron oxide. VASO and iron-oxide-based fMRI have conceptually different contrast mechanisms, resulting in different normalization of their CBV weightings (Eqs. 2 and 3). Hence, the baseline distribution of CBV_{rest} needs to be taken into account when comparing and interpreting differences between the two contrasts. Using Eq. 1, CBV_{rest} can be estimated (Fig. 4.17A-C) and used to convert the cortical profiles of normalized relative CBV change in units of CBV_{rest} (Fig. 4.17D) to cortical profiles of absolute blood volume change in units of ml/100ml. The resulting profiles (Fig. 4.17E) are strikingly similar for both VASO and iron-oxide-based fMRI, suggesting that the underlying contrast mechanisms have similar sensitivity to CBV. Furthermore, the profiles can be seen to be remarkably similar across species and brain regions (Fig. 4.17E). Cortical profiles of iron oxide CBV change in units of %, which are shown in Fig. 4.17E, are highly consistent with the results from previous studies in the respective animals [Goense et al., 2012][Kennerley et al., 2005].

4.2.4 Discussion of the layer-dependent results

It has been claimed that noninvasive CBV-based fMRI could be used to map local changes of neural activity in human brain with better specificity than GE BOLD [Kennerley et al., 2005][Zhao et al., 2006]. Previous low-resolution applications of VASO have suggested that the signal is more confined to GM than the GE BOLD signal, which is known to peak in voxels at the cortical surface (sections 3.1 and 4.1). In the current study, these insights are taken one step further with sub-millimeter resolution fMRI, allowing more specific layer-dependent analysis. The results presented here confirm that the VASO signal change is less dominated by the surface vasculature compared to GE BOLD signal, and represents functional tissue responses with less contamination by the macrovasculature. The SNR limitations of sub-millimeter non-BOLD fMRI in humans, which have, so far, hampered high-resolution comparisons of CBV and BOLD signal in humans, can be overcome with the intrinsically high CNR of SS-SI-VASO. The good inter-subject and across-species reproducibility of the results suggest that the method is highly robust. The slower VASO signal change in deeper cortical laminae and the stronger overshoot in superficial laminae are consistent with previous laminar-dependent results

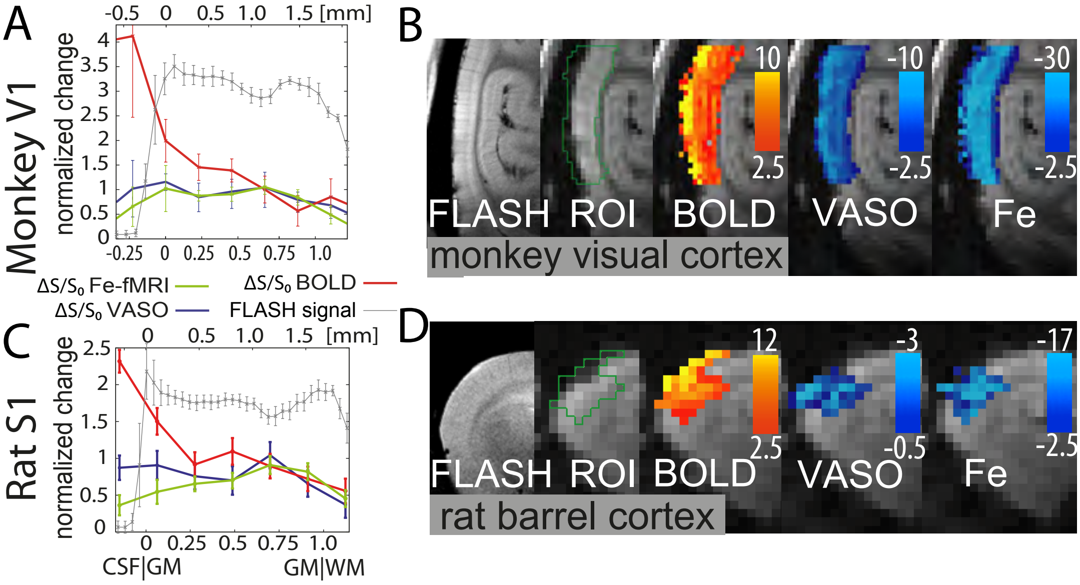

Figure 4.16: Cortical profiles of relative signal changes of BOLD, VASO, iron-oxide-based fMRI signal in monkey V1 and rat S1 are depicted in panels A) and C). BOLD and VASO signal distribution across the cortex is remarkably similar to human results (Fig. 4.13); BOLD signal peaks at the cortical surface with a more or less pronounced 'shoulder' in middle cortical laminae, while VASO shows a double peak distribution across species. Cortical profiles of VASO and iron-oxide-based functional responses are the same within the error of the measurements. However, a trend of higher VASO signal change close to the cortical surface can be noticed. For best comparison of the different contrasts, cortical profiles are scaled to the signal change in deeper cortical layers. The values of the unscaled signals are given in the main text. B) depicts monkey V1 (sagittal slice) and D) depicts rat S1 (coronal slice). The statistical z-score activation maps of BOLD, VASO, and iron-oxide-based signal correspond to cortical profiles depicted in panels A) and C). They are overlaid on the raw EPI images. The x-axis refers to cortical depth in volume units normalized to the cortical thickness. Cortical profiles of the ultra-high resolution FLASH signal can be used to reveal the approximate position of the cortical surface (peak) and layer IV (dip).

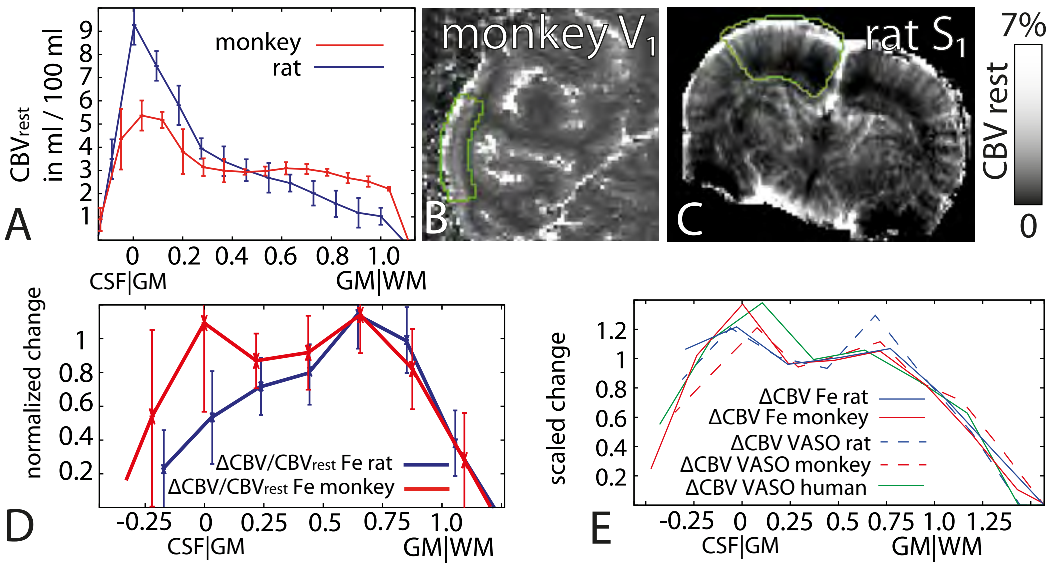

Figure 4.17: Comparison of VASO and iron-oxide-based fMRI: Due to the inherently different normalization of VASO and iron-oxide-based fMRI (Eqs. 2 and 3), layer-dependent baseline CBV_{rest} distribution must be considered. A-C) In monkey V1 and rat S1, CBV_{rest} is highest at the cortical surface. In rat S1, CBV_{rest} decreases continuously with cortical depth, while in monkey V1, CBV_{rest} is more homogeneous in deeper laminae, and layer IV is visible. D) depicts the cortical profiles of normalized iron-oxide-based signal change (ΔCBV / CBV_{rest}) of monkey V1 and rat S1 as in Figs. 4.16A and 4.16C. E) depicts the cortical profiles of CBV change in units of volume change (not in units of baseline CBV) in rat S1, monkey V1 and human M1 acquired with multiple contrasts. Iron-oxide-based results without normalization are obtained by the multiplication of profiles in panels A) and D). VASO results do not have the inherent CBV_{rest}-normalization of the iron-oxide-based fMRI so the depicted profiles directly correspond to relative signal change as given in Figs. 4.13, 4.16A, and 4.16C. The profiles are strikingly similar across imaging modalities and even species and brain regions and residual differences are not significant with respect to the inter-subject variation. For best comparison of the different species and contrasts, cortical profiles are scaled to the signal change in deeper cortical layers. The values of the unscaled CBV changes are given in the main text.

from studies with iron oxide contrast agents in cat V1 [Jin and Kim, 2008a][Yacoub et al., 2006]. The weaker relative post-activation undershoot in deeper cortical laminae is not consistent with earlier studies in cat V1 [Jin and Kim, 2008a] and human V1 [Siero et al., 2013], which may be due to different interactions of actively and passively controlled vasculature for different stimulus durations used in those studies.

Functional response in the ipsilateral hemisphere

Figure 4.15 shows that finger tapping surprisingly evokes a positive response in ipsilateral M1, but a negative response in ipsilateral S1. The task response in ipsilateral M1 has been found to be highly dependent on stimulus paradigm and strength. While low-force (usually 5% of individual maximal voluntary contraction) has been shown to evoke a negative BOLD response, and reductions in blood flow and metabolism in ipsilateral sensorimotor ROIs [Dettmers et al., 1995][Hamzei et al., 2002][Stefanovic et al., 2004], responses have been observed to become positive when stronger forces and more demanding tasks are used [Dettmers et al., 1995][Shibuya et al., 2014]. Even though the corticospinal tract is predominantly a crossed pathway, which suggests contralateral M1 responses only, bilateral motor representations have been reported in several studies [Cramer et al., 1999][Dettmers et al., 1995][Donchin et al., 2002]. Hence, the positive ipsilateral response during unilateral motion seen in the present study could be interpreted as part of the bilateral motor representation. This requires further investigation. Figure 4.15 showed that a unilateral sensory stimulation produces a robust negative ipsilateral response in S1. This is consistent with the literature for humans [Mullinger et al., 2014][Schäfer et al., 2012] and animals [Boorman et al., 2010]. However, none of the above-mentioned studies of ipsilateral sensorimotor activation had a sufficient resolution to distinguish or exclude the separate contributions from S1 and M1. Thus, direct comparisons with the results presented here (Fig. 4.15) could be misleading. It needs to be mentioned that partial volume effects of macrovasculature draining or feeding the opposing sides of the central sulcus can complicate layer-dependent interpretation of the results in Fig. 4.15. For example, pial veins within the sulcus can drain both M1 and S1, and hence their BOLD signal might reflect a mixture of activity in both areas. These types of specificity limitations of BOLD signal changes, arising from large veins in the sulcus, can make it difficult to interpret separately the corresponding BOLD signal from opposite sides of the sulcus. The robust detection of relatively small layer-dependent ipsilateral responses with VASO during a 12-min experiment suggests its applicability in future studies, for example, those investigating the afferent-efferent characteristics of the cortex.

Uncertainties in arterial and venous blood T_1

It has been shown recently that the arterial blood T_1 is approximately 100 - 200 ms longer than venous blood T_1 [Grgac et al., 2012][Rane and Gore, 2013]. When only one value is assumed for both blood compartments, as in this study, the chosen TI can differ from the true blood nulling time by 35 - 70 ms. The corresponding incomplete blood nulling can result in an error in the VASO signal change of about 8% relative to the total VASO signal change. This means that potentially different arterial and venous blood compositions in different cortical laminae can be accompanied with small biases in the VASO signal change. In a worst case, the measured CBV change of 2.3 ± 0.5 ml/100ml in human M1 might have an additional source of uncertainty, to become 2.3 ± 0.5 (inter-subject standard deviation) ± 0.17 (uncertainty in arterial and venous blood T_1) ml/100ml. Since the uncertainty in arterial and venous blood T_1 is considerably smaller than inter-subject variation, the ensuing error is considered to be tolerable here, and has no qualitative impact in the interpretation of the cortical profiles shown.

Potential artifacts of dynamic CSF volume change

Functional changes in the partial voluming of CSF and GM could affect VASO signal and make direct interpretation of ΔCBV in VASO experiments more difficult [Donahue et al., 2006][Jin and Kim, 2010][Piechnik et al., 2009]. CSF contamination in VASO could mimic VASO signal change at the cortical surface and distort the corresponding cortical profiles [Jin and Kim, 2010]. Here, the steady-state of CSF and GM magnetizations was manipulated independently of TR by increasing the nominal excitation pulse flip angle. Based on simulations of GM steady-state z-magnetization and CSF steady-state z-magnetization, a nominal flip angle of $\theta = 130°$ was chosen. These simulations are based on assumed T_1 values of 1.9 s and 4.0 s for GM and CSF, respectively. The application of a flip angle of $\theta = 130°$ results in an SNR penalty of 9% compared to the application of the Ernst angle. This flip angle results in a BOLD-corrected VASO image with almost no signal contrast between GM and CSF (see Fig. 4.10E), which is thus insensitive to any functional volume redistribution of GM and CSF. In contrast with the CSF-nulled ACDC VASO [Scouten and Constable, 2008] or VASO FLAIR [Donahue et al., 2006] techniques, the VASO signal changes in this study reflect both components of the CBV change - the CBV increase that is compensated by a GM volume decrease as well as the CBV increase that is compensated by CSF volume decrease - with the same weighting. Additional discussions of potential CSF-volume change and its effect in high resolution VASO results are carried out in section 5.4.

Comparison of VASO and iron-oxide-based fMRI in animals

VASO was applied in animals in order to validate its CBV weighting Jin and Kim compared the layer dependence of the VASO signal with that using an iron oxide contrast agent [Jin and Kim, 2006][Jin and Kim, 2008b]. In order to minimize inflow of ‘fresh’ blood during the inversion time, VASO images had to be acquired 500 ms before the blood nulling time, introducing a flow weighting as with ASL-FAIR experiments lacking a control condition. In these studies, differences of relative signal change obtained with VASO and iron oxides in upper cortical layers were interpreted to arise from inflow effects and limited BOLD contamination [Jin and Kim, 2006]. Further quantitative studies were needed to reveal the underlying CBV sensitivity of VASO in comparison to iron-oxide-based fMRI independent of such flow contaminations [Jin and Kim, 2008b]. Across

GM regions and species, the general vascular layout of large vessels is broadly similar. For example, larger arterioles or larger venules feed or drain the cortical laminae from the surface [Duvernoy et al., 1981]. The microvessels are distributed inside GM across the cortical layers. There are subtle and specific differences across cortical layers in different brain areas [Duvernoy et al., 1981]. For all three stimulation tasks used here, the major part of the neutrally driven energy consumption increase is not expected to occur at the cortical surface at the site of large pial vasculature, but it is expected to occur within the cortex, distributed across the cortical layers. Much of the energy use is expected in middle cortical layers, corresponding to the thalamocortical input layer IV in V1 and S1, and in M1 increased activity in thalamocortical and corticocortical input layer V [Porter and Lemon, 2012] and in corticocortical input layer II/III [Yu et al., 2014]. Because BOLD and VASO MRI data characterize lamina-dependent vascular changes, the exact correspondence between neural activity changes and vascular changes in individual cytoarchitecturally-defined cortical layers is still unknown. The resulting cortical profiles of BOLD and VASO signal changes are rather expected to reflect the neurally driven microvascular response in a particular cortical lamina combined with the signal response of diving arteries and veins passing through that layer. Depending on the MRI resolution, a given cortical lamina in the MRI data can contain multiple anatomically defined cortical layers of different cytoarchitecture.

Vascular origin of BOLD, VASO and iron-oxide-based fMRI

The different cortical profile shapes of BOLD, VASO, and iron-oxide-based signal depend partly on the influence of macrovascular contributions in the different modalities, so they must be discussed with respect to expected underlying vascular features. A qualitative schematic illustration of the expected vascular contributions in the respective methodologies is shown in Fig. 4.18. It is shown, how a certain layer-dependent response might be transformed into the detectable laminar signal change of the corresponding modalities. In order to discuss the different physiological point spread functions of BOLD, VASO and iron-oxide-based fMRI, a double peak response is used here as reported earlier in rat M1 [Yu et al., 2014]. This example is chosen for illustrative reasons because it clearly visualizes different macrovascular contamination in upper and deeper cortical laminae. The GE BOLD signal change at 7 T can be considered to be dominated by translaminar diving venules and pial veins rather than by intralaminar capillaries [Uludağ et al., 2009]. Hence, the majority of the BOLD signal reflects oxygenation changes in veins draining multiple layers, making it difficult to break down the signal into layer-dependent activity. The contribution of intralaminar capillary BOLD signal with layer-dependent specificity is expected to be relatively low compared to macrovascular BOLD signal (upper row in Fig. 4.18).

VASO fMRI is expected to capture CBV changes in small intralaminar arterioles [Tian et al., 2010], and in capillaries to some extent [Stefanovic et al., 2008], but almost no signal is expected to come from venules [Hillman et al., 2007]. Additionally, VASO fMRI is expected to capture CBV changes in larger translaminar diving arterioles [Tian et al., 2010]. The diameter of these diving arterioles is larger in the upper cortical laminae and

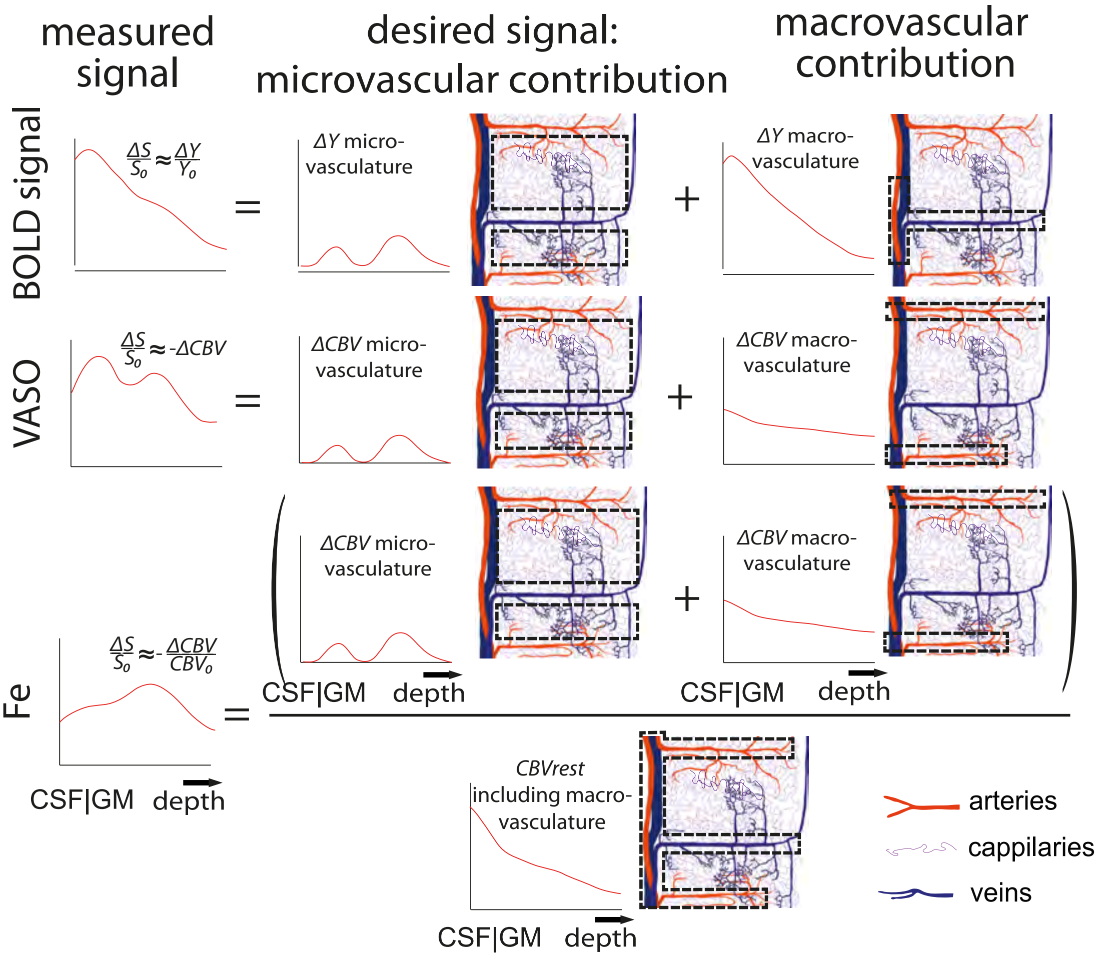

Figure 4.18: Schematic illustration of the investigated fMRI signals and their sensitivities to micro- and macrovasculature: All three contrasts, BOLD signal, VASO and iron-oxide-based fMRI are sensitive to both changes in microvasculature and changes in macrovasculature, but with different weightings. The black dashed regions refer to macrovasculature spreading across cortical layers, and microvasculature confined to individual cortical layers, respectively. The term ΔY refers to the changes in the blood oxygenation. The expected sensitivity is considered in an example of enhanced activity in upper and lower cortical layers. It reflects the corticocortical input response of rat M1 [Yu et al., 2014] for activity in M1 and is considered an illustrative example only. BOLD signal change has a large contamination from large diving veins and pial veins draining the activated layers. In VASO signal changes, the CBV change of feeding arteries supplying the activated layers introduces a weighting of macrovasculature beyond the activated laminae. In iron-oxide-based methods, the inherent normalization to total baseline CBV introduces an inverse weighting of large vessels at and below the cortical surface.

becomes smaller with increasing cortical depth [Duvernoy et al., 1981]. During functional activity, their relative vessel diameter increase is homogeneous across the cortical laminae [Tian et al., 2010]. This suggests that the absolute CBV change of those diving arterioles is smallest in deep cortical laminae and somewhat larger in upper cortical laminae. The ΔCBV contribution from pial arteries, which visibly dilate in optical imaging spectroscopy studies [Kennerley et al., 2012a] are also expected to contribute to the global CBV change. This macrovascular contribution could result in the highest VASO signal change in upper cortical laminae (middle row in Fig. 4.18). In contrast to VASO fMRI, the relative signal change recorded with iron oxide is inherently normalized to the local baseline blood volume. This normalization introduces severe inverse macrovascular weighting at the location of large translaminar arterial and venous vessels. Since the macrovascular baseline CBV can vary up to a factor of five across measured laminae at and below the cortical surface (see Fig. 4.17A or [Goense et al., 2007][Kennerley et al., 2005][Kim et al., 2013]), the intralaminar microvasculature response in upper cortical laminae appears suppressed in the resulting cortical profiles (Fig. 4.17D and bottom row in Fig. 4.18). The large macrovascular contribution at the surface and the fact that Fe-based CBV-changes are usually reported in percent change tends to underestimate the actual CBV change (ΔCBV) at the surface. Thus the widely reported feature that CBV-sensitive iron-oxide-based fMRI shows highest activity in deeper cortical layers [Kim et al., 2013] at the site of thalamocortical input layers does not necessarily suggest high local specificity, but might in fact be due to inverse macrovascular weighting in the upper cortical laminae. Furthermore, in iron-oxide-based fMRI, the high baseline CBV at the cortical surface can result in low MR signal intensity. If SNR at the surface is limited, the corresponding layer-dependent detection threshold can be higher than the signal change at the cortical surface [Goense et al., 2012].

In summary, among the three investigated fMRI contrasts in this study, GE BOLD contrast has the strongest relative macrovascular contamination. VASO and iron-oxide-based fMRI also have macrovascular weighting or contamination from the upper cortical laminae, but to a smaller extent than BOLD fMRI. Hence, those methods may not purely reflect the microvascular features closest to the site of neural activity either. VASO has been shown to have better specificity than GE BOLD; its layer-dependent cortical profiles, however, also can be considered to some extent as representing a microvascular response on top of macrovascular contributions, but with a relatively larger microvascular contribution. Future quantitative models relying on the layer-dependent micro- and macrovasculature distribution might be able to extend the above qualitative considerations to a quantitative level [Gagnon et al., 2013][Markuerkiaga et al., 2014].

Distribution of baseline MR signal across cortical depth and normalizing

The influence of normalization in iron oxide contrast agent CBV measurements is considered in more detail in Fig. 4.19. Quantitative estimations of CBV in ml per 100 ml of tissue are dominated from surface laminae for both conditions, for activity and rest (Fig. 4.19B). The functional difference between activity and rest is then visualized in two independent ways. Figure 4.19C depicts the relative CBV change normalized to the

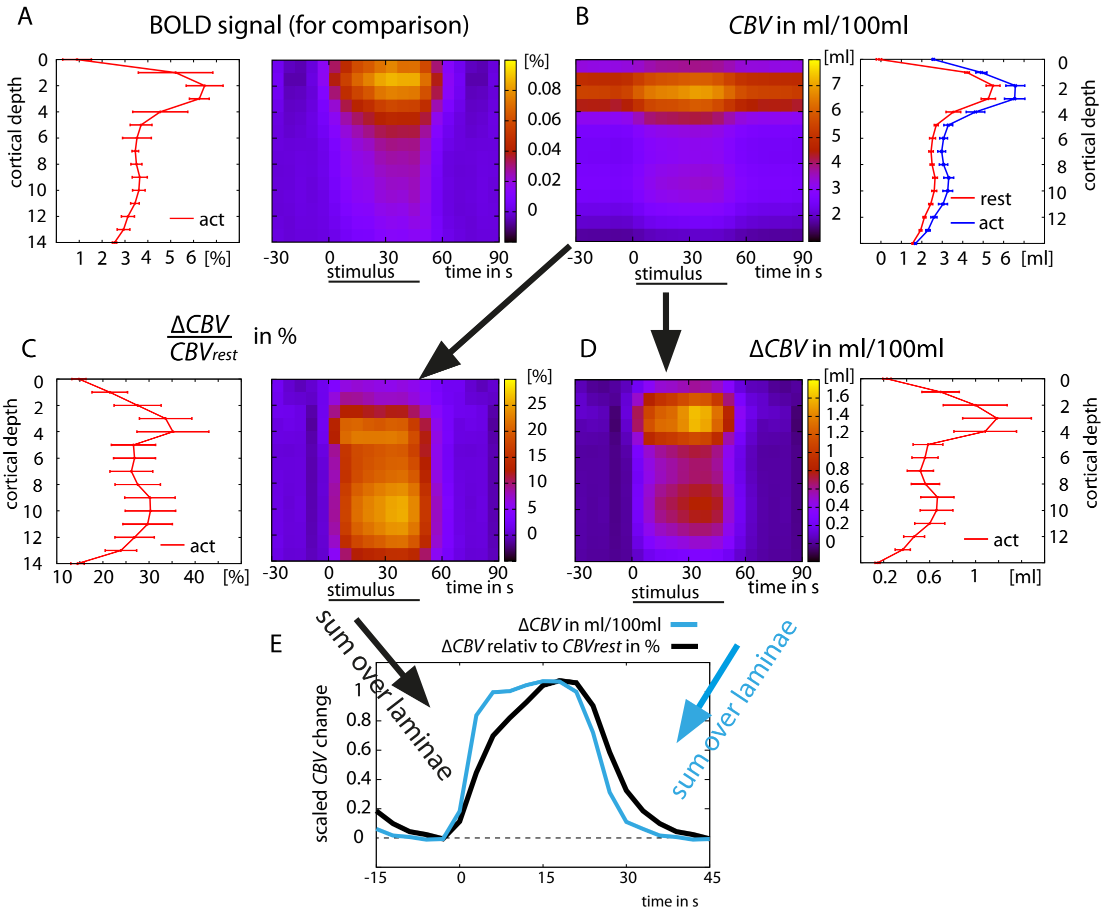

Figure 4.19: Influence of normalization in iron oxide contrast agent fMRI: 3D plots depict signal changes in different cortical laminar (rows) as a function of time (columns). Corresponding profiles of signal change are shown as projections next to them. A) depicts the BOLD signal change for sake of comparison with iron oxide results only. B) depicts the unnormalized results of CBV during rest and activity, respectively. C) depicts the normalized signal change between activation and rest in units of baseline CBV of the respective laminae. It can be seen that most of the relative CBV change is located in deeper cortical layers. D) depicts the absolute CBV change in units of ml per 100 ml of tissue. It refers to the total CBV values during activity, subtracted by the baseline CBV in the respective laminae. Note that the resulting absolute CBV change is dominated from the surface. E) depicts the time courses of CBV change averaged over all laminae for both normalization schemes. The relative CBV change dominated from deeper laminae shows slower response compared to the absolute CBV change dominated from the upper laminae.

baseline CBV in dimensionless units of %. Due to the higher baseline CBV in upper cortical laminae, the relative CBV change is comparatively small there. Figure 4.19D depicts the CBV change in absolute units of ml per 100 ml of tissue. In this subfigure, CBV change is dominated from the surface and shows a secondary peak in the deeper laminae. Comparing results in Fig. 4.19C and Fig. 4.19B makes clear, how the resulting cortical profiles of CBV change are highly dependent on the normalization scheme used. Note that unexceptionally all of the numerous studies using iron oxide contrast agents to investigating layer-dependent fMRI responses use the normalization procedure depicted in Fig. 4.19C (to the best of my knowledge). Since upper and lower laminae have a different hemodynamic response functions, the overall mean response is also dependent on the different ways of normalization (Fig. 4.19E). This can be a potential explanation why VASO-CBV measured in ml per 100 ml of tissue has often been reported to have a faster return to baseline compared to early MION-CBV results in rats.

Layer-dependent detection threshold

The nonuniform distribution of noise across cortical depth can introduce a layer-dependent bias in statistical activation maps. In an extreme case, it can even lead to exclusion of noisy voxels from the ROI and therefore distort the resulting cortical profiles of signal change. Therefore, any statistical- or tSNR-related threshold must be considered as a layer-dependent filter, which could distort cortical profiles. Corresponding effects are considered here by means of a so-called detection threshold. This detection threshold denotes the minimum signal change necessary to exceed the threshold of statistical significance. The cortical profiles of detection thresholds of VASO and iron oxide contrast agent fMRI signals are depicted in Fig. 4.20. It can be seen that the relative detection threshold in iron oxide contrast agent is up to a factor of 5 higher in upper cortical laminae, compared to deeper cortical lamina. In order to avoid such biases in this study, ROIs were manually selected covering all cortical laminae independent of their noise characteristics. All voxels within those ROIs are included in the analysis, even voxels that show negative response.

Other imaging modalities

Spin-echo BOLD fMRI has been suggested to have higher specificity to the microvasculature [Uludağ et al., 2009] and its utility for laminar and columnar fMRI has been demonstrated in animals [Goense et al., 2012][Harel et al., 2006][Zhao et al., 2006] and in humans [Yacoub et al., 2005][Yacoub et al., 2008]. However, it suffers from much lower sensitivity, especially at high resolution [Yacoub et al., 2005], which may limit widespread application of the technique [Boyacioğlu et al., 2014][Budde et al., 2014][Harmer et al., 2012].

4.2.5 Conclusion of this study

It has been shown that the SS-SI-VASO method can be used, at high field (7 T), to noninvasively and simultaneously investigate the cortical profiles of ΔCBV and BOLD

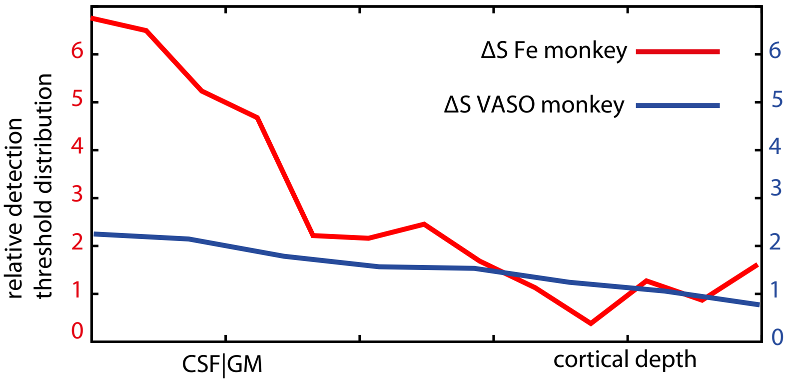

Figure 4.20: Layer-dependent detection threshold of VASO and iron oxide contrast agent fMRI signals: Due to tSNR variations across cortical depth, the same value of $\frac{\Delta S}{S_{rest}}$ might exceed the statistical detection threshold in deeper cortical layers but might not reach significant in upper cortical layers. For the sake of comparison of the two contrasts, the cortical profiles are scaled to the detection threshold in deeper cortical laminae. The detection threshold varies by a factor of 5 for the iron oxide contrast agent fMRI signal and varies by factor of 2 for VASO signal.

signal. This makes it possible to capture layer-dependent CBV responses robustly in humans, information that was previously only accessible in animal research. Considering the different macrovascular contributions and normalization features in VASO and iron-oxide-based fMRI, cortical profiles of both contrasts are in good agreement. The data presented here suggest that VASO can be used to investigate layer-dependent responses with much reduced macrovascular contributions compared to GE BOLD. VASO may thus play an important role in revealing top-down or afferent-efferent stimulus processing in the brain using layer-dependent fMRI, without the unwanted sensitivity to vascular changes in large draining veins that GE BOLD suffers from.

4.3 VASO during hypercapnia: application to calibrated BOLD fMRI[3]

Studies described in previous sections showed how SS-SI VASO can help overcome limitations of conventional BOLD fMRI to interpret signal changes as a result of neuronal and vascular responses. Here this is taken one step further and SS-SI VASO is used to quantity changes in oxygen metabolism independent of vascular responses by means of a biophysical tissue model. For calibration of this model, an additional calibration experiment is required, where the participants are breathing an air mixture with elevated CO_2 contributions.

The first part of this section describes a study dedicated to account for the challenges and possible contaminations applying SS-SI VASO in these calibration experiments. In order to do so and account for the faster blood flow velocities during breathing challenges, a novel adiabatic RF pulse is developed and experimentally tested in phantoms and in vivo.

The second part of this section describes a study using SS-SI VASO to estimate changes in oxygen metabolism for a simple visual stimulation paradigm. Experimental results are shown and discussed with respect to the inherent noise limitations of the nonlinear biophysical tissue models.

4.3.1 Implementation of VASO for application during hypercapnia

Introduction of using VASO during hypercapnia

Hypercapnia can be evoked by a breathing challenge with a gas composition containing elevated levels of CO_2. It is a widely applied tool to evoke hemodynamic changes with minimum change in brain metabolism. Hypercapnia is often used to investigate neurovascular coupling and to unravel the vascular or metabolic origin of fMRI signals. Examples are BOLD calibration for $CMRO_2$ estimation [Davis et al., 1998], investigation of the BOLD signal post-stimulus undershoot [Hua et al., 2011b][Zappe et al., 2008], or breaking down early and late hemodynamic responses in arteries, capillaries, and vein [Kennerley et al., 2012a].

During hypercapnia, arteriolar vessels dilate significantly and CBF can be substantially increased [Calamante et al., 1999]. This CBF increase is usually accompanied with a decrease in arterial arrival time [Ho et al., 2011]. When applying VASO fMRI, the shorter arterial arrival time and faster blood flow can result in the inflow of fresh, uninverted blood into the microvessels during the blood-nulling time TI. These inflow contaminations can have a severe effect on VASO signal change, especially with short TRs [Donahue et al., 2006]. At 1.5 T and 3 T, VASO-CBV imaging has been successfully implemented for applications during hypercapnia in multiple studies [Lu et al., 2003][Scouten and Constable, 2007][Scouten and Constable, 2008][Hsu et al., 2012][Lin et al., 2011][Hua et al., 2011b]. At these field strengths (< 7 T), a body RF coil can be used for the inversion

---

[3] This section is summarized in conference presentations [Huber et al., 2012] and [Huber et al., 2013]. Furthermore it is the basis of later applications in BOLD calibration published in the papers [Krieger et al., 2014a] and [Krieger et al., 2014c].

pulse in VASO minimizing such inflow contaminations. Due to SAR constraints at higher field strengths ($\geq$ 7 T), the RF coil infrastructure is limited and a head RF coil must be used for transmission of the inversion pulse, which then can result in severe inflow contamination of the VASO signal. Furthermore, due to relatively long blood T_1 at high field strengths, the blood-nulling time can become longer than the arterial arrival time, making it more likely of inflow contamination to occur.
The purpose of this study is to develop a novel approach to avoid these inflow contaminations in VASO during hypercapnia at 7 T. In order to do so, an adiabatic inversion pulse is designed with an adjustable, B_1 insensitive inversion efficiency. The final goal of this study is to investigate, whether the application of such an RF pulse can avoid inflow effects of VASO during hypercapnia.

Theory and background

In the original VASO approach, blood z-magnetization is expected to be in steady-state. Inflowing blood magnetization that is not in steady-state results in artifactual CBF driven signal decrease additional to the desired CBV driven VASO signal decrease [Donahue et al., 2009b]. In SS-SI VASO, on the other hand, blood in the imaging slice is assumed to be not in steady-state, but it is expected to be once inverted only. In SS-SI VASO, inflow of not inverted blood deposited positive z-magnetization into the imaging slice. CBF increase during hypercapnia results then in more inflow of positive z-magnetization and corresponding signal increase. This flow driven signal increase is counteracting the CBV driven VASO signal decrease. Hence, inflow effects can be easily identified in SS-SI VASO by considering all voxels with signal increase during hypercapnia.
Here, a convenient and efficient way to avoid inflow of fresh, uninverted blood in VASO is proposed. This approach is based on the usage of reduced blood-nulling times $TI1$ that are shorter than the arterial arrival time. In this way, the blood has not enough time to flow into the imaging slice to introduce contaminating effects in the VASO signal in the first place. The blood-nulling time can be shortened by reducing the inversion efficiency of the (adiabatic) preparation pulse. In order to achieve this, the concept of RF phase modulation during the RF pulse was applied. Such phase modulations are known from plane rotation pulses for flip-angle variations [Norris and Haase, 1989] and are here transferred to conventional adiabatic pulses. The reduction in inversion efficiency is achieved here by introducing a phase skip of the RF field, B_1, during the inversion exactly at the time when the frequency of the adiabatic pulse is on resonance. The corresponding shape functions of the amplitude and phase of the RF pulse is shown in Fig. 4.21. A more intuitive illustration of the working principle of the new partial inversion pulse is illustrated in Fig. 4.22. In conventional adiabatic inversion pulses, the magnetization precesses around the effective magnetic field B_{eff} at the surface of a narrow 'cone of precession' (see section 2.1.4). During the frequency sweep of adiabatic RF pulses this cone usually follows the effective magnetic field, while it changes its direction. When a phase skip of the RF pulse is applied, this 'cone of precession' opens up. After inversion, the 'cone of precession' points along anti-parallel to the z-direction. The B_1-independent

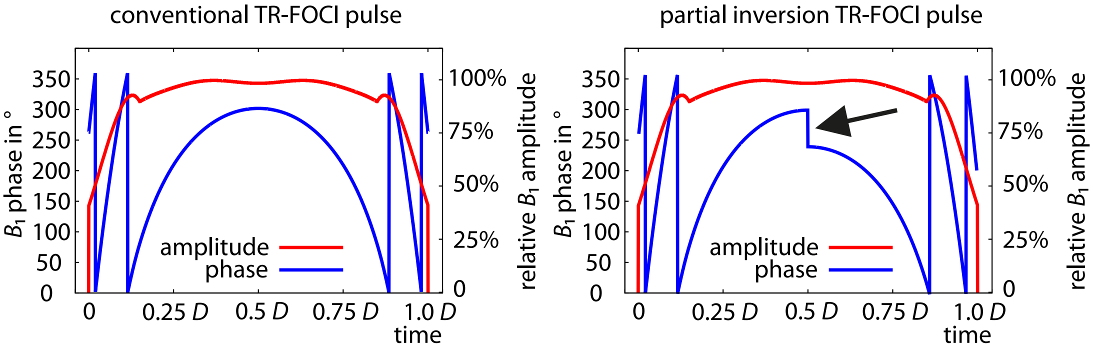

Figure 4.21: Amplitude and phase shape functions of the partial inversion RF pulse used to avoid inflow effects in SS-SI VASO: The partial inversion pulse is based on a TR-FOCI pulse with the pulse duration D. The partial inversion efficiency is adjusted by the phase skip (black arrow). Here, an example of 60° is depicted.

reduction in inversion efficiency is then given by the transverse component of the magnetization, which depends directly on the phase skip applied. The z-magnetization after the application of the partial inversion pulse and the respective inversion efficiency can be describes as a function of the phase skip (θ) applied:

$$cos(\theta) = \zeta = -\frac{M_{z,\text{ before inversion}}}{M_{z,\text{ after inversion}}} = 2\xi - 1. \tag{4.15}$$

Due to the utilization of an adiabatic pulse, this reduction is expected to be independent of B_1.

The application of a partial inversion pulse in VASO does not only affect the blood-nulling time. With shorter $TI1$, GM z-magnetization gets less time to relax before the readout at blood-nulling time. Hence, the application of partial inversion in VASO comes with the price of smaller GM z-magnetization at the blood-nulling time. Since GM signal variations are the basis of VASO signal change, VASO CNR decreases for shorter blood-nulling times. Figure 4.23 depicts an example of the expected z-magnetization of blood, GM and CSF in SS-SI VASO for an inversion efficiency of $\xi = 75\%$ ($\zeta = 50\%$). The z-magnetization of blood, GM and CSF at the blood-nulling time for a wide range of TRs and ζs is summarized in Fig. 4.24. The GM z-magnetization, responsible for the CNR in VASO, is almost linearly dependent on the inversion efficiency and shows highest values for full inversion. This means that the application of partial inversion pulses is accompanied with a tradeoff in sensitivity. Furthermore, Fig. 4.24 shows that GM z-magnetization and correspondingly VASO CNR is highest for shortest TR.

In conclusion, to achieve highest possible CNR in SS-SI VASO with partial inversion, it is suggested to use highest possible inversion efficiencies and shortest possible TRs.

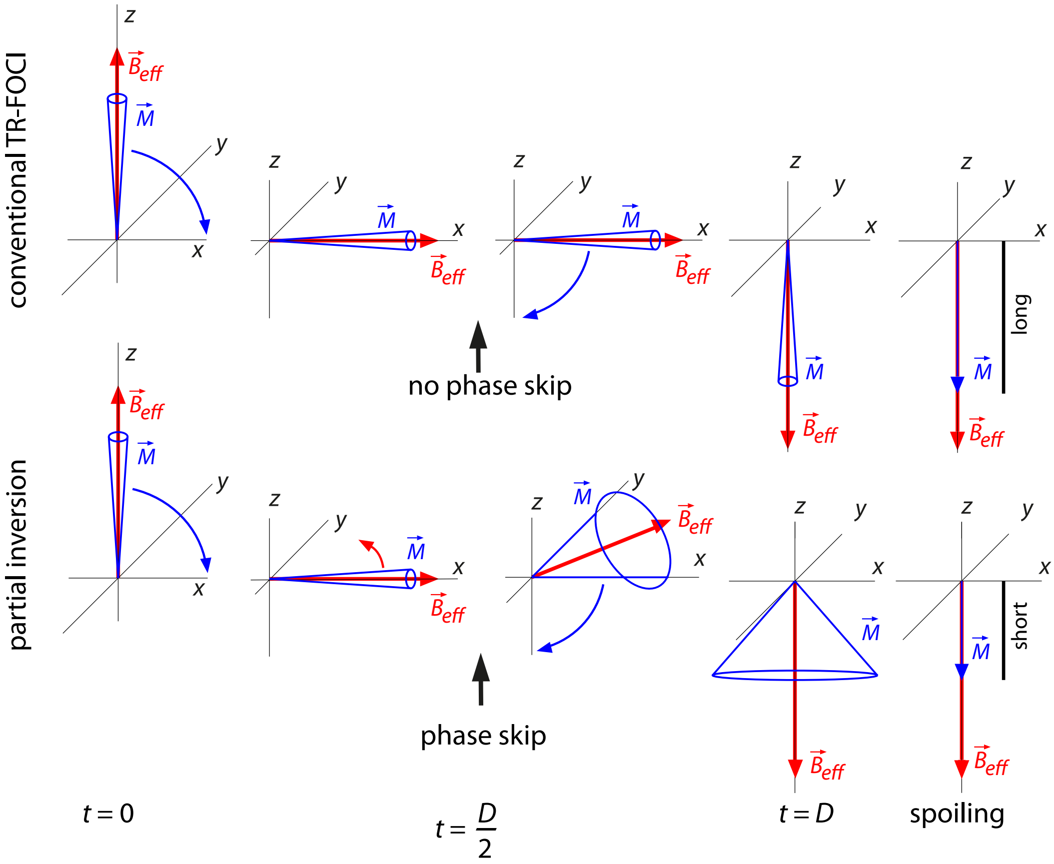

Figure 4.22: In conventional adiabatic inversion pulses of a pulse duration D, the magnetization follows the effective magnetic field in a narrow 'cone of precession' as the RF frequency offset is inverted (upper row). For partial inversion, the first half of the pulse is played out in the conventional manner. Half way throughout the pulse, when the RF-frequency is exactly the Larmor frequency, a phase skip is introduced that opens up the 'cone of precession'. The second half of the pulse is again played out in the conventional manner. After applying a spoiler gradient, the magnetization, pointing opposite to the external magnetic field, is reduced with respect to the conventional inversion pulse. This reduction can be qualitatively adjusted by setting the angel of the phase skip applied.

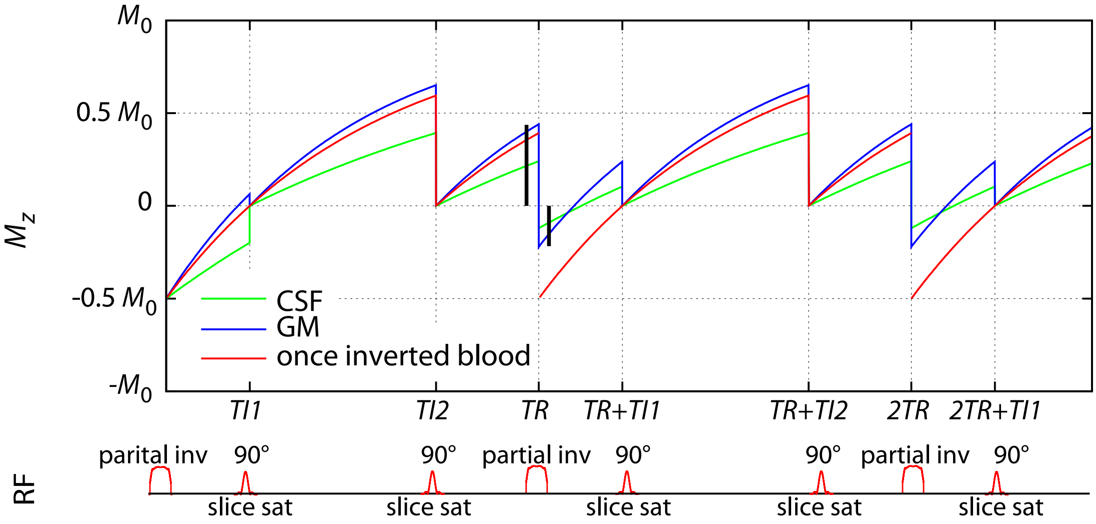

Figure 4.23: z-magnetization and RF transmission in SS-SI VASO with partial inversion: In the depicted example, the inversion efficiency is $\xi = 75\%$. This means, the absolute value of z-magnetization after the inversion is only half of absolute value the z-magnetization before the inversion (see black bars). Note that the z-magnetization of once inverted blood right after the inversion is only - 0.5 M_0. This fact results in shorter blood-nulling times compared to full inversion. The assumed T_1 values are $T_{1,GM}/T_{1,b}/T_{1,CSF}$ = 1.95/2.1/4.0 s according to literature values reviewed in Tab. 2.1.

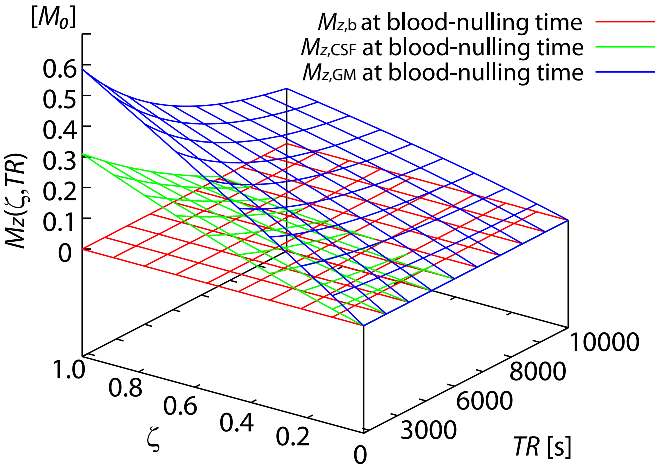

Figure 4.24: GM, CSF and blood z-magnetization in SS-SI VASO at the blood-nulling time as a function of inversion efficiency and TR.

Methods

Multi-TI (37/200/500/1000/3000/10000 ms) experiments were conducted in a water phantom with multiple B_1 amplitudes for investigations of the partial inversion pulse performance. Phantom parameters were: Cylindrical shape with radius = 16 cm, water with 1.24 g $NiSO_4$ $6H_2O$ and 2.62 g NaCl per liter, conductivity 0.52 S/m, relative permittivity 78 provided from Siemens (Siemens Medical Solutions, Erlangen, Germany). This phantom was chosen as a worst case example with maximal B_1 inhomogeneities.
Inversion efficiencies were calculated by combining Eqs. 2.17, 2.18, and 2.19 to:

$$\frac{M_z(TI)}{M_0} = 1 - e^{-\frac{TI}{T_1}}(1+\zeta) = 1 - 2\xi e^{-\frac{TI}{T_1}} \tag{4.16}$$

and fitting the parameters, T_1, ξ, and ζ to the multi-TI data acquired.
Additionally, three healthy participants (1 female, 27 to 32 years old) were scanned during a hypercapnia gas challenge. All breathing manipulation experiments where approved by local ethics committee of the University of Leipzig and all participants gave written informed consent for participation in this study. A medical doctor was present in the scanner room at all times during the breathing manipulation and was responsible for adjusting gas flow rates and monitoring pulse rate and arterial O_2 saturation measured via a pulse-oximeter on the participants' index finger. Gas flow was adjusted manually on a flow-meter to a flow rate of 15 liters per minute.
Image acquisition and signal evaluation was same as described earlier (section 3.1.3). In short: SS-SI VASO at 7 T, five axial slices with GE EPI, $TE/TR = 19/3000$ ms, nominal voxel size of 1.5 x 1.5 x 1.5 mm^3, TR-FOCI pulse duration of 5 ms. EPI T_1 maps were acquired for anatomical reference. MAFI B_1 maps [Boulant et al., 2009] were acquired for all participants to ensure that the spatial range of sufficient adiabaticity for proper inversion performance.
The gas challenge lasted 12-minutes consisting of 2/5/5 minutes of breathing air/5% CO_2, 21% O_2, balance N_2/air. The heart rate and respiratory gas composition were recorded with a BIOPAC MP150 unit (BIOPAC Systems Inc, USA). To investigate the reduced arterial arrival time effects in VASO during hypercapnia, the blood-nulling time was varied ($TI1 = 1330/1120/765$ ms) by adjusting the adiabatic inversion pulse efficiency to $\xi = 100\%$, 86%, and 75% in a B_1-independent way, as described above.

Results

The implementation and performance of the partial inversion pulse was tested in vivo and in a water phantom with considerable B_1 inhomogeneities. The experimentally measured maps of inversion efficiency ζ and the corresponding B_1 maps are shown in Fig. 4.25. Despite huge variations of B_1 up to a factor of 8, the inversion efficiency is very homogeneous with minimal variations. Subtle residual variation of inversion efficiency ζ in the range of ± 3% can be explained by transversal relaxation during the inversion pulse. For stronger B_1, the effective magnetic field is stronger tilted into the transverse plain (Eq. 2.9) during inversion, resulting in a higher susceptibility to transverse relaxation

[Norris, 2002]. Slightly visible outlines of the ventricles in the ζ map in vivo (Fig. 4.25B) might also suggest magnetization transfer effects during the off-resonant periods of the adiabatic inversion pulse [Hernandez-Garcia and Lewis, 2007].

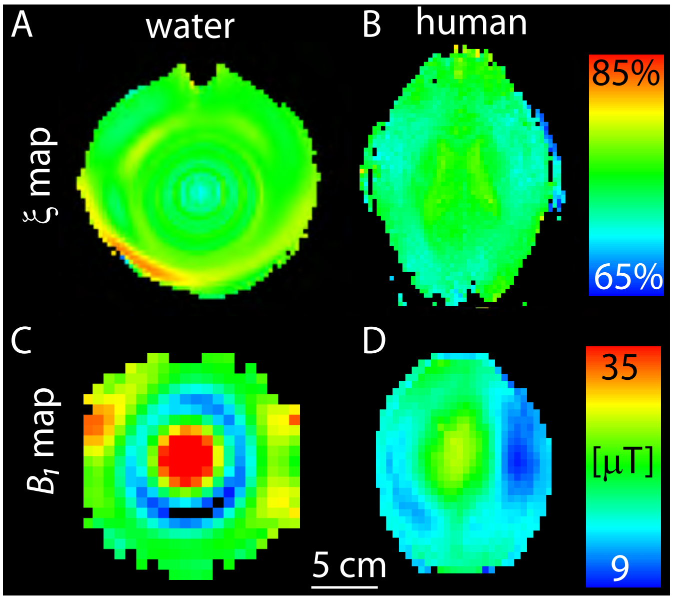

Figure 4.25: Measured partial inversion efficiency in a water phantom and in vivo with a phase skip of 60°: The corresponding desired inversion efficiency is 75%. The inversion efficiency is remarkably homogeneous despite huge B_1 variation up to a factor of 8. Note the different scaling window for inversion efficiencies and B_1 amplitudes.

The pulse performance was further tested with respect to a wide range of nominal B_1 field strengths for two desired inversion efficiencies. Table 4.3 demonstrates that for a 60°/90°-phase skip the inversion efficiency is reduced to $\zeta = (74 \pm 1)\%/(49 \pm 1)\%$ independently of the B_1 field applied. These numbers correspond well with the desired values of 75% and 50%.

The effect of inflow of fresh blood on VASO is examined with this partial inversion pulse in three volunteers with different $TI = 760/1120/1330$ ms during hypercapnia (Fig. 4.26). These results demonstrate the effect of inflow of fresh blood during the blood-nulling time and show whether these inflow effects can be minimized. With a long blood-nulling time of 1330 ms, the majority of GM voxels show VASO signal increase, suggesting inflow of fresh, uninverted blood magnetization (blue voxels in Fig. 4.26). The number of these voxels is minimized by decreasing TI, when the arterial arrival time is shorter than the blood-nulling time.

$\theta \backslash B_1$	23 μT	21 μT	16 μT	12 μT	7 μT	mean ± STD	$(1 + cos(\theta))/2$
60°	74%	75%	74%	74%	75%	(74 ± 1)%	75
90°	49%	50%	48%	51%	49%	(49 ± 1)%	50

Table 4.3: Measured inversion efficiencies for different B_1 phase skips and amplitudes in a water phantom: The standard deviation of all measured values listed are in the range of ± 1%. Data refer to the relative inversion efficiency with respect to the inversion efficiency without any phase skip of (93 ± 2)%. θ refers to the phase skip applied in the partial inversion pulse. The B_1 amplitude denotes the nominal peak amplitude of the partial inversion pulse. All values refer to an ROI covering the phantom within one acquired slice. The measured values are in very good agreement with the desired inversion efficiency (last column) for a wide range of B_1 amplitudes used.

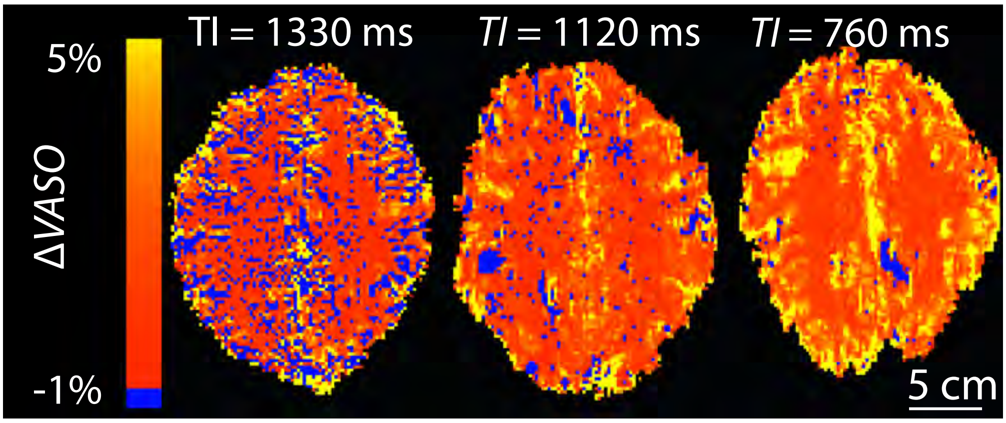

Figure 4.26: Maps of VASO signal change in three different participants with $TI1 = 760/1120/1330$ ms during hypercapnia: Voxels with significant VASO signal increase due to inflow of fresh blood magnetization during hypercapnia are depicted in blue. The number of these voxels decreases with shorter blood-nulling times, as inflow effects of fresh blood are reduced. Remaining voxels that show signal increase can be interpreted as arterial vessels going through the imaging slice.

Discussion and conclusion

Reduction in arterial arrival time during hypercapnia can introduce flow contamination in VASO signal. Here, a novel approach is proposed to avoid such inflow contaminations by making the inversion time shorter than the arterial arrival time, giving the blood not enough time to travel into the imaging slice. Shorter blood-nulling times in VASO can be achieved by reducing the inversion efficiency of the VASO preparation pulse. Such a pulse was developed in this study and thoroughly tested with respect to B_1 insensitivity in phantoms and in vivo. Applying VASO during hypercapnia, it could be shown that the application of partial inversion minimizes flow contamination of inflowing fresh blood.

4.3.2 BOLD calibration with VASO

Introduction

As discussed in previous sections (e.g. section 2.3.4), calibrated BOLD fMRI is a non-invasive MRI technique that can be used to estimate changes in $CMRO_2$ [Davis et al., 1998][Hoge et al., 1999]. The classic approach is based on simultaneous acquisition of CBF or CBV and BOLD weighted fMRI images during a gas-breathing manipulation. Based on these signals, the calibration constant M can be calculated. This calibration parameter can then be used to estimate changes in oxygen metabolism during another fMRI experiment with task induced brain activity changes.

Calibrated BOLD imaging based on hypercapnia calibration has found wide application and had tremendous influence on human neuroscience in the last twenty years and it has been reviewed in multiple recent articles [Blockley et al., 2013][Pike, 2012][Hoge, 2012]. There are two major limitations of this approach: (A) It is based on several biophysical assumptions made in the deoxyhemoglobin dilution model that may not be valid when comparing different tasks [Donahue et al., 2009c] or pathology. (B) The relative low CNR mostly limited by quantitative measurements of CBF or CBV makes voxel-wise investigations of $CMRO_2$ in individual volunteers difficult.

The purpose of this study is to assess, whether the intrinsically high CNR of quantitative vascular imaging in SS-SI VASO can overcome sensitivity limitations of BOLD calibration and provide maps of $CMRO_2$ on a the basis of individual volunteers.

Theory and background

Most studies of BOLD calibration are based on CBF and BOLD signal acquisition with ASL techniques. Here, it is tried to use CBV and BOLD signal acquired with SS-SI VASO for BOLD calibration. In order to substitute ASL with SS-SI VASO in this study, the deoxyhemoglobin dilution model must be reconsidered and adapted accordingly.

The standard approach of BOLD calibration requires three known quantities of $\Delta BOLD$, CBF, and CBV_v to estimate the calibration factor M, or $\Delta CMRO_2$. Usually $\Delta BOLD$ and CBF are measured with ASL and the term of CBV_v is inferred from the Grubb relation (Eq. 2.24). Here, CBV is measured with VASO and the term of CBF can then be inversely inferred from the Grubb relation. The Grubb equation for CBV_{tot} and

CBF_{tot} can be used to estimate the total contribution to CBV change.

$$\frac{\Delta CBV_{tot}}{CBV_{tot,rest}} + 1 = \frac{CBV_{tot}}{CBV_{tot,rest}} = \left(\frac{CBF_{tot}}{CBF_{tot,rest}}\right)^{\alpha_{tot}} \tag{4.17}$$

The venous CBV_v can be estimated similarly by using the established approach of assuming different Grubb coefficients for total and venous CBV. Blood is a conserved quantity and all the blood flowing into the arteries flows out of the veins eventually. Hence, CBF is the same in total blood and in the veins ($CBF_{tot} = CBF_v$). The Grubb equation (Eq. 4.17) can be rewritten as:

$$\left(\frac{\Delta CBV_{tot}}{CBV_{tot,rest}} + 1\right)^{\frac{1}{\alpha_{tot}}} = \left(\frac{\Delta CBF}{CBF_{rest}} + 1\right) = \left(\frac{\Delta CBV_v}{CBV_{v,rest}} + 1\right)^{\frac{1}{\alpha_v}}. \tag{4.18}$$

Equation 4.18 can be further manipulated to obtain a relationship between total and venous CBV changes.

$$\begin{aligned}
\left(\tfrac{\Delta CBV_{tot}}{CBV_{tot,rest}} + 1\right)^{\frac{1}{\alpha_{tot}}} &= \left(\tfrac{\Delta CBV_v}{CBV_{v,rest}} + 1\right)^{\frac{1}{\alpha_v}} \Leftrightarrow \\
\tfrac{\Delta CBV_{tot}}{CBV_{tot,rest}} &= \left(\tfrac{\Delta CBV_v}{CBV_{v,rest}} + 1\right)^{\frac{\alpha_{tot}}{\alpha_v}} - 1 \qquad \underbrace{\Leftrightarrow}_{\text{Taylor expansion}} \\
\tfrac{\Delta CBV_{tot}}{CBV_{tot,rest}} &\approx \tfrac{\alpha_{tot}}{\alpha_v}\tfrac{\Delta CBV_v}{CBV_{v,rest}} + \underbrace{\frac{\alpha_{tot}}{\alpha_v}\left(\frac{\alpha_{tot}}{\alpha_v} - 1\right)\frac{1}{2}\left(\frac{\Delta CBV_v}{CBV_{v,rest}}\right)^2}_{\ll 1 \text{ for physiological reasonable range}} + \mathcal{O}\left(\left(\tfrac{\Delta CBV_v}{CBV_{v,rest}}\right)^3\right)
\end{aligned} \tag{4.19}$$

In this study, relative changes in oxygen metabolism $\frac{CMRO_2}{CMRO_{2,rest}}$ are estimated by taking both Grubb values α_{tot} and α_v from the literature [Grubb et al., 1974][Chen and Pike, 2010b] and rearranging Eq. 2.37 to:

$$\frac{\Delta CMRO_2}{CMRO_{2,rest}} = \left(1 - \frac{\Delta BOLD}{M}\right)^{\frac{1}{\beta}} \left(\frac{CBV}{CBV_{rest}}\right)^{\frac{\beta - \alpha_v}{\beta \alpha_{tot}}} - 1. \tag{4.20}$$

Methods

Five healthy participants (3 female, 24 to 30 years old) were scanned during a 12-min hypercapnia gas challenge and a 10 min visual stimulation task consisting of a flickering checkerboard (alternating 30 s black background vs. 30 s flickering). Image acquisition and signal evaluation was same as described earlier (section 3.1.3): SS-SI VASO at 7 T, five axial slices with GE EPI, $TE/TR = 19/3000$ ms, nominal voxel size of 1.5 x 1.5 x 1.5 mm^3, TR-FOCI pulse duration of 5 ms. EPI T_1 maps were acquired for anatomical reference.

Experiments with breathing manipulations where conducted as described in the previous section: The gas challenge lasted 12-minutes consisting of 2/5/5 minutes of breathing

air/5% CO_2, 21% O_2, balance N_2/air. To deal with the reduced arterial arrival time during hypercapnia, the blood-nulling time was $TI1 = 765$ ms by adjusting the adiabatic inversion pulse efficiency to $\xi = 75\%$ as described in the previous section. Areas of stimulus induced activity where defined using FSL Feat (Version 5.98)[Worsley, 2001] as a cluster of voxels having z-values above 2.3 and a significance level of $p < 0.05$ (corrected for multiple comparisons). In order to account for possible head motion between the gas manipulation experiment and the visual stimulation experiments, the corresponding data where registered to each other with SPM8 (Welcome Department, University College London, UK).
The model values assumed to estimate $CMRO_2$ with Eq. 4.20 were:

- $\alpha_{tot} = 0.38$ [Grubb et al., 1974]
- $\alpha_v = 0.20$, in agreement with $\alpha_v = 0.23 \pm 0.05$ [Chen and Pike, 2009] and $\alpha_v = 0.18 \pm 0.02$ [Chen and Pike, 2010b]
- $\beta = 1$ [Kida et al., 2000][Martindale et al., 2008]
- $CBV_{rest} = 5.5\%$ [Lu et al., 2013]. This parameter is used to calculate $\frac{\Delta CBV}{CBV_{rest}}$ from VASO signal change (Eq. 3.4).

Results

BOLD and VASO signal changes could be acquired during hypercapnia and during stimulation to obtain maps of $\Delta BOLD_{HC}$, $\Delta BOLD_{stim}$, ΔCBV_{HC}, ΔCBV_{stim}, M, and $\Delta CMRO_2$. The maps of one representative participant are depicted in Fig. 4.27. $\Delta BOLD$ and ΔCBV can be nicely mapped with the resolution of 1.5 x 1.5 x 1.5 mm^3. Similarly, the M-value map estimated from $\Delta BOLD_{HC}$ and ΔCBV_{HC} seems not to be noise dominated and its voxel-wise values are in a physiological reasonable range $M \approx 5$ - 15 %. The map of $\Delta CMRO_2$ is calculated by means of four different kinds of signal change maps ($\Delta VASO_{vis}$, $\Delta BOLD_{vis}$, $\Delta VASO_{HC}$ and $\Delta BOLD_{HC}$), each with individual sources of error. Therefore, it is more noise dominated and the voxel-wise values cannot be considered to be meaningful as the vary between 0 and 100%. The relative noise contribution is substantially reduced, when $\Delta CMRO_2$ is averaged over the entire activated region. Doing so, a physiological meaningful value of $\Delta CMRO_2 = 28\%$ is obtained.
Maps of $\Delta BOLD$, ΔCBV, M, and $\Delta CMRO_2$ of all five participants are summarized in Fig. 4.28. It can be seen, how stable and reproducible these maps can be acquired. Table 4.4 depicts the mean values averaged over activation ROIs within individual participants.

The time courses of BOLD and VASO signals and the corresponding time courses of the end-tidal partial pressures during the hypercapnia scan are depicted in Fig. 4.29. Both, BOLD and VASO data show significant signal changes. However, considerable inter-subject variations can be seen as well, which is expected due to different baseline physiology such as venous baseline oxygenation [Lu et al., 2008]. These variations are part of the original motivation to do calibrated fMRI. In healthy participants they might be a result of from physiological effects, e.g. different fitness or breathing behavior of the participants during the scan.

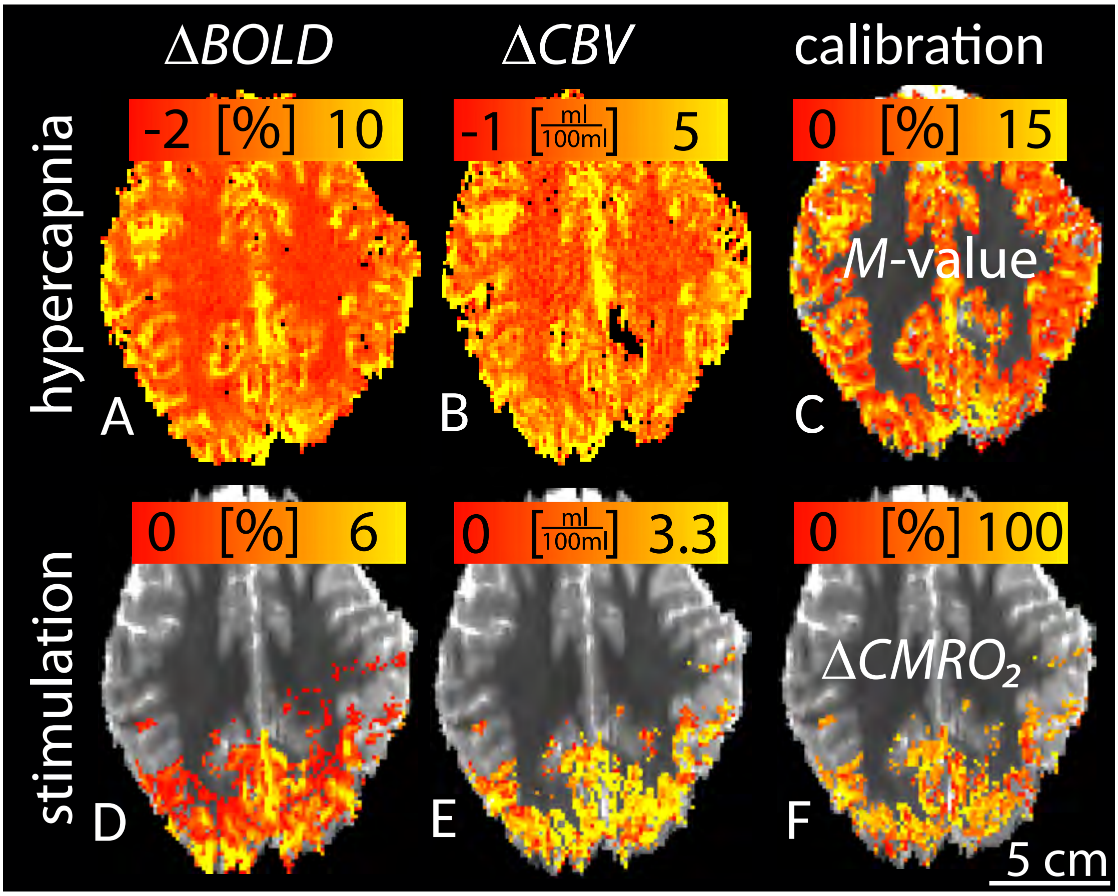

Figure 4.27: Maps of $\Delta BOLD_{HC}$, $\Delta BOLD_{stim}$, ΔCBV_{HC}, ΔCBV_{stim}, M, and $\Delta CMRO_2$ for one representative participant.

	$\Delta BOLD_{HC}$	$\Delta VASO_{HC}$	$\Delta BOLD_{stim}$	ΔCBV_{stim}	M	$\Delta CMRO_2$
1	4.4%	57%	2.3%	46%	10.2%	28%
2	3.5%	47%	2.0%	41%	12.0%	31%
3	2.4%	52%	1.9%	42%	13.8%	30%
4	3.1%	37%	2.1%	36%	13.9%	28%
5	3.6%	51%	1.1%	45%	12.6%	15%
Mean	3.4%	49%	1.8%	42%	12.3%	26%
STD	0.7%	7%	0.4%	4%	1.4%	7%

Table 4.4: Results of ΔCBV and $\Delta BOLD$ during hypercapnia and during stimulation and the corresponding M-values and $CMRO_2$ changes across five participants.

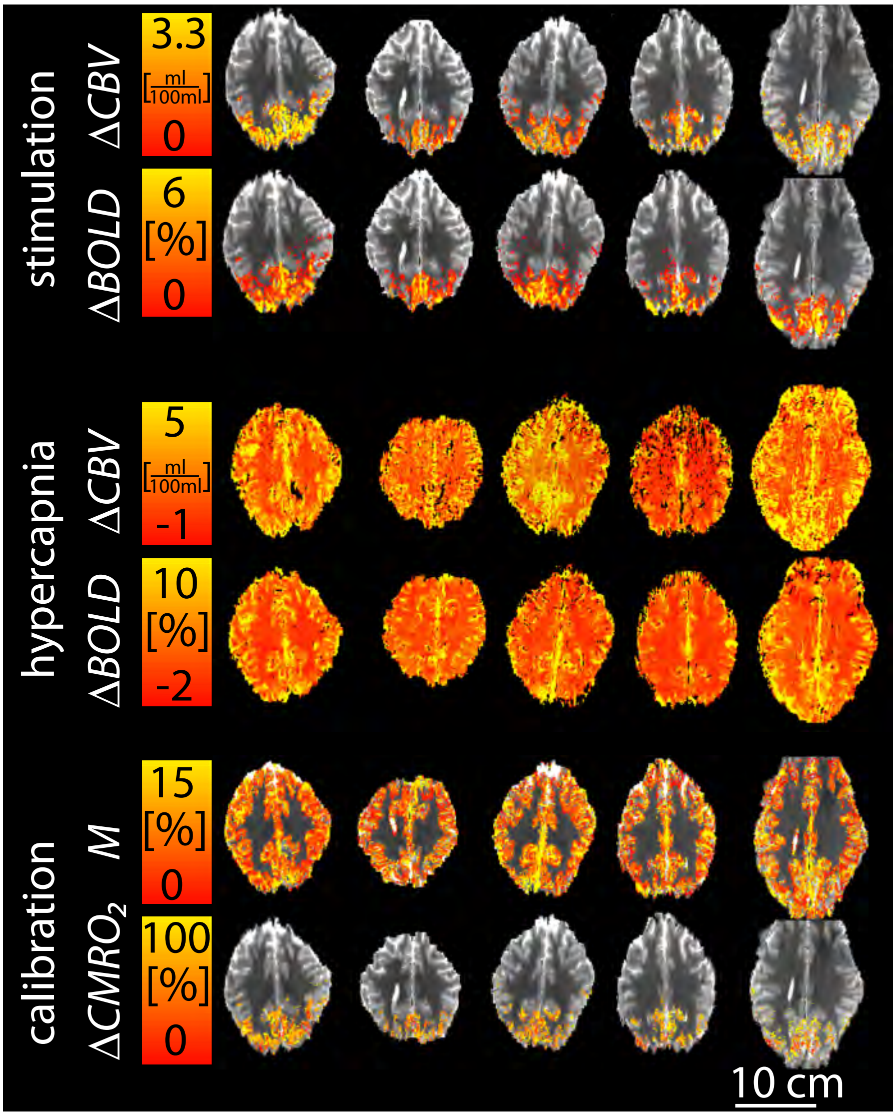

Figure 4.28: Maps of $\Delta BOLD$ and ΔCBV for visual stimulation and hypercapnia as well as the corresponding maps of M-value and $\Delta CMRO_2$ in all five participants. Note that ΔCBV is depicted in positive units of ml/100ml and not in units of negative VASO % signal change.

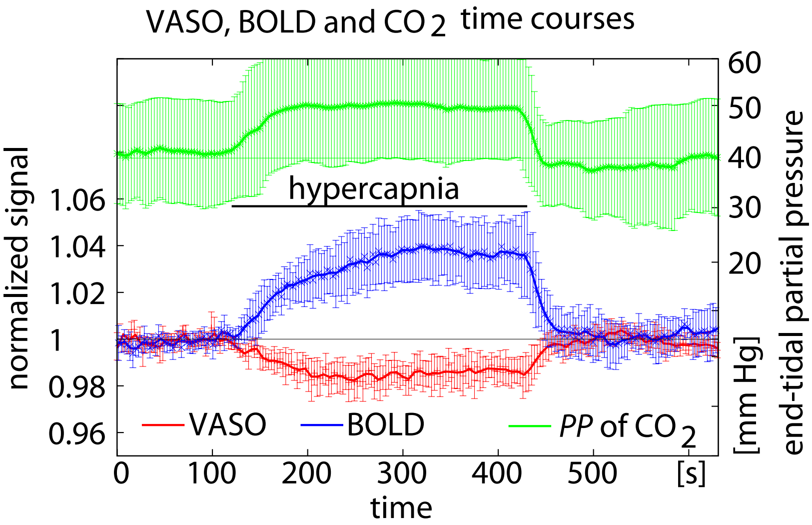

Figure 4.29: Average time courses of end-tidal partial pressure of CO_2 during hypercapnia and responses in BOLD and VASO signal.

Discussion and conclusion

Results shown here suggest that the high CNR of SS-SI VASO with partial inversion efficiency can be a useful tool in BOLD calibration to obtain high resolution maps of $\Delta CMRO_2$. Even though the individual $\Delta CMRO_2$ maps are noise dominated, the inter-subject variability of the calibrated parameters $CMRO_2$ is comparatively low. Despite one participant being an outlier (Nr. 5), this suggests a good reproducibility of the method applied and might potentially be due to the insensitivity of physiological variability, e.g. venous baseline oxygenation mentioned above. The measured value of $\Delta CMRO_2 = (26 \pm 7)\%$ is in good agreement with the literature of similar studies using visual stimuli (Tab. 4.5). Most of the values reported in the literature are only slightly lower than the value found in this study. This small trend might come from reduced partial volume effects in this study due to the high resolution of 1.5 x 1.5 x 1.5 mm^3, higher than any other study listed.

Limitations at high resolutions The deoxyhemoglobin dilution model is based on many biophysical assumption that are originally introduced for resolutions in the range of 3 - 5 mm and must be reconsidered for higher resolutions such as 1.5 mm used in this study. At these resolutions, different parts of the vascular tree such as large arteries, microvasculature, or large veins start to be locally distributed across different voxels. this can lead to false assumptions in the biophysical model applied. For example, when a voxel at the cortical surface is dominated from a large vein without much microvascular tissue Eq. 4.20 simplifies to $\frac{\Delta CMRO_2}{CMRO_{2,rest}} = \left(1 - \frac{\Delta BOLD}{M}\right)^{\frac{1}{\beta}} - 1 \approx -\frac{\Delta BOLD}{M}$. In this

reference	$\Delta CMRO_2$
[Marrett and Gjedde, 1997]	(25 ± 5)%
[Davis et al., 1998]	(16 ± 1)%
[Hoge et al., 1999]	(25 ± 4)%
[Kim et al., 1999]	(23 ± 9)%
[Leontiev and Buxton, 2007]	(27 ± 10)%
[Leontiev et al., 2007]	(31 ± 7)%
[Perthen et al., 2008]	(21 ± 3)%
[Ances et al., 2008]	(30 ± 6)%
[Lin et al., 2008]	(24 ± 3)%
[Lin et al., 2010]	(13 ± 4)%
[Moradi et al., 2012]	(9 ± 1)%
[Hutchison et al., 2013]	(13 ± 2)%
[Krieger et al., 2014a]	(20 ± 4)%
this study	(26± 4)%

Table 4.5: Literature values of $\Delta CMRO_2$.

case the deoxyhemoglobin dilution model would predict a change in $CMRO_2$ from the BOLD signal change, even though the vein in this voxel does not really contribute to the task induced oxygen metabolism change. Similarly, the distribution between ΔCBV_v and ΔCBV_{tot} and the corresponding Grubb values are expected to vary between surface voxels and deeper voxels. In conclusion, high resolution featured of estimated $\Delta CMRO_2$ must be interpreted with caution. Future research is needed to evaluate the applicability of calibrated BOLD at very high resolutions [Guidi et al., 2014].

Effect of variation in literature values assumed The values of physiological parameters of α_{tot}, α_v, β, and CBV_{rest} used in the deoxyhemoglobin dilution model for estimating $\Delta CMRO_2$ are taken from the literature. Potential deviations of these values compared to the true underlying physiology can result in systematic errors of M and $\Delta CMRO_2$. The effect of such false assumptions is summarized in Fig. 4.30 analogously to the way of depicting such uncertainties in previous studies [Griffeth and Buxton, 2011]. The five physiological parameters of α_{tot}, α_v, β, CBV_{rest}, and M are discussed in more detail below:

- The Grubb value α_{tot} describes the relationship between total CBF and total CBV. The default value was here chosen to be $\alpha_{tot} = 0.38$ [Grubb et al., 1974]. It has been shown, however, that the original data from Grubb et al. can be refitted with an exponent of $\alpha_{tot} = 0.5$ with a correlation coefficient larger than 0.9 [van Zijl et al., 1998]. Assuming laminar flow, the Grubb value can be deduced by means of Hagen-Poiseuille's law to be $\alpha_{tot} = 0.5$ (Eq. 2.23). Piechnik et al. simulated α_{tot} in a sophisticated model and report that α_{tot} is in the range of 0.4 up to 0.5 for all arterioles, capillaries and venules up to diameters of 30 μm [Piechnik et al.,

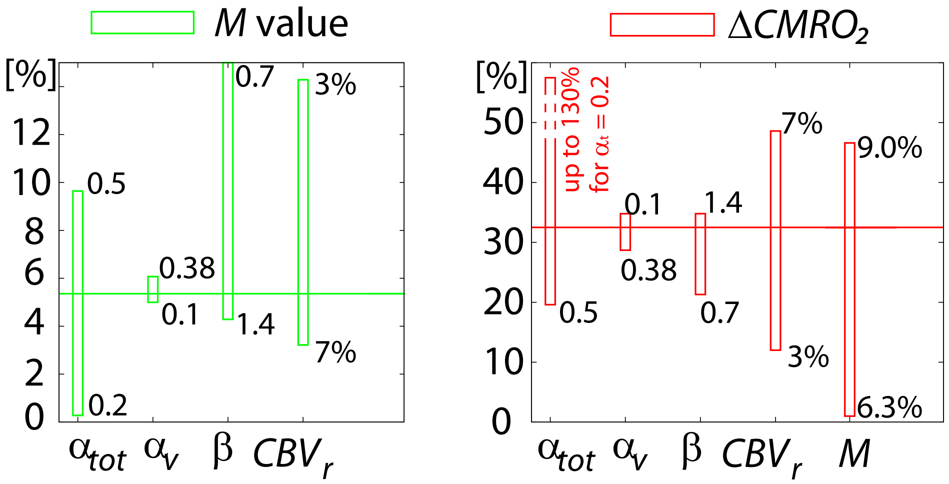

Figure 4.30: The influence of wrong assumed physiological model parameters is depicted analogously to previously published studies [Griffeth and Buxton, 2011]: The horizontal line corresponds to the 'true' values of M and $\Delta CMRO_2$. Vertical bars refer to the values of M and $\Delta CMRO_2$ for the denoted range of the assumed model parameters.

2008]. Veins with diameter larger than 30 μm would have lower Grubb values of ≈ 0.14. Experimental comparisons of CBF and CBV suggest that α_{tot} might not only be different for hypercapnia and stimulation, but it might even be depend on the stimulus paradigm used [Lin et al., 2008]. Fig. 4.30 shows that it is more problematic to overestimate α_{tot} than to underestimate it. Higher values of α_{tot} would correspond to a slightly lager M-value and a smaller value of $\Delta CMRO_2$. Compared with other physiological assumptions, the Grubb value α_{tot} has a great impact on estimated values of M and $\Delta CMRO_2$. Hence, small errors in assumed values of α_{tot} can render quantitative estimations of $\Delta CMRO_2$ impossible.

- The venous Grubb value α_v describes the relationship between total CBF and deoxygenated CBV. This value was measured by comparing ASL results with VERVE results, which are sensitive to change in deoxygenated CBV. The measured values are $\alpha_v = 0.18 \pm 0.02$ [Chen and Pike, 2010b] and $\alpha_v = 0.23 \pm 0.05$ [Chen and Pike, 2009]. More recently, Mark and Pike determined α_v by comparing M-values from hypercapnia calibration and hyperoxia calibration [Mark and Pike, 2012]. They found $\alpha_v = 0.12 \pm 0.04$ in the visual cortex and $\alpha_v = 0.18 \pm 0.02$ in the somatosensory cortex. Fig. 4.30 suggests that the model is relatively forgiving to moderate errors in α_v.
- In principle, deoxyhemoglobin dilution model describes the BOLD signal change for extravascular space only. The intravascular BOLD signal change is introduced into the model by inserting a β exponent. This exponent describes the connection between change in total T_2^* and the absolute change in deoxyhemoglobin. Since

the weighting between intravascular BOLD effect and extravascular BOLD effect depends on field strength, β is also field strength dependent. Usually β is determined by Monte-Carlo-simulations. At 7 T this β value becomes less important and approaches 1 [Kida et al., 2000][Martindale et al., 2008][Donahue et al., 2010]. This comes from the fact that the short intravascular T_2^* at high fields results in minimal intravascular BOLD effect compared to extravascular BOLD effect, almost independent of the vessel size [Uludağ et al., 2009]. Hence, the corresponding uncertainty in estimations of $\Delta CMRO_2$ is relatively small compared to other physiological parameters (Fig. 4.30).

- Blood volume at rest CBV_{rest} is used in order to calculate $\frac{CBV}{CBV_{rest}}$ from relative VASO signal change. Dependent on the error of CBV_{rest}, it can also result in significant errors in calculated $\Delta CMRO_2$ (Fig. 4.30). It must be noted that this parameter assumption is unique to the application of VASO in BOLD calibration. For alternative applications using ASL, other parameters in perfusion models are more important than CBV_{rest}.
- Assuming that the microvascular density and the venous baseline oxygenation are uniformly distributed in the brain, M-value could be used from literature in order to calculate $\Delta CMRO_2$ without any calibration measurement. For the sake of comparison with this approach, the effect of an assumed M-value is also considered in Fig. 4.30. It can be seen that a small error in the M-value assumed can significantly distort the calculated value of $\Delta CMRO_2$. In other words, an calibration scan is vital for good estimation of $\Delta CMRO_2$.

Noise in a nonlinear model Equation 4.20 is highly nonlinear. Therefore, the calculated values of M-value and $\Delta CMRO_2$ depend on the noise level and the way of averaging. Equation 4.21 represents a voxel-wise calculation of $\Delta CMRO_2$ and subsequent averaging over all voxels within the ROI. Equation 4.22 represents an ROI-wise calculation of $\Delta CMRO_2$ by averaging over all voxels within the ROI before the model calculations are done.

$$\frac{\Delta CMRO_2}{CMRO_{2,rest}} = \frac{1}{N_{\text{voxels}}} \sum_{i=1}^{N_{\text{voxels}}} \left[\left(1 - \frac{\Delta BOLD_i}{M_i}\right)^{\frac{1}{\beta}} \left(\frac{CBV_i}{CBV_{i,rest}}\right)^{\frac{\beta-\alpha_v}{\beta\alpha_{tot}}} - 1 \right] \tag{4.21}$$

$$\frac{\Delta CMRO_2}{CMRO_{2,rest}} = \left(1 - \frac{\frac{1}{N_{\text{voxels}}} \sum_{i=1}^{N_{\text{voxels}}} \Delta BOLD_i}{\frac{1}{N_{\text{voxels}}} \sum_{i=1}^{N_{\text{voxels}}} M_i} \right)^{\frac{1}{\beta}} \left(\frac{1}{N_{\text{voxels}}} \sum_{i=1}^{N_{\text{voxels}}} \frac{CBV_i}{CBV_{i,rest}} \right)^{\frac{\beta-\alpha_v}{\beta\alpha_{tot}}} - 1 \tag{4.22}$$

Both, Eqs. 4.21 and 4.22 represent mean values of $\Delta CMRO_2$, but they give very different results. The voxel-wise calculation evaluation results in the above reported values of $M = 12\%$ and $\Delta CMRO_2 = 26\%$, while the ROI-wise calculation results in completely different values of $M = 6\%$ and $\Delta CMRO_2 = 41\%$. Both evaluation schemes have advantages and disadvantages:

The ROI based evaluation scheme inherently implies that all voxels within an ROI would have the identical values of BOLD and VASO signal change. This picture, however, is highly unrealistic and unphysiological. Even with minimal partial volume effects at relatively high resolution of 1.5 x 1.5 x 1.5 mm^3, signal changes are unevenly distributed across active voxels (Figs. 4.27 and 4.28). Dependent on the distribution function of signal change across voxels, this can result in biases of the corresponding mean results. Due to these biases, this ROI-wise calculation scheme was believed to be unreliable here and hence it was not used in this thesis.

The voxel-wise calculation scheme, on the other hand, does not have such biases. However, it is more limited by noise. The equally distributed noise in the original data is transformed from the nonlinear model into nonequally distributed noise of $\Delta CMRO_2$ values. This noise transformation is associated with corresponding biases in the resulting average over all voxel. Independent of the nonlinear noise transformation, there is another potential source of bias the voxel-wise calculation scheme. In order to avoid any imaginary numbers in the results, the base in the exponential terms of the model must not be negative and corresponding voxels must be excluded. Such an asymmetric exclusion criterion can affect the overall mean result, and introduce an additional bias.

4.3.3 Summary

BOLD signal calibration is in the focus of current research because it has the potential to overcome many limitation of conventional fMRI, such as confined interpretability and lack of applicability in pathology. However, it suffers from CNR limitations in quantitative vascular imaging of CBF or CBV. In this study it was assessed, whether the high CNR of SS-SI VASO can overcome some of these limitations and whether it can provide maps of $\Delta CMRO_2$ on the basis of individual participants. In order to account for inflow effects of fresh blood in VASO during hypercapnia, a novel compensation framework based on B_1 insensitive partial inversion pulses is developed, implemented, validated, and applied.

For estimation of $\Delta CMRO_2$ from simultaneously acquired BOLD and VASO data during hypercapnia and stimulation, many physiological assumptions are needed within the BOLD deoxyhemoglobin dilution model. Based on these assumption it was possible to derive quantitative $\Delta CMRO_2$ maps on a basis of individual participants with unprecedented resolutions of 1.5 x 1.5 x 1.5 mm^3. The values of $\Delta CMRO_2 = (26 \pm 7)\%$ are highly reproducible across five participants and in good agreement with the literature. Even though the application of SS-SI VASO still could not overcome the limitations arising from the nonlinearity of the BOLD models applied, the improved sensitivity could minimize corresponding biases compared to the noisier alternative approach of using ASL [Ivanov, 2012][Krieger et al., 2014a].

5 Limitations of SS-SI VASO

There are multiple potential sources of artifacts in VASO including, inflow effects, permeability effects, incomplete blood nulling, BOLD contaminations, and partial voluming of CSF. They have been extensively discussed in the literature and methods to avoid these artifacts have been proposed. In previous chapters, it has been shown that the sensitivity of blood volume measurement can be dramatically increased by using SS-SI VASO compared to the original approach developed for lower field strengths. The mechanism underlying this sensitivity increase is based on additional physiological assumptions. Due to these new features, the above mentioned sources of artifacts must be revisited with respect to the novel contrast generation used in SS-SI VASO. This chapter focuses in particular on four potential sources of artifacts. The first section describes the effects of flow and perfusion contaminations in VASO. The second section focuses on limitations regarding the confined acquisition window during the blood-nulling time. The BOLD correction mechanism based on dynamic division and its limitations are discussed in the third section. Potential contaminations regarding partial volume effects of CSF and WM and dynamic changes of such effects are discussed in the last section of this chapter. All limitations and potential artifacts in this chapter are discussed and investigated with respect to experimental acquisition parameters used in the studies of this thesis. The chapter is concluded with guidelines for optimal acquisition parameters that are recommended to avoid or minimize contaminations in SS-SI VASO.

5.1 Effects of perfusion and capillary permeability on accuracy of VASO

This section describes a multi compartment perfusion model based on the Bloch equations to theoretically investigate effects of flow and perfusion in the VASO signal. Therefore, perfusion models that are established in the ASL literature are revisited and applied here. These models are adjusted to investigate the effects of inflow of fresh blood, effects of capillary permeability, and outflow of not nulled blood in SS-SI VASO. Such effects are quantified for a wide range of experimental parameters and compared with corresponding experimental results.

5.1.1 Introduction

The CBV-contrast in VASO is based on the assumption that all blood water stays within a closed intravascular compartment without any connection to extravascular space. Furthermore it is assumed that all of its z-magnetization relaxes in the same way, whether in arteries and in veins. As pointed out in the original paper [Lu et al., 2003] already, this model is an approximation and does not account for a number of processes including inflow of fresh blood, outflow of insufficiently nulled blood and water exchange between intra- and extravascular space. In VASO, capillary permeability and corresponding magnetization exchange between intravascular and extravascular space can result in incomplete blood nulling in the post arterial blood compartments and residual intravascular signal. Since this residual intravascular signal can depend on CBF_{rest} and ΔCBF, it can introduce unwanted flow weighting into the VASO contrast.

The amount of not nulled capillary z-magnetization caused by capillary permeability was firstly considered in [Lu et al., 2003] and [Donahue et al., 2006] using a single compartment model established in the ASL literature [Detre et al., 1992]. This model was further extended to a two compartment model [Parkes and Tofts, 2002] in [St. Lawrence, 2005] and [Wu et al., 2010] to estimate the resulting effects on VASO signal change. However, the effect of capillary permeability on VASO signal change in individual blood compartments of arteries, capillaries and veins has not been considered in these theoretical studies.

Additional to these permeability effects, inflow of fresh (not inverted) blood into the imaging slice can as well introduce CBF weighting into the resulting VASO signal, especially when a head coil is used for RF transmission. These inflow effects in VASO have been discussed extensively [Donahue et al., 2006][Donahue et al., 2009b][Lu, 2008].

In SS-SI VASO, the contrast relies of additional assumption compared to the original VASO approach, such as that all of the blood has been inverted only once. Furthermore, water z-magnetization has different relaxation history in SS-SI VASO as opposed to the original VASO method. Therefore, the resulting CSF weighting in SS-SI VASO might be different from the effects investigated earlier [Donahue et al., 2006][St. Lawrence, 2005][Wu et al., 2010].

The purpose of this study is to quantify and discuss the effect of inflow of fresh blood, the effect of capillary permeability and the effect of outflow of not nulled blood and the consequent flow dependence of SS-SI VASO. The magnitude of these contaminations can than be discussed with respect to similar effects in the original VASO approach. This flow weighting is tried to be investigated within a broad range of physiological parameters of CBF_{rest}, ΔCBF, and permeability area product (PS). The final goal of this study is to quantify the limitations of SS-SI VASO and if possible, find a set of acquisition parameters, where the flow weighting in VASO can be avoided or minimized. The found dependency of VASO signal on acquisition parameters used can then be directly compared with experimental in vivo results.

5.1.2 Physiological background

In order to establish a model for quantitative estimations of confounding signal contributions in VASO, a precise picture of blood in the vasculature, its arrival, transit, and outflow times is reviewed. This review can be based on the vast body of literature in the field of perfusion imaging, which can provide consistent figures of perfusion dynamics. Here, quantitative values of reasonable physiological variables are collected in order to use them later in a quantitative tissue perfusion model.

Values of perfusion and permeability In [Calamante et al., 1999], 14 perfusion studies in humans are reviews with respect to the CBF values at rest. The vast majority of the reviewed papers report values in the range of 70 ml/100ml/min up to 100 ml/100ml/min. Hence, any number in this range should be considered as physiologically reasonable and could be used here to estimate perfusion effects in VASO. In order to be consistent with previous VASO-perfusion models [Wu et al., 2010], the value used here is chosen accordingly to be $CBF_{rest} = 90$ ml/100ml/min.
The permeability is often described as the water exchange through the permeable capillary wall between intravascular and extravascular space by means of the so called permeability-surface area product (PS). This value was measured with PET to be approximately 150 ml/100ml/min [Herscovitch et al., 1987]. In compliance with earlier perfusion models [Wu et al., 2010][Parkes and Tofts, 2002], this value is also used here. This value is assumed to be independent of flow and brain activity.

Transit time through microvasculature The blood transit time through microvasculature is an important parameter in SS-SI VASO with respect to the assumption that all the blood in the imaging slice has been refilled during TR. This value can be taken from the literature to be 1 - 1.5 s (section 3.1.2). Alternatively it can be estimated from CBV and CBF values:

$$\frac{CBV \text{ [ml/100ml/min]}}{CBF \text{ [ml/100ml]}} = \tau \text{ [min]}, \tag{5.1}$$

as done in [Grubb et al., 1974]. For self consistency of the vascular model, the transit time is consisted here according to Eq. 5.1.

Blood arrival time In order to assess inflow contaminations in VASO, the arterial arrival time of fresh blood is needed to be known. The transit time is often divided into two parts. δt is the time needed for blood to reach the region of interest and δ_a is the time for blood to traverse the arterial compartment within the region of interest before reaching capillaries. The transit time to the occipital lobe is approximately 900 ms - 1300 ms (see Tab. 5.1).
The time δ_a to reach the capillary compartment in the region of interest takes approximately additional 400 ms - 500 ms [Hall et al., 2011][Francis et al., 2008]. These numbers suggest that there are no inflow effects in SS-SI VASO, when TI is smaller than $\delta t + \delta_a \approx 1000$ ms + 500 ms = 1500 ms. Using inversion times TI above ≈ 1500 ms uninverted blood would enter small vessels and introduce flow weighting in SS-SI VASO.
All physiological parameters used in the model are listed in Tabs. 5.2 and 5.3.

reference	δt	comment
[Wong et al., 1997]	1200 ms ± 100 ms	Gap between tag and imaging slice is 1 cm.
[Figueiredo et al., 2005]	960 ms ± 170 ms	Gap between tag and imaging slice is 1 - 3 cm.
[MacIntosh et al., 2010]	935 ms ± 108 ms	Gap between tag and imaging slice is 4 cm.
[Chen et al., 2012]	1300 ms ± 100 ms	In occipital lobe. Gap between tag and imaging slice is 4.5 cm.
[Qiu et al., 2010]	1251 ms ± 120 ms	In occipital lobe. Gap between tag and imaging slice is $\approx$ 2 - 3 cm.

Table 5.1: Literature values of the time that blood needs to arrive at the region of interest. After this time δt the blood begins to fill the imaging slice.

name	value	references and comments
CBV_a	20% of CBV_{tot}	[Weber et al., 2008][An and Lin, 2002][Donahue et al., 2009c] relative to total CBV
CBV_c	40% of CBV_{tot}	[Weber et al., 2008] relative to total CBV
CBV_v	40% of CBV_{tot}	[Weber et al., 2008][An and Lin, 2002] relative to total CBV
ΔCBV_a	60% of CBV_{tot}	[Griffeth and Buxton, 2011][Hua et al., 2011a][Lee et al., 2001] relative to CBV_a
ΔCBV_c	10% of CBV_{tot}	[Griffeth and Buxton, 2011] relative to CBV_c
ΔCBV_v	10% of CBV_{tot}	[Griffeth and Buxton, 2011][Kennerley et al., 2012a] relative to CBV_v
CBV	4% blood water per parenchyma volume	Often used value is 5.5% [Lu et al., 2013]. Here a lower value is assumed focusing on microvasculature.
ΔCBV	15% - 25%	Tab. 3.1

Table 5.2: Assumed volume changes across vascular compartments used in the model.

name	value	references and comments
CBF	90 ml/100ml/min	[Calamante et al., 1999]
ΔCBF	60%	[Calamante et al., 1999]
ρ_b	0.89 ml water/ml blood	[Donahue et al., 2009a]
ρ_{par}	0.87 ml water/ml parenchyma	[Donahue et al., 2009a]
V_{GM}	1 - $CBV \frac{\rho_b}{\rho_{GM}}$	assuming ρ_{GM} is equal to ρ_{par}, in units of ml per ml of tissue
PS	144 ml/100ml/min	[Herscovitch et al., 1987][Wu et al., 2010]
$TR_{original}$	3 s	often used in the original VASO approach [Lu et al., 2013]
TR_{SS-SI}	3 s	corresponding to acquisition of both, BOLD and VASO signal
$TI_{original}$	$T_{1,b}\ ln(1+\zeta)$	according to blood nulling condition (Eq. 2.30)
TI_{SS-SI}	$T_{1,b}\ ln(1+\zeta) - ln(1+\zeta e^{-\frac{TR}{T_{1,b}}})$	according to blood nulling condition (Eq. 3.1)
$T_{1,b}$	2.1 s	Tab. 2.1
$T_{1,GM}$	1.9 s	Tab. 2.1
τ	$\frac{CBV}{CBF}$	transit time according to Eq. 5.1
δt	1500 ms	arrival time of fresh blood. See body text for the choice of value used.
$\Delta\delta t$	200 ms	change in arterial arrival time due to stimulation [Ho et al., 2011]
TTH	1 s	transit time heterogeneity [Jespersen and Østergaard, 2012]

Table 5.3: Assumed physiological parameters that are used in the model: All parameters refer to human cortical GM tissue at 7 T. The most critical parameters that could introduce flow weighting in VASO are, CBF_{rest}, ΔCBF, PS, and δt. These parameters are investigated in more detail and with respect to a broad range of values.

5.1.3 Introduction to vascular perfusion models

Single compartment model

Detre et al. employed a single compartment model to quantify CBF changes in ASL [Detre et al., 1992]. In this single compartment model, water magnetization enters and leaves with the perfusion rate CBF and relaxes with tissue T_1 in the well mixed single compartment (Fig. 5.1A). The equation of motion that describes the behavior of magnetization in the single compartment is given by a modified Bloch equation.

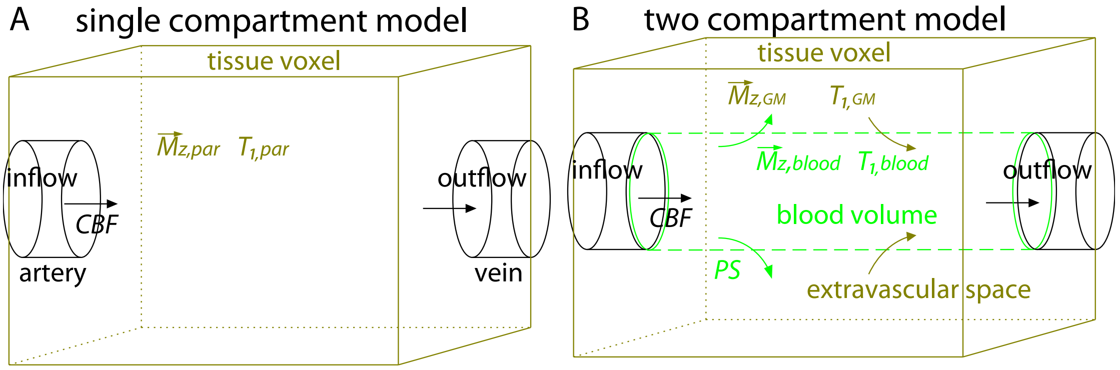

Figure 5.1: Illustration of single compartment model and two compartment model

$$\frac{dM_{z,par}(t)}{dt} = \underbrace{\frac{M_{0,par} - M_{z,par}(t)}{T_{1,par}}}_{\text{Bloch equation}} + \underbrace{\frac{CBF}{CBV} M_{z,a}(t)}_{\text{inflow}} - \underbrace{\frac{CBF}{CBV} M_{z,v}(t)}_{\text{outflow}} \qquad (5.2)$$

Where $M_{z,par}(t)$ is the z-magnetization from parenchyma; $M_{z,a}(t)$ and $M_{z,v}(t)$ are the z-magnetizations of inflowing and outflowing blood. Often, $M_{z,v}(t)$ is considered to be $M_{z,v}(t) = \frac{M_{z,par}(t)}{BBPC}$, where $BBPC$ is the brain-blood partition coefficient for water that corrects for the different proton density of tissue and blood and for finite permeability. $BBPC$ is believed to be in the range of $BBPC = 0.8$ ml/ml [Herscovitch and Raichle, 1985][Iida et al., 1989].

The most crucial simplifications and limitations in the single compartment model are:

- It is assumed that blood water decays with $T_{1,par}$ instantaneously, as soon as it arrives the microvasculature. However, due to finite permeability, water molecules remain in the blood for some time before entering the extravascular space and decays with $T_{1,b}$ until then.
- The single compartment model does not consider blood volume separately from tissue volume, which makes it impossible to investigate VASO contrast.
- In the single compartment model, the venous blood has the same magnetization as the tissue. This assumption is not completely physiologically reasonable, as some

water molecules pass directly through the microvasculature without ever exchanging [Ginsberg et al., 1985]. With a finite permeability, the outflowing magnetization is a combination of arterial blood water and tissue water.

Two compartment model

The assumption of infinite permeability of the capillary wall is particularly not fulfilled in the brain, where the blood-brain barrier facilitates water flow across capillary membranes. The finite permeability of the capillary wall is considered in the two compartment model developed by Parkes and Tofts [Parkes and Tofts, 2002] (see Fig. 5.1B). In this model blood water and extravascular tissue are considered with their corresponding volumes and relaxation times, separated by semipermeable endothelium. It was originally designed to quantitatively describe the ASL signal. This two compartment model was modified by Wu et al. to a general form of inversion recovery sequences, which can be used to describe both PASL and VASO [Wu et al., 2010] signal contrast. The magnetization of both compartments is given in Eq. 5.3.

$$\begin{aligned}
\tfrac{dM_{z,b}(t)}{dt} &= \underbrace{\frac{M_{0,b} - M_{z,b}(t)}{T_{1,b}}}_{\text{Bloch equation}} + \underbrace{\frac{CBF}{CBV}\left[M_{z,a}(t) - M_{z,v}(t)\right]}_{\text{inflow and outflow}} \\
&\quad + \underbrace{\frac{PS}{CBV}\left[M_{z,GM}(t) - M_{z,b}(t)\right]}_{\text{permeability}} \\
\tfrac{dM_{z,GM}(t)}{dt} &= \underbrace{\frac{M_{0,GM} - M_{z,GM}(t)}{T_{1,GM}}}_{\text{Bloch equation}} + \underbrace{\frac{PS}{V_{GM}}\left[M_{z,b}(t) - M_{z,GM}(t)\right]}_{\text{permeability}} \\
\tfrac{dM_{z,a}(t)}{dt} &= \underbrace{\frac{M_{0,a} - M_{z,a}(t)}{T_{1,b}}}_{\text{Bloch equation}}
\end{aligned} \tag{5.3}$$

Where $M_{z,b}(t)$ is the magnetization of capillary blood; $M_{z,GM}(t)$ is the magnetization of extravascular tissue; $M_{z,a}(t)$ is the magnetization of arterial blood flowing into the voxel. $T_{1,b}$ and $T_{1,GM}$ are intrinsic longitudinal relaxation times of blood and extravascular tissue. CBV and V_{GM} denote the blood volume and tissue volume in units of ml per ml of the voxel.

Limitations of the two compartment model

- In the two compartment model, it is inherently assumed that all intravascular blood magnetization is well mixed. Thus it is assumed that blood magnetization that has just entered the voxel is identical to the magnetization of venous blood. Since the inflowing, refilling, and outflow of blood occurs in a similar time scale as longitudinal relaxation, blood magnetization in arterial and venous compartments might have different relaxation history of their z-magnetizations. In order to estimate permeability and flow effects in VASO, the precise relaxation history of an individual 'drop' of blood water must be considered during its stay in the voxel. This relaxation history cannot be estimated by considering one well mixed intravascular compartment only.

- All blood in the voxel is assumed to be capillary blood. This might be not completely physiologically valid. Different vascular compartments within one voxel can have different contributions to permeability, inflow, of volume changes. For example, the arterioles are believed to change their diameter more than any other compartment [Hillman et al., 2007]. However, they do not significantly contribute to the exchange between intravascular and extravascular space. This means that the bulk of volume change that occurs in the arteriolar compartment is independent of permeability of the capillaries. The largest effect of capillary permeability on VASO signal change is expected to be located in the downstream capillary and venous compartments where blood is not completely nulled. Such dynamics cannot be captured in a two compartment model.

5.1.4 101 compartment model

Here, a new model is developed that is based on the two compartment model described in [Wu et al., 2010]. In this new model, the intravascular component is subdivided into 100 sub-compartments (additional to the extravascular compartment) in order to account for the issues mentioned above. The number 100 was chosen here as a compromise to model a smooth blood transition through the vascular tree [Xu et al., 2013] with minimum computational time necessary.

Fig. 5.2 depicts a schematic illustration of the longitudinal array of the subcompartments in the proposed model. There is only one extravascular compartment. The 100 intravascular compartments are assigned to be arterial, capillary and venous, according to the corresponding blood volume distribution at rest (see Tab. 5.2). The first 20 compartments are arterial vessels with 60% volume change during activation and no exchange between intravascular and extravascular space. The compartments 21 - 60 are capillary vessels with a blood volume change of 10% and permeable walls that enable water exchange between extravascular and intravascular space. The compartments 61 - 100 represent venous vessels with blood volume change of 10% and without water exchange with the extravascular compartment. The equations of motion of the magnetization in this model are given in Eq. 5.4.

$$\tfrac{dM^n_{z,b,i}(t)}{dt} = \underbrace{\frac{M_{0,b} - M^n_{z,b,i}(t)}{T^b_1}}_{\text{Bloch equation}} + \underbrace{\frac{CBF_i}{CBV^n_i}\left[M^{n-1}_{z,b,i}(t) - M^n_{z,b,i}(t)\right]}_{\text{inflow and outflow}} + \tag{5.4}$$

$$\underbrace{+\,\Theta(n)\frac{PS}{CBV^n_i}\left[M_{z,GM,i}(t) - M^n_{z,b,i}(t)\right]}_{\text{permeability}}$$

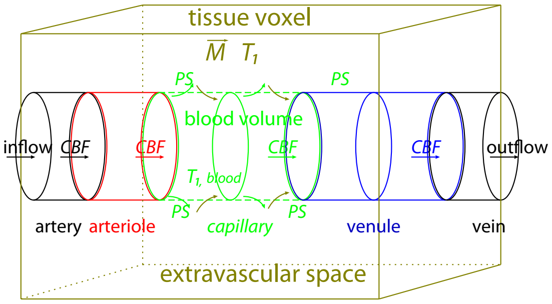

Figure 5.2: Schematic depiction of the multi compartment model: Blood flows from left to right. The black parts of the vasculature represent macrovessels outside of the imaging region. The depicted voxel is designed to contain all microvascular compartments of the vascular tree. Every colored cylinder depicted here represents 20 subcompartments.

$$\frac{dM_{z,GM,i}(t)}{dt} = \underbrace{\frac{M_{0,GM} - M_{z,GM,i}(t)}{T_{1,GM}}}_{\text{Bloch equation}} + \underbrace{\frac{PS}{V_{GM,i}}\left[\sum_{n=1}^{100} M^{n}_{z,b,i}(t) - M_{z,GM,i}(t)\right]}_{\text{permeability}}$$

$$\frac{dM^{n=0}_{z,b}(t)}{dt} = \underbrace{\frac{M^{n=0}_{0,b} - M^{n=0}_{z,b}(t)}{T_{1,b}}}_{\text{Bloch equation}} + \underbrace{H(t-\delta t)\frac{M^{n=0}_{0,b}}{dt}}_{\text{inflow of fresh blood}}$$

Here n denotes the compartment, and $i \in \{act, rest\}$ denotes the brain state. All volume indications are meant to reflect the relative water volume within a certain compartment. This means that the different proton density in water and in tissue is already considered. The Box-function $\Theta(n)$ distinguishes the capillary compartments from all the other compartments.

$$\Theta(n) = \begin{cases} 1 & \text{if } 20 < n \leq 60, \\ 0 & \text{else} \end{cases} \tag{5.5}$$

The permeability surface area product PS is normalized to the number of capillary compartments. All capillary compartments combined have the desired value of PS = 144 ml/100ml/min [Herscovitch et al., 1987]. The Heavyside-function $H(t - \delta t)$ denotes the start of inflow of fresh (uninverted) blood.

$$H(t-\delta t) = \begin{cases} 0 & \text{if } t - \delta t_i < 0, \\ 1 & \text{else} \end{cases} \tag{5.6}$$

The arterial arrival time δt denotes the time blood needs to flow from the lower border of the inversion slab into the imaging region.

Transit time heterogeneity

In the described model, only one vessel is considered. In order to account for heterogeneity of blood velocity through the different vessels, transit time heterogeneity must be considered as well [Jespersen and Østergaard, 2012]. Transit time heterogeneity can be introduced into the model by a asymmetric convolution of the blood magnetization across compartments with the convolution function $e^{-\frac{t}{TTH}}$, where the value of transit time heterogeneity (TTH) can taken from Tab. 5.3.

Resulting VASO signal change

The VASO signal can be considered as the sum the magnetizations across all blood and tissue compartments at the blood-nulling time TI weighted by their respective relative volumes:

$$S_i(t) \propto \sum_{n=0}^{100} M_{z,b}^{n}(TI)CBV_i^n + M_{z,GM}(TI)V_{GM,i} \text{ with } i \in \{act, rest\}, \tag{5.7}$$

where the z-magnetization in intravascular and extravascular compartments can be taken from Eq. 5.4. Activity induced VASO signal change is consequently:

$$\frac{\Delta S(TI)}{S_{rest}(TI)} = \frac{S_{act}(TI)-S_{rest}(TI)}{S_{rest}(TI)} = \tag{5.8}$$
$$\frac{\sum_{n=0}^{100} M_{z,b,act}^{n}(TI)CBV_{act}^{n}+M_{z,GM,act}(TI)V_{GM,act}}{\sum_{n=0}^{100} M_{z,b,rest}^{n}(TI)CBV_{rest}^{n}+M_{z,GM,rest}(TI)V_{GM,rest}}$$
$$-\frac{\sum_{n=0}^{100} M_{z,b,rest}^{n}(TI)CBV_{rest}^{n}+M_{z,GM,rest}(TI)V_{GM,rest}}{\sum_{n=0}^{100} M_{z,b,rest}^{n}(TI)CBV_{rest}^{n}+M_{z,GM,rest}(TI)V_{GM,rest}}.$$

5.1.5 Methods

Simulation parameters

The equations of the 101 compartment model (Eq. 5.4) were solved numerically in C++. The temporal resolution and simulation step size was 1 ms. Since the goal of this work was to evaluate CBF, and capillary permeability effects on VASO signal, wide ranges of CBF_{rest} (0 - 180 ml/100ml/min), ΔCBF (0 - 100%), and PS (0 - 200 ml/100ml/min) were utilized to evaluate these effects representing different physiological conditions. In order to evaluate these effects with respect to acquisition parameters used, a wide range of experimental parameters of TR (3 - 12 s), TI (0 - 1.5 s), and arterial arrival time δt (1.1 - 2.1 s) was simulated and compared with experimental results.

Experimental parameters

In order to investigate and confirm simulated model results with experimental data, SS-SI VASO data were acquired in vivo for a wide range of TR, TI, and inversion slab thickness.

Inflow effects of fresh (not inverted) blood were experimentally investigated by artificially altering the arterial arrival time. This could be achieved by successively reducing the inversion slab thickness in the steps of 15 cm, 10 cm, 7.1 cm, 5.6 cm, and 4.5 cm. Effects of inversion time (directly equivalent to inversion efficiency) was investigated in the steps of $TI = 700$ ms, $TI = 900$ ms, and $TI = 1100$ ms corresponding to $\zeta = 0.38$, $\zeta = 0.51$, and $\zeta = 0.65$ ($\zeta = e^{\frac{TI}{T_{1,b}}} - 1$). Effects of TR were investigated in the steps of $TR = 3$ s, $TR = 4$ s, $TR = 5$ s, and $TR = 6$ s. These TR values correspond to pair-wise acquisition of VASO and BOLD images. All other acquisition parameters stayed constant and were identical to the study described in section 3.1.3. In short: SS-SI VASO at 7 T, five axial slices with GE EPI, $TE = 19$ ms, nominal voxel size of 1.5 x 1.5 x 1.5 mm^3. MAFI B_1 maps [Boulant et al., 2009] were acquired to estimate the spatial range of proper inversion performance within the desired inversion slab thickness.

In order to avoid biases of tiredness or attention of the participants during the 90 min experiments, the order of experiments was permuted for every participant. Three volunteers participated in this study (1 female, 27 to 30 years old). Every volunteer was invited three times to participate in total of 12 experiments. All experiments where approved by local ethics committee of the University of Leipzig and all participants gave written informed consent for participation in the study.

All depicted data refer to activity in visual cortex during a 6 min moving star field paradigm (see section 3.1.3). All signal changes were considered in the same ROI defined as showing significant activity with acquisition parameters of $TI/TR = 1.1/3.0$ s and inversion slab thickness of approximately 10 cm.

5.1.6 Results

Understanding the mechanics of the 101 compartment model

The 101 compartment model contains several physical and physiological effects, such as inflow and refilling, relaxation, permeability induced tissue and blood water exchange. The interaction of all those effects makes it difficult to obtain an intuitive understanding of the results. In order to make it easier to understand, the individual features of the model are discussed step-by-step before combining them all together in the sections below.

In order to see how the model describes flow and permeability effects, they are firstly considered without relaxation. The upper section in Fig. 5.3 depicts the inflow of a bolus of blood without permeability or relaxation. It can be seen how blood magnetization flows from left to right through the vascular compartments. The speed of the flow is completely defined by the relationship between CBF and CBV. The transit time through the total vasculature is $\tau = \frac{CBV}{CBF} \approx 2.6$ s with the literature values used. It can be seen how the sharpness of the bolus onset blurs while it perfuses the vasculature. This is due the the incorporated transit time heterogeneity.

The lower section of Fig. 5.3 represents the same simulation, but with the capillaries having a finite permeability. It can be seen that for $PS \approx 144$ ml/100ml/min, approximately 20% of the bolus water remains in the vasculature and flows from arterial compartments to venous compartments without exchanging into extravascular space. In other words,

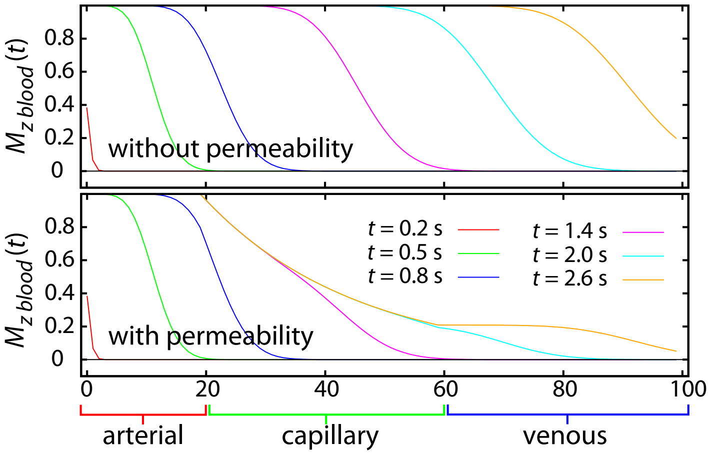

Figure 5.3: Distribution of inflowing blood magnetization: In the upper subfigure, permeability is set to $PS = 0$, to evaluate the blood propagation and transit time heterogeneity. It can be seen how the vasculature is refilled from left to right. Due to the transit time heterogeneity, inflowing blood has a diffuse border zone. In the lower subfigure, the capillary permeability is considered to be $PS = 144$ ml/100ml/min.

80% of the blood water magnetization is exchanged with extravascular water magnetization in the capillary compartments, in agreement with the literature [Ginsberg et al., 1985].

Application of the 101 compartment model to estimate VASO signal change

In order to individually understand and discuss the effects of vasculature refilling, permeability, relaxation, and CBF dependencies, the VASO signal change (Eq. 5.8) is considered for a set of multiple physiological conditions. Fig. 5.4 depicts the corresponding VASO signal changes.
By means of Fig. 5.4 many effect of permeability, flow and flow change can be understood and discussed.

- The red curve in Fig. 5.4 depicts the ideal VASO signal change, which it is dependent on CBV change only. Since arterial CBV change is assumed to contribute most to the total CBV change, the signal change is very large there.
- The green line in Fig. 5.4 depicts the VASO signal change for the case that there is only a CBV change and a constant CBF, without perfusion. In this case, VASO signal change in downstream venous compartments can slightly underestimate CBV change. This effect can be considered as a result of blood magnetization relaxation history. SS-SI VASO is based on the assumption that all the blood has experienced only one inversion pulse. If the refilling condition is not perfectly fulfilled, there is still some not nulled blood in the venous vessels. This case results in

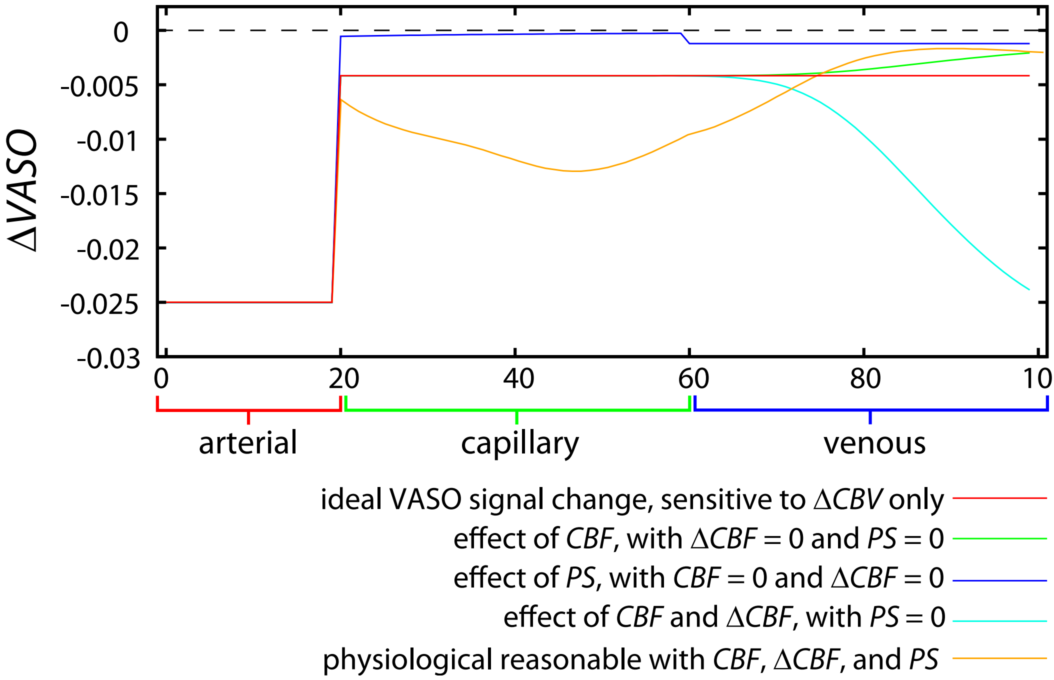

Figure 5.4: VASO signal change and its dependence on CBF, ΔCBF and permeability: The arterial compartments have the largest relative CBV change. Hence, the compartments 0 - 19 show the strongest VASO signal change. Since arterial vessel walls are assumed to be impermeable, there are no contaminating effects visible in those compartments. Capillary and venous compartments have limited contribution to overall VASO signal change. Though, permeability and CBF have a large affect on the post arterial compartments, with respect to their relative VASO signal contribution. 'Ideal VASO' signal change refers to the optimal case, when all the blood in all vascular compartments is completely nulled and no intravascular magnetization was permeated into extravascular space during the relaxation. For a set of reasonable physiological parameters (orange line), VASO signal change in post arterial compartments is overestimated compared to ideal VASO signal change. Individual effects of CBF_{rest}, ΔCBF, and PS in the individual lines are discussed in the main text.

VASO signal underestimation of $\approx 0.02\%$ (3.6% relative to the ideal VASO signal change).

- The blue line in Fig. 5.4 depicts the VASO signal change for the case that there is no flow, but a finite permeability. This means that all of the blood, which is in one compartment, stays in this compartment during TI, associated with sharp edges between the arteriolar, capillary and venous compartments. The arterial compartments are nulled at TI and the VASO signal change reflects the true blood volume change. Since the refilling condition cannot be fulfilled without flow, the magnetization in the venous compartments is insufficiently nulled. Additionally to this unmet refilling condition in the venous compartments, the capillary compartments experience an additional effect of permeability. Intravascular blood z-magnetization in capillaries approached the value of tissue z-magnetization. Therefore, almost no VASO signal change can be seen for the capillary compartments. This case underestimates total CBV change by $\approx 0.26\%$ (34% relative to the ideal VASO signal change).
- The pink line in Fig. 5.4 depicts the case, when there is flow, flow change but no permeability. The CBV change is properly quantified in the arteriolar and capillary compartments. The detected CBV change in the venous compartments is significantly overestimated. This can be understood by considering it as an unfulfilled outflow condition. In the case of the green line, the unmet outflow condition resulted in incomplete blood nulling. Here, an additional effects of ΔCBV comes into play. The refilling condition is better fulfilled during activity, when CBF is higher compared to rest. This results in not nulled venous blood during rest and nulled venous blood during activity. In other words, increased flow washes out the not nulled venous blood resulting in a CBF dependent signal decrease. The lower signal with increased washout during activity results in an CBV overestimation of $\approx 0.28\%$ (36% relative to the ideal VASO signal change).
- The orange line in Fig. 5.4 depicts the physiologically most reasonable case. Here, flow, flow change and permeability are all considered simultaneously. Aside from outflow effects, there is an additional effect that needs to be taken into account considering both, flow change and permeability. Permeability is independent of activation but flow is believed to increase substationally during activation. This means that the residence time of blood in permeable capillary compartments is smaller for activation compared to rest. Hence, less tissue z-magnetization is mixed with a unit capillary blood volume during activation compared to rest. In other words, during rest $\approx 80\%$ of the blood in the downstream compartments arises from extravascular tissue space. But, during activity, this number decreases. This means that during activation, capillary blood magnetization is less contaminated from tissue water magnetization compared to rest. The smaller z-magnetization of capillary and venous blood during activity results in an overall CBV overestimation of $\approx 0.13\%$ (16.4% relative to the ideal VASO signal change).

It can be concluded that VASO signal change can be severely contaminated by effects of flow, permeability and relaxation history. These effects can partly cancel each other out and they are differently pronounced across vascular compartments. The resulting mean signal change is highly sensitive to the set of physiological parameters assumed.

It must be noted that no inflow of fresh blood can be seen here. This is due to the fact that arterial arrival time is longer than the inversion time ($\delta t > TI$) with the physiological and measurement parameters assumed (Tab. 5.3). Inflow effects are discussed in more detail later in this section.

Flow weighting in VASO as a function of baseline perfusion, flow changes, and permeability

As shown above, physiological parameters such as CBF_{rest}, ΔCBF, and PS and their interplay can influence the flow weighting in VASO (Fig. 5.4). Their precise values, however, are believed to be highly variable. For example, they may be different across brain areas, species, anesthesia, and pathology [Calamante et al., 1999][Buxton et al., 2004]. Hence, flow weighting in VASO is investigated for a wide range of physiological parameters assumed: CBF_{rest} (0 - 190 ml/100ml/min), ΔCBF (0 - 90%), and PS (0 - 200 ml/100ml/min). The corresponding results of overall VASO signal change are shown in Fig. 5.5. For moderate CBF_{rest} values in the range of 50 - 70 ml/100ml/min, VASO signal change it very close to the value expecting from the ideal value, which is reflecting VASO signal change without any flow contaminations (Fig. 5.5A). For higher CBF_{rest} values in the range of 90 - 110 ml/100ml/min, VASO signal change is overestimated by approximately 20% of the total VASO signal change. For even higher CBF_{rest} values in the range of CBF_{rest} 150 - 200 ml/100ml/min, the VASO signal change overestimation is reduced again. For a value of $CBF_{rest} \approx 190$ ml/100ml/min, which is often found in rats [Calamante et al., 1999], VASO signal change is overestimated by approximately 10% (relative to the ideal VASO signal change).

Contaminations in VASO are also dependent on the ΔCBF parameter (Fig. 5.5B). Especially, for high ΔCBF values in the range of 80 - 100%, VASO signal change can be overestimated by up to 38% (relative to the ideal VASO signal change). For very low values of ΔCBF below 37%, this effects inverts and $\Delta VASO$ can be even underestimated.

Considering VASO signal change for different permeability values, a direct VASO signal dependence can be seen as well (Fig. 5.5C). For higher values of PS, VASO signal change is less overestimated.

Influence of repetition time, inversion time, and inversion slab thickness: How to minimize effects of inflow and permeability in an SS-SI VASO experiment?

In SS-SI VASO, there are three free experimental parameters that can be adjusted to manipulate the contrast mechanism: TR, TI, and the inversion slab thickness. These parameters can theoretically adjusted in such a way that contamination in SS-SI VASO signal change is minimized.

Since all the blood in the imaging slice is expected to be once inverted, TR can be adjusted independently of the blood-nulling time important for VASO. Note that this is not the case in the original VASO approach. When the experimental parameter TR

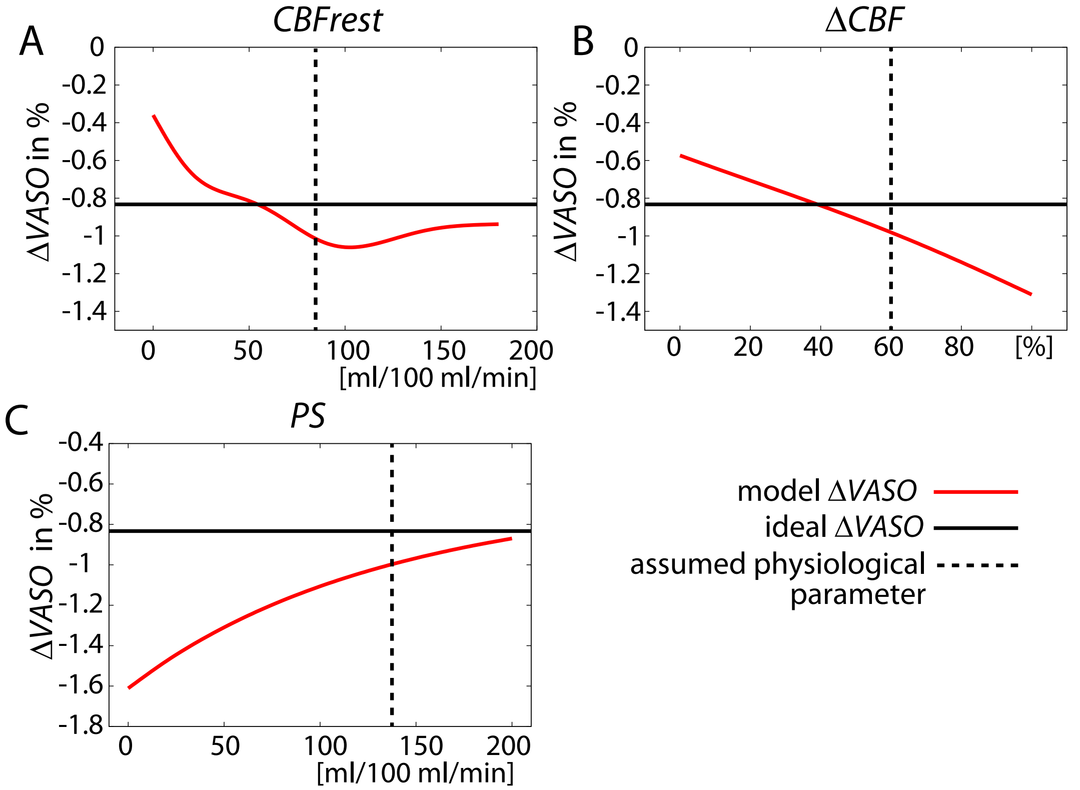

Figure 5.5: The effect of VASO signal change on the physiological parameters CBF_{rest}, ΔCBF, and PS: Within the wide range of parameters assumed, the VASO signal change can be highly affected. For the physiological values assumed here (dashed lines), $\Delta VASO$ signal is overestimated by approximately 15%, relative to the ideal VASO signal change. For example, such an overestimation would result in a measured value of $\Delta CBV = 17\%$ instead of the true value of $\Delta CBV = 15\%$.

is adapted, relaxation history effects of not nulled blood can be altered and minimized. Figure 5.6A depicts SS-SI VASO signal change distribution throughout the vascular compartments for a range of TR (3 s - 8 s). Independent of TR, VASO signal change is always overestimated in the capillary compartments. This over estimation can be compensated with a $\Delta VASO$ signal underestimation in the venous compartments for short TR (3 s - 4 s) and very long TR ($>$ 6 s).

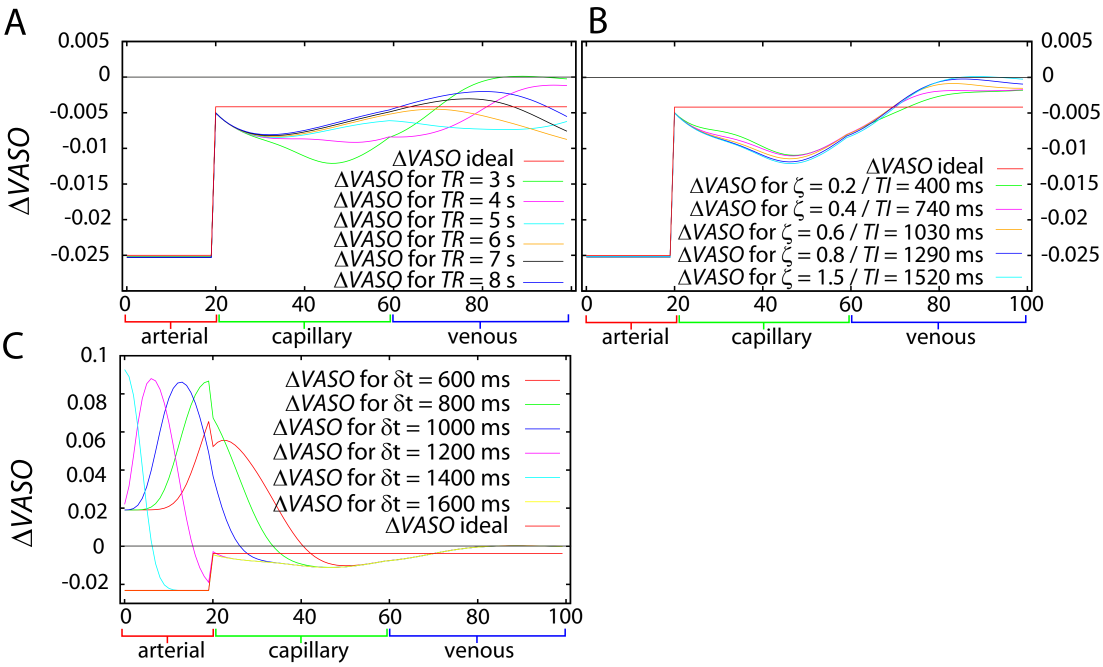

Figure 5.6: Vascular compartment-depend VASO signal change for a wide range of experimental parameters: A) depicts VASO signal change across vascular compartments for TR in the range of 3 - 8 s. B) depicts VASO signal change across vascular compartments for TI in the range of 400 - 1520 ms. C) depicts VASO signal change across vascular compartments for δt in the range of 600 - 1600 ms.

The experimental parameter TI can be manipulated by adapting the partial inversion efficiency. When the experimental parameter TI is adapted, the time that blood is exposed to exchange between intravascular and extravascular space can be experimentally manipulated. If TI is smaller than the venous outflow time, steady-state blood flows out of the voxel. If TI is larger than the venous outflow time, partly once inverted blood flows out of the voxel. Hence, by modulating TI, permeability and flow effects can be experimentally manipulated.

Figure 5.6B depicts VASO signal change distribution throughout the vascular compartments for a set of inversion efficiencies or TI, respectively. The parameter ζ describes the negative z-magnetization after inversion in units of maximal z-magnetization. TI is directly connected to the relative z-magnetization after inversion with the nulling condition: $TI = T_{1,b}\ ln(1+\zeta)$. It can be seen in Fig. 5.6B that there are only minor dependencies of ζ and TI on the resulting VASO signal change.

Inflow of fresh, uninverted blood can be experimentally investigated by manipulation of the experimental parameter δt. When the inversion slab is very thick, it takes longer until fresh blood flows into the microvasculature of the imaging slice. By making the inversion slab very thin, the arterial arrival time can be reduced, such that fresh blood flows into the imaging slice during TI. Figure 5.6C depicts how inflow of fresh blood affects VASO signal changes. Inflow of fresh blood has a considerable effect on the VASO signal change in arterial compartments. Inflow of fresh blood results in increased blood z-magnetization directly proportional to CBF, comparable to the label condition of a PASL FAIR experiment. Since inflow induced VASO signal increase is in the order of 10% relative to the signal at rest ($\approx$ 1200 % relative to the ideal VASO signal change), it is obvious that tiny inflow effects can render CBV estimations impossible.

Best choice of experimental parameters

Results shown in Fig. 5.6 can be evaluated to find a set of sequence parameters with minimum contamination in VASO signal change. The results of Fig. 5.6 are evaluated with respect to the total VASO signal change and summarized in Fig. 5.7.

Investigating dependencies of TR, it can be seen in that VASO signal change overestimation is highest for $TR \approx 5$ s (Fig. 5.7A). This suggests that for best CBV quantifiability, TR values far away from this value should be chosen. If impractical long TRs (> 7 s) want to be avoided, it is suggested to use TR values as short as possible. Due to the interleaved acquisition of BOLD and VASO images in the SS-SI VASO approach, TR cannot be smaller than $2TI$. Hence, TR should be chosen in the range of $TR = 3$ s. Fig. 5.7B suggests that VASO signal change is only weakly dependent on TI. There is only a small reduction of VASO signal overestimation with increasing TI. Hence it is suggested to prefer long TI values, which corresponds to a high inversion efficiency (e.g. $\zeta = 1.$ and $TI = ln(2)\ T_{1,b} \approx 1500$ ms).

Luckily the combination of shortest possible TR and the longest possible TI is also the combination that provides highest possible GM signal (see Fig. 4.24 on page 127) and therefore highest SNR.

Figure 5.7C shows that inflow effects severely distort VASO signal change. These effects can be avoided, if δt is longer than TI. Hence, when a head coil is available for RF transmission only, the inversion slab thickness should be as large as possible.

Comparison of simulated VASO results with experimental data

For the sake of validation, the simulated results are compared with experimental data acquired in vivo. Figure 5.8 depicts the measured VASO signal changes as a function of TR, TI, and inversion slab thickness. A superposition of measured and simulated VASO signal time courses is given in the right column. Experimental results are in good agreement with simulated results. SS-SI VASO signal is almost independent of TR and

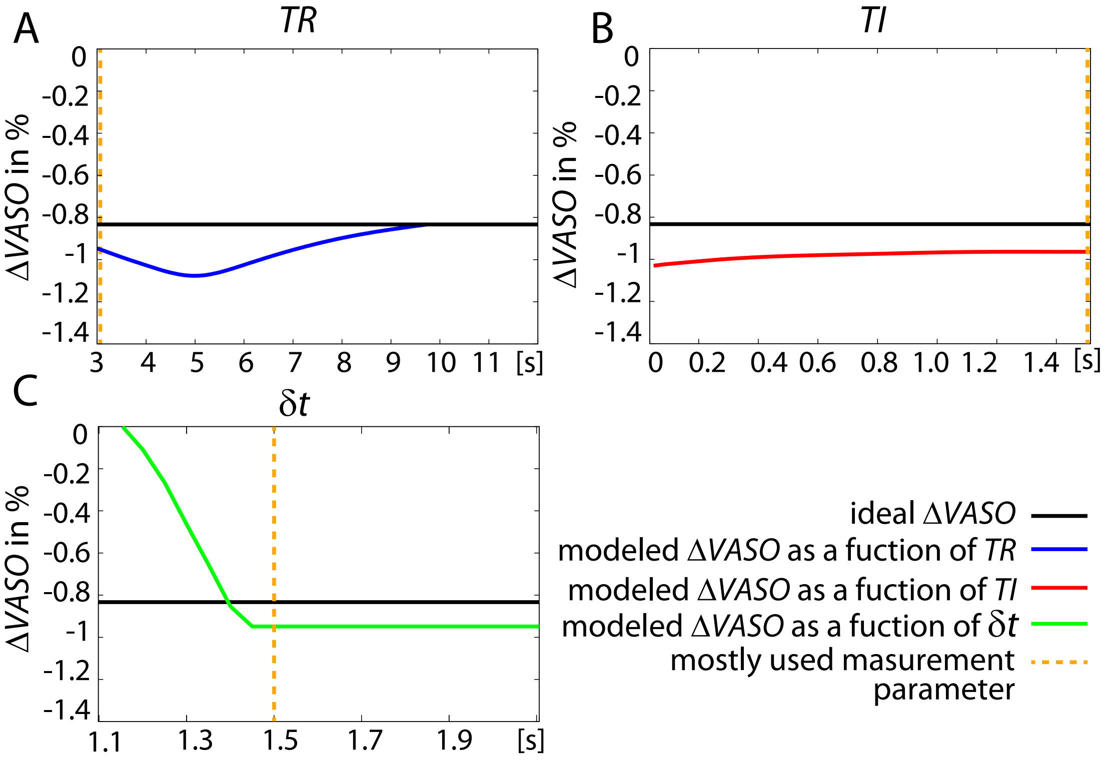

Figure 5.7: Overview of effects of experimental parameters TR, TI, and δt: The flow and permeability contamination in VASO depend on experimental sequence parameters. The depicted dependencies can be used to establish guidelines about a most advantageous set of experimental parameters. TR values in the range of 5 s should be avoided (A). Flow induced VASO signal overestimation is fairly independent of TI (B). There is only a minor trend that VASO signal changes of longer TI are closer to the optimal value compared to shorter TI, suggesting to use longer TIs. Inflow of fresh (uninverted) blood into the imaging slice has a large effect on the VASO signal change (C). This suggests that it is vital to chose an inversion slab thickness, such that the VASO image is acquired before fresh blood can flow into the imaging slice ($TI < \delta t$).

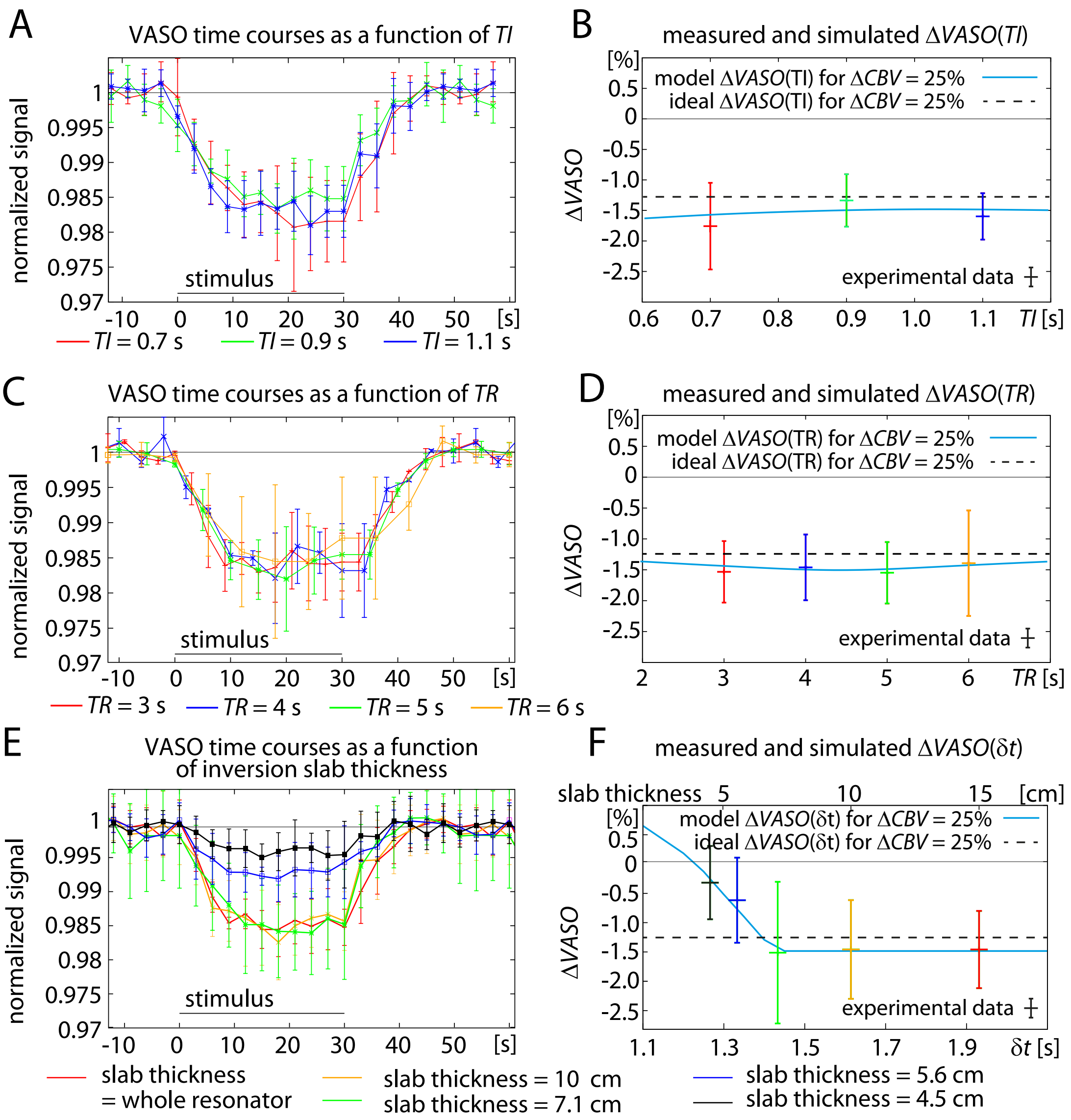

Figure 5.8: Comparison of simulated and experimentally measured VASO signal changes as a function of TI, TR, and δt: Subfigures in the left column depict the results of experimentally measured VASO signal as a function of TI (A), TR (C), and inversion slab thickness with the corresponding variations of δt (E). These raw VASO data are depicted to give an estimation of the noise and uncertainty on the resulting data points in the subfigures of the right column. Subfigures in the right column depict the corresponding mean values of $\Delta VASO$ on top of the simulated results. For best overlay of the experimental and simulated results, $\Delta CBV = 25\%$ was assumed here. The rest of the model parameters is taken from Tabs. 5.2 and 5.3. The experimental and simulated VASO results are in good agreement.

TI variations in both, the simulated and experimental results. The trends of a positive slope for increasing TI (Fig. 5.8B) and a 'U'-shape for increasing TR (Fig. 5.8D) are very faint and much smaller than the uncertainty of the experimental data. This is in contrast to significant inflow effects regarding the dependency of arterial arrival time (Fig. 5.8F). For both, simulated and experimental results, VASO signal is independent of δt above a certain threshold only. When δt is below that threshold, however, VASO signal is significantly reduced. Note that the experimental and the simulated data in Fig. 5.8F refer to different y-axes. Measured data are referred to inversion slab thicknesses, which is an indirect indicator for the arterial arrival time only.

Comparison with original VASO

The developed 101 compartment model can be easily adapted to consider the contrast mechanisms in original VASO or PASL. The only parameters that needs to be adapted are the blood-nulling time and the corresponding z-magnetization steady-state. For the sake of comparison of contaminations in SS-SI VASO, the 101 compartment model is applied to estimate such contaminations in original VASO. The results of these simulations are summarized in Fig. 5.9. Subfigure 5.9A shows for original VASO that the blood z-magnetization in the upstream capillary compartments is larger during rest than during activity. In downstream capillary compartments and in the venule compartments, however, the blood z-magnetization is smaller during rest than during activity. To understand this feature, it is helpful to consider the whole time period of exchange between intravascular and extravascular space. This time period starts at the previous excitation (90°-pulse). At this time, tissue and blood are saturated. Until the following inversion pulse (TR - TI), gray matter decays faster than blood and capillary exchange causes deposition of positive z-magnetization into the intravascular space. Due to higher CBF during activity and constant PS, the z-magnetization deposition per unit of blood is smaller (washout). And after inversion, the smaller z-magnetization during activity becomes a less negative. Therefore, the green line is above the red line in the venous compartments in Fig. 5.9A. Additionally to water exchange in the period between inversion and image acquisition, there is a second mechanism that has a compensating effect. In the time after inversion, tissue z-magnetization decays faster than blood z-magnetization and, again, deposits positive z-magnetization in the intravascular space. The net-magnetization at the blood-nulling time depends on the durations of the two periods. Most of the capillary blood at the blood-nulling time entered the capillary compartments after the inversion and hence, the second mechanism outweighs the first one. The blood in the venous compartment is dominated from the capillary permeability exposure before inversion. Therefore, in the venous compartment, the first mechanism outweighs the second one.

The interaction of the two competing effects can be experimentally manipulated by modulating the time distribution before and after inversion by means of adapting TI. Here, TI is modulated by adjusting TR. In original VASO both, blood and extravascular tissue are in steady-state. Hence, to fulfill the nulling condition, TR and TI are connected with Eq. 2.30. Figure 5.9B depicts the distribution of VASO signal change across the vascu-

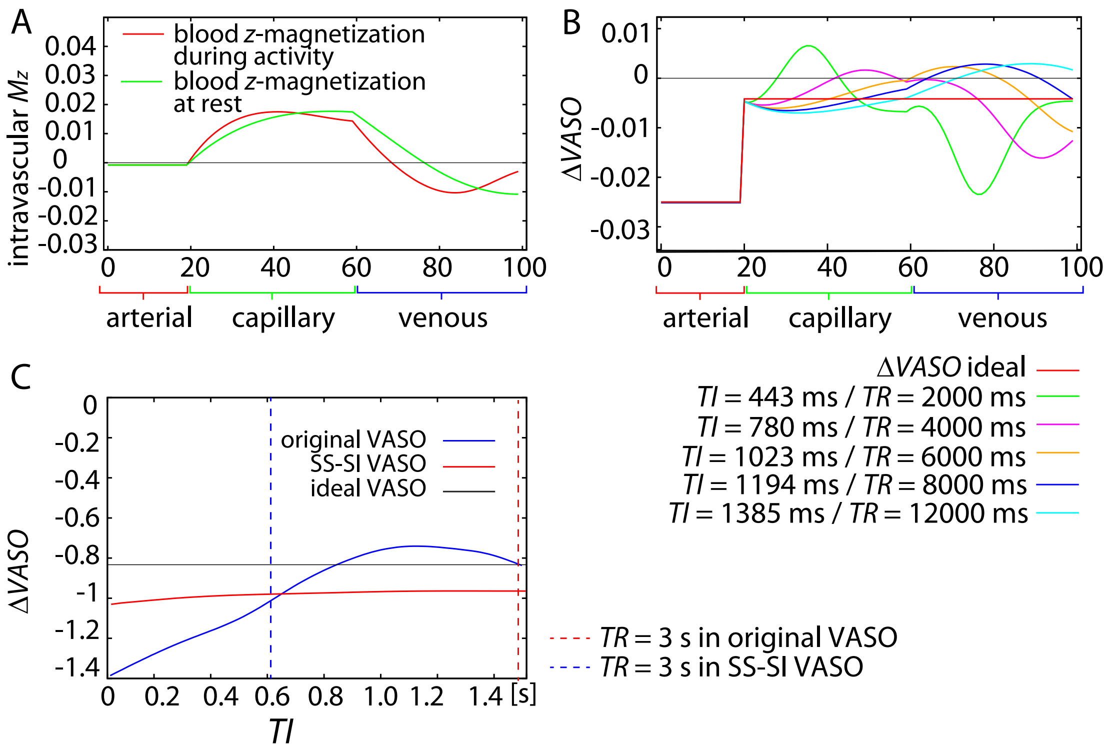

Figure 5.9: Effects of blood flow and capillary permeability in original VASO: A) depicts that intravascular magnetization is incompletely nulled in post arterial blood compartments. Dependent on the dwell time of magnetization in intravascular and extravascular space and its corresponding relaxation history, this effect is unevenly distributed across vascular compartments. B) depicts the resulting artifacts in VASO signal change for a wide range of TI (443 - 1385 ms) or TR (2 - 12 s) values. VASO overestimation in one compartment can be partly compensated with VASO underestimation in other compartments. C) depicts that flow contaminations in original VASO are highly dependent on the experimental parameters used. For the sake of comparison, the corresponding results of SS-SI VASO (from Fig. 5.7) are included into the figure. For most widely used TR of 3 s, flow effects result in the same VASO signal overestimation. The values of TR refer to pair-wise, interleaved acquisition of BOLD and VASO images.

lar compartments for various TI and TR, respectively. According to the magnetization depicted in Fig. 5.9A, VASO signal change is overestimated in the venous compartments and underestimated in the capillary compartments for reasonable values of TR and TI. Figure 5.9C depicts the overall VASO signal change for a wide range of TI values. The signal change of original VASO is similar to the ideal VASO signal change around $TI =$ 900 ms, consistent with earlier simulations of original VASO [Wu et al., 2010]. However, it must be stressed that this is not due to the fact that there are no contaminating flow or permeability effects. This is only due to compensation of venous CBV_v overestimation and capillary CBV_c underestimation. This means that at high resolutions when, pial veins are located in different voxels compared to microvasculature, the opposing effects are not canceled out.

The extent of flow and permeability contaminations in VASO is in the same order of magnitude for the original approach and for the SS-SI VASO approach. For reasonable temporal resolutions of $TR = 3$ s, the flow induced VASO signal overestimation is the same for both sequences (dotted lined in Fig. 5.9C).

5.1.7 Limitations of the 101 compartment model

Even though the 101 compartment model can describe a wide range of physical and physiological features, some higher order effects are not included into this model.

- It is assumed that all compartments including extravascular space are well mixed. This might not be entirely true. For example it might not be physiologically reasonable to describe the large extravascular space as one compartment only. Specifically, the intravascular water that perfuses into the extravascular space will be located close to the blood vessels for some time, before it distributes across the entire extravascular space. During that time, it has an enhanced probability to return back into the intravascular space. This effect would result in a smaller effective value of PS and it could be accounted for, by subdividing the extravascular compartment in radially distributed subcompartments [St. Lawrence et al., 2000].
- It is inherently assumed that CBF and PS are constant across all capillary compartments. This means that the blood velocity is the same across all capillaries compartments. More advanced hydrodynamic models, however, suggest that most of the blood flows out of the capillaries into extravascular space in the upstream capillary compartments and the inflow from extravascular space occurs in the downstream capillary compartments [Krieger et al., 2012]. This would be associated with a smaller blood velocity in the middle compartments. This effects could result in a slightly smaller effective CBF value compared to the ones assumed in this study.
- The exchange between intra- and extravascular space is considered to reflect the total blood (plasma and hematocrit). Since hematocrit cannot penetrate the capillary walls, this assumption is not entirely valid. However, because the water exchange between intracellular space and blood plasma (exchange rate $\kappa = 4.4 \pm 2.1$ ms [Gardener et al., 2010]) is much faster than the exchange between intravascular and extravascular space ($\kappa \approx 1.6$ s [Herscovitch et al., 1987]) and the relaxation

time ($T_1 \approx 2.1$ s Tab. 2.1), violations of the foregoing assumption are expected to be tolerable.

5.1.8 Summary and conclusion

A two compartment model that considers the permeability of the capillary wall [Wu et al., 2010] was adapted for quantitative estimations of flow and permeability artifacts in SS-SI VASO and original VASO. In comparison to previous simulation studies, the 101 compartment model of this study was extended with respect to two aspects. (A) The precise relaxation history of water magnetization is considered by introducing different longitudinal intravascular subcompartments. (B) It is considered that the blood volume change and the permeability is not equally distributed across arterioles, capillaries, and venules. For example, this can account for physiological features like the fact that arterioles contribute considerably to changes in CBV (in contrast to venules), but they are not permeable (in contrast to capillaries).

Permeability and flow weighting in VASO was investigated with respect to a wide range of physiological parameters CBF_{rest} (0 - 190 ml/100ml/min), ΔCBF (0 - 90%), and PS (0 - 200 ml/100ml/min). Comparisons of simulated model data with experimental in vivo results are in good agreement for a wide range of acquisition parameters of TR (3 - 12 s), TI (0.7 - 1.1 s) and inversion slab thickness (4.5 cm up to $\approx$ 15 cm).

The result of these investigations show that SS-SI VASO and original VASO can capture CBV change in arterial vessels properly without flow contaminations, when an appropriate inversion slab thickness is chosen. In post-arteriolar compartments, intravascular blood water magnetization is usually incompletely nulled across all physiological and experimental parameters assumed. During activity induced CBF increase, more of the not nulled blood magnetization is washed out, leading to reduced intravascular blood magnetization during activity and resulting in overestimation of the negative VASO contrast. Dependent on physiological and experimental parameters assumed, this overestimation is distributed differently across capillary and venous blood compartments.

For a reasonable set of physiological parameters, VASO signal is overestimated by approximately 0.15%. This corresponds to a relative overestimation of approximately 15% relative to the total VASO signal change. For example a true CBV change of ΔCBV = 25% would be over estimated to be ΔCBV = 28.75%. For widely used acquisition parameters (TR = 3 s and high inversion efficiency), permeability and flow contaminations are the similar for SS-SI VASO and original VASO. In SS-SI VASO, permeability and flow contaminations are minimized for short TR (e.g. 3 s), long TI (e.g. 1.5 s) and large inversion slab thickness of about 15 cm.

5.2 Necessity to image at the blood-nulling time

This section is about the limitations regarding the necessity to acquire VASO images at the blood-nulling time. In this section the error of CBV quantification is estimated for uncertainties in blood T_1 and the corresponding blood-nulling time. Finally, the potential extensibility of SS-SI VASO to a 3D readout scheme is briefly discussed. This section focuses on T_1 effects in VASO with respect to the experiments performed in this thesis. Therefore, all discussions and reported values refer to the field strength of 7 T.

5.2.1 VASO signal change with errors in longitudinal relaxation rate of blood

VASO is based on the idea that the entire intravascular signal is completely nulled in an inversion recovery sequence. The time of image acquisition is adjusted to coincide with the time, when the relaxing blood z-magnetization crosses zero. Knowing the longitudinal blood relaxation time T_1, the blood-nulling time can be directly calculated by means of Eq. 2.30.

Experimental measurements of blood T_1 at 7 T in individual volunteers is highly laborious [Rane and Gore, 2013][Francis et al., 2008][Grgac et al., 2012][Dobre et al., 2006], especially in vivo [Rooney et al., 2007][Zhang et al., 2013]. Therefore subject-wise determination of blood T_1 in a pre-scan like fashion was not performed in VASO studies in the literature so far. For estimation of the blood-nulling time in VASO, T_1 values are usually assumed on the basis group results from previous studies.

In this thesis, the blood-nulling time is chosen based on literature values of blood T_1 summarized in Tab. 2.1. Considering the distribution the various reported values, they scatter around the value of $T_1 = 2100$ ms with a standard deviation of ≈ 100 ms. Blood T_1 has been shown to be slightly dependent on oxygenation and hematocrit [Rane and Gore, 2013][Zhang et al., 2013][Grgac et al., 2012] and thus it might be slightly different in arteries and veins, or in men or women. These variations are also in the range of $\approx$ 100 ms [Rane and Gore, 2013][Grgac et al., 2012].

Here, the effect of such uncertainties in blood T_1 are investigated with respect to the not nulled blood signal and the corresponding error in VASO signal change.

The blood signal for any inversion time can be estimated with Eq. 2.29. Assuming T_1 = 2100 ms, Eq. 2.29 suggests that during 100 ms blood z-magnetization relaxes up to $\frac{M_z(TI)}{M_{0\ z}} = 2.5\%$ of its maximal magnetization. The corresponding error in VASO signal change can be calculated with Eq. 5.9.

$$\frac{\Delta VASO}{VASO_{rest}} = \frac{\left[(1-CBV_{rest})M_{z,GM}(TI)+CBV_{rest}M_{z,b}(TI)\right]-\left[(1-CBV_{act})M_{z,GM}(TI)+CBV_{act}M_{z,b}(TI)\right]}{(1-CBV_{rest})M_{z,GM}(TI)+CBV_{rest}M_{z,b}(TI)} \tag{5.9}$$

The corresponding blood T_1 uncertainty of 100 ms leads to an error in VASO signal change of 5.1%, relative to the total VASO signal change. This means that, for example, a CBV change of 25% would be overestimated to be 26.3% or underestimated to be 23.7%. Since the inter-subject variability of VASO signal change is in the range of 20%

- 30% of the VASO signal (see section 3.1), small uncertainties in the order of 5.1% resulting from uncertainties in blood T_1 are considered to be tolerable in this thesis.

Appropriate number of acquired slices

In the studies of this thesis, usually 1 - 5 slices are acquired with 2D EPI, and 1 - 3 slices are used in the evaluation. The optimal blood-nulling time TI was adjusted to the acquisition time of the middle slice. This means that the effective acquisition time of the adjacent slices differed from the optimal blood-nulling time. Depending on the acquisition duration per slice, the deviation from the blood-nulling can be negligible.

In this thesis the number of the used slices is chosen in such a way that the deviation of the slice acquisition time is smaller than the uncertainty of the literature value of blood T_1.

All studies of this thesis and the corresponding uncertainties in TI between slices are summarized in Tab. 5.4. In all studies of this thesis, the deviation of the acquisition time from the optimal blood-nulling time of all evaluated slices is below 100 ms.

#slices	time of outer most slice to optimal blood-nulling time	section in this thesis	comment
3	59 ms	3.1	1.5 mm resolution, no GRAPPA
1	0 ms	3.1	3 T, 3 mm resolution, no GRAPPA
3	76 ms	3.1	1.5 mm resolution, for 3 echoes
1	0 ms	3.2	0.5 mm resolution, in rats
1	0 ms	3.2	0.8 mm resolution, in human S1
3	76 ms	4.1	1.5 mm resolution, for 3 echoes
1	0 ms	4.1	0.7 mm resolution, in monkeys
1	0 ms	4.2	0.8 mm resolution, 64 matrix
1	0 ms	4.2	0.5 mm resolution, in rats
1	0 ms	4.2	$<$ 0.5 mm resolution, in monkeys
3	59 ms	4.3	1.5 mm resolution, no GRAPPA
3	59 ms	5.1	1.5 mm resolution, no GRAPPA
3	76 ms	5.3	1.5 mm resolution, for 3 echoes
3	76 ms	5.4	1.5 mm resolution, for 3 echoes, looking at negative BOLD responses
3	59 ms	5.4	1.5 mm resolution, no GRAPPA, looking at hypercapnia

Table 5.4: Overview of uncertainties in blood-nulling time of all experiments in this thesis.

5.2.2 Extensibility to a 3D method

VASO has been extended to a multi-slice method with several advanced readout strategies [Donahue et al., 2009a][Hua et al., 2012][Poser and Norris, 2007][Poser and Norris, 2009][Poser et al., 2011][Scouten and Constable, 2007][Cretti et al., 2013][Miao et al., 2014], or by means of advanced modeling [Ciris et al., 2013]. In SS-SI VASO, these methods can be used to increase the number of imaging slices, analogously. The additional requirements of the SS-SI VASO regarding the vasculature dynamics must be considered in adjusting the sequence parameters when it is applied with a 3D-acquisition. For example, if more imaging slices have to be acquired, TR must increase to give blood sufficient time to refill the vasculature between consecutive image acquisitions, and of course both the imaging slab thickness and the inversion slab thickness must be increased. The fundamental limitations of the imaging slab thickness in slab-selective VASO are comparable to limitations of PASL methods [Calamante et al., 1999], which are also given by refilling behavior of the vasculature within a slab.

The brain coverage of VASO can also be increased by combining the VASO preparation with a simultaneous multi-slice (SMS) acquisition [Moeller et al., 2010]. Fig. 5.10 depicts an example of using this approach to extend SS-SI VASO to cover multiple brain areas simultaneously.

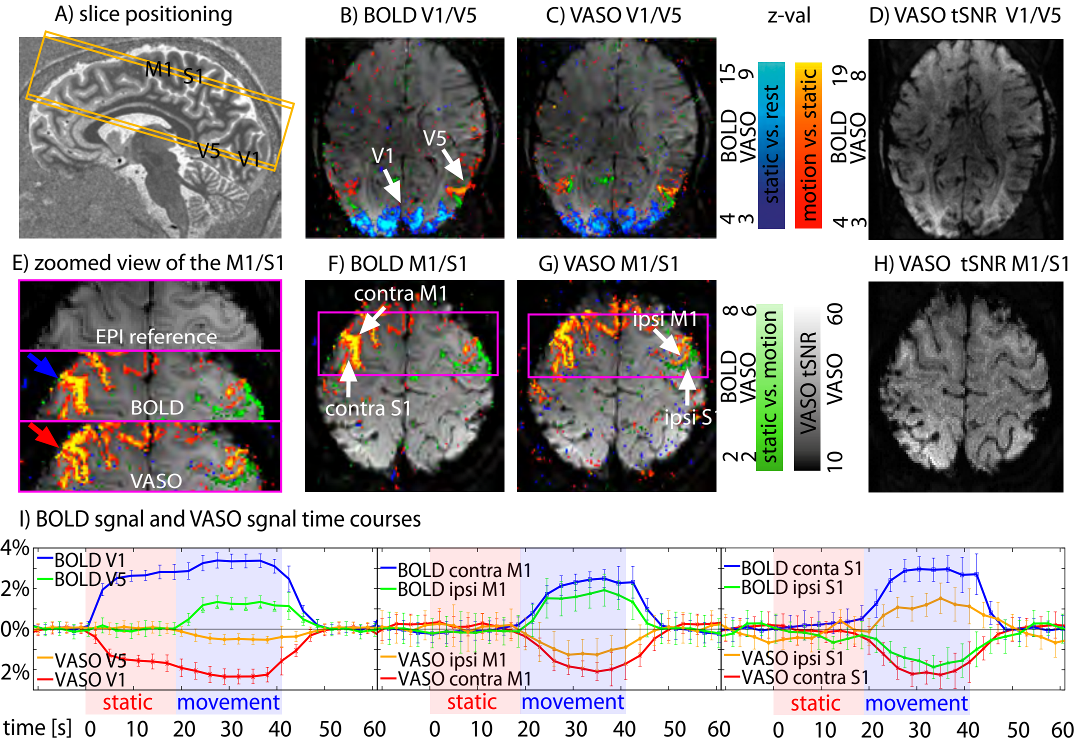

Figure 5.10: Example of simultaneous multi-slice VASO application for enlarged brain coverage: A) depicts the positioning of the two simultaneously acquires slice packages covering the visuo-motor system of brain areas V1, V5, M1, and S1. B), C), F), and G) depict the statistical activation maps. Blue colors refer to the response to static light changes. Red-yellow colors refer to increased activity during motion and finger movement. Green colors refer to negative response during motion/movement. E) depicts a zoomed view of the M1/S1 region indicating higher local specificity of VASO to the two GM banks compared to the BOLD signal. D) and H) depict the tSNR maps of the blood-nulled VASO time series. The mean tSNR in GM is 28 ± 9. Imaging parameters are: $TR/TI1/TI2/TE = 3000/1000/2500/24$ ms, SMS factor 2; CAIPI factor 2 [Setsompop et al., 2012], FLEET-GRAPPA 3 [Polimeni et al., 2013], nominal voxel size 0.9 x 0.9 x 1.1 mm^3 ([Huber et al., 2015b], *submitted*).

5.3 Limitations in BOLD correction based on dynamic division

In this section, the BOLD correction scheme based on dynamic division is regarded theoretically and experimentally with respect to potential contaminations of uncorrected intravascular BOLD effects. If the echo time is larger than few milliseconds, the T_1 driven VASO signal decrease during activation can be contaminated by a T_2^* driven BOLD signal increase during activation. In previous VASO studies at 1.5 T and 3 T, confounding BOLD signal contributions can be avoided by using a very short TE [Lu et al., 2003] or estimating the signal at $TE = 0$, while acquiring images at multiple echo times [Lu and van Zijl, 2005]. In this thesis, BOLD contaminations are corrected for by interleaved data acquisition with and without blood-nulling and with subsequent pairwise dynamic division of the two images. As described in section 3.1.2, this BOLD correction scheme is based on the assumption that the extravascular BOLD effect is much stronger than the intravascular BOLD effect at 7 T. When considering higher order effects, however, such approximations might not be perfectly valid and small intravascular BOLD effects could be overcorrected for.

In this section, these higher order effects are considered and corresponding errors in VASO signal change are quantified. In order to do so, a complete BOLD model needs to be derived containing intravascular and extravascular components in images with and without blood nulling. With this model, residual BOLD contamination in VASO can then be assessed. Additionally to these theoretical considerations, experimental multi-echo VASO data from previous sections of this thesis are discussed with respect to residual BOLD weighting in VASO.

5.3.1 Theoretical description of the BOLD correction scheme based on dynamic division

The gradient-echo VASO signal of a voxel that is only filled with GM and blood (see section 5.4 for deviations of this assumption) can be derived from the original VASO paper [Lu et al., 2003] for the nulling condition and for TI when blood is not nulled:

$$\begin{aligned} S \propto CBV\ \rho_b\ \frac{M_{z,b}(TI)}{M_0} e^{-\frac{TE}{T_{2,b}^*}} + V_{GM}\ \rho_{GM}\ \frac{M_{z,GM}(TI)}{M_0} e^{-\frac{TE}{T_{2,GM}^*}} &= \\ = \left[CBV\ \rho_b\ \frac{M_{z,b}(TI)}{M_0}\ C + V_{GM}\ \rho_{GM}\ \frac{M_{z,GM}(TI)}{M_0} \right]\ e^{-\frac{TE}{T_{2,GM}^*}} & \qquad (5.10) \\ \text{with } C = e^{TE\left(\frac{1}{T_{2,GM}^*} - \frac{1}{T_{2,b}^*}\right)}, & \end{aligned}$$

where all terms in Eq. 5.10 are listed in Tab. 5.5.

For SS-SI VASO the z-magnetization of blood and gray matter must be considered with and without previous inversion. According to Eq. 2.17, the z-magnetization in a VASO

symbol	name	value	reference
CBV_{rest}	cerebral blood volume	0.055 ml/ml	[Lu and van Zijl, 2012]
V_{GM}	volume of gray matter	0.945 ml/ml	1 - CBV_{rest}
ρ_b	blood water volume density	0.87 ml/ml	[Donahue et al., 2006]
ρ_{GM}	GM water volume density	0.89 ml/ml	[Donahue et al., 2006]
ρ_{par}	parenchyma water volume density	0.89 ml/ml	[Donahue et al., 2006]
$T_{1,b}$	blood T_1 at 7 T	2100 ms	Tab. 2.1
$T_{1,GM}$	gray matter T_1 at 7 T	1950 ms	Tab. 2.1
TI	blood-nulling time	1455 ms	$T_{1,b}\ ln(2)$
TR	repetition time	3000 ms	mostly used in thesis
TE	echo time	19 ms	mostly used in thesis
$T^*_{2,b}$	T^*_2 in vessel ROI at 7 T	12.8 ms	[Yacoub et al., 2001]
$T^*_{2,GM}$	T^*_2 in GM at 7 T	25.1 ms	[Yacoub et al., 2001]
$\Delta R^*_{2,b}$	change of inverse T^*_2 in vessel region at 7 T	1.43 ms^{-1}	[Yacoub et al., 2001]
$\Delta R^*_{2,GM}$	change of inverse T^*_2 in gray matter at 7 T	1.46 ms^{-1}	[Yacoub et al., 2001]

Table 5.5: Assumed values in the BOLD correction model simulation.

inversion recovery experiment is given by:

$$\frac{M_z(TI)}{M_0} = 1 - e^{-\frac{TI}{T_1}} \left(1 - \frac{M_z(0)}{M_0}\right). \tag{5.11}$$

Along Eq. 2.29 the steady-state, gray matter magnetization with foregone inversion (nc) is given by:

$$\frac{M^{nc}_{z,GM}(TI)}{M_{0,GM}} = 1 - 2e^{-\frac{TI}{T_{1,GM}}} + e^{-\frac{TR}{T_{1,GM}}}. \tag{5.12}$$

Blood z-magnetization at TI after inversion is zero by design. Without previous inversion (nn), gray matter or blood magnetization are given by:

$$\frac{M^{nn}_{z,i}(TI)}{M_{0,i}} = 1 - e^{-\frac{TR}{T_{1,i}}} \qquad i \in \{b, GM\}. \tag{5.13}$$

In order to estimate the BOLD-corrected VASO contrast, the blood-nulled signal is normalized with the blood-not-nulled signal as described in section 3.1.2.

$$\frac{S^{nc}}{S^{nn}} \overbrace{=}^{\text{Eq. 5.10}} \frac{V_{GM}\ \rho_{GM}\ M^{nc}_{z,GM}(TI) e^{-\frac{TE}{T^*_{2,GM}}}}{\left[CBV\ \rho_b\ M^{nn}_{z,b}(TI)\ C + V_{GM}\ \rho_{GM}\ M^{nn}_{z,GM}(TI)\right] e^{-\frac{TE}{T^*_{2,GM}}}} \tag{5.14}$$

Here, the $e^{-\frac{TE}{T^*_{2,GM}}}$-term cancels out. To obtain an expression only dependent on CBV, $V_{GM}\ \rho_{GM}$ is substituted with:

$$V_{GM}\ \rho_{GM} = V_{par}\ \rho_{par} - CBV\ \rho_b, \tag{5.15}$$

such that Eq. 5.14 becomes:

$$\frac{S^{nc}}{S^{nn}} = \frac{(V_{par}\ \rho_{par} - CBV\ \rho_b)\, M^{nc}_{z,GM}(TI)}{CBV\ \rho_b\ M^{nn}_{z,b}(TI)\ C + (V_{par}\ \rho_{par} - CBV\ \rho_b)\ M^{nn}_{z,GM}(TI)}. \tag{5.16}$$

In VASO, the blood volume change is assumed to arise only from water exchange between gray matter tissue and blood water. Hence, V_{par} is assumed to be independent of functional activation (see section 5.4.3 for more details). Equation 5.16 can be rearranged to:

$$\frac{S^{nc}}{S^{nn}} = \frac{\rho_{par} - \frac{CBV}{V_{par}}\ \rho_b}{\rho_{par}\ \frac{M^{nn}_{z,GM}(TI)}{M^{nc}_{z,GM}(TI)} + \frac{CBV}{V_{par}}\ \rho_b \left(C\ \frac{M^{nn}_{z,b}(TI)}{M^{nc}_{z,GM}(TI)} - \frac{M^{nn}_{z,GM}(TI)}{M^{nc}_{z,GM}(TI)} \right)}. \tag{5.17}$$

Therewith, the theoretical VASO signal change during activation becomes:

$$\Delta\frac{S^{nc}}{S^{nn}} = \frac{S^{nc\ act}}{S^{nnact}} - \frac{S^{nc\ rest}}{S^{nn\ rest}} = \tag{5.18}$$

$$\frac{\rho_{par} - \frac{V_b^{act}}{V_{par}}\ \rho_b}{\rho_{par}\ \frac{M^{nn}_{z,GM}(TI)}{M^{nc}_{z,GM}(TI)} + \frac{V_b^{act}}{V_{par}}\ \rho_b \left(C^{act}\ \frac{M^{nn}_{z,b}(TI)}{M^{nc}_{z,GM}(TI)} - \frac{M^{nn}_{z,GM}(TI)}{M^{nc}_{z,GM}(TI)} \right)} -$$

$$\frac{\rho_{par} - \frac{V_b^{rest}}{V_{par}}\ \rho_b}{\rho_{par}\ \frac{M^{nn}_{z,GM}(TI)}{M^{nc}_{z,GM}(TI)} + \frac{V_b^{rest}}{V_{par}}\ \rho_b \left(C^{rest}\ \frac{M^{nn}_{z,b}(TI)}{M^{nc}_{z,GM}(TI)} - \frac{M^{nn}_{z,GM}(TI)}{M^{nc}_{z,GM}(TI)} \right)}.$$

Equation 5.18 describes the VASO signal change corrected for BOLD contaminations by dynamic division. This theoretical signal change contains both, intravascular and extravascular BOLD effects in form of the $T^*_{2,b/GM}$ dependency of the C-term. The VASO signal described by Eq.5.18 is simulated for a wide range of CBV changes and depicted in Fig. 5.11B.

It can be seen that the signal change is nearly directly proportional to ΔCBV as desired in VASO imaging. Fig. 5.11B depicts the VASO after BOLD correction with dynamic division described in Eq. 5.18 as a function of intravascular BOLD contamination $\Delta R^*_{2,b}$. It can be seen that the VASO signal is almost independent of the intravascular BOLD contamination. Without BOLD contamination, VASO signal change would be $\Delta VASO$ = -1.08 (ideal value in Fig. 5.11). Due to incomplete BOLD correction with the proposed correction method, $\Delta VASO$ = -1.15 (measured value in Fig. 5.11) would be measured. The simulation results shown here, suggest that the BOLD correction mechanism based on dynamic division can essentially correct for the major BOLD contamination in VASO at high fields. The small residual intravascular BOLD contamination in VASO leads to an tolerable overestimation of VASO signal change. For a physiologically reasonable value of $\Delta R^*_{2,b} = 1.43$ s^{-1} [Donahue et al., 2010], VASO signal change is overestimated by 7%. This means that a true CBV change such as 25% would be overestimated to be 26.5%.

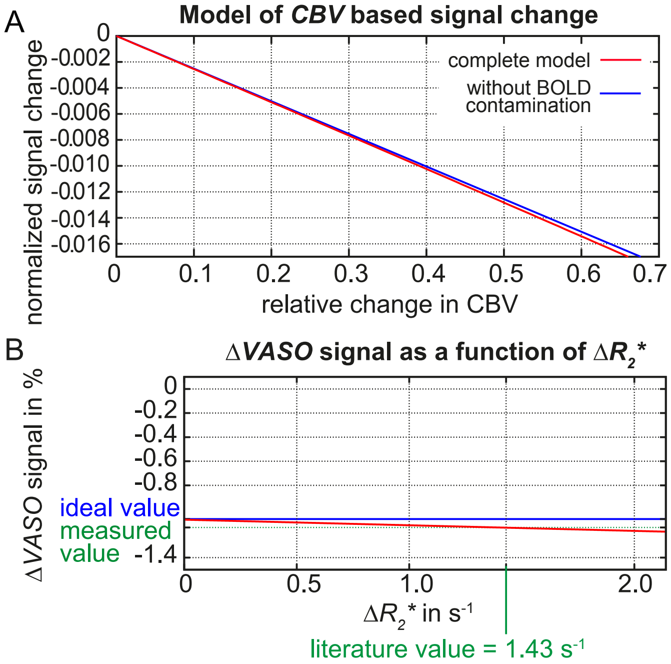

Figure 5.11: Evaluation of BOLD correction in SS-SI VASO: A) depicts results of Eq. 5.18. Relative signal change as a function of CBV change is in the linear range, despite the small dependence on $\Delta R^*_{2,b}$. B) depicts VASO signal change as a function of blood $\Delta R^*_{2,b}$ for a physiologically reasonable range. Value of $\Delta R^*_{2,b} = 1.43$ s^{-1} refers to the literature [Donahue et al., 2010]. It can be seen that VASO signal change is almost independent of $\Delta R^*_{2,b}$.

5.3.2 Experimental validation of the BOLD correction scheme based on dynamic division

The proposed BOLD correction scheme based on a dynamic division of images with and without blood nulling is compared with an alternative previously established BOLD correction scheme based on a mono-exponential T_2^* decay in a multi-echo EPI readout [Lu and van Zijl, 2005]. Figure 5.12 depicts VASO signal time course for different BOLD correction schemes applied. All depicted data refer to the same multi-echo experiments but different BOLD correction methods applied. The data are taken from previous studies of this thesis depicted in Fig. 3.8. It can be seen that the VASO signal time courses are almost identical for the different BOLD correction schemes applied. The concordance in amplitude and temporal characteristics suggests that BOLD correction with dynamic

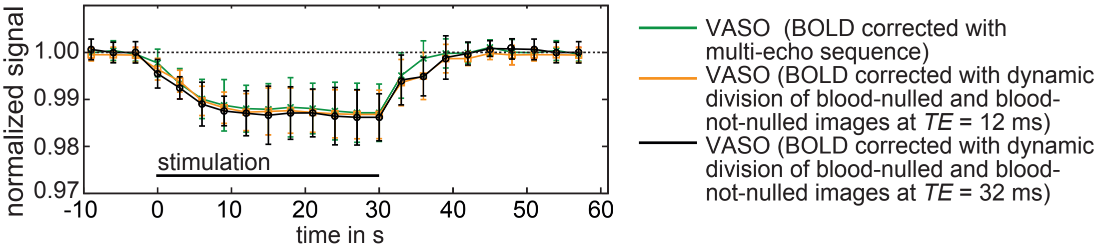

Figure 5.12: VASO results for different BOLD correction schemes: VASO signal change is almost independent of the BOLD correction scheme. There is only a minor trend of VASO signal overestimation for the BOLD correction based on dynamic division compared to BOLD correction based on multi-TE acquisition. The depicted time courses refer to the same data shown in Fig. 3.8.

division can account for BOLD contamination as accurately as BOLD correction with multi-echo acquisition. Minor differences between the time courses are smaller than the inter-subject variation and might reflect residual BOLD weighting due to intravascular effects. These small differences are the basis of the algorithm to distinguish arterial and venous CBV components described in section 4.1.2.

In conclusion, the BOLD correction scheme based on dynamic division can account for the BOLD contamination in SS-SI VASO at 7 T. Higher order effects of intravascular BOLD signal introduce a small, tolerable VASO signal change overestimation of about 7%.

5.4 Effect of partial voluming of CSF and WM[1]

In this section, the quantifiability of CBV changes from VASO signal changes is discussed with respect to partial volume effects of CSF and WM. First, it is considered how the partial voluming of WM and CSF can affect the BOLD correction scheme based on dynamic division. In the second part of this section, the propagation of error in CBV estimation is discussed with respect to errors in estimated partial voluming. In the final part of this section, potential dynamic changes in CSF partial voluming are discussed with respect to all experimental results shown in this thesis.

5.4.1 Partial voluming in the BOLD correction scheme based on dynamic division

The partial voluming of CSF or WM can distort the VASO signal change sensitivity to CBV change and is discussed in the original VASO paper for the traditional VASO approach [Lu et al., 2013]. The unique way of BOLD correction in SS-SI VASO is based on a nonlinear model and SS-SI VASO might be affected differently from partial voluming compared to the original VASO approach. The effect of partial voluming in the BOLD correction mechanism done with dynamic division of blood-nulled and blood-non-nulled images can be discussed in a multi compartment model. The z-components of the magnetization are considered only. The magnetization of a voxel with partial voluming of WM or CSF can be considered as

$$S_{nc} \propto M_{z,GM}(TI_{nc}) + M_{z,CSF/WM}(TI_{nc}) \tag{5.19}$$

for the nulling condition and as

$$S_{nn} \propto M_{z,par}(TI_{nn}) + M_{z,CSF/WM}(TI_{nn}) \tag{5.20}$$

for the not nulled condition. In the BOLD correction scheme based on dynamic division, the resulting signal change is given as (based on Eq. 5.18):

$$\frac{\Delta \frac{S_{nc}}{S_{nn}}}{\frac{S_{nc}^{rest}}{S_{nn}^{rest}}} = \frac{\frac{S_{nc}^{act}}{S_{nn}^{act}} - \frac{S_{nc}^{rest}}{S_{nn}^{rest}}}{\frac{S_{nc}^{rest}}{S_{nn}^{rest}}} = \frac{\frac{M_{z,GM}^{act}(TI_{nc})+M_{z,CSF/WM}^{act}(TI_{nc})}{M_{z,par}^{act}(TI_{nn})+M_{z,CSF/WM}^{act}(TI_{nn})} - \frac{M_{z,GM}^{rest}(TI_{nc})+M_{z,CSF/WM}^{rest}(TI_{nc})}{M_{z,par}^{rest}(TI_{nn})+M_{z,CSF/WM}^{rest}(TI_{nn})}}{\frac{M_{z,GM}^{rest}(TI_{nc})+M_{z,CSF/WM}^{rest}(TI_{nc})}{M_{z,par}^{rest}(TI_{nn})+M_{z,CSF/WM}^{rest}(TI_{nn})}}. \tag{5.21}$$

For the blood-not-nulled condition, the z-magnetization of the parenchyma is believed to be independent of stimulation [Jochimsen et al., 2005]. In other words, if no VASO preparation is applied, all signal changes come from changes in T_2^*, and not from changes of z-magnetization. The partial voluming of CSF/WM is considered to be independent of activity (violations of this assumption are discussed in the sections below). Therefore,

---

[1] Parts of this section have been discussed in the paper [Huber et al., 2014b] and in the conference presentations [Huber et al., 2013] and [Huber et al., 2014c].

the denominator of every sub-fraction in Eq. 5.21 is the same and can be canceled out. Thus Eq. 5.21 can be simplified to:

$$\frac{\Delta \frac{S_{nc}}{S_{nn}}}{\frac{S_{nc}^{rest}}{S_{nn}^{rest}}} = \frac{M_{z,GM}^{act}(TI_{nc}) + M_{z,CSF/WM}^{act}(TI_{nc}) - (M_{z,GM}^{rest}(TI_{nc}) + M_{z,CSF/WM}^{rest}(TI_{nc}))}{M_{z,GM}^{rest}(TI_{nc}) + M_{z,CSF/WM}^{rest}(TI_{nc})}. \tag{5.22}$$

The term in Eq.5.22 is exactly the same as it would be in the original VASO [Lu et al., 2003]. Since the z-magnetization of the CSF/WM volume inside the voxel is believed to be constant during activation and rest, Eq. 5.22 can be further simplified to:

$$\frac{\Delta \frac{S_{nc}}{S_{nn}}}{\frac{S_{nc}^{rest}}{S_{nn}^{rest}}} = \frac{M_{z,GM}^{act}(TI_{nc}) - M_{z,GM}^{rest}(TI_{nc})}{M_{z,GM}^{rest}(TI_{nc}) + M_{z,CSF/WM}^{rest}(TI_{nc})}. \tag{5.23}$$

Since $M_{z,CSF/WM}^{rest}(TI_{nc})$ in the denominator is not known, it introduces an uncertainty in the proportionality factor between signal change and blood volume change. In other words, if the voxel is only filled with half of the GM volume the activity induced VASO signal change is correspondingly smaller. This partial voluming dependent CBV quantification is discussed in the review paper [Lu et al., 2013].

5.4.2 Estimation of changes in blood volume with uncertainties in partial voluming

In order to convert VASO signal changes into relative changes in CBV, the gray matter signal fraction of the voxel must be known (Eq. 5.23). In the studies of this thesis, the GM signal fraction is determined my means of acquired T_1 maps (see section 3.1.3). The relative change in CBV is calculated with $\frac{\Delta CBV}{CBV_{rest}} = \frac{S_{rest}-S_{act}}{S_{rest}} \frac{1}{CBV_{rest}} \frac{1}{V_{GM}}$. Figure 5.13 depicts the relative error in ΔCBV for errors in estimated GM fraction in the voxel for six different magnitudes of partial voluming. It can be seen that the error in the calculation of $\frac{\Delta CBV}{CBV_{rest}}$ from $\frac{\Delta S}{S_{rest}}$ is highly dependent on the error in GM signal contribution. To understand this more intuitively, Fig. 5.13 is explained by means of an example (see dotted blue line in Fig. 5.13). In this example, a voxel with 40% GM contribution is considered (purple line in Fig. 5.13). The GM contribution of this voxel is overestimated by only 10% to be filled with 44% GM instead of the true value of 40% GM contribution. In this case, the calculated percent CBV change would be underestimated by almost 20% for example to an estimated CBV change of 20% instead of the true value of 25%. Hence, it is clear that any systematic error in the calculation of GM signal contribution will have a significant impact on the calculation of $\frac{\Delta CBV}{CBV_{rest}}$. This is particularly problematic, when the error in GM is so large that the error propagation of Fig. 5.13 is out of the linear range. In such a case, equally distributed noise in GM fraction is not canceled out after averaging.

To minimize the error in GM fraction determination, special attention is focused on its generation with T_1 maps in this thesis. Although, two images at different TI are enough to generate a GM mask according to the algorithm described in 3.1.3, in the studies of this thesis images at six different TI were acquired to minimize noise in the fitting

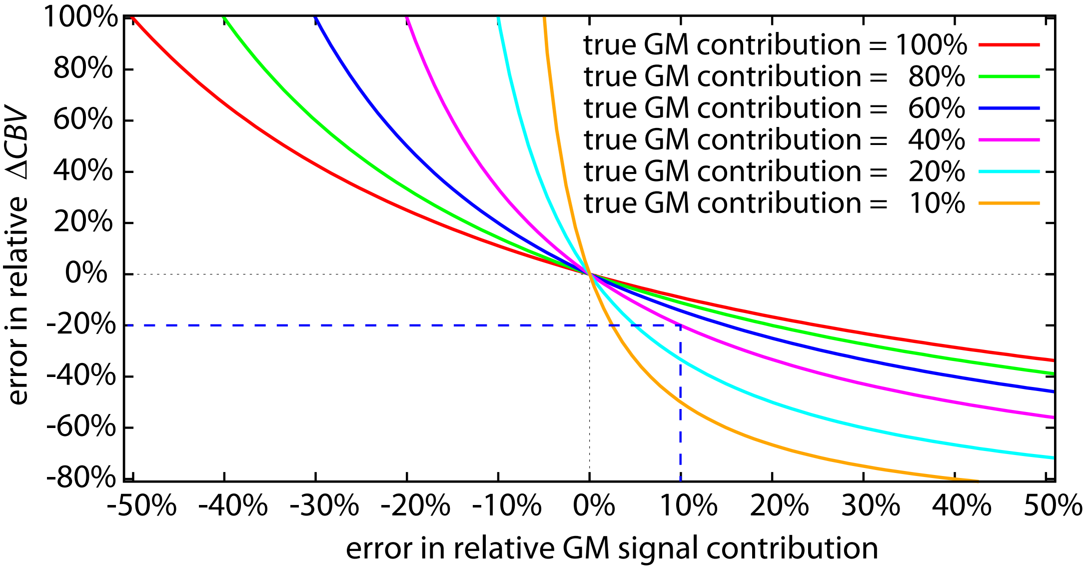

Figure 5.13: The error in $\frac{\Delta CBV}{CBV_{rest}}$ as a function of the error in GM signal contribution is depicted for six values of true GM signal contributions.

algorithm. For every TI, 5 identical images are acquired and averaged for further noise reduction.

5.4.3 Changes in CSF volume

Introduction and background

In VASO fMRI, blood magnetization is selectively nulled, leaving only tissue magnetization for signal detection. Its CBV sensitivity is based on the assumption that CBV increase is compensated by GM volume decrease. This compensation mechanism, however, is poorly understood and is subject of current research [Krieger et al., 2012]. The underlying physiology of CBV increase compensation mechanisms and corresponding effects in VASO contrast generation is estimated and discussed here.

According to the Monro-Kellie doctrine, all cranial compartments are incompressible and the total volume inside the cranium remains constant [Mokri, 2001]. Hence, volume increase of one compartment of the brain must be compensated by a decrease in volume of another component. It has been shown that a fast bolus injection of fluid into CSF space of only 4 ml can cause a temporary doubling of intracranial pressure [Czosnyka et al., 2004], which poses a health risk. This fact has been used to argue that for a normal healthy condition, the functional increase in CBV is not compensated by a CSF volume decrease [Turner and Thomas, 2006]. It has been proposed that the increase in CBV happens through exchange of water between the capillaries and the endothelial cells surrounding them [Turner and Thomas, 2006], as well as water exchange between intravascular space and tissue. Since endothelial cells occupy up to 20% of the volume inside the vessel wall, volume decrease of endothelial cells can result in CBV increase. This increase could be a accompanied by water draining of endothelial cells during activation. Recently, a hydrodynamic model was introduced that can explain the mechanism how the capillaries volume could increase, while the bulk volume remains constant, in reference to the permeability of the capillary walls [Krieger et al., 2012]. This hydrodynamic model suggests that capillary volume increase up to $(17 \pm 1)\%$ can be compensated for by water redistribution between intravascular and extravascular space.

Despite this compensation mechanism for CBV increase, most of the empirical studies report of additional compensation components of CSF volume decrease in the range of 0.5% - 10% [Donahue et al., 2006][Jin and Kim, 2010][Piechnik et al., 2009][Scouten and Constable, 2007]. This CSF volume change can affect the VASO signal and introduce artifacts in CBV quantifications. The relative CSF volume change contamination in VASO was found to be highly area specific. During hypercapnia, CSF volume change is negligible small in visual cortex ($(0.6 \pm 1.4)\%$) and highest in auditory cortex ($(5.8 \pm 4.8)\%$) [Scouten and Constable, 2008].

Since the spinal canal provides only a limited extra space, during CBV increase most of the compensating CSF volume is leaving the skull presumably along the normal evacuation pathway via dural venous sinuses [Czosnyka et al., 2004], which has a draining capacity in the order of 2 ml/min [Ekstedt, 1978].

Aside from tissue or CSF volume decrease, a third volume compartment has been suggested to reduce its volume during activity. Using hemoglobin as an contrast agent during hyperoxia, venous blood volume has been suggested to decrease during activation [Blockley et al., 2011]. Since baseline venous CBV is assumed to constitute about 40% - 70% [van Zijl et al., 1998] to the total CBV, it can provide a volume buffer for compensating arterial and capillary volume increase to some extent as well. Dependent on the compensation mechanism, functional changes in the partial voluming of CSF and GM could affect VASO signal and make direct interpretation of ΔCBV in VASO signal change more difficult [Donahue et al., 2006][Jin and Kim, 2010][Piechnik et al., 2009][Scouten and Constable, 2007]. In the original VASO approach, this effect is particularly pronounced using $TR < 4$ s [Donahue et al., 2006]. It can result in biased CBV estimations when voxels with different CSF partial voluming are compared. This can be the case, when comparing voxels at the cortical surface with voxels deeper inside GM or it can be the case comparing ROIs of positive BOLD response with ROIs of negative BOLD, as it is done in this thesis.

In this section, such effect of CSF partial voluming are sought to be quantified and discussed. VASO contaminations due to CSF volume changes are investigated with respect to the experiments described in this thesis, such as (A) visual stimulation including positive and negative hemodynamic responses, (B) layer-dependent VASO in primary motor cortex, and (C) VASO signal change during hypercapnia.

CSF contamination in regions of positive and negative BOLD signal change

Introduction Investigating VASO signal change in positive and negative ROIs, surface voxels with more partial voluming of CSF were found to show significantly different CBV response compared to deeper GM voxels without partial voluming of CSF (see section 4.1.4). This feature was interpreted to be a result from different CBV contributions in surface macrovasculature as opposed to the tissue microvasculature. However, it remains to be shown that these results are not due to contaminations of dynamic CSF volume changes.

The purpose of the study in this section is to quantify such CSF volume dynamics on a voxel-wise basis. This is done to investigate, whether potential CSF contaminations can mimic the cortical depth-dependence of CBV changes. The study of this section is based on quantitative analysis of VASO data that are acquired with and without CSF nulling in analogy to previous studies [Scouten and Constable, 2008][Donahue et al., 2006].

Theory In SS-SI VASO, the blood-nulling time is independent of the repetition time. Hence, stationary CSF z-magnetization can be manipulated by adapting TR, independent of TI. Thus, the relative signal contribution of CSF in VASO signal can be actively controlled. As already indicated in section 3.1.5, when relatively short TRs are used, CSF magnetization is not nulled, but blood magnetization is nulled only (Fig. 5.14A). In this case, VASO signal change reflects volume changes of both compartments, GM and CSF. With longer TRs, both, blood and CSF z-magnetizations are nulled (Fig. 5.14B). In this case, VASO signal change reflects volume changes of GM only.

Having VASO signal data acquired with and without CSF nulling, a dynamic model can be developed that is able to describe changes in both, CBV and V_{CSF}. In previous studies, such a model has been developed and applied to investigate changes of CSF volume in signal change of the original VASO approach [Donahue et al., 2006][Scouten and Constable, 2008]. Due to the unique contrast of SS-SI VASO as opposed to original VASO, a new model is developed here. Following previous studies [Donahue et al., 2006][Scouten and Constable, 2008], this model is based on the idea that every voxel is composed of CSF, GM, WM and blood volume.

$$V_{CSF} + V_{GM} + V_{WM} + CBV = V_{voxel} = 1 \tag{5.24}$$

CBV increase is assumed to be compensated by either GM volume decrease or CSF volume decrease.

$$\Delta V_{CSF} + \Delta V_{GM} + \Delta CBV = 0 \tag{5.25}$$

By means of Eq. 5.24 and Eq. 5.25, VASO signal change can be described for the case, when CSF-GM contrast is minimal and for the case when, CSF signal is nulled.

$$\frac{\Delta S_{CSF\approx GM}}{S_{CSF\approx GM}} \approx \frac{\overbrace{\Delta V_{GM} + \Delta V_{CSF}}^{=-\Delta CBV}}{V_{voxel} - CBV_{rest}} \tag{5.26}$$

$$\frac{\Delta S_{CSF\approx 0}}{S_{CSF\approx 0}} \approx \frac{\Delta V_{GM}}{V_{voxel} - CBV_{rest} - V_{CSF}} \tag{5.27}$$

Baseline volume composition of CSF, GM, WM, and CBV can be taken from T_1-based tissue segmentation and assuming $CBV_{rest} = 5.5\%$, as done in previous VASO studies [Lu et al., 2013]. Finally, the two Eqs. 5.26 and 5.27 can be combined to solve explicitly for ΔCBV and ΔV_{CSF}.

Methods In order to empirically estimate the CSF contamination in VASO, four volunteers (24-30 years old, two females) were scanned during both conditions, with and without CSF nulling. One of these VASO experiments was conducted with nulling of both, CSF and blood magnetization (TR = 5 s). Another experiment was conducted with nulling of blood only, but without nulling of CSF (TR = 3 s). Two 12-min experiments with a small flickering checkerboard stimulation were conducted to evoke positive and negative hemodynamic responses, as described in section 4.1.3. All imaging parameters were identical to the ones described in section 4.1.3. In short, field strength 7 T, resolution 1.3 x 1.3 x 1.5 mm^3, $TI1/TI2/TR = 1.0/2.5/3.0$ s, three GE-EPI echoes with $TE = 12/32/52$ ms. Additionally, to functional VASO experiments, multi-TI experiments were conducted for estimation of partial volume of WM, GM, and CSF.

Results and discussion The expected z-magnetization of CSF, GM, and once inverted blood and the corresponding MR images of one representative participant are shown in Fig. 5.14. In the CSF-nulled condition, GM signal is reduced by (32 ± 12)% compared to the GM signal without CSF-nulling. In the case of shorter TR, CSF, GM, and WM have very similar signal intensities (Figs. 5.14B). Although CSF has slightly smaller z-magnetization than GM at the blood-nulling time (arrow in Fig. 5.14A), signals are comparable due to higher proton density and longer T_2^* in CSF. Multi-TI experiments were conducted additionally to estimate partial voluming of WM, GM, and CSF. It can be seen in Fig. 5.15 that the corresponding T_1 map has sufficient quality for estimations of voxel-wise tissue composition. Figure 5.16 depicts CBV and BOLD signal time courses with and without CSF nulling averaged over four participants. CBV change is calculated from VASO signal change using Eqs. 5.26 and 5.27. CBV time courses are the same within error for both conditions, with and without CSF nulling. Figure 5.17 depicts cortical laminar dependent BOLD and VASO signal changes in ROIs of positive and negative responses for the conditions with and without CSF nulling. The measured laminar dependence of BOLD and VASO signal change is very similar with and without CSF nulling. In ROIs of the positive response, no specific surface dominance can be seen in VASO. In ROIs of the negative response, VASO signal change is significantly dominated from the surface voxels. These insights can be taken from both VASO data sets, acquired with and without CSF nulling.

Even though, VASO signal profiles are similar with and without CSF nulling, the absolute VASO signal change is up to 30% larger for the CSF nulled condition compared to the condition without CSF nulling. This effect has been simulated earlier [Lu et al., 2013] and corresponds to the smaller denominator in Eq. 5.27 for the CSF nulled condition as opposed to the condition without CSF nulling (Eq. 5.26).

Such dependencies of partial volume effects need to be considered, when inferring to CBV

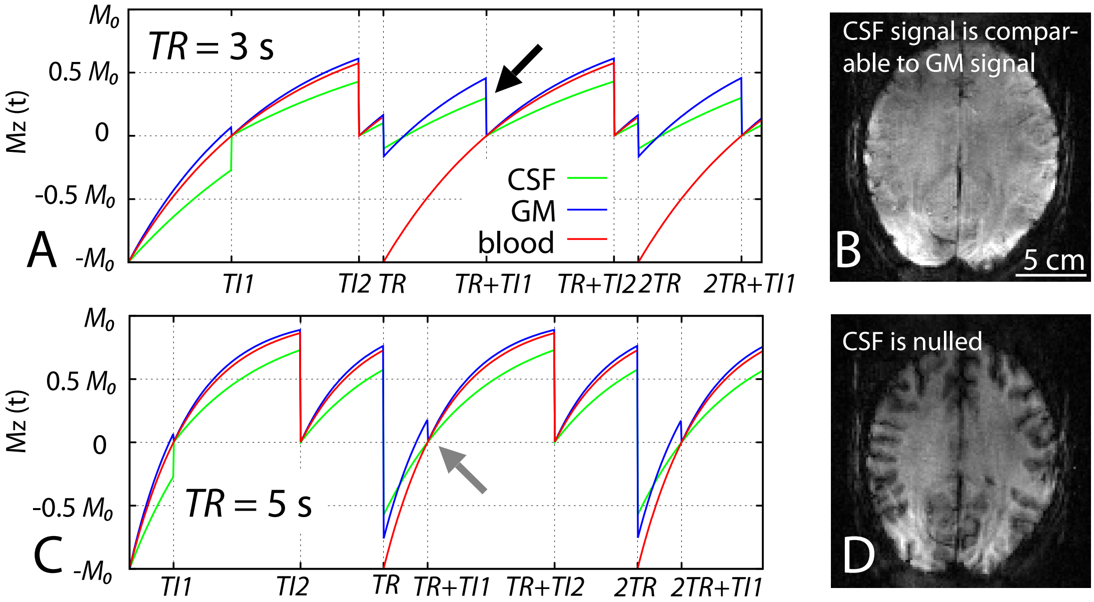

Figure 5.14: Expected z-magnetization of CSF, GM, and once inverted blood in SS-SI VASO for $TR = 3$ s (A) and $TR = 5$ s (C). For $TR = 3$ s, CSF and GM z-magnetization are in the same order of magnitude (black arrow). Due to higher proton density and longer T_2^* in CSF, GM and CSF signals become comparable. This results in a VASO image with minimum CSF-GM contrast (B). For $TR = 5$ s, both, CSF and blood z-magnetizations are nulled simultaneously (gray arrow). In the CSF nulled condition with a long TR, GM signal is reduced with respect to the condition of a shorter TR (D). Depicted z-magnetizations in (A) and (C) are based on assumed relaxation values of blood, GM and CSF of $T_{1,b}/T_{1,GM}/T_{1,CSF} = 2.1/1.9/4.0$ s according to Tab. 2.1.

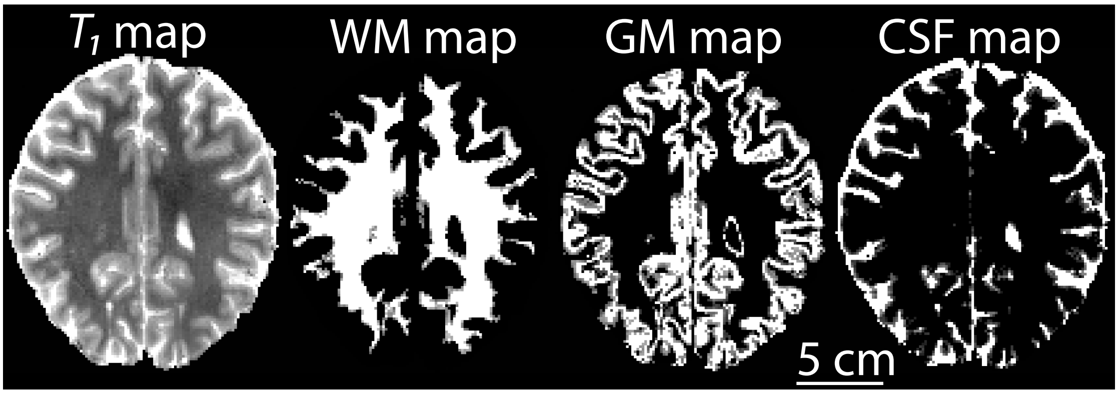

Figure 5.15: Mult-TI inversion recovery experiment are used to acquire EPI T_1 maps with identical distortions as the functional scans. These T_1 maps are further processed to estimate partial voluming of CSF, GM, and WM in every voxel.

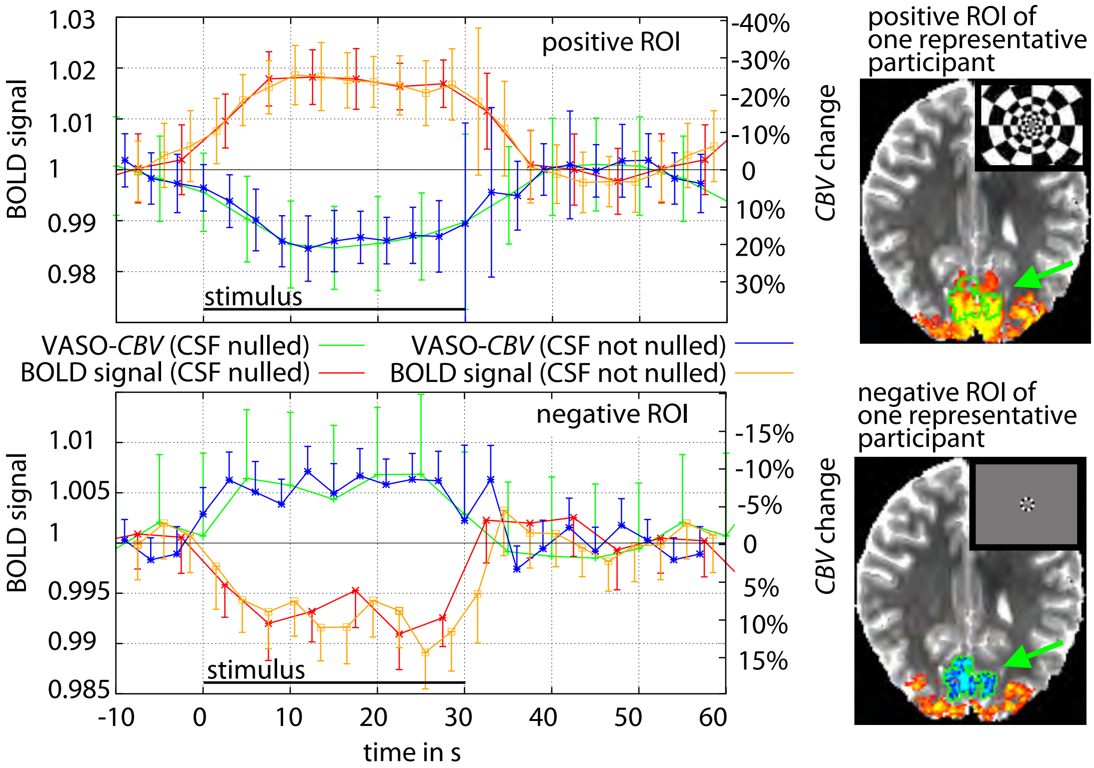

Figure 5.16: CBV and BOLD signal time courses with and without CSF nulling in ROIs of positive and negative responses averaged over four participants: There is no significant difference in signal changes. Signal changes of positive and negative ROIs refer to the same brain region, but during different stimulation paradigms (schematically depicted in right subfigures).

changes from raw VASO signal changes. These biases can be avoided by calculating CBV changes with respect to the fraction of GM volume in the voxel only, as it is done in this thesis. Comparing VASO signal changes with and without CSF nulling, CSF volume change can be estimated independently of CBV changes. Corresponding CSF volume time courses are depicted in Fig. 5.18. No significant CSF volume change can be seen for tasks evoking positive or negative responses.

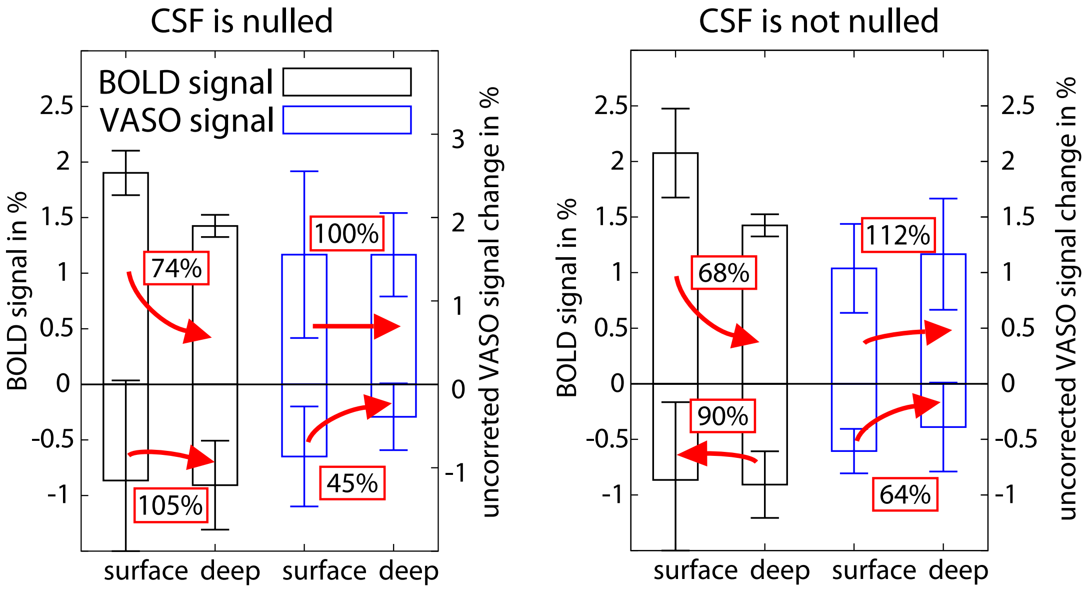

Figure 5.17: Surface dependence of BOLD and VASO signal change with and without CSF nulling: The right and the left subfigures are same within error and there is no qualitative difference of BOLD and VASO signal change whether CSF is nulled or not nulled. In both cases VASO is similar across of cortical layers for the positive response, but it is dominated from surface for the negative response. 'Uncorrected' VASO signal change refers to the raw VASO signal change. It is not corrected for different baseline partial voluming with and without CSF nulling (different denominator in Eqs. 5.26 and 5.27).

Conclusion The results shown in Figs. 5.21, 5.17, and 5.18 suggest that there is no significant change in CSF volume in the occipital lobe during the visual stimulation paradigms in humans. There is no qualitatively difference in cortical profiles of VASO with and without CSF nulling. Hence, it is suggested that the corresponding VASO results are not contaminated from dynamic CSF volume changes. Similarly to the results shown here, Scouten and Constable found no significant dynamic change of CSF volume in occipital lobe compared to other cortical regions [Scouten and Constable, 2007][Scouten and Constable, 2008]. This is consistent with the results in cats: Using a spin-lock contrast, absolute CSF volume change of 0.6% is measured in V1 at the cortical

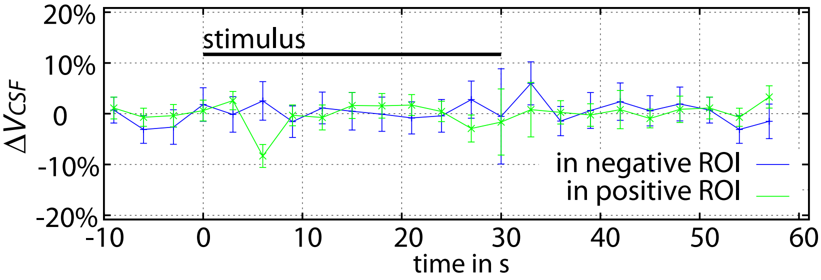

Figure 5.18: There is no significant CSF volume change in regions of positive and negative hemodynamic response. Data refer to the average across four participants. In order to calculate CSF volume change from VASO signal changes with and without CSF nulling, temporal resolution of CSF nulled time courses are linearly resampled from $TR = 5$ s to $TR = 3$ s.

border between GM and CSF at ultra high resolution of 156 μm [Jin and Kim, 2010]. Such small CSF volume changes are expected to be negligible at the resolutions used in this study (1.3 mm - 1.5 mm).

CSF contamination in VASO at ultra high resolutions

Potential CSF contaminations in VASO have been shown to be undetectable small, when investigating VASO signal change in ROIs of positive and negative BOLD responses in the previous section. Another VASO study of this thesis, where potential CSF contaminations need to be discussed is the laminar-dependent investigation of VASO signal changes described in section 4.2. In layer-dependent VASO fMRI, CSF contaminations are expected to be confined to voxels at the cortical surface and can therefore introduce artifacts in the corresponding cortical profiles of VASO signal change.
fMRI at ultra high resolutions is limited by thermal noise. Hence, the above mentioned strategy for minimizing CSF contaminations in VASO by using longer TR is discouraged. It results in a GM signal penalty of about 30% (Fig. 5.14). Additionally, the lower temporal resolution of longer TRs applied, results in an additional decrease of statistical power. Similarly, other possible CSF compensation methods such as VASO-FLAIR [Donahue et al., 2006] or ACDC VASO [Scouten and Constable, 2007] have SNR penalties loosing up to 90% of the signal, unaffordable at submillimeter resolutions. Hence, a novel and very simple strategy is introduced to minimize CSF effects in VASO without reducing GM signal by more than 20%.
The steady-state of CSF and GM magnetizations cannot only be manipulated by adapting TR, but also by increasing the excitation flip angle. Increasing the nominal flip angle to $\alpha = 130°$, CSF z-magnetization at the blood-nulling time can be increased to approach GM z-magnetization. This results in a BOLD corrected VASO image with almost no signal contrast between GM and CSF (black arrow in Fig. 5.19A). Therefore the resulting VASO contrast is insensitive to any functional volume redistribution

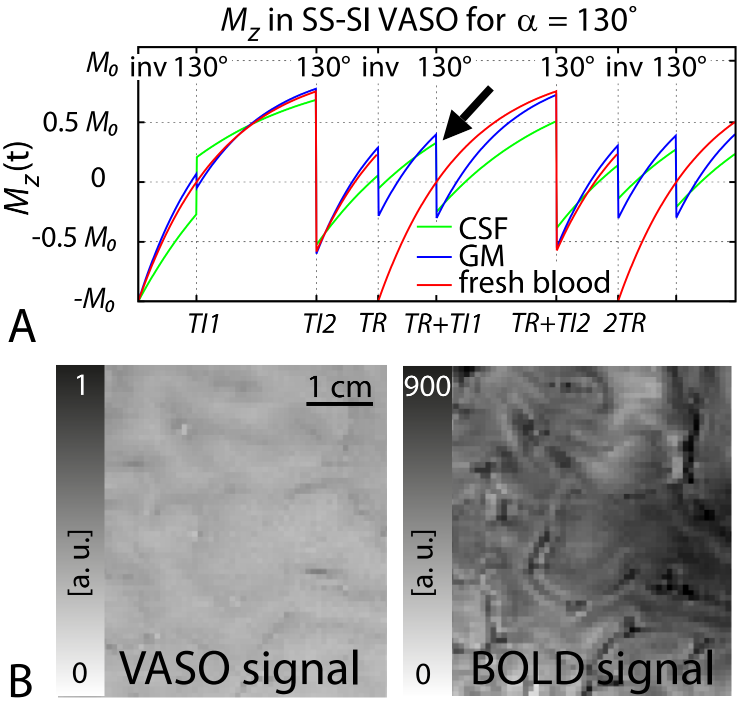

Figure 5.19: Strategy to minimize CSF contamination in VASO by manipulating z-magnetization steady-state with an increased flip angle: A) depicts the expected z-magnetization evolution in SS-SI VASO with a flip angle of $\alpha = 130°$. This value is chosen such that CSF and GM signal at the blood-nulling time are very similar (arrow). Depicted z-magnetizations are based on assumed relaxation values of blood, GM and CSF of $T_{1,b}/T_{1,GM}/T_{1,CSF}$ = 2.1/1.9/4.0 s according to Tab. 2.1. B) depicts BOLD and VASO signal maps of one representative participant using this strategy. Due to the manipulated CSF magnetization steady-state, the VASO signal map has almost no contrast, which is making it independent of volume redistribution between CSF and GM.

of GM and CSF. In contrast with the CSF-nulled ACDC VASO [Scouten and Constable, 2007] or VASO FLAIR [Donahue et al., 2006], the VASO signal changes in this study, therefore, reflect both components of the CBV change - all the CBV increase that is compensated by a GM volume decrease, as well as the CBV increase that is compensated by CSF volume decrease - with the same weighting. Since all high resolution VASO experiments were conducted with a desired excitation flip angle of $\alpha = 130°$ (see section 4.2), contaminations of CSF dynamics are expected to be negligible in the corresponding results.

Volume redistribution during hypercapnia

Introduction It has been shown in previous sections that CSF volume change is undetectable small for focal visual activity. This does not mean, however, that CSF volume is constant for all kinds of hemodynamic changes. During strong and global vessel dilation in all brain compartments, for example during hypercapnia, CSF volume changes might play a more important role of volume change compensation.

While moderate capillary volume increase during focal activation can be compensated from water redistribution across the permeable endothelium [Krieger et al., 2012], it is unknown how the considerable global arteriolar CBV change of $(65 \pm 8)\%$ [Hua et al., 2011a] during hypercapnia is compensated for. The interpretation of VASO during hypercapnia, as done in this thesis (section 4.3) might depend on the compensation mechanism involved.

The purpose of the study, described in this section, is to address the question of volume redistributions during hypercapnia empirically. This is done with measurements of dynamic volume changes in CSF and blood across the vascular tree during hypercapnia compared to stimulation with OIS and VASO in rats and with VASO in humans.

Methods VASO experiments in 5 humans volunteers (27-34 years old, 3 females) during hypercapnia and visual stimulation were conducted in the identical manner as described in section 4.3. In short: SS-SI VASO at 7 T in humans, 1.5 mm resolution, $TR/TI1/TI2/TE$ = 3.0/0.7/2.2/0.019 s, 5% CO_2 breathing for 5 min and 12 times flickering checkerboard for 30 s. OIS experiments in 5 rats during hypercapnia and whisker pad stimulation were conducted in the identical manner as described in section 3.2. In short: OIS in rats, thinned cranial window, 4 wavelengths, 5% CO_2 breathing for 5 min, 15 times whisker stimulation for 12 s. Results were evaluated in ROIs dominated from macro- or microvasculature and arteries or veins, respectively.

In order to investigate potential CSF volume change directly, the lateral ventricles were imaged in three human volunteers during hypercapnia. This was done with a turbo spin-echo sequence [Hennig et al., 1984] using long echo times (TE = 84 ms) and a nominal resolution of 0.4 x 0.4 x 1 mm^3 to distinguish CSF from surrounding tissue and to assess its volume. 38 slices where acquired to obtain a complete 3D volume of at least one lateral ventricle and therefore be able to account for potential motion artifacts. The acquisition duration of one volume was approx. 5 min. Hence, potential volume changes across the heart beat are believed to be averaged out.

Results and discussions Results shown in Fig. 5.20 depict maps of CBV change in rats and in humans during hypercapnia and focal activation. CBV changes across arteries and veins are different for focal activation compared to hypercapnia. It can be seen that during focal stimulation, CBV increase is more homogeneously distributed across all vascular compartments, while CBV increase during hypercapnia is confined to the arterial compartments.

Figure 5.21 shows that for a hypercapnia challenge, it takes about 2 - 3 minutes until the CBV increase reaches its maximal amplitude. For normal physiological conditions in humans, during such a period, 1.2 ml of new CSF is produced and 1.2 ml of CSF is evacuated [Ekstedt, 1978]. The fact that the volume redistribution is in the time scale of minutes, suggests that CSF volume reductions could follow the normal path way of evacuation via the dural venous sinuses.

Volume changes of lateral ventricles are depicted in Fig. 5.22. It can be seen that there is a significant signal reduction in region of the border zone between CSF and brain tissue around the ventricles. This suggests that the ventricles constrict during hypercapnia. Quantitative calculations (voxel counting) suggest a CSF volume decrease of 0.8 ± 0.2 ml in both lateral ventricles. This is approximately 5% of their volume at rest.

Conclusion The data shown here suggest that the volume redistribution between different volume compartments including arteries, veins, and CSF is different for hypercapnia compared to focal activity. The significant CSF volume change during hypercapnia makes it difficult to interpret VASO signal changes directly as CBV signal changes. Hence, in order to avoid corresponding contaminations in VASO, CSF volume redistributions must be accounted for. In the studies of this thesis, this is done by specifically minimizing the GM-CSF contrast with corresponding adjustments of TR or flip angles (see previous sections).

The different volume redistributions during hypercapnia and their underlying mechanisms are not only important in VASO interpretations. The vascular effects seen here could make it difficult to obtain a straight-forward interpretation of neurovascular features during hypercapnia in other research areas, e.g. in BOLD calibration (section 4.3) or in cerebrovascular reactivity imaging [Thomas et al., 2013]. The data shown here suggest a negative Grubb coefficient right in those regions that are suggested to have the highest BOLD signal change (black arrows in Fig. 5.20), which might have strong implications in biophysical models used in BOLD calibration.

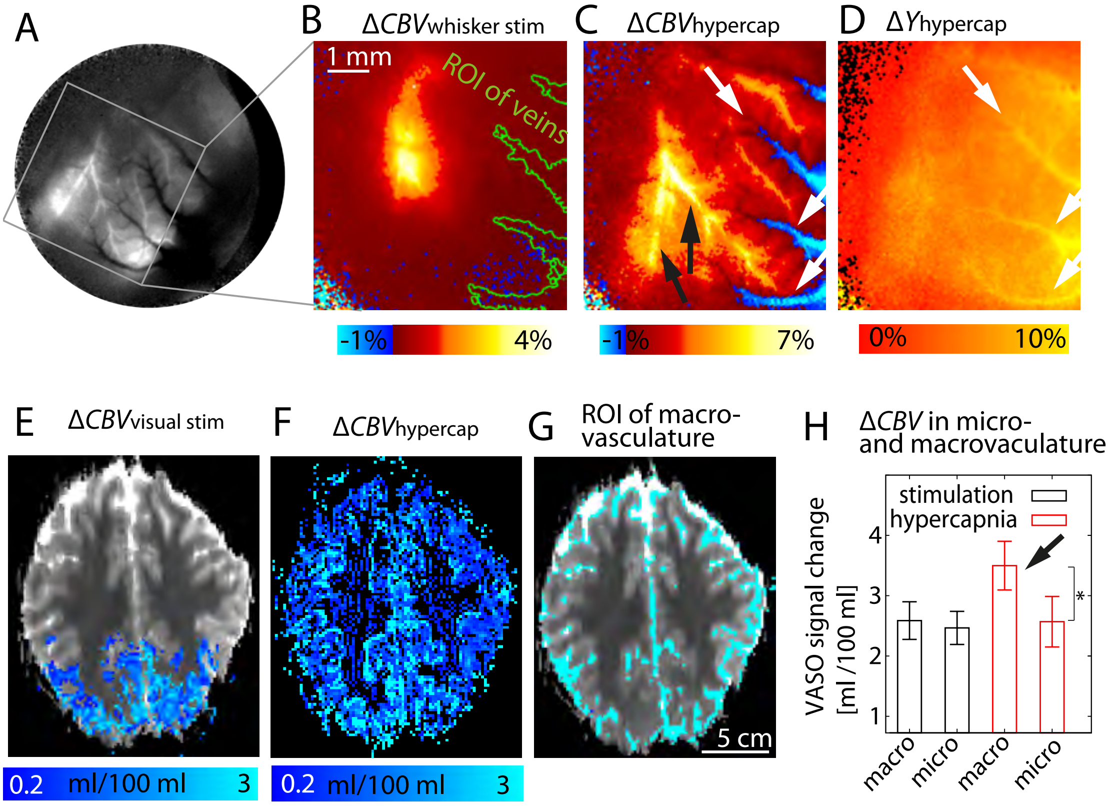

Figure 5.20: Maps of CBV change during hypercapnia: The subfigures in the upper row depict results from OIS in rats. The activation induced CBV response peaks in barrel cortex (zoomed view of panel A). Widespread small CBV responses can be seen throughout the map including ROIs of large draining veins (B). During hypercapnia, the CBV increase is dominated from large pial arteries (black arrows), while large draining veins that have the strongest change in blood oxygenation level ΔY (white arrows), show very small CBV decrease (C and D). The subfigures in the lower row depict VASO results in humans during visual stimulation (E) and hypercapnia (F). VASO results are broken down to voxels containing surface vasculature and voxels without surface vasculature (G and H). During hypercapnia, VASO signal change is significantly higher in voxels of surface vasculature than in voxels containing microvasculature only (H), in contrast to focal visual stimulation induced vasodilation.

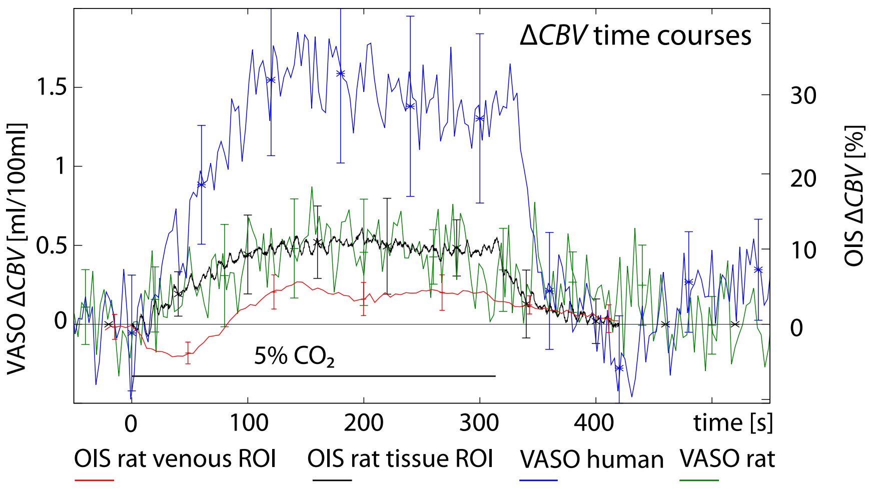

Figure 5.21: Time courses of CBV change during hypercapnia corresponding to the maps depicted in Fig. 5.20: In humans and in rats, it takes slightly longer than two minutes until tissue CBV increase reaches its maximal amplitude. In the time period shortly after hypercapnia onset, CBV in venous regions decreases in contrast to CBV in regions of the barrel cortex.

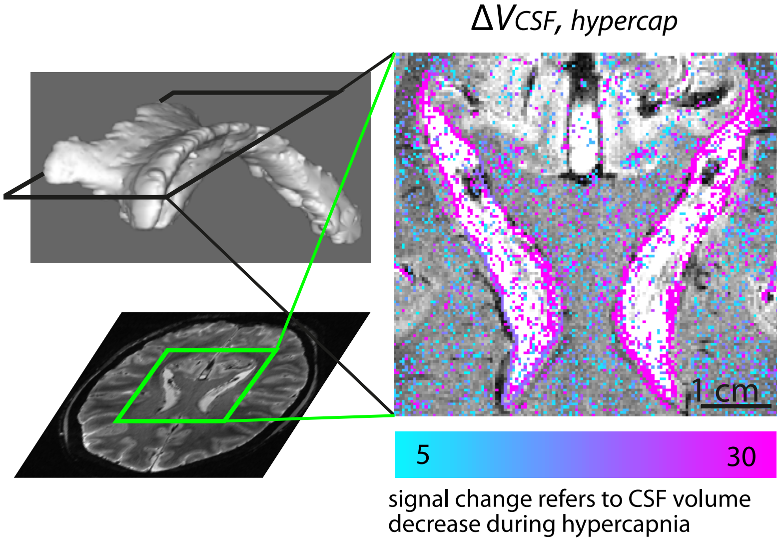

Figure 5.22: High resolution (0.4 x 0.4 x 1 mm^3) turbo spin-echo acquisition with TE = 84 ms enables direct volume estimation of the lateral ventricles. Signal change between breathing hypercapnia and air are highest at the border zone between CSF and WM. This suggests constriction of the ventricles during hypercapnia.

6 Summary and conclusion

The goals

The original purpose of this thesis was to develop a new fMRI method that can help to understand and overcome the limitations of conventional BOLD fMRI. In order to do so, it was sought to map correlates of neural activity with high specificity by means of CBV measurements. The motivation was that CBV measurements can provide quantitative results with physiologically meaningful parameters in physical units. The purely vascular nature of CBV measurements in comparison with conventional BOLD fMRI, could then help to distinguish between neuronal and hydrodynamically-driven effects of the brain vasculature and could help to make BOLD fMRI more interpretable.

The challenges

There were many technological challenges that needed to be identified and overcome to achieve these goals. The main challenge was to take the existing VASO methods and make them more applicable for investigations of neurovascular mechanisms in fMRI. In order to do so, it was necessary to substantially improve the limited sensitivity of the existing VASO methods by an order of magnitude. Considerable challenges and physical limitations in implementing the novel high sensitivity SS-SI VASO approach were (A) large inhomogeneities in the radio frequency fields making it difficult to manipulate the blood and tissue magnetizations as desired, (B) contaminations by blood oxygenation driven susceptibility changes, (C) contaminations by inflowing blood magnetization that could not be manipulated as desired, and (D) contaminations by dynamic changes in volume compartments aside of blood, e.g. CSF.

The accomplishments

In order to meet the sensitivity challenges, a novel approach was developed for high magnetic fields, where stationary tissue magnetization is manipulated differently from the magnetization of flowing blood. This could improve the signal magnitude up to a factor of 10. Such improvements in sensitivity could be accomplished by application of sophisticated slab-inversion and slice-saturation pulses adjusted to the vascular physiology of the human brain. Further sensitivity enhancement could be achieved by optimized MRI signal acquisition strategies, tailored to the person's brain geometry and noise characteristics. In order to successfully manipulate the inflowing blood magnetization despite severe interferences of radio frequency fields, new versions of partial inversion adiabatic RF pulses were successfully designed, validated, and implemented. BOLD contamination could be assessed and eliminated by separation and individual analysis of longitudinal

and transversal relaxation components in the acquired MR signal.
After all the challenges had been successfully addressed, the novel SS-SI VASO method could be applied to fulfill the main goal of this thesis. Namely, SS-SI VASO was used to investigate the limits of conventional BOLD fMRI. This was accomplished in the context of some of the most debated fMRI research topics, where the interpretation of conventional BOLD fMRI results is highly problematic:

- Negative BOLD responses occur in regions close to positive BOLD response or for a short period right after positive activation. The origin and the underlying mechanism of the negative BOLD responses were still unclear. The application of the new SS-SI VASO method in this thesis helped to improve the understanding of negative BOLD responses up to the level of individual vascular compartments of arteries, microvascular arterioles, venules, and veins. It was shown that negative BOLD is accompanied by different vascular mechanisms and has different hydrodynamic contaminations compared to positive activation.
- One of the most severe limitation of BOLD fMRI beside its interpretability is its local specificity at high resolutions, e.g. investigating responses across cortical layers. In the studies of this thesis, it could be shown that the new SS-SI VASO method can map layer-dependent neural activity with higher localization specificity than the conventional BOLD fMRI.
- The good quantifiability of SS-SI VASO in this thesis was even taken one step further. It was possible to not only estimate the vascular response, but also to assess the oxidative energy metabolism accompanying neural activity changes. In order to accomplish this, an existing biophysical tissue model was adapted for the use of the new SS-SI VASO method. The corresponding results shown here, suggest that the high intrinsic sensitivity of the new SS-SI VASO method can be useful to estimate oxygen metabolism despite the noise limitations of such calculations.
- With the development and application of the new SS-SI VASO method, important neurovascular features, which were only accessible in animal models so far, became visible in human volunteers. In this respect, the new SS-SI VASO method has been helpful to translate results from animal research to humans. Therefore, the new method could help to reduce the necessity of animal research by conducting the corresponding experiments directly and noninvasively in human volunteers.

The future

Even with all the signal enhancements applied, sensitivity of conventional BOLD fMRI is still superior to the new SS-SI VASO method. Hence, VASO fMRI will probably never find as wide application as BOLD fMRI. However, it plays an indispensable role, when it comes to quantitative, noninvasive imaging of CBV in human volunteers. Therefore, the new SS-SI VASO method might become an important neuroimaging tool for applications, when the interpretation of conventional BOLD fMRI is ambiguous. This is particularly the case when the interplay of neuronal and vascular effects in the fMRI BOLD signals is unknown and the individual effects of their signal components need to be considered separately. In this respect, SS-SI VASO can help to enlarge the extent of the fMRI research field. The information obtained from SS-SI VASO can be useful to indicate if the BOLD signal can or can't be trusted to be neural in origin or if BOLD signal is dominated from vascular artifacts. Hence, SS-SI VASO can make it possible to address questions in research areas like brain plasticity, aging, and the effects of psychotropic substances (e.g. caffeine), where the interpretability of conventional BOLD fMRI is limited by potential vascular contaminations.

In the studies of this thesis, it could be shown that SS-SI VASO has sufficient sensitivity to detect very small responses, which suggests its principle applicability to cognitive studies. The actual application of SS-SI VASO to address cognitive research questions, like the afferent and efferent activity characteristics during more cognitive tasks remains to be shown in the future. Technical signal acquisition improvements regarding an enlarged 3D coverage and therefore higher acquisition efficiency can help in the future to extend the usage of SS-SI VASO to a wider range of applications.

The experimental developments and technical approaches in this thesis to meet the challenges at high magnetic field strengths could be transferred to other methods aside from VASO in the future. Therefore, the work of this thesis could help other imaging methods to harvest the full potential SNR increase at high magnetic fields, as well. For example, the application of specifically designed adiabatic radio frequency pulses, using EPI-T_1 maps as anatomical reference, and multi-echo models to distinguish between different T_2^* components can be directly transferred to other MRI methods, such as high field ASL or high resolution BOLD fMRI in humans.

SS-SI VASO is based on a very simple, widely accessible inversion-recovery sequence and thus it could be easily applies by any researcher without essential technical or physiological background knowledge. However, due to the need to account for numerous potential artifacts in SS-SI VASO, its application becomes nontrivial. All the necessary work in adjusting the sequence parameters to eliminate these artifacts can hamper the straightforward application of SS-SI VASO. However, investing the time to implement these application-dependent customizations can be worthwhile. It is shown here that doing so, the clear quantifiability, and better localization specificity of SS-SI VASO compared to conventional fMRI methods can be highly rewarding.

Acknowledgments

Doing my thesis as part of a multi-discipline research team, it is based on the enormous help of many contributors. First of all, I want to express my deepest gratitude to my supervisors Prof. Dr. Harald Möller and Prof. Dr. Robert Turner. I thank Harald Möller for his positive attitude, his firm belief in this project and the calm guidance throughout the three years of this work. He provided me a free, friendly, and most stimulating research environment I can imagine. I thank Bob Turner for his scientific rigor, his inquiring mind, and his enthusiasm, which has been greatly inspiring during the time co-supervising this thesis. His idea about BOLD correction based on dynamic division has turned out to be highly rewarding in this thesis. He introduced me into the global fMRI community enabling most beneficial discussions with experts in the field. I thank my supervisors for giving me the opportunity with this PhD project to pursue working on the subject of my master studies, in which I gained the first experiences with VASO already.

I would like to sincerely thank my collaborator from the Max Planck Institute in Tübingen Dr. Jozien Goense for the original motivation of investigating CBV changes in regions of negative BOLD responses. She managed all monkey experiments of this thesis, she helped me in stimulus design to evoke negative BOLD responses. She kindly provided me many helpful tips for the high resolution fMRI acquisition and evaluations. Furthermore, I appreciated her rigorous critique of multiple publications and the corresponding chapters of this thesis. I am particularly thankful to my friend and collaborator Dr. Aneurin Kennerley from the University of Sheffield, UK. His continuous believe in the ignorance of the experts resulted in the motivation of many studies of this thesis, e.g. quantitative validation of CBV weighting in VASO, investigating arterial and venous contribution to CBV change in the post-stimulus period, and investigating of ventricular volume during hypercapnia. He helped me conducting all rat experiments of this thesis and he did the calculation of OIS wavelengths to CBV.

I am thankful to Benedikt Poser for helping with the implementation of additional echoes into the sequence code. Furthermore, his sequence for simultaneous multi-slice acquisition was the basis of the implementation of SMS-VASO shown in Fig. 5.10. I sincerely thank Dr. Dimo Ivanov. He taught me how to operate an MR scanner and a gas system for breathing challenges. His enormous knowledge about the fMRI literature helped me to get a good and fast overview of the current scientific discussions. I want to sincerely thank Prof. Dr. Claudine Gauthier for many valuable discussions on fMRI. Her brilliant and thorough understanding of brain physiology and modest attitude has been highly inspiring. I want to thank Prof. Dr. Hanzhang Lu for insightful discussions about effects of permeability in SS-SI VASO giving the motivation of developing the 101 compartment model in section 5.1. I want acknowledge helpful discussions with Prof. Dr. Seong-

Gi Kim regarding the possible volume change of CSF at the cortical surface leading to section 5.4. I am thankful to Prof. Dr. Jun Hua for continuous discussion about VASO at high fields and for the numerous literature recommendations. I thank Prof. Dr. Bruce Pike for sharing unpublished data of his student Claire Cohalan comparing VASO and VERVE.

I would like to express my gratitude to my colleagues Dr. Andreas Schäfer, Dr. Robert Trampel for support, valuable discussions, keeping the scanner functional and making me smile. I want to thank Maria Guidi and Kathrin Lorenz, who are not only smart and talented office mates, but became good friends as well. I thank Steffen Krieger for his help with the implementation of the double-echo EPI and multiple discussions about the FAIR sequence used in section 4.1. Maria Guidi, Robert Trampel, Cornelius Eichner, Steffen Krieger and Lena Mueller are also acknowledged for proof reading this thesis. I acknowledge my friend and colleague Carsten Stüber for kindly sharing histological images used as background in Fig. 2.2. I thank Dr. Chloe Hutton for sharing her Matlab scripts used for processing of end-tidal partial pressures during gas experiments. I want to thank Jöran Lepsien for helping me with eye-tracking measurements inside the scanner bore. I thank Dr. Toralf Mildner for insightful discussions about the inflow effects in SS-SI VASO, introducing me to sequence programming in for Bruker scanners, and helping me performing two in vivo experiments at 3 T. I thank Dr. Ilona Henseler, Dr. Elisabeth Roggenhofer, Dr. Stephan Kabisch and especially Dr. Leonie Lampe for medical supervision of experiments in humans with hypercapnia. I thank Domenica Wilfling and Elisabeth Wladimirow for helping take care of the volunteers. I am grateful to Daniel Zaldivar, Thomas Steudel, and Deniz Ipek for assistance with the monkey experiments and to Prof. Dr. Nikos Logothetis for allowing me to perform them in his laboratory. I appreciated the help from Heike Schmidt-Duderstedt in designing many figures of this thesis. I thank Enrico Reimer for continuous IT-support regarding MRI data conversion, providing the framework for C++ based MRI data evaluation, and for developing a 3D MRI data projection viewer for planning of experiments. I thank Dr. Alexis Amadon for sharing his MAFI sequence code that was used for B_1-mapping. I thank Alexander Kranz for access to a Bruker Paravision 5.1 System needed for validation of SS-SI VASO sequence code applied in monkeys. I thank Dr. Nicole Neef for shared excitement in negative BOLD and for allowing me to continue in working with high resolution VASO, although she was also interested in using this method. I am thankful to all volunteers participating in the studies of this thesis. I thank Dr. Robin Heidemann and the Siemens AG for helping me setting up a sequence programming environment and for continuously challenging my programming skills with their software distribution politics. I want to thank Dr. Jason Berwick for his financial support to travel to Sheffield and conduct VASO experiments in rats with Dr. Aneurin Kennerley. I thank Prof. Dr. Ǩamil Uludağ for inviting me to an MR sequence programming seminar in Maastricht in 2013. I thank the ISMRM for financial support regarding the travels expenses to numerous conferences and workshops in the form of educational stipends.

Lastly, I want to thank my loved ones, my family and friends for being there for me during my first three decades of education. I am looking forward to the next one.

Bibliography

[Abbas, 2009] Abbas, Z. (2009). *MR-parameter mapping of human brain at 7 tesla.* Master thesis.

[Abraham, 1961] Abraham, A. (1961). *The principles of nuclear magnetism.* Oxford University Press.

[An and Lin, 2002] An, H. and Lin, W. (2002). Cerebral venous and arterial blood volumes can be estimated separately in humans using magnetic resonance imaging. *Magnetic Resonance in Medicine*, 48:583–588.

[Ances et al., 2008] Ances, B. M., Leontiev, O., Perthen, J. E., Liang, C., Lansing, A. E., and Buxton, R. B. (2008). Regional differences in the coupling of cerebral blood flow and oxygen metabolism changes in response to activation: Implications for BOLD-fMRI. *NeuroImage*, 39:1510–1521.

[Anderson et al., 2006] Anderson, J., Shafi, N. I., and Brayan, R. M. (2006). Endothelial influence on cerebrovascular tone. *Journal of Applied Physiology*, 100:318–327.

[Bandettini, 2012] Bandettini, P. A. (2012). The BOLD plot thickens: sign- and layer-dependent hemodynamic changes with activation. *Neuron*, 76:468–469.

[Bandettini et al., 1992] Bandettini, P. A., Wong, E. C., Hinks, R. S., Tikofsky, R. S., and Hyde, J. S. (1992). Time course EPI of human brain function during task activation. *Magnetic Resonance in Medicine*, 25:390–397.

[Bause et al., 2014] Bause, J., Ehses, P., Shajan, G., Scheffler, K., and Pohmann, R. (2014). Functional ASL at 9.4 T - a comparison between balanced SSFP and GRE-EPI readout. In *Proceedings of the International Society of Magnetic Resonance in Medicine*, volume 22, page 1425.

[Bazin et al., 2013] Bazin, P.-l., Schäfer, A., Dinse, J., Tardif, C., Waehnert, M., Hashim, E., Huber, L., Geyer, S., Bock, N., and Turner, R. (2013). Fine details of cortical and sub-cortical anatomy revealed in-vivo by ultra-high resolution quantitative T1 mapping. In *Proceedings of the Organisation of Human Brain Mapping*, number 1, page 3384.

[Belliveau et al., 1991] Belliveau, J. W., Kennedy, D. N., McKinstry, R. C., Buchbinder, B. R., Weisskoff, R. M., Cohen, M. S., Vevea, J. M., Brady, T. J., and Rosen, B. R. (1991). Functional mapping of the human visual cortex by magnetic resonance imaging. *Science*, 254:716–719.

[Bereczki et al., 1993] Bereczki, D., Wei, L., Otsuka, T., Hans, F. J., Acuff, V., Patlak, C., and Fenstermacher, J. (1993). Hypercapnia slightly raises blood volume and sizably elevates flow velocity in brain microvessels. *American Journal of Physiology-Heart and Circulatory Physiology*, 264:H1360–H1369.

[Berwick et al., 2005] Berwick, J., Johnston, D., Jones, M., McLaughlin, A. C., Redgrave, P., McLoughlin, N., Schiessl, I., and Mayhew, J. E. (2005). Neurovascular coupling investigated with two-dimensional optical imaging spectroscopy in rat whisker barrel cortex. *European Journal of Neuroscience*, 22:1655–1666.

[Berwick et al., 2002] Berwick, J., Martin, C., McLaughlin, A. C., Jones, M., Johnston, D., Zheng, Y., Redgrave, P., and Mayhew, J. E. (2002). Hemodynamic response in the unanesthetized rat: Intrinsic optical imaging and spectroscopy of the barrel cortex. *Journal of Cerebral Blood Flow and Metabolism*, 22:670–679.

[Blockley et al., 2011] Blockley, N. P., Driver, I. D., Fisher, J. A., Francis, S. T., and Gowland, P. A. (2011). Measuring venous blood volume changes during activation using hyperoxia. *NeuroImage*, 59:3266–3274.

[Blockley et al., 2013] Blockley, N. P., Griffeth, V. E. M., Simon, A. B., and Buxton, R. B. (2013). A review of calibrated blood oxygenation level-dependent (BOLD) methods for the measurement of task-induced changes in brain oxygen metabolism. *NMR in Biomedicine*, 26:987–1003.

[Boas et al., 2014] Boas, D. a., Elwell, C. E., Ferrari, M., and Taga, G. (2014). Twenty years of functional near-infrared spectroscopy: Introduction for the special issue. *NeuroImage*, 85:1–5.

[Bohraus et al., 2013] Bohraus, Y., Goense, J. B. M., and Logothetis, N. K. (2013). Decreased cerebral blood volume and flow in areas with negative BOLD indicates the mechanism for negative BOLD may be stimulus- and area-specific. In *Proceedings of the International Society of Magnetic Resonance in Medicine*, volume 21, page 2341.

[Boorman et al., 2010] Boorman, L., Kennerley, A. J., Johnston, D., Jones, M., Zheng, Y., Redgrave, P., and Berwick, J. (2010). Negative blood oxygen level dependence in the rat: A model for investigating the role of suppression in neurovascular coupling. *Journal of Neuroscience*, 30:4285–4294.

[Boulant et al., 2009] Boulant, N., Mangin, J.-F., and Amadon, A. (2009). Counteracting radio frequency inhomogeneity in the human brain at 7 tesla using strongly modulating pulses. *Magnetic Resonance in Medicine*, 61:1165–1172.

[Boyacioğlu et al., 2014] Boyacioğlu, R., Schulz, J., Müller, N. C. J., Koopmans, P. J., Barth, M., and Norris, D. G. (2014). Whole brain, high resolution multiband spin-echo EPI fMRI at 7T: A comparison with gradient-echo EPI using a color-word Stroop task. *NeuroImage*, 97:142–150.

[Brodmann, 1909] Brodmann, K. (1909). *Vergleichende Lokalisationslehre der Großhirnrinde*. Verlag von Johann Ambrosian Barth, Leipzig.

[Budde et al., 2014] Budde, J., Shajan, G., Zaitsev, M., Scheffler, K., and Pohmann, R. (2014). Functional MRI in human subjects with gradient-echo and spin-echo EPI at 9.4 T. *Magnetic Resonance in Medicine*, 71:209–218.

[Buxton, 2009] Buxton, R. B. (2009). *Introduction to functional magnetic resonance imaging*. Cambridge University Press.

[Buxton, 2010] Buxton, R. B. (2010). Interpreting oxygenation-based neuroimaging signals: The importance and the challenge of understanding brain oxygen metabolism. *Frontiers in Neuroenergetics*, 2:Article 8.

[Buxton et al., 2014] Buxton, R. B., Griffeth, V. E. M., Simon, A. B., and Moradi, F. (2014). Variability of the coupling of blood flow and oxygen metabolism responses in the brain: A problem for interpreting BOLD studies but potentially a new window on the underlying neural activity. *Frontiers in Neuroscience*, 8:Article 139.

[Buxton et al., 2004] Buxton, R. B., Uludağ, K., Dubowitz, D. J., and Liu, T. T. (2004). Modeling the hemodynamic response to brain activation. *NeuroImage*, 23 Suppl. 1:S220–S233.

[Buxton et al., 1998] Buxton, R. B., Wong, E. C., and Frank, L. R. (1998). Dynamics of blood flow and oxygenation changes during brain activation: The balloon model. *Magnetic Resonance in Medicine*, 39:855–864.

[Calamante et al., 1999] Calamante, F., Thomas, D., Pell, G. S., and Wiersma, J. (1999). Measuring cerebral blood flow using magnetic resonance imaging techniques. *Journal of Cerebral Blood Flow and Metabolism*, 19:701–735.

[Chen et al., 2014a] Chen, B. R., Kozberg, M. G., Bouchard, M. B., Shaik, M. A., and Hillman, E. M. C. (2014a). A critical role for the vascular endothelium in functional neurovascular coupling in the brain. *Journal of the American Heart Association*, 3:e000787.

[Chen et al., 2014b] Chen, G., Cloos, M., Lattanzi, R., Sodickson, D., and Wiggins, G. (2014b). Bent electric dipoles: A novel coil design inspired by the ideal current pattern for central SNR at 7 tesla. In *Proceedings of the International Society of Magnetic Resonance in Medicine Resonance in Medicine*, volume 22, page 402.

[Chen and Pike, 2009] Chen, J. J. and Pike, G. B. (2009). Origins of the BOLD post-stimulus undershoot. *NeuroImage*, 46:559–568.

[Chen and Pike, 2010a] Chen, J. J. and Pike, G. B. (2010a). Global cerebral oxidative metabolism during hypercapnia and hypocapnia in humans: Implications for BOLD fMRI. *Journal of Magnetic Resonance Imaging*, 30:1094–1099.

[Chen and Pike, 2010b] Chen, J. J. and Pike, G. B. (2010b). MRI measurement of the BOLD-specific flow-volume relationship during hypercapnia and hypocapnia in humans. *NeuroImage*, 53:383–391.

[Chen et al., 2012] Chen, Y., Wang, D. J. J., and Detre, J. A. (2012). Comparison of arterial transit times estimated using arterial spin labeling. *Magnetic Resonance Materials in Physics, Biology and Medicine*, 25:135–144.

[Chiarelli et al., 2007] Chiarelli, P. A., Bulte, D. P., Wise, R. G., Gallichan, D., and Jezzard, P. (2007). A calibration method for quantitative BOLD fMRI based on hyperoxia. *NeuroImage*, 37:808–820.

[Ciris et al., 2013] Ciris, P. A., Qiu, M., and Constable, R. T. (2013). Non-invasive quantification of absolute cerebral blood volume during functional activation applicable to the whole human brain. *Magnetic Resonance in Medicine*, 71:580–590.

[Cohalan et al., 2009] Cohalan, C., Chen, J. J., and Pike, G. B. (2009). Neuronal activity-induced cerebral blood volume changes in humans: Measurements with VASO and VERVE. In *Proceedings of the International Society of Magnetic Resonance in Medicine*, volume 17, page 13.

[Cramer et al., 1999] Cramer, S. C., Finklestein, S. P., Schaechter, J. D., Bush, G., and Rosen, B. R. (1999). Activation of distinct motor cortex regions during ipsilateral and contralateral finger movements. *Journal of Neurophychology*, 81:383–7.

[Cretti et al., 2013] Cretti, F. R., Summers, P. E., and Porro, C. A. (2013). Multi-shot turbo spin-echo for 3D vascular space occupancy imaging. *Magnetic Resonance Imaging*, 31:875–881.

[Czosnyka et al., 2004] Czosnyka, M., Czosnyka, Z., Pickard, J. D., and Momjian, S. (2004). Cerebrospinal fluid dynamics. *Physiological Measurement*, 25:R51–R76.

[Davis et al., 1998] Davis, T. L., Kwong, K. K., Rosen, B. R., and Weisskoff, R. M. (1998). Calibrated functional MRI: Mapping the dynamics of oxidative metabolism. *Proceedings of the National Academy of Sciences*, 95:1834–1839.

[De Martino et al., 2013] De Martino, F., Zimmermann, J., Muckli, L., Uğurbil, K., Yacoub, E., and Goebel, R. (2013). Cortical depth dependent functional responses in humans at 7T: Improved specificity with 3D GRASE. *PloS one*, 8:e60514.

[Dechent et al., 2011] Dechent, P., Schütze, G., Helms, G., Merboldt, K. D., and Frahm, J. (2011). Basal cerebral blood volume during the poststimulation undershoot in BOLD MRI of the human brain. *Journal of Cerebral Blood Flow and Metabolism*, 31:82–89.

[Detre et al., 1992] Detre, J. A., Leigh, J. S., Williams, D. S., and Koretsky, A. P. (1992). Perfusion Imaging. *Magnetic Resonance in Medicine*, 23:37–45.

[Dettmers et al., 1995] Dettmers, C., Fink, G. R., Lemon, R. N., Stephan, K. M., Passingham, R. E., Silbersweig, D., Holmes, A., Ridding, M. C., Brooks, D. J., and Frackowiak, S. J. (1995). Relation Between Cerebral Activity the Human Brain and Force in the Motor Areas of. *Journal of Neurophychology*, 74:802–816.

[Devor and Boas, 2012] Devor, A. and Boas, D. A. (2012). Neurovascular imaging. *Frontiers in Neuroenergetics*, 4:Article 1.

[Devor et al., 2008] Devor, A., Hillman, E. M. C., Tian, P., Waeber, C., Teng, I. C., Ruvinskaya, L., Shalinsky, M. H., Zhu, H., Haslinger, R. H., Narayanan, S. N., Ulbert, I., Dunn, A. K., Lo, E. H., Rosen, B. R., Dale, A. M., Kleinfeld, D., and Boas, D. A. (2008). Stimulus-induced changes in blood flow and 2-deoxyglucose uptake dissociate in ipsilateral somatosensory cortex. *Journal of Neuroscience*, 28:14347–14357.

[Devor et al., 2012] Devor, A., Sakadzic, S., Srinivasan, V. J., Yaseen, M. A., Nizar, K., Saisan, P. A., Tian, P., Dale, A. M., Vinogradov, S. A., Franceschini, M. A., and Boas, D. A. (2012). Frontiers in optical imaging of cerebral blood flow and metabolism. *Journal of Cerebral Blood Flow and Metabolism*, 32:1259–1276.

[Dobre et al., 2006] Dobre, M. C., Uludağ, K., and Marjanska, M. (2006). Determination of longitudinal relaxation time (T1) at high magnetic field strengths. *Magnetic Resonance Imaging*, 25:733–735.

[Donahue et al., 2009a] Donahue, M. J., Blicher, J. U., Østergaard, L., Feinberg, D. A., MacIntosh, B. J., Miller, K. L., Günther, M., and Jezzard, P. (2009a). Cerebral blood flow, blood volume, and oxygen metabolism dynamics in human visual and motor cortex as measured by whole-brain multi-modal magnetic resonance imaging. *Journal of Cerebral Blood Flow and Metabolism*, 29:1856–1866.

[Donahue et al., 2010] Donahue, M. J., Hoogduin, H., van Zijl, P. C. M., Jezzard, P., Luijten, P. R., and Hendrikse, J. (2010). Blood oxygenation level-dependent (BOLD) total and extravascular signal changes and ΔR2* in human visual cortex at 1.5, 3.0 and 7.0 T. *NMR in Biomedicine*, 24:25–34.

[Donahue et al., 2009b] Donahue, M. J., Hua, J., Pekar, J. J., and van Zijl, P. C. M. (2009b). Effect of inflow of fresh blood on vascular-space-occupancy (VASO) contrast. *Magnetic Resonance in Medicine*, 61:473–480.

[Donahue et al., 2006] Donahue, M. J., Lu, H., Jones, C. K., Edden, R. A. E., Pekar, J. J., and van Zijl, P. C. M. (2006). Theoretical and experimental investigation of the VASO contrast mechanism. *Magnetic Resonance in Medicine*, 56:1261–1273.

[Donahue et al., 2009c] Donahue, M. J., Stevens, R. D., de Boorder, M., Pekar, J. J., Hendrikse, J., and van Zijl, P. C. M. (2009c). Hemodynamic changes after visual stimulation and breath holding provide evidence for an uncoupling of cerebral blood flow and volume from oxygen metabolism. *Journal of Cerebral Blood Flow and Metabolism*, 29:176–185.

[Donchin et al., 2002] Donchin, O., Gribova, A., Steinberg, O., Mitz, A. R., Bergman, H., and Vaadia, E. (2002). Single-unit activity related to bimanual arm movements in the primary and supplementary motor cortices. *Journal of Neurophychology*, 88:3498–3517.

[Duvernoy et al., 1981] Duvernoy, H. M., Delon, S., and Vannson, J. L. (1981). Cortical blood vessels of the human brain. *Brain Research*, 7:519–579.

[Edelstein et al., 1986] Edelstein, W. A., Glover, G. H., Hardy, C. J., and Redington, R. W. (1986). The intrinsic signal-to-noise ratio in NMR imaging. *Magnetic Resonance in Medicine*, 3:604–618.

[Ekstedt, 1978] Ekstedt, J. (1978). CSF hydrodynamic studies in man. *Journal of Neurology, and Psychiatry*, 41:345–353.

[Ewing et al., 2013] Ewing, J. R., Bonekamp, D., and Barker, P. B. (2013). Imaging of flow: Basic principles. In Barker, P. B., Golay, X., and Zaharchuk, G., editors, *Clinical Perfusion MRI Techniques and Applications*, pages 1–15.

[Feynman et al., 1957] Feynman, R. P., Vernon, F. L., and Hellwarth, R. W. (1957). Geometrical representation of the Schrödnger equation for solving maser problems. *Journal of Applied Physics*, 28:49–52.

[Figueiredo et al., 2005] Figueiredo, P., Clare, S., and Jezzard, P. (2005). Quantitative perfusion measurements using pulsed arterial spin labeling: Effects of large region-of-interest analysis. *Journal of Magnetic Resonance Imaging*, 21:676–682.

[Fischl and Dale, 2000] Fischl, B. and Dale, A. M. (2000). Measuring the thickness of the human cerebral cortex from magnetic resonance images. *Proceedings of the National Academy of Sciences*, 97:11050–11055.

[Francis et al., 2008] Francis, S. T., Bowtell, R., and Gowland, P. A. (2008). Modeling and optimization of Look-Locker spin labeling for measuring perfusion and transit time changes in activation studies taking into account arterial blood volume. *Magnetic Resonance Imaging*, 59:316–325.

[Frank et al., 1994] Frank, J. A., Massay, V., Duyn, J. H., Soberin, G., Barrios, F., Zigun, J., Sexton, R., Kwok, P., Woo, J., and Moonen, C. (1994). Measurement of relative cerebral blood volume changes with visual stimulation by double dose gadopentate dimeglumine enhanced dynamic magnetic resonance imaging. *Investigative Radiology*, 29:157–160.

[Gagnon et al., 2013] Gagnon, L., Sakadzic, S., Devor, A., Fang, Q., Lesage, F., Mandeville, E. T., Srinivasan, V. J., Yaseen, M. A., Roussakis, E., Lo, E. H., Vinogradov, S. A., Buxton, R. B., Dale, A. M., and Boas, D. A. (2013). Modeling the fMRI signals at the microscopic level using quantitative optical microscopy measurements. In *Proceedings of the International Society of Magnetic Resonance in Medicine*, volume 21, page 3244.

[Galassi et al., 2009] Galassi, M., Gough, B., and Booth, M. (2009). *GNU scientific library reference manual*. Network Theory Ltd.

[Gardener et al., 2010] Gardener, A. G., Francis, S. T., Prior, M., Peters, A., and Gowland, P. A. (2010). Dependence of blood R2 relaxivity on CPMG echo-spacing at 2.35 and 7 T. *Magnetic Resonance in Medicine*, 64:967–974.

[Gardener et al., 2009] Gardener, A. G., Gowland, P. A., and Francis, S. T. (2009). Implementation of quantitative perfusion imaging using pulsed arterial spin labeling at ultra-high field. *Magnetic Resonance in Medicine*, 61:874–882.

[Gauthier and Hoge, 2012] Gauthier, C. J. and Hoge, R. D. (2012). Magnetic resonance imaging of resting OEF and CMRO2 using a generalized calibration model for hypercapnia and hyperoxia. *NeuroImage*, 60:1212–1225.

[Germuska and Bulte, 2014] Germuska, M. A. and Bulte, D. P. (2014). MRI measurement of oxygen extraction fraction, mean vessel size and cerebral blood volume using serial hyperoxia and hypercapnia. *NeuroImage*, 92:132–142.

[Ginsberg et al., 1985] Ginsberg, M. D., Busto, R., and Harik, S. I. (1985). Regional blood-brain barrier permeability to water and cerebral blood flow during status epilepticus: Insensitivity to norepinephrine depletion. *Brain Research*, 337:59–71.

[Giovacchini et al., 2002] Giovacchini, G., Chang, M. C., Channing, M. A., Toczek, M., Mason, A., Bokde, A. L., Connolly, C., Vuong, B. K., Ma, Y., Der, M. G., Doudet, D. J., Herscovitch, P., Eckelman, W. C., Rapoport, S. I., and Carson, R. E. (2002). Brain incorporation of 11C-arachidonic acid in young healthy humans measured with positron emission tomography. *Journal of Cerebral Blood Flow and Metabolism*, 22:1453–1462.

[Glielmi et al., 2009] Glielmi, C. B., Schuchard, R. A., and Hu, X. P. (2009). Estimating cerebral blood volume with expanded vascular space occupancy slice coverage. *Magnetic Resonance in Medicine*, 61:1193–1200.

[Goense and Logothetis, 2008] Goense, J. B. M. and Logothetis, N. K. (2008). Neurophysiology of the BOLD fMRI signal in awake monkeys. *Current Biology*, 18:631–640.

[Goense et al., 2010] Goense, J. B. M., Logothetis, N. K., and Merkle, H. (2010). Flexible, phase-matched, linear receive arrays for high-field MRI in monkeys. *Magnetic Resonance Imaging*, 28:1183–1191.

[Goense et al., 2012] Goense, J. B. M., Merkle, H., and Logothetis, N. K. (2012). High-resolution fMRI reveals laminar differences in neurovascular coupling between positive and negative BOLD responses. *Neuron*, 76:629–639.

[Goense et al., 2007] Goense, J. B. M., Zappe, A.-C., and Logothetis, N. K. (2007). High-resolution fMRI of macaque V1. *Magnetic Resonance Imaging*, 25:740–747.

[Gordon et al., 2011] Gordon, G. R., Howarth, C., and MacVicar, B. A. (2011). Bidirectional control of arteriole diameter by astrocytes. *Experimental Physiology*, 98:393–399.

[Gray and Steadman, 1964] Gray, L. H. and Steadman, J. M. (1964). Determination of the oxyhaemoglobin dissociation curves for mouse and rat blood. *Journal of Physiology*, 175:161–171.

[Grgac et al., 2012] Grgac, K., van Zijl, P. C. M., and Qin, Q. (2012). Hematocrit and oxygenation dependence of blood H2O T1 at 7 tesla. *Magnetic Resonance in Medicine*, 70:1153–1159.

[Griffeth and Buxton, 2011] Griffeth, V. E. M. and Buxton, R. B. (2011). A theoretical framework for estimating cerebral oxygen metabolism changes using the calibrated-BOLD method: Modeling the effects of blood volume distribution, hematocrit, oxygen extraction fraction, and tissue signal properties on the BOLD signal. *NeuroImage*, 58:198–212.

[Grubb et al., 1974] Grubb, R. L., Raichle, M. E., Eichling, J. O., and Ter-Pogossian, M. M. (1974). The effects of changes in PaCO2 on cerebral blood volume, blood flow, and vascular mean transit time. *Stroke*, 5:630–639.

[Gu et al., 2006] Gu, H., Lu, H., Ye, F. Q., Stein, E. A., and Yang, Y. (2006). Noninvasive quantification of cerebral blood volume in humans during functional activation. *NeuroImage*, 30:377–387.

[Guidi et al., 2014] Guidi, M., Huber, L., Lampe, L., Gauthier, C. J., and Möller, H. E. (2014). Layer-dependent calibrated BOLD response in human M1. In *Imaging Cerebral Physiology: Manipulating Magnetic Resonance Contrast through Respiratory Challenges*, volume 2, page O1.

[Hall et al., 2014] Hall, C. N., Reynell, C., Gesslein, B., Hamilton, N. B., Mishra, A., Sutherland, B. A., O Farrell, F. M., Buchan, A. M., Lauritzen, M., and Attwell, D. (2014). Capillary pericytes regulate cerebral blood flow in health and disease. *Nature*, 508:55–60.

[Hall et al., 2011] Hall, E. L., Gowland, P. A., and Francis, S. T. (2011). Look-Locker 3D-EPI ASL at 7 T. In *Proceedings of the International Society of Magnetic Resonance in Medicine*, volume 19, page 3984.

[Hamilton et al., 2010] Hamilton, N. B., Attwell, D., and Hall, C. N. (2010). Pericyte-mediated regulation of capillary diameter: A component of neurovascular coupling in health and disease. *Frontiers in Neuroenergetics*, 2:Article 5.

[Hamzei et al., 2002] Hamzei, F., Dettmers, C., Rzanny, R., Liepert, J., Büchel, C., and Weiller, C. (2002). Reduction of excitability (inhibition) in the ipsilateral primary motor cortex is mirrored by fMRI signal decreases. *NeuroImage*, 17:490–496.

[Hanson, 2008] Hanson, L. G. (2008). Is quantum mechanics necessary for understanding magnetic resonance ? *Concepts in Magnetic Resonance*, 32A:329–340.

[Harel et al., 2002] Harel, N., Lee, S.-P., Nagaoka, T., Kim, D.-S., and Kim, S.-G. (2002). Origin of negative blood oxygenation level-dependent fMRI signals. *Journal of Cerebral Blood Flow and Metabolism*, 22:908–917.

[Harel et al., 2006] Harel, N., Lin, J., Moeller, S., Uğurbil, K., and Yacoub, E. (2006). Combined imaging-histological study of cortical laminar specificity of fMRI signals. *NeuroImage*, 29:879–887.

[Harmer et al., 2012] Harmer, J., Sanchez-Panchuelo, R. M., Bowtell, R., and Francis, S. T. (2012). Spatial location and strength of BOLD activation in high-spatial-resolution fMRI of the motor cortex: A comparison of spin echo and gradient echo fMRI at 7 T. *NMR in Biomedicine*, 25:717–25.

[Harrison et al., 2002] Harrison, R. V., Harris, N. G., Panesar, J., Mount, R. J., and Harel, N. (2002). Blood capillary distribution correlates with hemodynamic-based functional imaging in cerebral cortex. *Cerebral Cortex*, 12:225–233.

[Hennig et al., 1984] Hennig, J., Nauerth, A., Friedburg, H., and Ratzel, D. (1984). Ein neues Schnellbildverfahren für die Kernspintomographie. *Der Radiologe*, 24:579–580.

[Herman et al., 2009] Herman, P., Sanganahalli, B. G., and Hyder, F. (2009). Multi-modal measurements of blood plasma and red blood cell volumes during functional brain activation. *Journal of Cerebral Blood Flow and Metabolism*, 29:19–24.

[Hernandez-Garcia and Lewis, 2007] Hernandez-Garcia, L. and Lewis, D. (2007). Magnetization transfer effects on the efficiency of flow-driven adiabatic fast passage inversion of arterial blood. *NMR in Biomedicine*, 20:733–742.

[Herscovitch and Raichle, 1985] Herscovitch, P. and Raichle, M. E. (1985). What is the correct value for the brain-blood partition coefficient for water? *Journal of Cerebral Blood Flow and Metabolism*, 5:65–69.

[Herscovitch et al., 1987] Herscovitch, P., Raichle, M. E., Kilbourn, M. R., and Welch, M. J. (1987). Positron emission tomographic measurement of cerebral blood flow and permeability-surface area product of water using [15O] water and [11C] butanol. *Journal of Cerebral Blood Flow and Metabolism*, 7:527–542.

[Hetzer et al., 2011] Hetzer, S., Mildner, T., and Möller, H. E. (2011). A modified EPI sequence for high resolution imaging at ultra-short echo time. *Magnetic Resonance in Medicine*, 65:165–175.

[Hillman et al., 2007] Hillman, E. M. C., Devor, A., Bouchard, M. B., Dunn, A. K., Krauss, G. W., Skoch, J., Bacskai, B. J., Dale, A. M., and Boas, D. A. (2007). Depth-resolved optical imaging and microscopy of vascular compartment dynamics during somatosensory stimulation. *NeuroImage*, 35:89–104.

[Ho et al., 2011] Ho, Y.-C. L., Petersen, E. T., Zimine, I., and Golay, X. (2011). Similarities and differences in arterial responses to hypercapnia and visual stimulation. *Journal of Cerebral Blood Flow and Metabolism*, 31:560–571.

[Hoge, 2012] Hoge, R. D. (2012). Calibrated fMRI. *NeuroImage*, 62:930–937.

[Hoge et al., 1999] Hoge, R. D., Atkinson, J., Gill, B., Crelier, G. R., Marrett, S., and Pike, G. B. (1999). Investigation of BOLD signal dependence on cerebral blood flow and oxygen consumption: The deoxyhemoglobin dilution model. *Magnetic Resonance in Medicine*, 42:849–863.

[Howarth, 2014] Howarth, C. (2014). The contribution of astrocytes to the regulation of cerebral blood flow. *Frontiers in Neuroscience*, 8:Article 103.

[Hsu et al., 2012] Hsu, Y.-Y., Chu, W.-C., Lim, K.-E., and Liu, H.-L. (2012). Vascular space occupancy MRI during breathholding at 3 tesla. *Journal of Magnetic Resonance Imaging*, 36:1179–1185.

[Hua et al., 2009] Hua, J., Donahue, M. J., Zhao, J. M., Grgac, K., Huang, A. J., Zhou, X. J., van Zijl, P. C. M., and Zhou, J. (2009). Magnetization transfer enhanced vascular-space-occupancy (MT-VASO) functional MRI. *Magnetic Resonance in Medicine*, 61:944–951.

[Hua et al., 2012] Hua, J., Jones, C. K., Qin, Q., and van Zijl, P. C. M. (2012). Implementation of vascular-space-occupancy MRI at 7T. *Magnetic Resonance in Medicine*, 69:1003–1013.

[Hua et al., 2011a] Hua, J., Qin, Q., Donahue, M. J., Zhou, J., Pekar, J. J., and van Zijl, P. C. M. (2011a). Inflow-based vascular-space-occupancy (iVASO) MRI. *Magnetic Resonance in Medicine*, 66:40–56.

[Hua et al., 2011b] Hua, J., Stevens, R. D., Huang, A. J., Pekar, J. J., and van Zijl, P. C. M. (2011b). Physiological origin for the BOLD poststimulus undershoot in human brain: Vascular compliance versus oxygen metabolism. *Journal of Cerebral Blood Flow and Metabolism*, 31:1599–1611.

[Huber, 2011] Huber, L. (2011). *Magnetic resonance imaging method for measuring functional cerebral blood volume changes at 7 tesla.* Master thesis, downloadable at: http://pubman.mpdl.mpg.de/pubman/item/escidoc:1752750:2.

[Huber et al., 2015a] Huber, L., Goense, J., Kennerley, A. J., Trampel, R., Guidi, M., Ivanov, D., Gauthier, C. J., Turner, R., and Möller, H. E. (2015a). Cortical lamina-dependent blood volume changes in human brain at 7 T. *NeuroImage*, 107:23–33.

[Huber et al., 2014a] Huber, L., Goense, J. B. M., Kennerley, A. J., Ivanov, D., Krieger, S. N., Lepsien, J., Trampel, R., Turner, R., and Möller, H. E. (2014a). Investigation of the neurovascular coupling in positive and negative BOLD responses in human brain at 7T. *NeuroImage*, 97:349–362.

[Huber et al., 2015b] Huber, L., Ivanov, D., Guidi, M., Turner, R., Uludağ, K., Möller, H. E., and Poser, B. A. (2015b). Simultaneous multi-slice functional CBV measurements at 7 T. In *Proceedings of the Inernational Society of Magnetic Resonance in Medicine*, volume 23, submitted.

[Huber et al., 2013] Huber, L., Ivanov, D., Krieger, S. N., Gauthier, C. J., Roggenhofer, E., Turner, R., and Möller, H. E. (2013). Measurements of cerebral blood volume and BOLD signal during hypercapnia and functional stimulation in humans at 7T: Application to calibrated BOLD. In *Proceedings of the International Society of Magnetic Resonance in Medicine*, volume 21, page 3339.

[Huber et al., 2014b] Huber, L., Ivanov, D., Krieger, S. N., Streicher, M. N., Mildner, T., Poser, B. A., Möller, H. E., and Turner, R. (2014b). Slab-selective, BOLD-corrected VASO at 7 tesla provides measures of cerebral blood volume reactivity with high signal-to-noise ratio. *Magnetic Resonance in Medicine*, 72:137–148.

[Huber et al., 2012] Huber, L., Ivanov, D., Roggenhofer, E., Henseler, I., Möller, H. E., and Turner, R. (2012). Hypercapnia-induced and stimulus-induced changes in cerebral blood volume in humans at 7T. In *ISMRM Brain Function Workshop in Whistler.*

[Huber et al., 2014c] Huber, L., Kennerley, A. J., Gauthier, C. J., Krieger, S. N., Maria Guidi, D. I., Turner, R., and Möller, H. E. (2014c). Cerebral blood volume redistribution during hypercapnia. In *Imaging Cerebral Physiology: Manipulating Magnetic Resonance Contrast through Respiratory Challenges*, volume 2, page O4.

[Huk et al., 2002] Huk, A. C., Dougherty, R. F., and Heeger, D. J. (2002). Retinotopy and functional subdivision of human areas MT and MST. *Journal of Neuroscience*, 22:7195–7205.

[Hurley et al., 2010] Hurley, A. C., Al-Radaideh, A., Bai, L., Aickelin, U., Coxon, R., Glover, P., and Gowland, P. A. (2010). Tailored RF pulse for magnetization inversion at ultrahigh field. *Magnetic Resonance in Medicine*, 63:51–58.

[Hutchinson et al., 2006] Hutchinson, E., Stefanovic, B., Koretsky, A. P., and Silva, A. C. (2006). Spatial flow-volume dissociation of the cerebral microcirculatory response to mild hypercapnia. *NeuroImage*, 32:520–530.

[Hutchison et al., 2013] Hutchison, J. L., Lu, H., and Rypma, B. (2013). Neural mechanisms of age-related slowing: The ΔCBF/ΔCMRO2 ratio mediates age-differences in BOLD signal and human performance. *Cerebral Cortex*, 23:2337–2346.

[Iadecola and Nedergaard, 2007] Iadecola, C. and Nedergaard, M. (2007). Glial regulation of the cerebral microvasculature. *Nature Neuroscience*, 10:1369–1376.

[Iida et al., 1989] Iida, H., Kanno, I., Miura, S., Murakami, M., Takahashi, K., and Uemura, K. (1989). A determination of the regional brain/blood partition coefficient of water using dynamic positron emission tomography. *Journal of Cerebral Blood Flow and Metabolism*, 9:874–885.

[Ito et al., 2001] Ito, H., Takahashi, K., Hatazawa, J., Kim, S.-G., and Kanno, I. (2001). Changes in human regional cerebral blood flow and cerebral blood volume during visual stimulation measured by positron emission tomography. *Journal of Cerebral Blood Flow and Metabolism*, 21:608–612.

[Ivanov, 2012] Ivanov, D. (2012). *Functional mapping of hemodynamic parameters and oxygen utilization in human brain using magnetic resonance imaging techniques at 7 tesla.* Phd thesis.

[Ivanov et al., 2013] Ivanov, D., Schäfer, A., Deistung, A., Streicher, M. N., Kabisch, S., Henseler, I., Roggenhofer, E., Jochimsen, T. H., Reichenbach, J., Uludağ, K., and Turner, R. (2013). In vivo estimation of the transverse relaxation time dependence of blood on oxygenation at 7 tesla. In *Proceedings of the International Society of Magnetic Resonance in Medicine*, volume 21, page 2472.

[Ivanov et al., 1981] Ivanov, K. P., Kalinina, M. K., and Levkovich, Y. I. (1981). Blood flow velocity in capillaries of brain and muscles and its physiological significance. *Microvascular Research*, 22:143–155.

[Jespersen and Østergaard, 2012] Jespersen, S. N. and Østergaard, L. (2012). The roles of cerebral blood flow, capillary transit time heterogeneity, and oxygen tension in brain oxygenation and metabolism. *Journal of Cerebral Blood Flow and Metabolism*, 32:264–277.

[Jiang et al., 2009] Jiang, J., Zhu, W., Shi, F., Liu, Y., Li, J., Qin, W., Li, K., Yu, C., and Jiang, T. (2009). Thick visual cortex in the early blind. *Journal of Neuroscience*, 29:2205–2211.

[Jin and Kim, 2006] Jin, T. and Kim, S.-G. (2006). Spatial dependence of CBV-fMRI: a comparison between VASO and contrast agent based methods. In *Conference Proceedings of the IEEE Engineering in Medicine and Biology Society.*, number 10, pages 25–28.

[Jin and Kim, 2008a] Jin, T. and Kim, S.-G. (2008a). Cortical layer-dependent dynamic blood oxygenation, cerebral blood flow and cerebral blood volume responses during visual stimulation. *NeuroImage*, 43:1–9.

[Jin and Kim, 2008b] Jin, T. and Kim, S.-G. (2008b). Improved cortical-layer specificity of vascular space occupancy fMRI with slab inversion relative to spin-echo BOLD at 9.4 T. *NeuroImage*, 40:59–67.

[Jin and Kim, 2010] Jin, T. and Kim, S.-G. (2010). Change of the cerebrospinal fluid volume during brain activation investigated by T1rho-weighted fMRI. *NeuroImage*, 51:1378–1383.

[Jochimsen et al., 2005] Jochimsen, T. H., Norris, D. G., and Möller, H. E. (2005). Is there a change in water proton density associated with functional magnetic resonance imaging? *Magnetic Resonance in Medicine*, 53:470–473.

[Jochimsen and von Mengershausen, 2004] Jochimsen, T. H. and von Mengershausen, M. (2004). ODIN-object-oriented development interface for NMR. *Journal of Magnetic Resonance*, 170:67–78.

[Keller et al., 2011] Keller, A. L., Schüz, A., Logothetis, N. K., and Weber, B. (2011). Vascularization of cytochrome oxidase-rich blobs in the primary visual cortex of squirrel and macaque monkeys. *Journal of Neuroscience*, 31:1246–1253.

[Kemper et al., 2014] Kemper, V. G., De Martino, F., Vu, A. T., Feinberg, D. A., Yacoub, E., and Goebel, R. (2014). Variable flip angle 3D-GRASE for increased spatial coverage and improved point spread function in high resolution fMRI at 7T. In *Proceedings of the Inernational Society of Magnetic Resonance in Medicine*, volume 22, page 2986.

[Kennerley et al., 2005] Kennerley, A. J., Berwick, J., Martindale, J., Johnston, D., Papadakis, N. G., and Mayhew, J. E. (2005). Concurrent fMRI and optical measures for the investigation of the hemodynamic response function. *Magnetic Resonance in Medicine*, 54:354–565.

[Kennerley et al., 2012a] Kennerley, A. J., Harris, S., Bruyns-Haylett, M., Boorman, L., Zheng, Y., Jones, M., and Berwick, J. (2012a). Early and late stimulus-evoked cortical hemodynamic responses provide insight into the neurogenic nature of neurovascular coupling. *Journal of Cerebral Blood Flow and Metabolism*, 32:468–480.

[Kennerley et al., 2013] Kennerley, A. J., Huber, L., Mildner, T., Mayhew, J. E., Turner, R., Möller, H. E., and Berwick, J. (2013). Does VASO contrast really allow measurement of CBV at high field (7 T)? An in-vivo quantification using concurrent optical imaging spectroscopy. In *Proceedings of the International Society of Magnetic Resonance in Medicine*, volume 21, page 0757.

[Kennerley et al., 2010] Kennerley, A. J., Mayhew, J. E., Berwick, J., and Redgrave, P. (2010). Vascular origins of BOLD and CBV fMRI signals: Statistical mapping and histological sections compared. *Open Neuroimaging Journal*, 4:1–8.

[Kennerley et al., 2012b] Kennerley, A. J., Mayhew, J. E., Boorman, L., Zheng, Y., and Berwick, J. (2012b). Is optical imaging spectroscopy a viable measurement technique for the investigation of the negative BOLD phenomenon? A concurrent optical imaging spectroscopy and fMRI study at high field (7 T). *NeuroImage*, 61:10–20.

[Keyeux et al., 1995] Keyeux, A., Ochrymowicz-Bemelmans, D., and Charlier, A. A. (1995). Induced response to hypereapnia in the two compartment total cerebral blood volume: Influence on brain vascular reserve and flow efficiency. *Journal of Cerebral Blood Flow and Metabolism*, 15:1121–1131.

[Kida et al., 2000] Kida, I., Kennan, R. P., Rothman, D. L., Behar, K. L., and Hyder, F. (2000). High-resolution CMRO2 mapping in rat cortex: A multiparametric approach to calibration of BOLD image contrast at 7 tesla. *Journal of Cerebral Blood Flow and Metabolism*, 20:847–860.

[Kida et al., 2007] Kida, I., Rothman, D. L., and Hyder, F. (2007). Dynamics of changes in blood flow, volume, and oxygenation: Implications for dynamic functional magnetic resonance imaging calibration. *Journal of Cerebral Blood Flow and Metabolism*, 27:690–696.

[Kim, 1995] Kim, S.-G. (1995). Quantification of relative cerebral blood flow change by flow-sensitive alternating inversion recovery (FAIR) technique: Application to functional mapping. *Magnetic Resonance in Medicine*, 34:293–301.

[Kim and Bandettini, 2010] Kim, S.-G. and Bandettini, P. A. (2010). *Principles of Functional MRI*, chapter Principles, pages 3–22. Springer-Verlag.

[Kim et al., 2013] Kim, S.-G., Harel, N., Jin, T., Kim, T., Lee, P., and Zhao, F. (2013). Cerebral blood volume MRI with intravascular superparamagnetic iron oxide nanoparticles. *NMR in Biomedicine*, 26:949–962.

[Kim and Ogawa, 2012] Kim, S.-G. and Ogawa, S. (2012). Biophysical and physiological origins of blood oxygenation level-dependent fMRI signals. *Journal of Cerebral Blood Flow and Metabolism*, 32:1188–1206.

[Kim et al., 1999] Kim, S.-G., Rostrup, E., Larsson, H. B. W., Ogawa, S., and Paulson, O. B. (1999). Determination of relative CMRO2 from CBF and BOLD changes: Significant increase of oxygen consumption rate during visual stimulation. *Magnetic Resonance in Medicine*, 41:1152–1161.

[Kim et al., 2007] Kim, T., Hendrich, K. S., Masamoto, K., and Kim, S.-G. (2007). Arterial versus total blood volume changes during neural activity-induced cerebral blood flow change: Implication for BOLD fMRI. *Journal of Cerebral Blood Flow and Metabolism*, 27:1235–1247.

[Kim and Kim, 2005] Kim, T. and Kim, S.-G. (2005). Quantification of cerebral arterial blood volume and cerebral blood flow using MRI with modulation of tissue and vessel (MOTIVE) signals. *Magnetic Resonance in Medicine Resonance in Medicine*, 54:333–342.

[Kim and Kim, 2010] Kim, T. and Kim, S.-G. (2010). Cortical layer-dependent arterial blood volume changes: improved spatial specificity relative to BOLD fMRI. *NeuroImage*, 49:1340–1349.

[Kim and Kim, 2011] Kim, T. and Kim, S.-G. (2011). Temporal dynamics and spatial specificity of arterial and venous blood volume changes during visual stimulation: Implication for BOLD quantification. *Journal of Cerebral Blood Flow and Metabolism*, 31:1211–1222.

[Kleinfeld et al., 1998] Kleinfeld, D., Mitra, P. P., Helmchen, F., and Denk, W. (1998). Fluctuations and stimulus-induced changes in blood flow observed in individual capillaries in layers 2 through 4 of rat neocortex. *Proceedings of the National Academy of Sciences*, 95:15741–15746.

[Koopmans et al., 2010] Koopmans, P. J., Barth, M., and Norris, D. G. (2010). Layer-specific BOLD activation in human V1. *Human Brain Mapping*, 31:1297–1304.

[Koopmans et al., 2011] Koopmans, P. J., Barth, M., Orzada, S., and Norris, D. G. (2011). Multi-echo fMRI of the cortical laminae in humans at 7 T. *NeuroImage*, 56:1276–1285.

[Koopmans et al., 2008] Koopmans, P. J., Manniesing, R., Niessen, W. J., Viergever, M. a., and Barth, M. (2008). MR venography of the human brain using susceptibility weighted imaging at very high field strength. *Magnetic Resonance Materials in Physics, Biology and Medicine*, 21:149–158.

[Krieger et al., 2014a] Krieger, S. N., Gauthier, C. J., Ivanov, D., Huber, L., Roggenhofer, E., Sehm, B., Turner, R., and Egan, G. F. (2014a). Regional reproducibility of calibrated BOLD functional MRI: Implications for the study of cognition and plasticity. *NeuroImage*, 101:8–20.

[Krieger et al., 2014b] Krieger, S. N., Huber, L., Poser, B. A., Turner, R., and Egan, G. F. (2014b). Simultaneous acquisition of cerebral blood volume-, blood flow-, and blood oxygenation-weighted MRI signals at ultra-high magnetic field. *Magnetic Resonance in Medicine*, in print, doi:10.1002/mrm.25431.

[Krieger et al., 2014c] Krieger, S. N., Ivanov, D., Huber, L., Roggenhofer, E., Sehm, B., Turner, R., Egan, G. F., and Gauthier, C. J. (2014c). Using carbogen for calibrated fMRI at 7 tesla: comparison of direct and modelled estimation of the M parameter. *NeuroImage*, 84:605–614.

[Krieger et al., 2012] Krieger, S. N., Streicher, M. N., Trampel, R., and Turner, R. (2012). Cerebral blood volume changes during brain activation. *Journal of Cerebral Blood Flow and Metabolism*, 32:1618–1631.

[Kuschinsky, 1996] Kuschinsky, W. (1996). Capillary perfusion in the brain. *European Journal of Physiology*, 432:R42–R46.

[Kuschinsky and Wahl, 1979] Kuschinsky, W. and Wahl, M. (1979). Perivascular pH and pial arterial diameter during bicuculline induced seizures in cats. *European Journal of Physiology*, 85:81–85.

[Laurterbur, 1973] Laurterbur, C. P. (1973). Image formation by induced local interactions: Examples employing nuclear magnetic resonance. *Nature*, 242:190 – 191.

[Lee et al., 2001] Lee, S.-P., Duong, T. Q., Yang, G., Iadecola, C., and Kim, S.-G. (2001). Relative changes of cerebral arterial and venous blood volumes during increased cerebral blood flow: Implications for BOLD fMRI. *Magnetic Resonance in Medicine*, 45:791–800.

[Leontiev and Buxton, 2007] Leontiev, O. and Buxton, R. B. (2007). Reproducibility of BOLD, perfusion, and CMRO2 measurements with calibrated-BOLD fMRI. *NeuroImage*, 35:175–184.

[Leontiev et al., 2007] Leontiev, O., Dubowitz, D. J., and Buxton, R. B. (2007). CBF/CMRO2 coupling measured with calibrated-BOLD fMRI: Sources of bias. *NeuroImage*, 36:1110–1122.

[Lin et al., 2010] Lin, A.-L., Fox, P. T., Hardies, J., Duong, T. Q., and Gao, J.-H. (2010). Nonlinear coupling between cerebral blood flow, oxygen consumption, and ATP production in human visual cortex. *Proceedings of the National Academy of Sciences*, 107:8446–8451.

[Lin et al., 2008] Lin, A.-L., Fox, P. T., Yang, Y., Lu, H., Tan, L.-H., and Gao, J.-H. (2008). Evaluation of MRI models in the measurement of CMRO2 and its relationship with CBF. *Magnetic Resonance in Medicine*, 60:380–389.

[Lin et al., 2011] Lin, A.-L., Lu, H., Fox, P. T., and Duong, T. Q. (2011). Cerebral blood volume measurements: Gd DTPA vs. VASO and their relationship with cerebral blood flow in activated human visual cortex. *Open Neuroimaging Journal*, 5:90–95.

[Liu et al., 2011] Liu, Y., Shen, H., Zhou, Z., and Hu, D. (2011). Sustained negative BOLD response in human fMRI finger tapping task. *PloS one*, 6:e23839.

[Logothetis, 2008] Logothetis, N. K. (2008). What we can do and what we cannot do with fMRI. *Nature*, 453:869–878.

[Logothetis et al., 2010] Logothetis, N. K., Augath, M., Murayama, Y., Rauch, A., Sultan, F., Goense, J. B. M., Oeltermann, A., and Merkle, H. (2010). The effects of electrical microstimulation on cortical signal propagation. *Nature Neuroscience*, 13:1283–1291.

[Logothetis et al., 1999] Logothetis, N. K., Guggenberger, H., Peled, S., and Pauls, J. (1999). Functional imaging of the monkey brain. *Nature Neuroscience*, 2:555–562.

[Logothetis et al., 2001] Logothetis, N. K., Pauls, J., Augath, M., Trinath, T., and Oeltermann, A. (2001). Neurophysiological investigation of the basis of the fMRI signal. *Nature*, 412:150–157.

[Lu, 2008] Lu, H. (2008). Magnetization reset for non-steady-state blood spins in vascular-space-occupancy (VASO) fMRI. In *Proceedings of the International Society of Magnetic Resonance in Medicine*, volume 16, page 406.

[Lu et al., 2003] Lu, H., Golay, X., Pekar, J. J., and van Zijl, P. C. M. (2003). Functional magnetic resonance imaging based on changes in vascular space occupancy. *Magnetic Resonance in Medicine*, 50:263–274.

[Lu et al., 2004a] Lu, H., Golay, X., Pekar, J. J., and van Zijl, P. C. M. (2004a). Sustained poststimulus elevation in cerebral oxygen utilization after vascular recovery. *Journal of Cerebral Blood Flow and Metabolism*, 24:764–770.

[Lu et al., 2013] Lu, H., Hua, J., and van Zijl, P. C. M. (2013). Noninvasive functional imaging of cerebral blood volume with vascular-space-occupancy (VASO) MRI. *NMR in Biomedicine*, 26:932–948.

[Lu et al., 2004b] Lu, H., Patel, S., Luo, F., Li, S.-J., Hillard, C. J., Ward, B. D., and Hyde, J. S. (2004b). Spatial correlations of laminar BOLD and CBV responses to rat whisker stimulation with neuronal activity localized by Fos expression. *Magnetic Resonance in Medicine*, 52:1060–1068.

[Lu and van Zijl, 2005] Lu, H. and van Zijl, P. C. M. (2005). Experimental measurement of extravascular parenchymal BOLD effects and tissue oxygen extraction fractions using multi-echo VASO fMRI at 1.5 and 3.0 T. *Magnetic Resonance in Medicine*, 53:808–816.

[Lu and van Zijl, 2012] Lu, H. and van Zijl, P. C. M. (2012). A review of the development of vascular-space-occupancy (VASO) fMRI. *NeuroImage*, 62:736–742.

[Lu et al., 2008] Lu, H., Zhao, C., Ge, Y., and Lewis-Amezcua, K. (2008). Baseline blood oxygenation modulates response amplitude: Physiologic basis for intersubject variations in functional MRI signals. *Magnetic Resonance in Medicine*, 60:364–372.

[MacIntosh et al., 2010] MacIntosh, B. J., Filippini, N., Chappell, M. A., Woolrich, M. W., Mackay, C. E., and Jezzard, P. (2010). Assessment of arterial arrival times derived from multiple inversion time pulsed arterial spin labeling MRI. *Magnetic Resonance in Medicine*, 63:641–647.

[Mandeville, 2012] Mandeville, J. B. (2012). IRON fMRI measurements of CBV and implications for BOLD signal. *NeuroImage*, 62:1000–1008.

[Mandeville et al., 1999] Mandeville, J. B., Marota, J. J., Ayata, C., Zaharchuk, G., Moskowitz, M. A., Rosen, B. R., and Weisskoff, R. M. (1999). Evidence of a cerebrovascular postarteriole windkessel with delayed compliance. *Journal of Cerebral Blood Flow and Metabolism*, 19:679–689.

[Mandeville et al., 1998] Mandeville, J. B., Marota, J. J., Kosofsky, B. E., Keltner, J. R., Weissleder, R., Rosen, B. R., and Weisskoff, R. M. (1998). Dynamic functional imaging of relative cerebral blood volume during rat forepaw stimulation. *Magnetic Resonance in Medicine*, 39:615–624.

[Mansfield and Grannell, 1973] Mansfield, P. and Grannell, P. K. (1973). NMR 'diffraction' in solids? *Journal of Physics C-Solid State Physics*, 6:422–426.

[Mark and Pike, 2012] Mark, C. I. and Pike, G. B. (2012). Indication of BOLD-specific venous flow-volume changes from precisely controlled hyperoxic vs. hypercapnic calibration. *Journal of Cerebral Blood Flow and Metabolism*, 32:709–719.

[Markuerkiaga et al., 2014] Markuerkiaga, I., Barth, M., and Norris, D. G. (2014). Towards a vascular model of layer specific activation. In *Proceedings of the International Society of Magnetic Resonance in Medicine*, volume 22, page 3093.

[Marques et al., 2010] Marques, J. P., Kober, T., Krueger, G., van der Zwaag, W., Van de Moortele, P.-F., and Gruetter, R. (2010). MP2RAGE, a self bias-field corrected sequence for improved segmentation and T1-mapping at high field. *NeuroImage*, 49:1271–1281.

[Marrett and Gjedde, 1997] Marrett, S. and Gjedde, A. (1997). Changes of blood flow and oxygen consumption in visual cortex of living humans. *Advances in Experimental Medicine and Biology*, 413:205–208.

[Martin et al., 2006] Martin, C., McLaughlin, A. C., Berwick, J., and Mayhew, J. E. (2006). Investigating neural-hemodynamic coupling and the hemodynamic response function in the awake rat. *NeuroImage*, 32:33–48.

[Martindale et al., 2008] Martindale, J., Kennerley, A. J., Johnston, D., Zheng, Y., and Mayhew, J. E. (2008). Theory and generalization of Monte Carlo models of the BOLD signal source. *Magnetic Resonance in Medicine*, 59:607–618.

[Miao et al., 2014] Miao, X., Gu, H., Yan, L., Lu, H., Wang, D. J. J., Zhou, X. J., Zhuo, Y., and Yang, Y. (2014). Detecting resting-state brain activity by spontaneous cerebral blood volume fluctuations using whole brain vascular space occupancy imaging. *NeuroImage*, 84:575–584.

[Mildner et al., 2014] Mildner, T., Müller, K., Hetzer, S., Trampel, R., Driesel, W., and Möller, H. E. (2014). Mapping of arterial transit time by intravascular signal selection. *NMR in Biomedicine*, 27:594–609.

[Mispelter et al., 2006] Mispelter, J., Lupu, M., and Briguet, A. (2006). *NMR probeheads for biophysical and biomedical experiments: Theoretical principles & practical guidelines*. Imperial College Press.

[Moeller et al., 2010] Moeller, S., Yacoub, E., Olman, C. a., Auerbach, E., Strupp, J., Harel, N., and Uğurbil, K. (2010). Multiband multislice GE-EPI at 7 tesla, with 16-fold acceleration using partial parallel imaging with application to high spatial and temporal whole-brain fMRI. *Magnetic Resonance in Medicine*, 63:1144–1153.

[Mokri, 2001] Mokri, B. (2001). The Monro-Kellie hypothesis: Applications in CSF volume depletion. *Neurology*, 56:1746–1748.

[Moradi et al., 2012] Moradi, F., Buračas, G. T., and Buxton, R. B. (2012). Attention strongly increases oxygen metabolic response to stimulus in primary visual cortex. *NeuroImage*, 59:601–607.

[Mullinger et al., 2014] Mullinger, K. J., Mayhew, S. D., Bagshaw, A. P., Bowtell, R., and Francis, S. T. (2014). Evidence that the negative BOLD response is neuronal in origin: A simultaneous EEG-BOLD-CBF study in humans. *NeuroImage*, 94:263–274.

[Murphy et al., 2007] Murphy, K., Bodurka, J., and Bandettini, P. A. (2007). How long to scan? The relationship between fMRI temporal signal to noise ratio and necessary scan duration. *NeuroImage*, 34:565–574.

[Nakagawa et al., 1995] Nakagawa, S.-Z., Lin, D., and Bereczki, G. (1995). Blood volumes, hematocrits, and transit-times in parenchymal microvascular system of the rat brain. In LeBihan, D., editor, *Diffusion and Perfusion Magnetic Resonance Imaging. Applications to functional MRI.*, page 193 ff.

[Nizar et al., 2013] Nizar, K., Uhlirova, H., Tian, P., Saisan, P. A., Cheng, Q., Reznichenko, L., Weldy, K. L., Steed, T. C., Sridhar, V. B., MacDonald, C. L., Cui, J., Gratiy, S. L., Sakadzic, S., Boas, D. A., Beka, T. I., Einevoll, G. T., Chen, J., Masliah, E., Dale, A. M., Silva, G. A., and Devor, A. (2013). In vivo stimulus-induced vasodilation occurs without IP3 receptor activation and may precede astrocytic calcium increase. *The Journal of Neuroscience*, 33:8411–8422.

[Norris, 2002] Norris, D. G. (2002). Adiabatic radiofrequency pulse forms in biomedical nuclear magnetic resonance. *Concepts in Magnetic Resonance*, 14:89–101.

[Norris, 2012] Norris, D. G. (2012). Spin-echo fMRI: The poor relation? *NeuroImage*, 62:1109–1115.

[Norris and Haase, 1989] Norris, D. G. and Haase, A. (1989). Variable excitation angle AFP pulses. *Magnetic Resonance in Medicine*, 9:435–440.

[Ogawa et al., 1990] Ogawa, S., Lee, T. M., and Nayak, A. S. (1990). Oxygenation-sensitive contrast in magnetic resonance image of rodent brain at high magnetic fields. *Magnetic Resonance in Medicine*, 14:68–78.

[Parkes and Tofts, 2002] Parkes, L. M. and Tofts, P. S. (2002). Improved accuracy of human cerebral blood perfusion measurements using arterial spin labeling: Accounting for capillary water permeability. *Magnetic Resonance in Medicine*, 48:27–41.

[Pasley et al., 2007] Pasley, B., Inglis, B., and Freeman, R. D. (2007). Analysis of oxygen metabolism implies a neural origin for the negative BOLD response in human visual cortex. *NeuroImage*, 36:269–276.

[Pawlik et al., 1981] Pawlik, G., Rackl, A., and Bing, R. J. (1981). Quantitative capillary topography and blood flow in the cerebral cortex of cats: An in vivo microscopic study. *Brain Research*, 208:35–58.

[Payne, 2006] Payne, S. J. (2006). A model of the interaction between autoregulation and neural activation in the brain. *Mathematical Biosciences*, 204:260–281.

[Pears et al., 2003] Pears, J., Francis, S. T., Butterworth, S., Bowtell, R., and Gowland, P. A. (2003). Investigating the BOLD effect during infusion of Gd DTPA using rapid T2 imaging. *Magnetic Resonance in Medicine*, 49:61–70.

[Peppiatt and Attwell, 2004] Peppiatt, C. M. and Attwell, D. (2004). Feeding the brain. *Nature*, 431:137–138.

[Perthen et al., 2008] Perthen, J. E., Lansing, A. E., Liau, J., Liu, T. T., and Buxton, R. B. (2008). Caffeine-induced uncoupling of cerebral blood flow and oxygen metabolism: A calibrated BOLD fMRI study. *NeuroImage*, 40:237–247.

[Petzold and Murthy, 2011] Petzold, G. C. and Murthy, V. N. (2011). Role of astrocytes in neurovascular coupling. *Neuron*, 71:782–797.

[Pfeuffer et al., 2002] Pfeuffer, J., Adriany, G., Shmuel, A., Yacoub, E., Van de Moortele, P.-F., Hu, X., and Uludağ, K. (2002). Perfusion-based high-resolution functional imaging in the human brain at 7 tesla. *Magnetic Resonance in Medicine*, 47:903–911.

[Pfeuffer et al., 2004] Pfeuffer, J., Merkle, H., Beyerlein, M., Steudel, T., and Logothetis, N. K. (2004). Anatomical and functional MR imaging in the macaque monkey using a vertical large-bore 7 tesla setup. *Magnetic Resonance Imaging*, 22:1343–1359.

[Piechnik et al., 2008] Piechnik, S. K., Chiarelli, P. A., and Jezzard, P. (2008). Modelling vascular reactivity to investigate the basis of the relationship between cerebral blood volume and flow under CO2 manipulation. *NeuroImage*, 39:107–118.

[Piechnik et al., 2001] Piechnik, S. K., Czosnyka, M., Harris, N. G., Minhas, P. S., and Pickard, J. D. (2001). A model of the cerebral and cerebrospinal fluid circulations to examine asymmetry in cerebrovascular reactivity. *Journal of Cerebral Blood Flow and Metabolism*, 21:182–192.

[Piechnik et al., 2009] Piechnik, S. K., Evans, J., Bary, L. H., Wise, R. G., and Jezzard, P. (2009). Functional changes in CSF volume estimated using measurement of water T2 relaxation. *Magnetic Resonance in Medicine*, 61:579–586.

[Pike, 2012] Pike, G. B. (2012). Quantitative functional MRI: Concepts, issues and future challenges. *NeuroImage*, 62:1234–1240.

[Pohmann and Scheffler, 2014] Pohmann, R. and Scheffler, K. (2014). Brain Imaging with 7T vs. 9.4T: A direct Comparison of MR parameters and SNR. In *Proceedings of the International Society of Magnetic Resonance in Medicine*, volume 22, page 1421.

[Polimeni et al., 2013] Polimeni, J. R., Bhat, H., Benner, T., Feiweier, T., Inati, S. J., Witzel, T., Heberlein, K., and Wald, L. L. (2013). Sequential-segment multi-shot auto-calibration for GRAPPA EPI: Maximizing temporal SNR and reducing motion sensitivity. In *Proceedings of the International Society of Magnetic Resonance in Medicine*, volume 21, page 2646.

[Polimeni et al., 2010] Polimeni, J. R., Fischl, B., Greve, D. N., and Wald, L. L. (2010). Laminar analysis of 7T BOLD using an imposed spatial activation pattern in human V1. *NeuroImage*, 52:1334–1346.

[Porter and Lemon, 2012] Porter, R. and Lemon, R. (2012). *Corticospinal function and voluntary movement*. Number August 2014. Oxford University Press.

[Poser and Norris, 2007] Poser, B. A. and Norris, D. G. (2007). Measurement of activation-related changes in cerebral blood volume: VASO with single-shot HASTE acquisition. *Magnetic Resonance Materials in Physics, Biology and Medicine*, 20:63–67.

[Poser and Norris, 2009] Poser, B. A. and Norris, D. G. (2009). 3D single-shot VASO using a Maxwell gradient compensated GRASE sequence. *Magnetic Resonance in Medicine*, 62:255–262.

[Poser et al., 2011] Poser, B. A., van Mierlo, E., Norris, D. G., and Mierlo, E. (2011). Exploring the post-stimulus undershoot with spin-echo fMRI: Implications for models of neurovascular response. *Human Brain Mapping*, 32:141–153.

[Preuss et al., 1999] Preuss, T. M., Qi, H., and Kaas, J. H. (1999). Distinctive compartmental organization of human primary. *Proceedings of the National Academy of Sciences*, 96:11601–11606.

[Qiu et al., 2012] Qiu, D., Zaharchuk, G., Christen, T., Ni, W. W., and Moseley, M. E. (2012). Contrast-enhanced functional blood volume imaging (CE-fBVI): Enhanced sensitivity for brain activation in humans using the ultrasmall superparamagnetic iron oxide agent ferumoxytol. *NeuroImage*, 62:1726–1731.

[Qiu et al., 2010] Qiu, M., Paul Maguire, R., Arora, J., Planeta-Wilson, B., Weinzimmer, D., Wang, J., Wang, Y., Kim, H., Rajeevan, N., Huang, Y., Carson, R. E., and Constable, R. T. (2010). Arterial transit time effects in pulsed arterial spin labeling CBF mapping: Insight from a PET and MR study in normal human subjects. *Magnetic Resonance in Medicine*, 63:374–384.

[Rane and Gore, 2013] Rane, S. D. and Gore, J. C. (2013). Measurement of T1 of human arterial and venous blood at 7T. *Magnetic Resonance Imaging*, 31:477–479.

[Raz et al., 2005] Raz, A., Lieber, B., Soliman, F., Buhle, J., Posner, J., Peterson, B. S., and Posner, M. I. (2005). Ecological nuances in functional magnetic resonance imaging (fMRI): Psychological stressors, posture, and hydrostatics. *NeuroImage*, 25:1–7.

[Ress et al., 2007] Ress, D., Glover, G. H., Liu, J., and Wandell, B. (2007). Laminar profiles of functional activity in the human brain. *NeuroImage*, 34:74–84.

[Rooney et al., 2007] Rooney, W. D., Johnson, G., Li, X., Cohen, E. R., Kim, S.-G., Uludağ, K., and Springer, C. S. (2007). Magnetic field and tissue dependencies of human brain longitudinal 1H2O relaxation in vivo. *Magnetic Resonance in Medicine*, 57:308–318.

[Roy and Sherrington, 1890] Roy, C. S. and Sherrington, C. S. (1890). On the regulation of blood-supply of the brain. *Journal of Physiology*, 11:85–108.

[Schäfer et al., 2012] Schäfer, K., Blankenburg, F., Kupers, R., Grüner, J. M., Law, I., Lauritzen, M., and Larsson, H. B. W. (2012). Negative BOLD signal changes in ipsilateral primary somatosensory cortex are associated with perfusion decreases and behavioral evidence for functional inhibition. *NeuroImage*, 59:3119–3127.

[Schridde et al., 2008] Schridde, U., Khubchandani, M., Motelow, J. E., Sanganahalli, B. G., Hyder, F., and Blumenfeld, H. (2008). Negative BOLD with large increases in neuronal activity. *Cerebral Cortex*, 18:1814–1827.

[Schroeter et al., 2006] Schroeter, M. L., Kupka, T., Mildner, T., Uludağ, K., and v. Cramon, D. Y. (2006). Investigating the post-stimulus undershoot of the BOLD signal–a simultaneous fMRI and fNIRS study. *NeuroImage*, 30:349–358.

[Scouten and Constable, 2007] Scouten, A. and Constable, R. T. (2007). Application and limitations of whole-brain MAGIC VASO functional imaging. *Magnetic Resonance in Medicine*, 58:306–315.

[Scouten and Constable, 2008] Scouten, A. and Constable, R. T. (2008). VASO-based calculations of CBV change: Accounting for the dynamic CSF volume. *Magnetic Resonance in Medicine*, 58:308–315.

[Setsompop et al., 2012] Setsompop, K., Gagoski, B. a., Polimeni, J. R., Witzel, T., Wedeen, V. J., and Wald, L. L. (2012). Blipped-controlled aliasing in parallel imaging for simultaneous multislice echo planar imaging with reduced g-factor penalty. *Magnetic Resonance in Medicine*, 67:1210–1224.

[Shen et al., 2009] Shen, Y., Kauppinen, R. A., Vidyasagar, R., and Golay, X. (2009). A functional magnetic resonance imaging technique based on nulling extravascular gray matter signal. *Journal of Cerebral Blood Flow and Metabolism*, 29:144–156.

[Shibuya et al., 2014] Shibuya, K., Kuboyama, N., and Tanaka, J. (2014). Changes in ipsilateral motor cortex activity during a unilateral isometric finger task are dependent on the muscle contraction force. *Physiological Measurement*, 35:417–428.

[Shih et al., 2009] Shih, Y.-Y. I., Chen, C.-C. V., Shyu, B.-C., Lin, Z.-J., Chiang, Y.-C., Jaw, F.-S., Chen, Y.-Y., and Chang, C. (2009). A new scenario for negative functional magnetic resonance imaging signals: Endogenous neurotransmission. *Journal of Neuroscience*, 29:3036–3044.

[Shin et al., 2010] Shin, W., Geng, X., Gu, H., Zhan, W., Zou, Q., and Yang, Y. (2010). Automated brain tissue segmentation based on fractional signal mapping from inversion recovery Look-Locker acquisition. *NeuroImage*, 52:1347–1354.

[Shmuel et al., 2006] Shmuel, A., Augath, M., Oeltermann, A., and Logothetis, N. K. (2006). Negative functional MRI response correlates with decreases in neuronal activity in monkey visual area V1. *Nature Neuroscience*, 9:569–577.

[Shmuel et al., 2002] Shmuel, A., Yacoub, E., Pfeuffer, J., Van de Moortele, P.-F., Adriany, G., Hu, X., and Uludağ, K. (2002). Sustained negative BOLD, blood flow and oxygen consumption response and its coupling to the positive response in the human brain. *Neuron*, 36:1195–1210.

[Shulman and Rothman, 2005] Shulman, R. G. and Rothman, D. L. (2005). *Brain energetics and neuronal activity: Applications to fMRI and medicine.* John Wiley & Sons.

[Sicard et al., 2003] Sicard, K., Shen, Q., Brevard, M. E., Sullivan, R., Ferris, C. F., King, J. A., and Duong, T. Q. (2003). Regional cerebral blood flow and BOLD responses in conscious and anesthetized rats under basal and hypercapnic conditions: implications for functional MRI studies. *Journal of Cerebral Blood Flow and Metabolism*, 23:472–481.

[Siero et al., 2011] Siero, J. C. W., Petridou, N., Hoogduin, H., Luijten, P. R., and Ramsey, N. F. (2011). Cortical depth-dependent temporal dynamics of the BOLD response in the human brain. *Journal of Cerebral Blood Flow and Metabolism*, 31:1999–2008.

[Siero et al., 2013] Siero, J. C. W., Ramsey, N. F., Hoogduin, H., Klomp, D. W. J., Luijten, P. R., and Petridou, N. (2013). BOLD specificity and dynamics evaluated in humans at 7 T: comparing gradient-echo and spin-echo hemodynamic responses. *PloS one*, 8:e54560.

[Slichter, 1989] Slichter, C. P. (1989). *Principles of magnetic resonance.* Springer-Verlag.

[Smirnakis et al., 2007] Smirnakis, S. M., Schmid, M. C., Weber, B., Tolias, A. S., Augath, M., and Logothetis, N. K. (2007). Spatial specificity of BOLD versus cerebral blood volume fMRI for mapping cortical organization. *Journal of Cerebral Blood Flow and Metabolism*, 27:1248–1261.

[Smith et al., 2004] Smith, A. T., Williams, A. L., and Singh, K. D. (2004). Negative BOLD in the visual cortex: Evidence against blood stealing. *Human Brain Mapping*, 21:213–220.

[St. Lawrence, 2005] St. Lawrence, K. S. (2005). Effects of water exchange and venous outflow on VASO contrast: A theoretical study. In *Proceedings of the International Society of Magnetic Resonance in Medicine*, volume 13, page 1418.

[St. Lawrence et al., 2000] St. Lawrence, K. S., Frank, J. A., and McLaughlin, A. C. (2000). Effect of restricted water exchange on cerebral blood flow values calculated with arterial spin tagging: A theoretical investigation. *Magnetic Resonance in Medicine*, 44:440–449.

[Stefanovic et al., 2008] Stefanovic, B., Hutchinson, E., Yakovleva, V., Schram, V., Russell, J. T., Belluscio, L., Koretsky, A. P., and Silva, A. C. (2008). Functional reactivity of cerebral capillaries. *Journal of Cerebral Blood Flow and Metabolism*, 28:961–972.

[Stefanovic and Pike, 2005] Stefanovic, B. and Pike, G. B. (2005). Venous refocusing for volume estimation: VERVE functional magnetic resonance imaging. *Magnetic Resonance in Medicine*, 53:339–347.

[Stefanovic et al., 2004] Stefanovic, B., Warnking, J. M., and Pike, G. B. (2004). Hemodynamic and metabolic responses to neuronal inhibition. *NeuroImage*, 22:771–778.

[Tajima et al., 2010] Tajima, S., Watanabe, M., Imai, C., Ueno, K., Asamizuya, T., Sun, P., Tanaka, K., and Cheng, K. (2010). Opposing effects of contextual surround in human early visual cortex revealed by functional magnetic resonance imaging with continuously modulated visual stimuli. *Journal of Neuroscience*, 30:3264–3270.

[Takano et al., 2006] Takano, T., Tian, G.-F. F., Peng, W., Lou, N., Libionka, W., Han, X., and Nedergaard, M. (2006). Astrocyte-mediated control of cerebral blood flow. *Nature Neuroscience*, 9:260–267.

[Thomas et al., 2013] Thomas, B. P., Liu, P., Aslan, S., King, K. S., van Osch, M. J. P., and Lu, H. (2013). Physiologic underpinnings of negative BOLD cerebrovascular reactivity in brain ventricles. *NeuroImage*, 83:505–512.

[Tian et al., 2010] Tian, P., Teng, I. C., May, L. D., Kurz, R., Lu, K., Scadeng, M., Hillman, E. M. C., Crespigny, A. J. D., Arceuil, H. E. D., Mandeville, J. B., Marota, J. J. A., Rosen, B. R., Liu, T. T., Boas, D. A., Buxton, R. B., Dale, A. M., and Devor, A. (2010). Cortical depth-specific microvascular dilation underlies laminar differences in blood oxygenation level-dependent functional MRI signal. *Proceedings of the National Academy of Sciences*, 34:15246–15251.

[Tjandra et al., 2005] Tjandra, T., Brooks, J. C. W., Figueiredo, P., Wise, R. G., Matthews, P. M., and Tracey, I. (2005). Quantitative assessment of the reproducibility of functional activation measured with BOLD and MR perfusion imaging: Implications for clinical trial design. *NeuroImage*, 27:393–401.

[Trampel et al., 2012] Trampel, R., Bazin, P.-l., Schäfer, A., Heidemann, R. M., Ivanov, D., Lohmann, G., Geyer, S., and Turner, R. (2012). High resolution functional mapping of primary motor cortex and primary somatosensory cortex in humans at 7 T. In *Proceedings of the International Society of Magnetic Resonance in Medicine*, volume 20, page 663.

[Triantafyllou et al., 2005] Triantafyllou, C., Hoge, R. D., Krueger, G., Wiggins, C. J., Potthast, A., Wiggins, G., and Wald, L. L. (2005). Comparison of physiological noise at 1.5 T, 3 T and 7 T and optimization of fMRI acquisition parameters. *NeuroImage*, 26:243–250.

[Triantafyllou et al., 2011] Triantafyllou, C., Polimeni, J. R., and Wald, L. L. (2011). Physiological noise and signal-to-noise ratio in fMRI with multi-channel array coils. *NeuroImage*, 55:597–606.

[Tropres et al., 2001] Tropres, I., Grimault, S., Vaeth, A., Grillon, E., Julien, C., Payen, J., Lamalle, L., and Decorps, M. (2001). Vessel size imaging. *Magnetic resonance in medicine*, 45:397–408.

[Turner, 2002] Turner, R. (2002). How much cortex can a vein drain? Downstream dilution of activation-related cerebral blood oxygenation changes. *NeuroImage*, 16:1062–1067.

[Turner et al., 1993] Turner, R., Jezzard, P., and Wen, H. (1993). Functional mapping of the human visual cortex at 4 and 1.5 tesla using deoxygenation contrast EPI. *Magnetic Resonance Imaging*, 29:277–279.

[Turner and Thomas, 2006] Turner, R. and Thomas, D. (2006). Cerebral blood volume: Measurement and change. In *Proceedings of the International Society of Magnetic Resonance in Medicine*, volume 14, page 2771.

[Tuunanen et al., 2006] Tuunanen, P. I., Vidyasagar, R., and Kauppinen, R. A. (2006). Effects of mild hypoxic hypoxia on poststimulus undershoot of blood-oxygenation-level-dependent fMRI signal in the human visual cortex. *Magnetic Resonance Imaging*, 24:993–999.

[Uh et al., 2009] Uh, J., Lewis-Amezcua, K., Varghese, R., and Lu, H. (2009). On the measurement of absolute cerebral blood volume (CBV) using vascular-space-occupancy (VASO) MRI. *Magnetic Resonance in Medicine*, 61:659–667.

[Uh et al., 2011] Uh, J., Lin, A.-L., Lee, K., Liu, P., Fox, P. T., and Lu, H. (2011). Validation of VASO cerebral blood volume measurement with positron emission tomography. *Magnetic Resonance in Medicine*, 65:744–749.

[Uludağ, 2010] Uludağ, K. (2010). To dip or not to dip: Reconciling optical imaging and fMRI data. *Proceedings of the National Academy of Sciences*, 107:E23–E24.

[Uludağ et al., 2009] Uludağ, K., Müller-Bierl, B., and Uğurbil, K. (2009). An integrative model for neuronal activity-induced signal changes for gradient and spin echo functional imaging. *NeuroImage*, 48:150–165.

[Vafaee and Gjedde, 2004] Vafaee, M. S. and Gjedde, A. (2004). Spatially dissociated flow-metabolism coupling in brain activation. *NeuroImage*, 21:507–515.

[Van de Moortele et al., 2005] Van de Moortele, P.-F., Akgun, C., Adriany, G., Moeller, S., Ritter, J., Collins, C. M., Smith, M. B., Vaughan, J. T., and Uludağ, K. (2005). B(1) destructive interferences and spatial phase patterns at 7 T with a head transceiver array coil. *Magnetic Resonance in Medicine*, 54:1503–1518.

[van Zijl et al., 1998] van Zijl, P. C. M., Eleef, S. M., Ulatowski, J. A., Oja, J. M., Ulug, A. M., Traystman, R. J., Kauppinen, R. A., Ulatowski, S. M., and Eleff, J. A. (1998). Quantitative assessment of blood flow, blood volume and blood oxygenation effects in functional magnetic resonance imaging. *Nature Medicine*, 4:159–167.

[van Zijl et al., 2012] van Zijl, P. C. M., Hua, J., and Lu, H. (2012). The BOLD post-stimulus undershoot, one of the most debated issues in fMRI. *NeuroImage*, 62:1092–1102.

[Vaughan et al., 2001] Vaughan, J. T., Garwood, M., Collins, C. M., Liu, W., DelaBarre, L., Adriany, G., Andersen, P., Merkle, H., Goebel, R., Smith, M. B., and Uğurbil, K. (2001). 7T vs. 4T: RF power, homogeneity, and signal-to-noise comparison in head images. *Magnetic Resonance in Medicine*, 46:24–30.

[Vaughan and Griffiths, 2012] Vaughan, J. T. and Griffiths, J. R. (2012). *RF coils for MRI.* John Wiley & Sons.

[Villringer et al., 1994] Villringer, A., Them, A., Lindauer, U., Einhäupl, K., and Dirnagl, U. (1994). Capillary perfusion of the rat brain cortex. An in vivo confocal microscopy study. *Circulation Research*, 75:55–62.

[Wade and Rowland, 2010] Wade, A. R. and Rowland, J. (2010). Early suppressive mechanisms and the negative blood oxygenation level-dependent response in human visual cortex. *Journal of neuroscience*, 30:5008–5019.

[Waehnert et al., 2014] Waehnert, M. D., Dinse, J., Weiss, M., Streicher, M. N., Waehnert, P., Geyer, S., Turner, R., and Bazin, P.-L. (2014). Anatomically motivated modeling of cortical laminae. *NeuroImage*, 93:210–220.

[Weber et al., 2008] Weber, B., Keller, A. L., Reichold, J., and Logothetis, N. K. (2008). The microvascular system of the striate and extrastriate visual cortex of the macaque. *Cerebral Cortex*, 18:2318–2330.

[Wehrli et al., 2014] Wehrli, F. W., Rodgers, Z. B., Jain, V., Langham, M. C., Li, C., Licht, D. J., and Magland, J. (2014). Time-resolved MRI oximetry for quantifying CMRO2 and vascular reactivity. *Academic Radiology*, 21:207–214.

[Wong et al., 1997] Wong, E. C., Buxton, R. B., and Frank, L. R. (1997). Implementation of quantitative perfusion imaging techniques for functional brain mapping using pulsed arterial spin labeling. *NMR in Biomedicine*, 10:237–249.

[Wong et al., 1998] Wong, E. C., Buxton, R. B., and Frank, L. R. (1998). Quantitative imaging of perfusion using a single subtraction (QUIPPS and QUIPSS II). *Magnetic Resonance in Medicine*, 39:702–708.

[Woolsey et al., 1996] Woolsey, T. A., Rovainen, C. M., Cox, S. B., Henegar, M. H., Liang, G. E., Liu, D., Moskalenko, Y. E., Sui, J., and Wei, L. (1996). Neuronal units linked to microvascular modules in cerebral cortex: Response elements for imaging the brain. *Cerebral Cortex*, 6:647–660.

[Worsley, 2001] Worsley, K. J. (2001). *Statistical analysis of activation images*, chapter 14. Oxford University Press.

[Wright et al., 2008] Wright, P. J., Mougin, O. E., Totman, J. J., Peters, A. M., Brookes, M. J., Coxon, R., Morris, P. E., Clemence, M., Francis, S. T., Bowtell, R., and Gowland, P. A. (2008). Water proton T1 measurements in brain tissue at 7, 3, and 1.5 T using IR-EPI, IR-TSE, and MPRAGE: Results and optimization. *Magnetic Resonance Materials in Physics, Biology and Medicine*, 21:121–130.

[Wu et al., 2008] Wu, C. W., Chuang, K.-H., Wai, Y.-Y., Wan, Y.-L., Chen, J.-H., and Liu, H.-L. (2008). Vascular space occupancy-dependent functional MRI by tissue suppression. *Journal of Magnetic Resonance Imaging*, 226:219–226.

[Wu et al., 2010] Wu, C. W., Liu, H.-L., Chen, J.-H., and Yang, Y. (2010). Effects of CBV, CBF, and blood-brain barrier permeability on accuracy of PASL and VASO measurement. *Magnetic Resonance in Medicine*, 63:601–608.

[Wu et al., 2007] Wu, W.-C., Buxton, R. B., and Wong, E. C. (2007). Vascular space occupancy weighted imaging with control of residual blood signal and higher contrast-to-noise ratio. *IEEE Transactions on Medical Imaging*, 26:1319–1327.

[Wyss et al., 2013] Wyss, M., Kircher, T., Ringenbach, A., Prüssmann, K., and Hennig, A. (2013). Relaxation parameter mapping adapted for 7T and validation against optimized single voxel MRS. In *Proceedings of the International Society of Magnetic Resonance in Medicine*, volume 21, page 2464.

[Xie et al., 2013] Xie, L., Kang, H., Xu, Q., Chen, M. J., Liao, Y., Thiyagarajan, M., O'Donnell, J., Christensen, D. J., Nicholson, C., Iliff, J. J., Takano, T., Deane, R., and Nedergaard, M. (2013). Sleep drives metabolite clearance from the adult brain. *Science*, 342:373–377.

[Xu et al., 2013] Xu, C., Kiselev, V. G., Möller, H. E., and Fiebach, J. B. (2013). Dynamic hysteresis between gradient echo and spin echo attenuations in dynamic susceptibility contrast imaging. *Magnetic Resonance in Medicine*, 69:981–991.

[Yablonskiy and Haacke, 1994] Yablonskiy, D. A. and Haacke, E. M. (1994). Theory of NMR signal behavior in magnetically inhomogeneous tissues: The static dephasing regime. *Magnetic Resonance in Medicine*, 32:749–763.

[Yacoub et al., 2008] Yacoub, E., Harel, N., and Uğurbil, K. (2008). High-field fMRI unveils orientation columns in humans. *Proceedings of the National Academy of Sciences*, 105:10607–106012.

[Yacoub et al., 2001] Yacoub, E., Shmuel, A., Pfeuffer, J., Van de Moortele, P.-F., Adriany, G., Andersen, P., Vaughan, J. T., Merkle, H., Uludağ, K., and Hu, X. (2001). Imaging brain function in human at 7 tesla. *Magnetic Resonance in Medicine*, 45:588–594.

[Yacoub et al., 2006] Yacoub, E., Uludağ, K., and Harel, N. (2006). The spatial dependence of the poststimulus undershoot as revealed by high-resolution BOLD- and CBV-weighted fMRI. *Journal of Cerebral Blood Flow and Metabolism*, 26:634–644.

[Yacoub et al., 2005] Yacoub, E., Van de Moortele, P.-F., Shmuel, A., and Uğurbil, K. (2005). Signal and noise characteristics of Hahn SE and GE BOLD fMRI at 7 T in humans. *NeuroImage*, 24:738–750.

[Yang et al., 2004] Yang, Y., Gu, H., and Stein, E. A. (2004). Simultaneous MRI acquisition of blood volume, blood flow, and blood oxygenation information during brain activation. *Magnetic Resonance in Medicine*, 52:1407–1417.

[Yaseen et al., 2011] Yaseen, M. A., Srinivasan, V. J., Sakadzic, S., Radhakrishnan, H., Gorczynska, I., Wu, W., Fujimoto, J. G., and Boas, D. A. (2011). Microvascular oxygen tension and flow measurements in rodent cerebral cortex during baseline conditions and functional activation. *Journal of Cerebral Blood Flow and Metabolism*, 31:1051–1063.

[Yu et al., 2014] Yu, X., Qian, C., Chen, D., Dodd, S. J., and Koretsky, A. P. (2014). Deciphering laminar-specific neural inputs with line-scanning fMRI. *Nature Methods*, 11:55–58.

[Zappe et al., 2008] Zappe, A.-C., Uludağ, K., and Logothetis, N. K. (2008). Direct measurement of oxygen extraction with fMRI using 6% CO2 inhalation. *Magnetic Resonance Imaging*, 26:961–967.

[Zhang et al., 2013] Zhang, X., Petersen, E. T., Ghariq, E., De Vis, J. B., Webb, A. G., Teeuwisse, W. M., Hendrikse, J., and van Osch, M. J. P. (2013). In vivo blood T(1) measurements at 1.5 T, 3 T, and 7 T. *Magnetic Resonance in Medicine*, 70:1082–1086.

[Zhao et al., 2006] Zhao, F., Wang, P., Hendrich, K. S., Uludağ, K., and Kim, S.-G. (2006). Cortical layer-dependent BOLD and CBV responses measured by spin-echo and gradient-echo fMRI: Insights into hemodynamic regulation. *NeuroImage*, 30:1149–1160.

[Zong et al., 2012] Zong, X., Kim, T., and Kim, S.-G. (2012). Contributions of dynamic venous blood volume versus oxygenation level changes to BOLD fMRI. *NeuroImage*, 60:2238–2246.

Curriculum vitae

Laurentius Huber born on November 9th 1985 in Salzburg, Austria

Bleichertstr. 11, 04155 Leipzig, Germany

renzohuber@gmx.at

Scientific career

School education

1992–2004	Integrated school: Freie Waldorfschule, Ludwigsburg, Germany
2004–2006	General qualification for university (Matura) Rudolf Steiner Schule, Salzburg, Austria
2006–2009	Bachelor courses of physics at the Ludwig Maximilians University Munich, Germany
2009–2011	Master courses of physics at the Ludwig Maximilians University Munich, Germany
2012–dato	PhD student at the Max Planck Institute for Human Cognitive and Brain Sciences Leipzig, Germany

Research experience

2009–2010	Academic assistant at the Ludwig Maximilians University Munich, Germany: PHP, SQL programming, budgeting, activity accounting at the department of computational physics at the LMU
2013–2014	Employed consultant on MRI at the Fraunhofer Institute in Leipzig, Germany: Sequence development and protocol development at small bore 7T MRI scanner

Teaching experience

2008–2009	Student assistant at the Ludwig Maximilians University Munich, Germany: Theoretical Quantum Mechanics: Class leader
2008–2009	Student assistant at the Ludwig Maximilians University Munich, Germany: Calculation in Physics: Designing and building of experiments for practical work of younger students

Articles during this PhD project

1. Trampel, R., Reimer, E., **Huber, L.**, Ivanov, D., Heidemann, R. M., Schäfer, A., and Turner, R. (2013) Anatomical brain imaging at 7 T using two-dimensional GRASE. *Magnetic Resonance in Medicine*, 27:594–609.

2. Streicher, M. N., Schäfer, A., Ivanov, D., Müller, D. K., Amadon, A., Reimer, E., **Huber, L.**, Dhital, B., Rivera, D., Kögler, C., Trampel, R., Pampel, A., and Turner, R. (2013) Fast accurate MR thermometry using phase referenced asymmetric spin-echo EPI at high field. *Magnetic Resonance in Medicine*, 71:524–533.

3. Krieger, S. N., Ivanov, D., **Huber, L.**, Roggenhofer, E., Sehm, B., Turner, R., Egan, G. F., and Gauthier, C. J. (2014) Using carbogen for calibrated fMRI at 7 tesla: Comparison of direct and modeled estimation of the M parameter. *NeuroImage*, 84:605–614.

4. **Huber, L.**, Ivanov, D., Krieger, S. N., Streicher, M. N., Mildner, T., Poser, B. A., Möller, H. E., and Turner, R. (2014). Slab-selective, BOLD-corrected VASO at 7 tesla provides measures of cerebral blood volume reactivity with high signal-to-noise ratio. *Magnetic Resonance in Medicine*, 72:137–148.

5. **Huber, L.**, Goense, J., Kennerley, A. J., Ivanov, D., Krieger, S. N., Lepsien, J., Trampel, R., Turner, R., and Möller, H. E. (2014) Investigation of the neurovascular coupling in positive and negative BOLD responses in human brain at 7 T. *NeuroImage*, 97:349–362.

6. Krieger, S. N., Gauthier, C. J., Ivanov, D., **Huber, L.**, Roggenhofer, E., Sehm, B., Turner, R., and Egan, G. F. (2014) Regional reproducibility of calibrated BOLD functional MRI: implications for the study of cognition and plasticity. *NeuroImage*, 101:8–20.

7. Krieger, S. N., **Huber, L.**, Poser, B. A., Turner, R., and Egan, G. F. (2015) Simultaneous acquisition of cerebral blood volume-, blood flow-, and blood oxygenation-weighted MRI signals at ultra-high magnetic field. *Magnetic Resonance in Medicine*, ahead of print (doi: 10.1002/mrm.25431).

8. **Huber, L.**, Goense, J., Kennerley, A. J., Trampel, R., Guidi, M., Ivanov, D., Neef, N., Gauthier, G. J., Turner, R., and Möller, H. E. (2015) Cortical lamina-dependent blood volume changes in human brain at 7 T. *NeuroImage*, 107:23–33.

Conference talks and invited talks during this PhD project

1. **Huber, L.**, Ivanov, D., Streicher, M. N., and Turner, R. (2012) Slab-selective, BOLD-corrected VASO (SS-VASO) in human brain at 7 T. In *ISMRM Brain Function Workshop, Whistler, Canada.*

2. **Huber, L.**, Ivanov, D., Roggenhofer, E., Henseler, I., Möller, H. E., and Turner, R. (2012) Hypercapnia-induced and stimulus-induced changes in cerebral blood volume (CBV) in humans at 7 T. In *ISMRM Brain Function Workshop, Whistler, Canada.*
3. **Huber, L.**, Ivanov, D., Streicher, M. N., and Turner, R. (2012) Slab-selective, BOLD-corrected VASO (SS-VASO) in human brain at 7 T. In *Proceedings of the 20th Annual Meeting of ISMRM, Melbourne, Australia*, abstract 381.
4. **Huber, L.** (2012) Measuring blood volume at 7 T with VASO. Invited talk at the *University of Sheffield, department Psychology, Sheffiled, UK.*
5. **Huber, L.**, Goense, J., Ivanov, D., Krieger, S. N., Turner, R., and Möller, H. E. (2013) Cerebral blood volume changes in negative BOLD regions during visual stimulation in humans at 7 T. In *Proceedings of the 21st Annual Meeting of ISMRM, Salt Lake City, USA*, abstract 847.
6. Kennerley, A. J., **Huber, L.**, Mildner, T., Mayhew, J. E., Turner, R., Möller, H. E., and Berwick, J. (2013) Does VASO contrast really allow measurement of CBV at high field ($\geq$7 T)? An in vivo quantification using concurrent optical imaging spectroscopy. In *Proceedings of the 21st Annual Meeting of ISMRM, Salt Lake City, USA*, abstract 757.
7. Krieger, S. N., **Huber, L.**, Egan, G. F., and Turner, R. (2013) Simultaneous acquisition of cerebral blood volume, blood flow and blood oxygenation weighted MRI signals at 7 T. In *Proceedings of the 21st Annual Meeting of ISMRM, Salt Lake City, USA*, abstract 107.
8. Gauthier, C. J., Krieger, S. N., **Huber, L.**, Hoge, R. D., and Turner, R. (2013) Baseline oxygen metabolism quantification at 7 T using QUO2. In *Proceedings of the 19th Annual Meeting of the Organization of Human Brain Mapping, Seattle, USA.*
9. **Huber, L.**, Kennerley, A. J., Ivanov, D., Gauthier, C. J., Möller, H. E., and Turner, R. (2014) Measuring changes in arterial and venous cerebral blood volume in human brain at 7 T. In *Proceedings of the 22nd Annual Meeting of ISMRM, Milan, Italy*, abstract 1015.
10. **Huber, L.**, Goense, J., Kennerley, A. J., Trampel, R., Guidi, M., Gauthier, C. J., Turner, R., and Möller, H. E. (2014) Layer-dependent CBV and BOLD responses in humans, monkeys, and rats at 7 T. In *ISMRM Brain Function Workshop, Charleston, USA.*
11. **Huber, L.**, Kennerley, A. J., Smuda, S. N., Schäfer, A., Guidi, M., Ivanov, D., Poser, B. A., Gauthier, C. J., Turner, R., and Möller, H. E. (2014) Volume redistribution during hypercapnia. In *Proceedings of the 2nd Workshop on Imaging Cerebral Physiology: Manipulating Magnetic Resonance Contrast through Respiratory Challenges, Leipzig, Germany.*

12. Guidi, M., **Huber, L.**, Lampe, L., Gauthier, C. J., and Möller, H. E. (2014) Layer-dependent calibrated BOLD response in human M1. In *Proceedings of the 2nd Workshop on Imaging Cerebral Physiology: Manipulating Magnetic Resonance Contrast through Respiratory Challenges, Leipzig, Germany.*

Conference posters during this PhD project

1. Ivanov, D., **Huber, L.**, Kabisch, S., Streicher, M. N., Schloegl, H., Henseler, I., Roggenhofer, E., Heinke, W., and Turner, R. (2012) Mapping of CMRO2 changes in visual cortex during a visual motion paradigm at 7 T. In *Proceedings of the 20th Annual Meeting of ISMRM, Melbourne, Australia*, abstract 2187.

2. Streicher, M. N., Schäfer, A., Ivanov, D., **Huber, L.**, Dhital, B., Rivera, D., Kögler, C., Trampel, R., Pampel, A., and Turner, R. (2012) Fast accurate MR thermometry using phase referenced asymmetric spin-echo EPI at high field. In *Proceedings of the 20th Annual Meeting of ISMRM, Melbourne, Australia*, abstract 2664.

3. **Huber, L.**, Ivanov, D., Krieger, S. N., Gauthier, C. J., Roggenhofer, E., Henseler, I., Turner, R., and Möller, H. E. (2013) Measurements of cerebral blood volume and BOLD signal during hypercapnia and functional stimulation in humans at 7 T: Application to calibrated BOLD. In *Proceedings of the 21st Annual Meeting of ISMRM, Salt Lake City, USA*, abstract 3339.

4. Kennerley, A. J., **Huber, L.**, Mildner, T., Mayhew, J. E., Turner, R., Möller, H. E., and Berwick, J. (2013) Does VASO contrast really allow measurement of CBV at high field ($\geq$ 7 T)? An in vivo quantification using concurrent optical imaging spectroscopy. In *Proceedings of the British Chapter of ISMRM in York, UK.*

5. Krieger, S. N., **Huber, L.**, Egan, G. F., and Turner, R. (2013) CBV, CBF and BOLD weighted functional MRI at 7 T using combined multi RF excitation and EPI readout. In *Proceedings of the 5th Asia-Pacific NMR Symposium, Brisbane, Australia.*

6. Trampel, R., Schäfer, A., **Huber, L.**, Heidemann, R. M., Lohmann, G., and Turner, R. (2013) Negative BOLD in somatosensory cortex during simple finger tapping. In *Proceedings of the 21st Annual Meeting of ISMRM, Salt Lake City, USA*, abstract 2339.

7. Bazin, P. L., Schäfer, A., Dinse, J., Tardif, C., Wähnert, M., Hashim, E., **Huber, L.**, Geyer, S., Bock, N., and Turner, R. (2013) Fine details of cortical and sub-cortical anatomy revealed in vivo, by ultra-high resolution quantitative T1 mapping. In *Proceedings of the 19th Annual Meeting of the Organization of Human Brain Mapping, Seattle, USA*, abstract 3384.

8. Trampel, R., Schäfer, A., **Huber, L.**, Heidemann, R. M., Lohmann, G., and Turner, R. (2013) Negative BOLD in somatosensory cortex during simple finger

tapping. In *Proceedings of the 19th Annual Meeting of the Organization of Human Brain Mapping, Seattle, USA*, abstract 1064.

9. Krieger, S. N., Gauthier, C. J., Roggenhofer, E., Sehm, B., **Huber, L.**, Ivanov, D., Turner, R., and Egan, G. F. (2013) Comparison of directly measured and modeled calibrated BOLD M-values at 7 T. In *Proceedings of the 19th Annual Meeting of the Organization of Human Brain Mapping, Seattle, USA*, abstract 3427.

10. **Huber, L.**, Kennerley, A. J., Ivanov, D., Gauthier, C. J., Möller, H. E., and Turner, R. (2014) Trial-wise investigation of cerebral blood volume change in human brain at 7 T. In *Proceedings of the 22nd Annual Meeting of ISMRM, Milan, Italy*, abstract 3095.

11. Ivanov, D., Poser, B. A., **Huber, L.**, Pfeuffer, J., and Uludağ, K. (2014) Whole-brain perfusion measurements at 7 T using pulsed arterial spin labeling and simultaneous multi-slice multi-echo planar imaging. In *Proceedings of the 22nd Annual Meeting of ISMRM, Milan, Italy*, abstract 2698.

12. Krieger, S. N., Gauthier, C. J., Ivanov, D., **Huber, L.**, Roggenhofer, E., Sehm, B., Turner, R., and Egan, G. F. (2014) Repeatability of M, BOLD, CBF, and CMRO2 for cognitive tasks at 7 tesla. In *Proceedings of the 22nd Annual Meeting of ISMRM, Milan, Italy*, abstract 3101.

13. Trampel, R., Schmidt, J., **Huber, L.**, Schäfer, A., and Turner, R. (2014) The gray-white contrast in spin-echo imaging at 7 T. (2014) In *Proceedings of the 22nd Annual Meeting of ISMRM, Milan, Italy*, abstract 1490.

14. Ivanov, D., Poser, B. A., **Huber, L.**, Pfeuffer, J., and Uludağ, K. (2014) Whole-brain perfusion measurements at 7 T using pulsed arterial spin labeling and simultaneous multi-slice multi-echo planar imaging. In *Proceedings of the 20th Annual Meeting of the Organization of Human Brain Mapping, Hamburg, Germany*, abstract 1062.

15. Trampel, R., Schmidt, J., **Huber, L.**, Schäfer, A., and Turner, R. (2014) The gray-white contrast in spin-echo imaging at 7 T. In *Proceedings of the 20th Annual Meeting of the Organization of Human Brain Mapping, Hamburg, Germany*, abstract 1978.

16. **Huber, L.**, Goense, J., Kennerley, A. J., Trampel, R., Guidi, M., Gauthier, C., Turner, R., and Möller, H. E. (2014) Layer-dependent CBV and BOLD responses in humans, monkeys, and rats at 7 T. In *ISMRM Brain Function Workshop in Charleston, USA*.

Awards and stipends during this PhD project

1. Certificate of Merit at *ESMRMB Annual Meeting in Leipzig, Germany,* 2011.

2. ISMRM Trainee (Educational) Stipend, for the *21st ISMRM Annual Meeting and Exhibition in Melbourne, Australia*, 2012.

3. ISMRM Magna Cum Laude Merit Award for the conference talk: Cerebral blood volume changes in negative BOLD regions during visual stimulation in humans at 7 T. At the *22nd ISMRM Annual Meeting and Exhibition in Salt Lake City, USA*, 2013.

4. ISMRM Trainee (Educational) Stipend, for the *22nd ISMRM Annual Meeting and Exhibition in Salt Lake City, USA*, 2013.

5. ISMRM Trainee (Educational) Stipend, for the *23rd ISMRM Annual Meeting and Exhibition in Milan, Italy*, 2014.

6. ISMRM Summa Cum Laude Merit Award for the conference talk: Measuring changes in arterial and venous cerebral blood volume in human brain at 7 T. At the *23rd ISMRM Annual Meeting and Exhibition in Milan, Italy*, 2014.

7. ISMRM Magna Cum Laude Merit Award for the conference presentation: Trial-wise investigation of cerebral blood volume change in human brain at 7 T. At the *23rdISMRM Annual Meeting and Exhibition in Milan, Italy*, 2014.

8. Educational Stipend, for the *ISMRM Brain Function Workshop in Charleston, USA*, 2014.

9. Young Investigator Award for the talk entitled: Layer-dependent CBV and BOLD responses in humans, monkeys, and rats at 7 T. At the *ISMRM Workshop Functional MRI: Emerging Techniques and New Interpretations in Charleston, USA*, 2014.